The physical processes of star formation and the properties of the interstellar medium in the Magellanic clouds

Antigone Lambert-Huyghe

Université de Paris
Ecole doctorale d'astronomie et d'astrophysique d'Ile-de-France

Thèse de doctorat

présentée pour obtenir le grade de

docteur de l'Université de Paris
Spécialité : Astronomie et Astrophysique

par

Antigone Lambert-Huyghe

The physical processes of star formation and the properties of the interstellar medium in the Magellanic Clouds

Thèse dirigée par

Suzanne Madden

Présentée et soutenue publiquement le 26 février 2021

Jury composé de :

Isabelle Grenier,	Professeur des Universités, Université de Paris,	*présidente du jury*
Shobita Satyapal ,	University Professor, George Mason University,	*rapporteur*
Amelie Saintonge,	University Professor, University College London,	*rapporteur*
Carsten Kramer,	Directeur de Recherche, IRAM,	*examinateur*
Nicholas Abel,	University Professor, University of Cincinnati,	*examinateur*
Ilse De Looze,	University Professor, University of Ghent,	*examinatrice*
Suzanne Madden,	Directrice de Recherche, CEA AIM,	*directrice*

Quand on ne sait pas où l'on va, il faut y aller le plus vite possible - Les Shadoks

Abstract

The Interstellar Medium (ISM) harbours processes that play key roles in the evolution of galaxies. It hosts the signatures of the many feedback processes induced by star formation, including the metal enrichment (metallicity). This work aims to study the structure of the different gas and dust phases in star-forming regions, the cooling and heating processes at play, and how they are affected by the metallicity.

We focus on the Large and Small Magellanic Clouds (LMC and SMC), two dwarf satellites of the Milky Way: they have sub-solar metallicities, and their proximity allows us to have spatially detailed observations of star-forming regions. We complete those observations with the Dwarf Galaxy Sample (DGS) observations, that target 48 mostly unresolved dwarf galaxies of the Local Universe with different physical conditions.

We predict the emission lines [O III] 88μm, [O I] 63μm, [C II] 157μm, and the *Spitzer*/MIPS 24μm and 70μm bands using photoionization model grids. We develop a new method based on those tracers that infers the physical conditions of star-forming regions and we investigate the proportion of neutral phase of the star-forming ISM with respect to the ionized phase. We also calibrate a relation between [O III] 88μm and MIPS 24μm that holds for our resolved regions and the unresolved DGS, which can be useful to prepare future observations.

To study the heating and cooling processes, we focus on the neutral region, and compared two classical tracers of the heating in this phase, the PAHs emission and the total infrared luminosity to the main cooling lines, [C II] 157μm and [O I] 63μm. We show that in the LMC the PAHs are better tracers of heating in the neutral ISM.

Key words: ISM – galaxies: Magellanic Clouds – PAH – modeling: ISM – HII regions – fine structure cooling lines – infrared – IR spectroscopy – dwarf galaxies – star formation – ISM phases – photodissociation regions

Résumé

Le milieu interstellaire (MIS) abrite des processus jouant un rôle clé dans l'évolution des galaxies. Il contient la signature de nombreux processus induits par la formation stellaire, dont l'enrichissement en métaux (métallicité). Ce travail a pour but d'étudier la structure des différentes phases des régions de formation stellaire, les processus de chauffage et de refroidissement, et le rôle de la métallicité.

Nous nous concentrons sur les Grands et Petit Nuages de Magellan (GNM et PNM), deux galaxies satellites de la Voie Lactée: elles ont une métallicité sub-solaire, et leur proximité permet d'obtenir une excellente résolution spatiale des régions de formation stellaire. Nous complétons ces observations avec celles du Dwarf Galaxy Sample (DGS), 48 galaxies naines non résolues de l'Univers Local ayant des conditions physiques différentes.

Nous utilisons des grilles de modèles de photoionisation et photodissociation pour prédire les raies d'émission [O III] 88μm, [O I] 63μm, [C II] 157μm, et les bandes *Spitzer*/MIPS 24μm et 70μm. Nous avons développé une nouvelle méthode basée sur ces traceurs pour obtenir les conditions physiques des zones de formation stellaire et nous avons étudié la proportion de la phase neutre du MIS par rapport à sa phase ionisée. Nous avons également calibré une relation entre [O III] 88μm et MIPS 24μm, fonctionnant aussi bien pour les régions résolues des Nuages de Magellan que pour les régions intégrées et les galaxies du DGS. Cette relation peut être utilisée pour préparer de futures observations.

Pour les processus de chauffage et de refroidissement, nous avons restreint notre étude à la phase neutre, et comparé deux traceurs classiques du chauffage de cette phase, les PAH et la luminosité infrarouge totale, aux principales raies de refroidissement, [C II] 157μm et [O I] 63μm, montrant que les PAHs sont de meilleurs traceurs pour le chauffage.

Mots-clefs: MIS – galaxies: Nuages de Magellan – PAH – modélisation: MIS – régions HII – raies de refroidissement de structure fine – infrarouge – spectroscopie IR – galaxies naines – formation stellaire – phases du MIS – régions de photodissociation

Acknowledgements

Cette thèse a été effectuée au CEA Saclay, dans le laboratoire AIM CEA/Irfu/DAp. Elle a été co-financée par le CEA et une bourse universitaire.

Cette thèse est l'achèvement de trois ans de travail, mais aussi la réalisation d'un rêve d'enfance, et je voudrais remercier les nombreuses personnes qui y ont contribué. Tout d'abord, Jacques Le Bourlot, alors directeur de l'Ecole Doctorale, et Simona Mei, qui m'ont soutenue pour obtenir une demi-bourse universitaire malgré des conditions difficiles, et Suzanne, qui a permis de compléter ce financement grâce au CEA. Je souhaiterais également remercier Anne Decourchelle, ainsi que toute l'équipe administrative du Dap, pour m'avoir donné les moyens de réaliser ce travail.

Je remercie évidemment Suzanne pour son accompagnement tout au long de cette thèse, pour m'avoir laissé une grande liberté dans mon travail tout en surveillant avec bienveillance mon avancée, et pour ses encouragements fréquents qui m'ont beaucoup soutenue moralement. Je remercie également mes collaborateurs proches, Maud, Dangning, Lise, Fred, Diane, Sacha, Fiorella, Vianney, pour leur aide et leur disponibilité, mais aussi pour toutes les conversations non scientifiques, les blagues de Fred qui m'ont rappelé l'humour de ma famille, les discussions endiablées avec Dangning sur les expressions françaises, pour les séances d'escalade, pour avoir pu garder une ambiance de groupe malgré les confinements et problèmes dus à la pandémie de 2020, et surtout pour m'avoir considérée non pas comme une étudiante, mais comme une collègue. Je voudrais également remercier Vianney pour son aide précieuse sur les derniers mois de thèse, et tout spécialement lors de la réduction du manuscrit.

Ces trois années ont également été marquées par les voyages que j'ai réalisés, et de multiples rencontres. Merci à Mélanie, Ronin, Ilse, Albrecht, Xander, Nick, Margaret pour leur présences et nos discussions, longues ou courtes, scientifiques ou non. J'espère pouvoir collaborer avec eux à l'avenir.

Je voudrais aussi remercier tous ceux qui ont participé à l'animation du Dap, avec les conférences des invités et des post-docs, les Star Formation Lunch qui m'ont permis d'en apprendre plus et de me changer les idées tout à la fois, les petits-déjeuners du labo, les déjeuners et cafés avec les autres doctorants, et les réunions d'astromind2 qui m'ont permis de faire le lien entre mes recherches et celles de mon père, chercheur en chimie sur les origines de la vie.

Merci également à ma famille, qui à suivi mon travail, m'ont écouté présenter mes posters, et disserter sur la formation stellaire, alors qu'ils comprenaient généralement un mot sur deux (≪ C'est quoi déjà, le titre de ta thèse ? ≫). Merci à mes amis scientifiques pour leur moult discussions enthousiastes, en particulier Antoine, pour son soutient sans failles lors de la rédaction, et merci à mes amis non scientifiques, pour avoir tenté eux aussi de s'intéresser à mon travail lors de nos sorties. Merci à mon conjoint, pour avoir patiemment supporté mes crises de folie et mes humeurs lors de la rédaction du manuscrit, et pour m'avoir remonté le moral quand je pensais que je ne finirais jamais.

Je n'aurais jamais pu réaliser cette thèse sans l'aide et la collaboration de toutes ces personnes, et je tiens encore à les remercier du fond du coeur.

CONTENTS

Bibliography **157**

LIST OF FIGURES

LIST OF TABLES

INTRODUCTION

Galaxy formation and evolution from the primordial Universe to present days involve different processes. Some are linked to the environment, such as gravitational interactions, merger events, or inflow of intergalactic gas, but internal processes of the galaxy, such as star formation and their feedback, in the form of ionizing radiation, stellar winds, etc., are also thought to take part in the global evolution of galaxies. Stars create elements heavier than helium by nuclear fusion in the vicinity of stellar cores up to iron and through effects linked to the explosion of the most massive stars in supernovae (SN), for elements beyond iron, although the exact processes are still largely debated. This interplay between the stellar activity and the interstellar medium (ISM) is continually transforming the physical state of the phases of the ISM, the constituents of which are the gas and dust filling the space between the stars. Throughout its life cycle, the ISM harbors the reservoir of gas from which new stars form, and the cradle where older stars recycle their matter. Stars also inject energy in the ISM through radiative processes and dynamical effects, with jets and winds at the youngest stages, or winds and outflows from SN. Star formation also affects the dust formation and evolution, and is thus controlling the full evolution of baryonic matter in galaxies. A detailed investigation of the ISM phases probes the physical conditions and processes occurring and allows us to acquire a better understanding of the evolution of the phases within galaxies along with the stellar evolution taking place.

The quantity of heavy elements, also called metals, has a strong influence on the ISM of galaxies and star formation process and the precise details of how low metal abundance effects stellar formation activity and its surrounding ISM is still tainted with large uncertainties. Thus, the study of the ISM with low metallicity could give us some insight into star formation conditions and interplay with the ISM, of galaxies existing in the early Universe, where distance forbids us to have spatially resolved observations. In the local Universe, there is a wide variety of dwarf galaxies with low metallicity ISM, that can be used as proxies to study conditions that might resemble those of early universe galaxies or perhaps help us to more accurately speculate to these conditions.

The Large Magellanic Cloud (LMC) and the Small Magellanic Cloud (SMC), are the closest neighbours of the Milky Way. With their low metallicity ISM (1/2 $Z_\odot$ for the LMC and 1/5 $Z_\odot$ for the SMC), and their proximity to us (50 kpc and 61 kpc respectively), they are ideal laboratories to investigate the effects of metallicity on the physical properties and processes with excellent spatial resolution of different ISM phases.

In Chapter 1, we give a general overview of the different phases in galaxies with a specific focus on their star-forming ISM. We then describe some effects specifically induced by the low metallicity in dwarf galaxies, and give more detail on the Magellanic Clouds, which are at the center of our study. We describe in Chapter 2 the specific star-forming regions of the Magellanic Clouds we study, with a detailed examination of the observations we use, and the facilities from which the observations originate, namely the space telescopes *Spitzer* and *Herschel*. We also describe the photoionization and photodissociation software Cloudy, which we use to prepare models of the ISM (Chapter 3). We describe the inputs we used to prepare the model grids, and the evolution of the output within the grids. We pay particular attention to tracers that we use in the following chapters, some far-infrared (FIR) lines ([C II] 157μm, [O I] 63μm, [O III]

88μm), some mid-infrared (MIR) and FIR continuum bands (24μm, 70μm, 100μm) and the total infrared luminosity, TIR.

We then focus on the use of dust and gas in the ionized phase (Chapter 4) to constrain the properties of the H II regions with the use of Cloudy model grids. More precisely, we discuss the relation between [O III] 88μm which is an unambiguous tracer of the ionized gas (Chapter 3), and the 24μm band, which is often implicitly considered as a tracer for dust emission in the ionized phase. We then try to understand the physical conditions that could be probed by the tracers we have, for the complete sample and for each region taken individually. We also investigate the predictive capabilities of some tracers, in order to provide a calibration for future follow-up observations. Finally, we investigate the heating and cooling processes in photo-dissociation regions (PDRs) in Chapter 5. We focus particularly on the heating of PDR gas by the photoelectric effect (PE), which involves very small grains or very large molecules (PAHs), and tested different tracers of the PE heating efficiency to determine their accuracy at tracing the PDR gas heating and search for potential contamination by the ionized phase in the PDR tracers.

CHAPTER 1

THE INTERSTELLAR MEDIUM

Contents

Galaxies are complex networks of physical components and processes that work together to influence how stars are being formed, driving galaxies along their evolutionary paths. As this study delves into the details of the different phases of the ISM of galaxies, in order to be able to put this study into the context of the big picture of galaxies, we look into the global view of the current knowledge of the interstellar medium (ISM) in galaxies, their composition, structure and physical conditions. We will describe some general properties of galaxies, and present the gas and dust properties, as they represent two main components of the ISM. Then, we will focus on the observational probes of the ISM, bringing to light the diagnostic tracers that can be used. We will finally describe the characteristics of low metallicity dwarf galaxies, with a focus on the Large and Small Magellanic Clouds (LMC and SMC respectively), which are at the center of this study.

1.1 Overview on the ISM of galaxies

1.1.1 Galaxy composition

As a first approximation, galaxies can be considered as gravitationally bound ensembles of stars, gas and dust, embedded in a halo of dark matter. The stars are separated by large distances ($\sim$ 2 pc in the solar neighbourhood), but the space between them is filled with a mixture of gas and dust comprising the *interstellar medium* (ISM). The ISM is mostly composed of hydrogen and helium, with a small fraction of heavier elements and represents a few percent of the total baryonic mass of a galaxy. It exists as an ensemble of different phases, the chemical and physical

properties of which depend on the local sources of energy and other environmental factors. The relative importance of the different galactic components can vary significantly from one galaxy to another, in term of mass or luminosity, depending on the morphology and the star formation activity, for example. We give an idea of the mass and luminosity of each component in the Milky Way in Table 1.1, as an example.

Component	Mass ($M_\odot$)	Luminosity ($L_\odot$)
Stars	1.8×10^{11}	$\sim 4.8 \times 10^{10}$
Gas	4.5×10^{9}	$\sim 2 \times 10^{8}$
Dust	$\sim 4.5 \times 10^{7}$	$\sim 1.7 \times 10^{10}$
Dark matter	$\geq 10^{12}$	–

TABLE 1.1: Mass and luminosities of the different components of the Milky Way. Adapted from Tielens (2005).

The gas and dust are heated by photons emitted by stars mostly in UV and optical wavelength range, by interactions with cosmic rays, by winds of energetic particles, and by X-rays emitted by hot gas. The cooling processes depend on the local physical conditions, in particular density and temperature, leading to the production of line and continuum ISM coolants, especially in the optical and infrared (IR) wavelength domains. Some specific events and highly energetic objects (gamma-ray bursts, cataclysmic binaries, neutron stars, black hole accretion, etc.) contribute to radiation ranging from hard X-rays to gamma rays. Thus, galaxies emit in the entire electromagnetic wavelength range, and the energy at each wavelength is controlled by a variety of physical processes. As an example, the spectral energy distribution (SED) of a galaxy is illustrated in Figure 1.1.

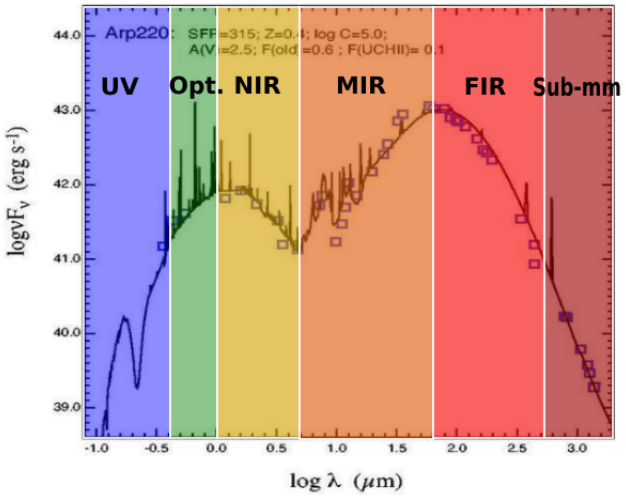

FIGURE 1.1: Illustration of the SED of a galaxy (here Arp 220) from UV to sub-mm, adapted from Groves et al. (2008).

The wavelength domains represented in Figure 1.1 cover photons from ultraviolet (UV, from 0.1 to 0.4μm), visible (from 0.4 to 0.7-1μm), near infrared (NIR, 0.7-1 to 5μm), mid-infrared (MIR, 5 to 40μm), far infrared (FIR, 40 to 350μm) and sub-millimeter (sub-mm, 350 to a few $10^3\mu$m) wavelengths. Stars are mostly emitting in the UV and visible range, while the most massive stars ($\geq$8 $M_\odot$), are strong emitters of UV photons which are then often absorbed by dust, creating

an obscured view of their activities. This absorbed energy is re-emitted in the IR wavelength range. Therefore, having a complete picture of a galaxy requires observations over the largest wavelength range possible, and constructing models of a galaxy's SED requires accounting for a wide variety of physical processes and conditions.

1.1.2 Metal enrichment of the ISM

At the beginning of the Universe, the formation process of the first atoms mainly created hydrogen and helium, with traces of lithium and beryllium. Most of the elements heavier than helium, up to iron, are called metals and were created by nuclear fusion in the core of stars and subsequently released by stellar winds and the death of stars. Elements heavier than iron are created by other mechanisms still debated, but are probably linked to supernova events and/or the merging of two neutron stars. The metallicity is defined as the mass fraction of metals, noted as Z. Mass fractions of hydrogen and helium are often noted X and Y, leading to the total baryonic mass ($M_{\rm baryon}$) as:

$$M_{\rm baryon} = X + Y + Z \tag{1.1}$$

An other way to express metallicity is:

$$\begin{aligned} Metallicity &= 12 + \log\left(\frac{N_{\rm X}}{N_{\rm H}}\right) \\ &= 12 + \left[\frac{X}{H}\right] \end{aligned} \tag{1.2}$$

where $N_{\rm X}$ is the column density of any element, X, depending on what is chosen for the measurement, and $N_{\rm H}$ is the column density of hydrogen. This method relies on only one element, and on the column density, thus an appropriate choice of the reference element can lead to a relatively easy estimate, in principle. However, inferring the abundances of the other elements based on the estimation of only one element, can bring challenges if the abundances of the different heavy elements are not scaling together. The metallicity, defined with Equation 1.2 is often based on the oxygen abundance for ISM studies, but the iron abundance is preferred in stellar studies. The determination of metallicity is often stated by comparison of its value in the solar neighbourghood, where we have $Z_\odot = 0.0142$, or $12 + \log[O/H] = 8.69$ (e.g. Asplund et al., 2009).

As each generation of stars forms metals and releases them at their death into the ISM of galaxies, the metallicity of a galaxy is a tracer of the history of stellar activity, and should, overall, increase while the galaxy ages and experiences more star formation cycles. However, most massive stars have shorter lifetimes compared to lower mass stars, and inflows of pristine gas and outflows of chemically enriched gas can complicate the simple picture of metal enrichment of a galaxy by its star formation. Other events like merging of galaxies can also blur the evolution of a single galaxy. Thus, the relation between age and metallicity is not thought to be so simple. The relative abundances of the different elements is also subject to variations between galaxies, and with time. As an example, oxygen is produced by massive stars, which have a lifetime of a few Myrs, whereas carbon and nitrogen are also formed by intermediate and low-mass stars, which can live for a few Gyrs. Thus, the ratios C/O and N/O are thought to be low after a starburst event, as the oxygen abundance is enhanced before carbon and nitrogen. The metallicity may also not be uniform within a galaxy: dying stars inject newly formed metals into their close surrounding, from which heavy elements diffuse throughout all the ISM, with a speed that depend on the mixing processes and their timescales. Thus, galaxies can show a metallicity

gradient, or even patchy metallicity (see e.g., Grand et al., 2019; Peña & Flores-Durán, 2019; Lian et al., 2019, and references therein).

There are several methods to determine the metallicity from observations (see Kunth & Östlin, 2000, for a review). Those methods include: spectroscopic determination from H II regions, (Pagel, 1997; Izotov et al., 2006) spectroscopic observations of planetary nebulae (PNe), focusing expecilaly on the oxygen element (Pagel, 1997), photometry of resolved stellar population, with the colour of the red giant branch in the Hertzsprung-Russell diagram (e.g. Lee et al., 1993), or spectroscopic study of individual stars, which requires high spatial resolution, and is thus only possible in the Milky Way and nearby galaxies (e.g. Haser et al., 1998, in the LMC).

1.1.3 Evolution of galaxies and scaling relations

Galaxies are not static environments: they evolve through cosmic time, form stars, accrete gas or merge together. The hierarchical scenario of galaxy evolution is one of the proposed scenarios (Dekel & Silk, 1986), where large, massive galaxies form from smaller building blocks. In that scenario, dwarf galaxies at high redshift are the progenitors of large galaxies in the today's nearby universe, including the Milky Way.

Among the important drivers of galaxy evolution is the process through which baryons are cycled within galaxies over time. Figure 1.2 illustrates the evolution of baryonic matter through the ISM, star formation, and ejection of matter by dying stars and SN events.

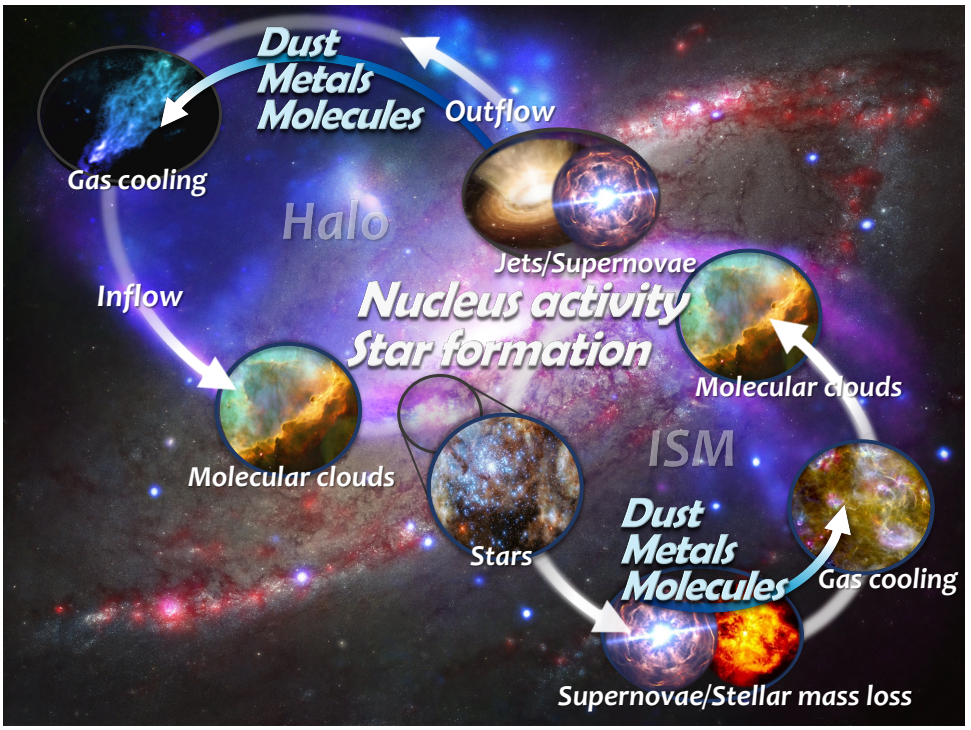

FIGURE 1.2: Illustration of the baryon cycle of galaxies. Figure credit: H. Kaneda.

The evolution of galaxies and its drivers have been studied through relations between different physical parameters, among which are the stellar mass, the gas mass, the luminosity or the star formation rate (SFR). Among the scaling relation commonly used to relate gas and star formation in galaxies is the Kennicutt-Schmidt relation (Schmidt, 1959; Kennicutt, 1998), which has recently been expanded cover a wide range of galaxies including extreme, luminous galaxies,

as well as more normal, non-starbursting galaxies (Kennicutt & de los Reyes, 2020). A tight empirical relation shows that the surface density of the star formation rate (SFR) varies as a power law with the surface density of neutral and molecular cold gas in a galaxy with the power law index, when combining all of the galaxies in the most recent study, to be 1.5±0.05. At the scale of giant molecular clouds (GMCs), which are the birth sites of star formation in the galaxies, it seems that SFR can be more tightly correlated with the molecular gas than with the total neutral gas (e.g., Bigiel et al., 2009; Daddi et al., 2010; Chevance et al., 2020a).

In star-forming galaxies, star formation rate also roughly correlates with the stellar as a power law (see e.g., Popesso et al., 2019; Johnston et al., 2015, and references therein), giving rise to the so-called main sequence of galaxies (Figure 1.4). This relation seems to suggest that galaxies form stars at a regular rate which seems to decline smoothly for lower mass galaxies. There is also an evolution of SFR with redshift (e.g., Shin et al., 2020) which shows that the star formation activity was growing from the early epochs and peaked at a redshift of z∼2 and has been declining since then to today (Madau et al., 1996; Madau & Dickinson, 2014). Evolution of the SFR with redshift is illustrated in Figure 1.5.

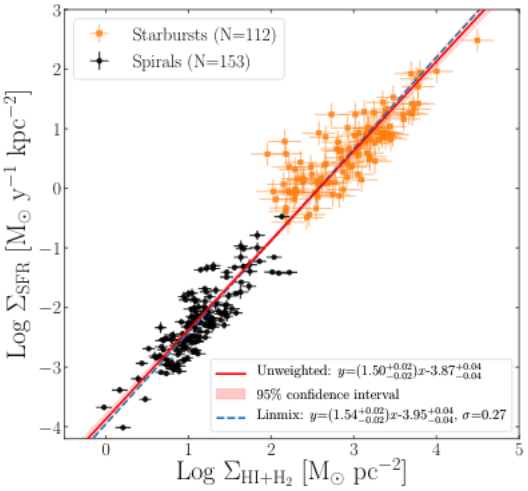

FIGURE 1.3: Empirical relation of the log of the surface density of star formation, ΣSFR vs. the log of the surface density of the total neutral gas, Σ(HI + H_2) from Kennicutt & de los Reyes (2020)

From all of these relations, we see that star formation is a major driver of galaxy evolution. It is at the center of different processes, such as chemical enrichment, outflows, exhaustion of gas reservoir, and it controls the baryonic cycle in galaxies (Figure 1.2). Thus, understanding star formation is a critical aspect in understanding the behaviour and evolution of galaxies. As the ISM is the reservoir from which new stars form, but also the cradle where stars recycle their material at their death, it is in constant interplay with stars, and is key to understanding the star formation and its role in shaping galaxies.

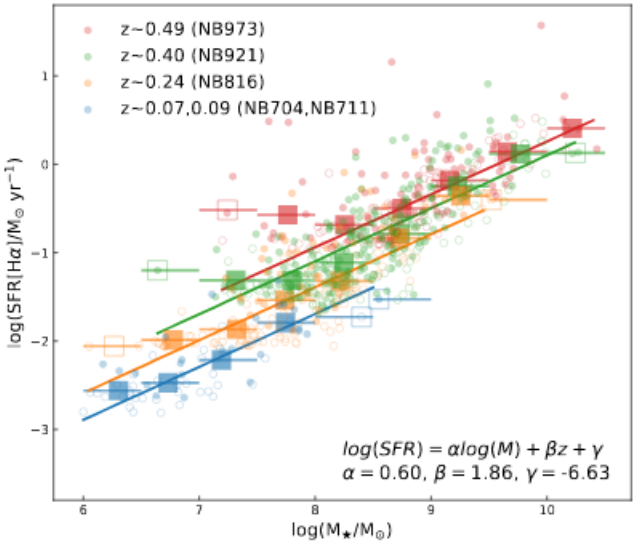

FIGURE 1.4: Main sequence of galaxies demonstrating the scaling relation of star formation with stellar mass, from Shin et al. (2020). Different slopes are derived for the different redshift bins, already showing an evolution of the relation with time.

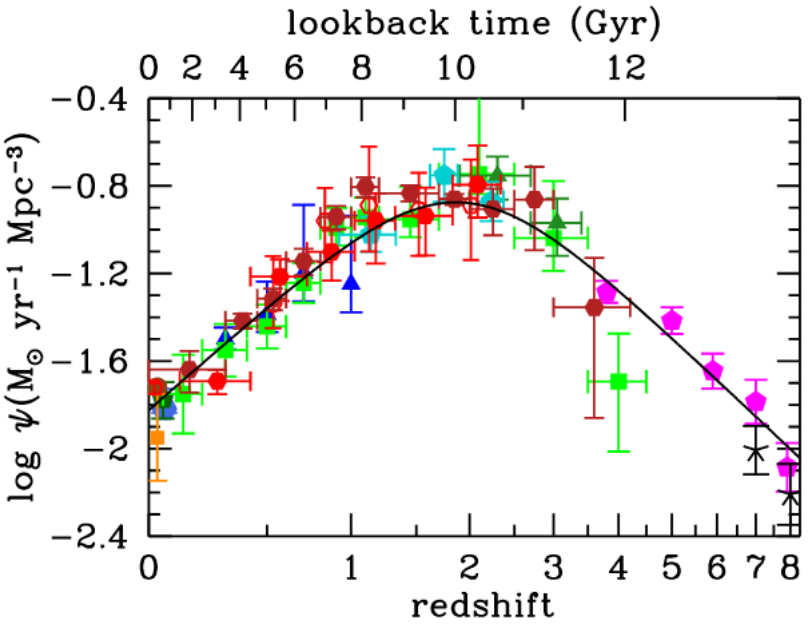

FIGURE 1.5: Evolution of the surface density of SFR, $\Sigma_{\rm SFR}$, with redshift (Madau & Dickinson, 2014), where data is compiled from local Universe to high-z surveys. The various colors and/or symbols differenciate the surveys used for the study.

1.2 Galaxies are made up of different ISM phases

1.2.1 General view of dust and gas properties

The ISM is complex and multiphase. It can be described by many physical parameters, among which are the density, the pressure, the radiation field, the magnetic field and the temperature.

Some general characteristics of the major phases in galaxies are summarized in Table 1.2.

Phase		Density cm^{-3}	Temperature K	Mass $M_\odot$
Ionized	H II region	$\simeq$ 1 - 10^4	$\simeq$ 10,000	5×10^7
	Warm diffuse	$\simeq$ 0.03	$\simeq$ 8,000	10^9
	Hot	$\simeq 6\times10^{-3}$	$\simeq 5\times10^5$	10^8?
Atomic (H I)	Cold	$\simeq$ 25	$\simeq$ 100	1.5×10^9
	Warm	$\simeq$ 0.25	$\simeq$ 8,000	1.5×10^9
Molecular (H_2)		$\geq$ 1,000	$\leq$ 100	$\simeq 10^9$

TABLE 1.2: The different phases defined in the ISM and some of their main characteristics, as summarized in Lequeux (2003)

The composition of the ISM is often divided, in simple terms, into two components: the gas and the dust. The ISM harbors neutral and ionized atoms as well as molecules that are formed through a chemical network that depends on the local conditions. Molecules, neutral atoms and ions are detected through line emission, some of which arise from fine structure (atomic and ionic species), and from rotational and/or vibrational transitions (molecules). The emitting species depend on the physical conditions of the phases. The ISM is often thought to be globally in pressure equilibrium (Tielens & Hollenbach, 1985; Hollenbach & Tielens, 1999; Tielens, 2005; Osterbrock & Ferland, 2006), although dynamical feedbacks (winds, jets, shocks...) complicate the picture.

Among the important and pervasive molecules of the ISM, are the polycyclic aromatic hydrocarbons (PAHs), composed of carbon and hydrogen atoms and covering a large variety of sizes and shapes (Figure 1.6). They were originally proposed to explain unidentified bands of IR emission, between 3 and $\sim$20μm (Leger & Puget, 1984), and play an important role in the heating of ISM gas (Tielens & Hollenbach, 1985; Weingartner & Draine, 2001c,c; Draine & Li, 2007; Tielens, 2008). PAHs lie between the properties of molecules and dust grains, although they are more often included in dust models than in gas models. Their emission bands are due to stretching and bending of the C-C and C-H bonds. They are found preferentially in photodissociation regions (PDRs; see Section 1.2.3), as they are often destroyed in highly ionized regions or in the presence of shocked medium (e.g. Lebouteiller et al., 2011).

Dust in the ISM is composed of refractory elements, such as the silicon, carbon or iron, that are depleted from the gas phase (see e.g., Galliano et al., 2018a, for a review of dust properties). The dust grains can have a variety of sizes and composition, and can be covered by ice mantles under some conditions. Dust absorbs starlight from UV and optical wavelengths, and re-emits in IR wavelengths.

The emission and absorption of dust depend on many physical parameters including grain size, dust composition, grain structure and porosity, grain temperature etc. Dust temperature will also shape the global IR SED of a galaxy, by changing the position of the peak of the continuum, depending on the temperature. The SED peak normally lies between MIR and FIR wavelengths, with shorter wavelengths emission characteristic of warmer dust and longer wavelength emission often dominated by cooler dust (see Figure 1.1).

1.2.2 Ionized phase

When they are interacting with the ISM surrounding young stars, UV photons with energies greater than 13.6 eV ionize the gas, and create bubbles and H II regions in which hydrogen is almost fully ionized. The H II regions are typically extending around O and B-type stars, which

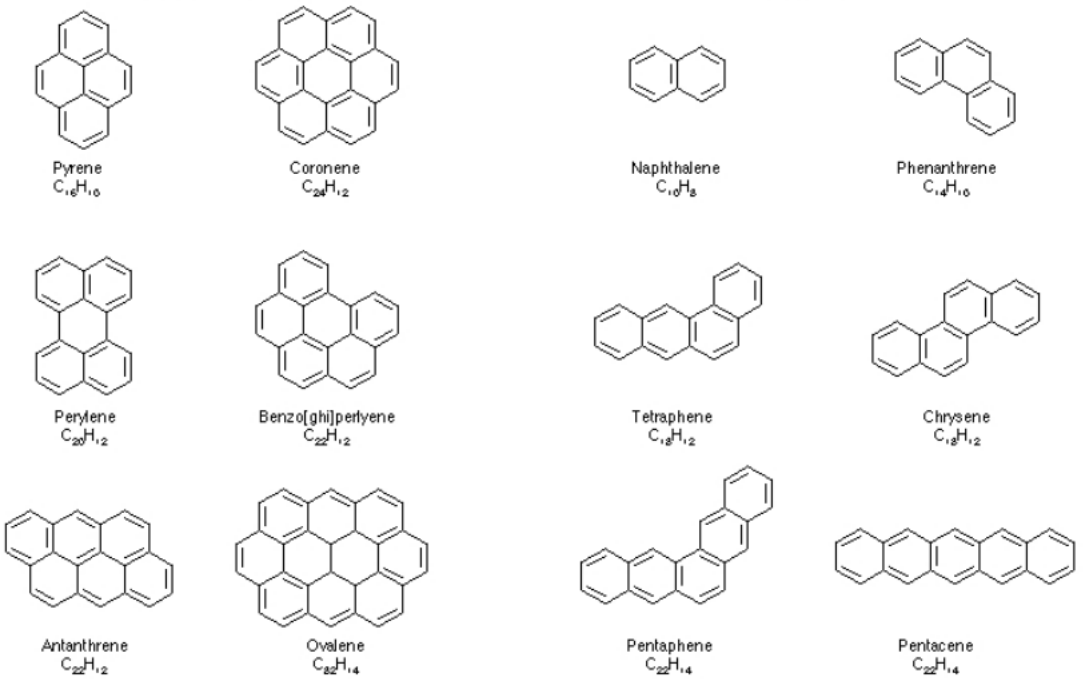

FIGURE 1.6: Examples of PAH molecules that can be found in the ISM. All the molecules presented here are planar.

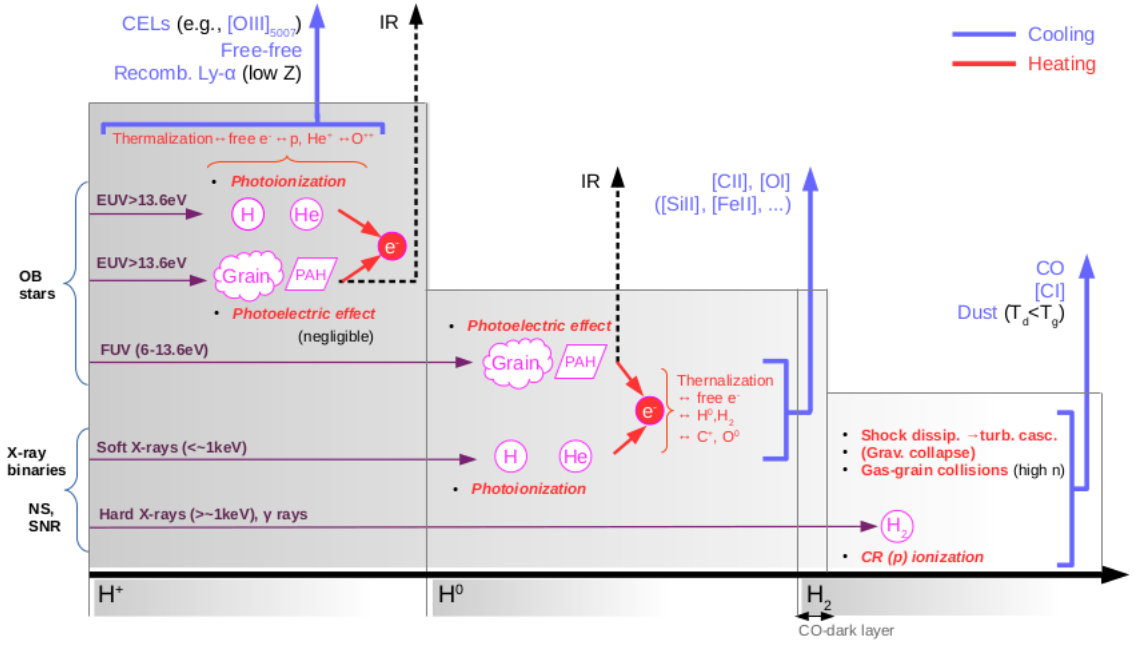

FIGURE 1.7: This figure illustrates the heating and cooling processes in the ISM for the different phases (blue for the cooling, red for the heating). The mechanical heating (e.g., shocks) are ignored in this figure. Sources of ionization are indicated to the left of the figure, with NS for neutron star and SNR for supernova remnant. CELs is for collisionally-excited lines. Figure credit: V. Lebouteiller.

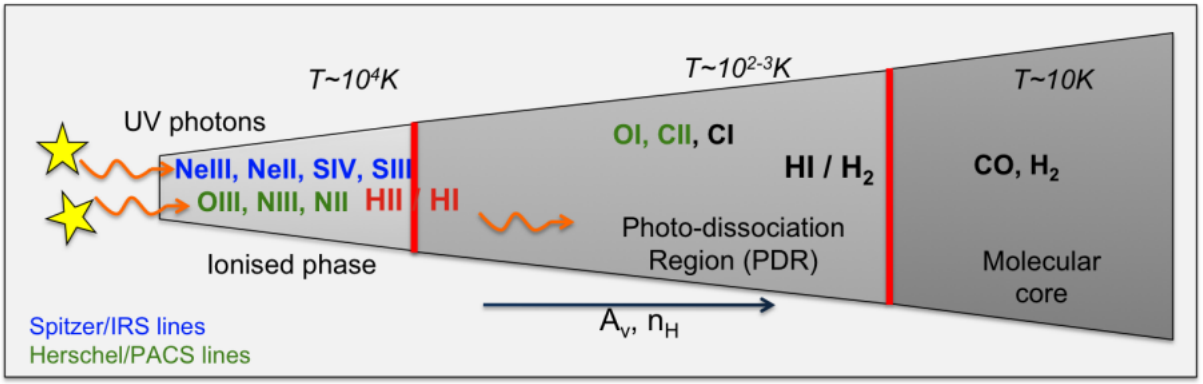

FIGURE 1.8: This figure illustrates the main gas phases of the H II regions, PDRs and molecular clouds surrounding stellar sources, and indicates some of the specific tracers for each of the regions of H II regions and PDRs. Figure adapted from (Tielens & Hollenbach, 1985)

are the most massive and the shortest-lived stars. They have typical temperature of $\sim 10^4$ K, and densities that spawn a large range, between 1 cm^{-3} and 10^5 cm^{-3}. When the high energy photons escape from the surroundings of young massive stars, they can ionize a low density medium ($\sim 10^{-1}$ cm^{-3}), the warm ionized medium (WIM; see Table 1.2). In the Milky Way, the WIM corresponds to 95% of the ionized gas, and up to 25% of the total volume (Tielens, 2005).

In H II regions the principal heating process is the photoionization of hydrogen by high energy UV photons. In the process of photoionization, the energy released to the gas corresponds to the difference between the initial photon energy and the energy needed to eject the electron from the hydrogen atom. The cooling of H II regions is essentially made by collisionally-excited lines (CELs) of metals, such as the MIR forbidden fine-structure lines [S IV] 10.5μm, [S III] 18.7μm, [Ne II] 12.8μm or [O III] 88μm. IR emission lines are efficient coolants of the ionized ISM, and normally suffer little extinction by dust. The Ly-α line is also a cooling line in the ionized phase, and it is even one of the main cooling processes in extremely metal-poor galaxies (Barnes et al., 2014), due to the low abundance of metals. The ionized gas components in galaxies can also be characterized via their free-free radio emission.

1.2.3 Photodissociation regions

Photodissociation regions are the transition regions between H II region and molecular cores of clouds (Figure 1.8). The most energetic photons are absorbed before the ionization front, which is the transition from ionized to neutral hydrogen. In this region, the chemistry and heating are dominated by FUV photons with energies between 6 and 13.6 eV. PDRs include cold and dense atomic material, as well as a transition into the molecular region. As some of the FUV photons traverse into the PDRs beyond the ionization front, neutral atomic species such as H^0, C^0 and O^0 can co-exist with some ionic species that have an ionizing potential lower than 13.6 eV, such as C^+ and Si^+. Deeper into the cloud ($A_V \geq 1$), the flux of photons capable of photodissociating H_2 have been attenuated by previous gas and dust layers, and molecular hydrogen can form. It is difficult to observe rotational transitions of H_2 directly, as it is a symmetric molecule. CO, as the next most abundant molecule, is easily observed at millimetre wavelengths and, through the use of a conversion factor, X_{CO} (e.g., Bolatto et al., 2013), is most often used to quantify the total molecular gas in local as well as high redshift galaxies (Leroy et al., 2009; Bigiel et al., 2011; Schruba et al., 2012; Heyer & Dame, 2015; Saintonge et al., 2017; Tacconi et al., 2010, 2020;

Daddi et al., 2010, 2015; Combes et al., 2013; Walter et al., 2014; Kamenetzky et al., 2018). Due to differences of formation conditions, and especially self-shielding, other molecules like CO may not always co-exist with H_2. For example, CO is dissociated by UV photons, where H_2 is mostly dissociated by photons from the Lyman-Werner band, which become optically thick for moderate A_V, allowing H_2 to be self-shielded from photodissociation, where CO relies more on shielding by dust see e.g., Gnedin & Draine, 2014. Thus, molecular gas which is not traced by CO, called the CO-dark gas (Grenier et al., 2005; Wolfire et al., 2010), can exist outside of the CO region. This CO-dark molecular gas can be an important reservoir of H_2 gas particularly in low metallicity galaxies (e.g., Madden et al., 2020), where CO is mostly photodissociated due to the low dust abundance available to shield it from UV radiation and, therefore, difficult to detect. Efforts have been made to produce calibration of the X_{CO} factor depending on physical conditions of the galaxies, including the metallicity (Schruba et al., 2012; Bolatto et al., 2013; Accurso et al., 2017b). In metal-rich galaxies, dust grains produce efficient shielding for molecules, and this layer of CO-dark gas is thin, allowing CO to be an accurate proxy for H_2 gas mass measure. Deeper into the cloud, $A_V \simeq 2.5$, oxygen transforms from atomic to molecular form, being fully into the denser molecular core.

The principal heating process of the PDR gas is via the photoelectric ejection of electrons from very small dust grains (VSGs) or PAHs (Bakes & Tielens, 1994; Tielens & Hollenbach, 1985; Croxall et al., 2012; Weingartner & Draine, 2001c,b). Deeper in the cloud, when H_2 is formed, FUV pumping of H_2 can become an important source of heating: the absorption of a FUV photon pumps the molecule to a bound electronic state, and in 10-15% of the cases it de-excites by dissociating the molecule. In the other cases (85-90%), it falls down to an excited state of the molecule and cascades down to the ground state by emitting IR photons from rovibrationnal transitions or by collisions in the densest media ($\geq 10^4$-10^5 cm^{-3}). The cooling in this region is due to IR emission lines from fine structure levels. Major coolants are [C II] 157μm and [O I] 63μm, although some other lines can also play an important coolant role (e.g., [Fe II] 26μm or [Si II] 34.8μm, and [C I] 370μm and [C I] 609μm).

1.2.4 Molecular phase

The molecular phase is the coldest ($\sim$10 K) and the densest phase ($\geq$ 200 cm^{-3}), characterised by the presence of a wide variety of molecules, which can exist mainly due to dust shielding. Molecular clouds only fill a very small volume fraction in the ISM, but they cover a wide range of properties, in terms of mass (10^3 to 10^6 $M_\odot$), size (typical size of a few tens of pc) and temperature (10s of K). Molecular clouds are the sites of star-formation with typical lifetimes of $\sim 10^7$ yrs, while the actual period of star-formation is much shorter ($\sim$5 Myrs Chevance et al., 2020a).

Molecules form from a number of processes,in the gas phase, mostly from ion-molecule induced chemistry initiated by cosmic rays. Molecules also commonly form on the surface of dust grains at cold temperature, and can be evaporated to the gas phase. With sufficient self-shielding some molecules (e.g., H_2) may also form from collisional processes. While molecules can be formed in an excited state, and then transmit this energy to the gas, the major sources of heating in the molecular gas phase are X-rays from energetic sources, gamma-rays and cosmic rays. The cooling of the gas is primarily due to molecular rotational and rovibrational transitions in the FIR, sub-millimeter and millimeter wavelength domains. At low density, the cooling in molecular clouds is dominated by CO transitions, as it is one of the most abundant molecules. At higher densities, the cooling is dominated by other molecules, such as HCO^+, HCN, CO_2 and H_2O.

Line	Wavelength (μm)	Transition	E.P. (eV)	I.P. (eV)	ΔE/k (K)	Critical density (cm^{-3})
Spitzer/IRS			(a)	(b)	(c)	(d)
[Ar II]	6.99	$^2P_{1/2}$ - $^2P_{3/2}$	15.76	27.63	1 600	4×10^5[e]
[Ar III]	8.99	$^3P_1$ - $^3P_2$	27.63	40.74	2 060	3×10^5[e]
[**S** IV]	10.51	$^2P_{3/2}$ - $^2P_{1/2}$	34.7	47.22	1 369	5×10^4[e]
[**Ne** II]	12.81	$^2P_{1/2}$ - $^2P_{3/2}$	21.56	40.96	1 123	7×10^5[e]
[Ne V]	14.32	$^3P_2$ - $^3P_1$	97.12	126.21	592	3×10^4[e]
[**Ne** III]	15.55	$^3P_1$ - $^3P_2$	40.96	63.45	925	3×10^5[e]
[Fe II]	17.93	$^4F_{7/2}$ - $^4F_{9/2}$	7.90	16.19	802	5×10^4[e]
[**S** III]	18.71	$^3P_2$ - $^3P_1$	23.34	34.7	769	2×10^4[e]
[Ar III]	21.82	$^3P_0$ - $^3P_1$	27.63	40.74	659	4.7×10^4[e]
[Fe III]	22.92	$^5D_3$ - $^5D_4$	16.19	30.65	627	1×10^5[e]
[Ne V]	24.20	$^3P_1$ - $^3P_0$	40.96	63.45	592	5×10^4[e]
[Fe II]	26.55	$a^6D_{7/2}$ - $a^6D_{9/2}$	7.90	16.19	554	1×10^4[e]|2×10^6[H]
[**S** III]	33.47	$^3P_1$ - $^3P_0$	23.34	34.7	430	7×10^3[e]
[Si II]	34.81	$^2P_{3/2}$ - $^2P_{1/2}$	8.15	16.35	413	1×10^3[e]|3×10^5[H]
[Ne III]	36.00	$^3P_0$ - $^3P_1$	40.96	63.45	400	2×10^4[e]
Herschel/PACS						
[O III]	51.80	$^3P_2$ - $^3P_1$	35.12	54.94	278	3.6×10^3[e]
[N III]	57.32	$^2P_{3/2}$ - $^2P_{1/2}$	29.60	47.45	251	3×10^3[e]
[**O** I]	63.17	$^3P_1$ - $^3P_2$	-	13.62	228	5×10^5[H]
[**O** III]	88.33	$^3P_1$ - $^3P_0$	35.12	54.94	163	5×10^2[e]
[N II]	121.77	$^3P_2$ - $^3P_1$	14.53	29.60	118	3×10^2[e]
[O I]	145.49	$^3P_0$ - $^3P_1$	-	13.62	99	1×10^5[H]
[**C** II]	157.64	$^2P_{3/2}$ - $^2P_{1/2}$	11.26	24.38	91	50[e]|3×10^3[H]
[N II]	205.24	$^3P_1$ -$^3P_0$	14.53	29.60	70	45[e]
Other lines						
[C I]	370.27	$^3P_2$ - $^3P_1$	-	11.26	39	1.2×10^3[H,H_2]
[C I]	609.59	$^3P_1$ - $^3P_0$	-	11.26	24	4.7×10^2[H,H_2]
CO	2600.05	J $\leftrightarrow$ 1−0	11.09	14.01	5.5	1.1×10^3[H_2]

(a) Excitation potential: energy needed to create the specie
(b) Ionization potential: energy needed to ionize the specie
(c) Excitation temperature T=ΔE/k necessary to populate the transition upper level
(d) Critical densities are noted with [e] when collisions are made by electrons ($T = 10,000K$) and [H] with atomic hydrogen ($T = 100K$)
References: Malhotra et al. (2001); Giveon et al. (2002); Tielens (2005); Osterbrock & Ferland (2006); Kaufman et al. (2006); Ferland et al. (2009); Stacey (2011); Walker et al. (2015).

TABLE 1.3: Characteristics of emission lines observed with *Spitzer* and *Herschel* telescopes, with some FIR and mm lines of importance. The lines in bold are those used in this study.

1.2.5 Tracers of the phases

Table 1.3 summarises the characteristic of lines that are tracers of the different phases of the ISM in star-forming regions. Most of these tracers were available with *Spitzer* and *Herschel* telescopes, and some available today with the *SOFIA* telescope.

To trace the ISM conditions, in this study we rely on IR lines obtained by spectroscopy and complement these with continuum broad band observations. We list some of the emission lines that were accessible with the *Herschel* and *Spitzer* space telescopes in Table 1.3, with some of their important characteristics. The broad range in critical densities and energy potential of these IR lines illustrates their valuable diagnostic capabilities to probe different ISM phases (Figure 1.9). IR lines have the advantage of being mostly extinction-free in most cases. However, some of these are faint, and were not well detected in some of our sample (see Chapter 2 for

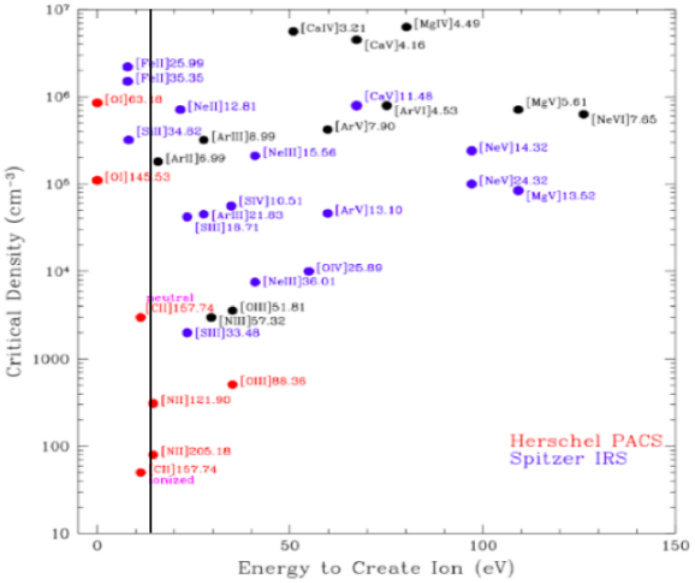

FIGURE 1.9: Energy potential (E.P.), i.e., energy needed to create the ion, versus the critical density for the fine structure lines accessible with *Spitzer* and *Herschel* telescopes. A black vertical line indicates the energy of 13.6 eV. Emission lines from ions requiring an energy below this limit trace mostly the neutral phase. The lines arising from ions that require an energy higher are mostly tracers of the ionized phase. Figure from Kennicutt et al. (2011).

more details). The tracers used in this study are indicated in bold in Table 1.3.

The accumulation of observations of the IR range can bring a clearer view of the ISM, and one advantage is the possibility to analyse the emission of a galaxy in terms of its different components. In Figure 1.10, we show a decomposition of the spectrum of a normal late-type galaxy. The local galactic conditions influence the characteristics of the different spectral components, which lead to changes in the observed global SED of a galaxy.

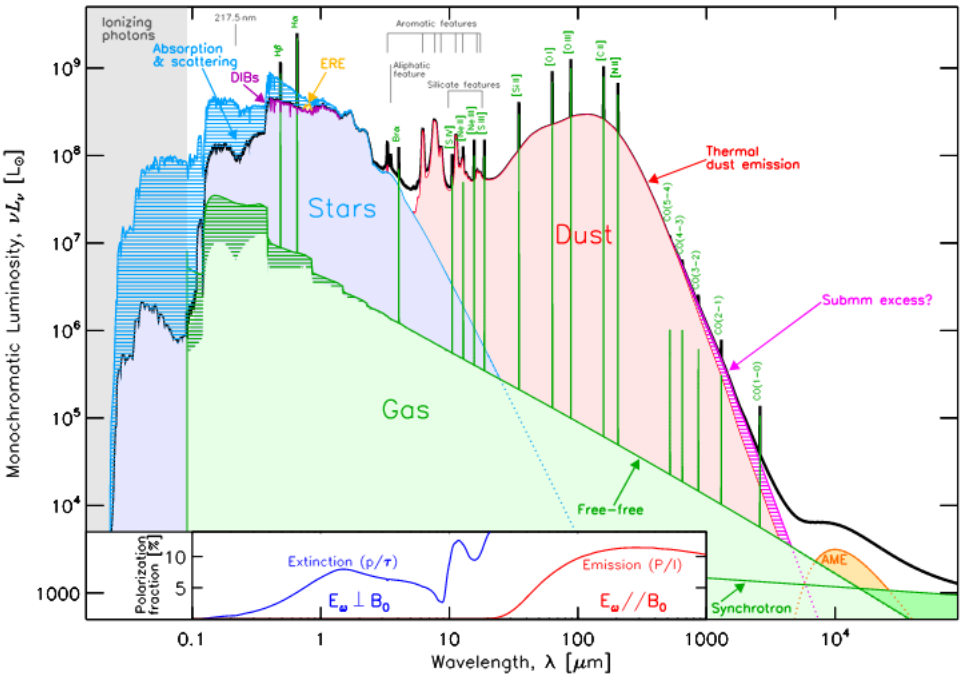

FIGURE 1.10: SED of a normal late-type galaxy. Emission from the different components is displayed, including PAH bands and fine-structure lines from atoms and ions, and lines from molecules. Blue hatched area shows the part of stellar emission absorbed by dust. AME: Anomalous Microwave Emission. Figure from Galliano et al. (2018a).

1.3 Low-metallicity dwarf galaxies

While it is not yet feasible to study in detail the earliest galaxies which would have almost pristine ISM conditions, without having undergone numerous episodes of star formation to enrich their ISM, we do have in our local universe many dwarf galaxies which have a wide range of low metallicity ISM conditions. These local dwarf galaxies are convenient laboratories to study the interplay between star formation and metal-poor ISM to attempt to understand the conditions for star formation in the early universe.

1.3.1 Definition and classification

There is no exact criteria to define dwarf galaxies, but they are considered to be small galaxies of low mass and low luminosity. Dwarf galaxies can have masses lower than 10^{10} $M_\odot$ and stellar masses lower than 10^9 $M_\odot$, 100 times lower than that of the Milky Way. Dwarf galaxies are the most numerous type of galaxies in the Universe (70 out of 100 in the Local Volume, see e.g., McConnachie, 2012; Marzke & da Costa, 1997), but due to their low luminosity they are more difficult to observe than their most massive counterparts. Their study is thus limited to the Local Universe. Classification of the wide range of dwarf galaxies was described by Grebel (2001), with the following types:

1. **Dwarf Spirals**: they are smaller equivalents of large spiral galaxies, with clear spiral arms patterns, a bulge and a disk component. They are gas-rich, usually more massive than the other dwarf galaxies and exhibit rotation signatures.

2. **Dwarf Irregulars**: they show irregular shapes, especially in optical wavelengths, and they have scattered bright H II regions, with very different morphologies from one region to another, which is especially visible in Hα emission. They are gas-rich, and exhibit clumpy H I emission around star-forming regions, and more diffuse emission in the surroundings. More often, the center of H I emission is coincident with the optical emission, but some can have more peculiar emission, with the H I peak being off-centered or even showing an annular distribution. The most massive ones have well-defined rotation curves.

3. **Blue Compact Dwarfs**: also referred to as H II region galaxies, they are compact star-forming galaxies that do not show precise shapes. They often consist of several compact stellar clusters, with large amounts of gas, and show signs of global rotation. Their name arise from their color, as measured in the B-band, which is due to young stars from recent starbursts.

4. **Dwarf Ellipticals**: they exhibit elliptical or spherical shapes with a compact central stellar density. They usually show little and asymmetric gaseous content, without rotation or distinct kinematics. They are often found close to more massive galaxies. Some dwarf ellipticals have luminous H II knots forming a nucleus, but no global structure.

5. **Dwarf Spheroidals**: they are the faintest and less massive dwarf galaxies, with no rotation, no central concentrations and very little gaseous content. The H I emission is diffuse, and they have no H II emission.

6. **Tidal Dwarfs**: these are dwarfs that form from tidal interactions with a larger galaxy, or debris of mergers. Their characteristics are thus diverse, and essentially depend on their progenitors. In particular, they often do not contain dark matter, and they can have high metallicity or more mass than classical dwarfs.

1.3.2 Metallicity effects on the ISM of dwarf galaxies

Dwarf galaxies, being low in mass, are also generally low in metallicity. Mass and metallicity are related through the well-established mass-metallicity relation (MZR; Figure 1.11), which shows a correlation over a wide range of masses - over 4 orders of magnitude (e.g., Lequeux et al., 1979; Garnett & Shields, 1987; Brodie & Huchra, 1991; Tremonti et al., 2004; Zahid et al., 2012). This relation links the stellar mass, metallicity and gas through a galaxy's star formation activity, stellar feedback, outflows and winds, etc. Some of the effects of the low mass and low metallicity are evident in the observed properties of the dust, gas and radiation field, from which the global SEDs can be studied and the structure of the ISM can be deduced.

Dust content As less metals are available to form dust, the overall dust content in dwarf galaxies is lower than in normal metallicity galaxies (Rémy-Ruyer et al., 2014). The consequences of the reduced dust content is an increased porosity of the ISM, where the UV photons suffer less attenuation and can travel further (Lebouteiller et al., 2012a; Galametz et al., 2016; Cormier et al., 2015, 2019). The composition of dust grains can also be affected. Weingartner & Draine (2001a) reproduced the extinction curve of the SMC by decreasing the quantity of very small carbonaceous grains in the mixture of dust, including PAHs, and Galliano et al. (2011) proposed to replace graphite by amorphous carbon grains for the Magellanic Clouds. The size distribution is also affected, as starbursting dwarf galaxies can show relatively enhanced quantities of small grains produced by fragmentation and erosion of big grains by shocks, for example (Jones et al., 1996; Galliano et al., 2003, 2005).

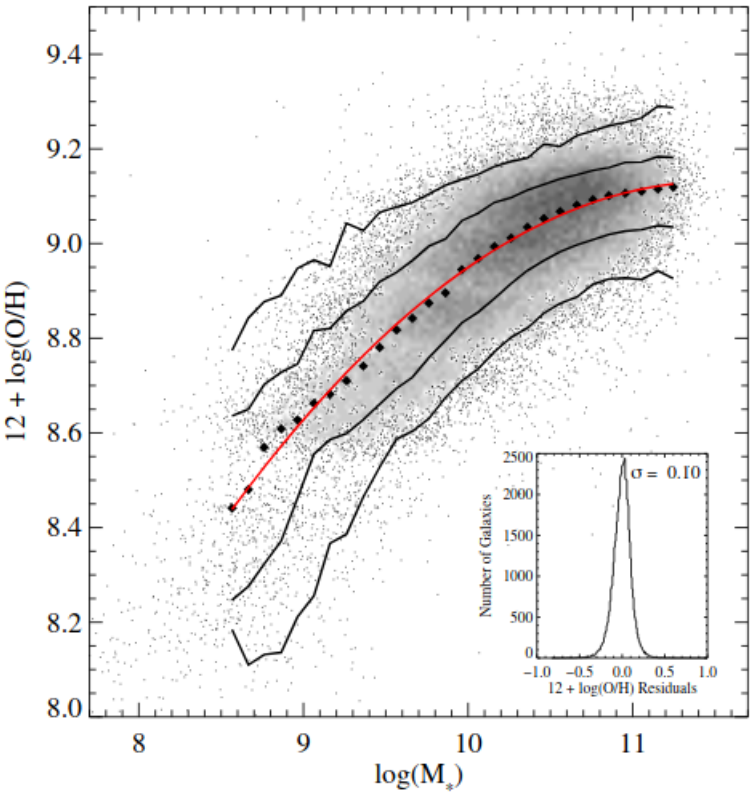

FIGURE 1.11: The relation between metallicity (12+log(O/H)), and stellar mass (M*). Data are from SDSS. The red line is the result of a polynomial fit of the data. Figure from Tremonti et al. (2004).

Cloud structure The consequence of the metal-poor ISM in dwarf star-forming galaxies results in the structure of clouds being affected by the penetrating UV radiation field (Figure 1.12). For example, in the low-metallicity ISM, molecular clouds are less shielded by dust, and UV photons can propagate deeper into molecular clouds and dissociate molecules on a larger scale than more metal-rich environments (Hollenbach & Tielens, 1999; Wolfire et al., 2010; Sternberg et al., 2014; Cormier et al., 2015, 2019). Due to its efficient self-shielding, H_2 can survive in more irradiated environments than other molecules associated with the molecular phase, leaving a potentially thick layer of CO-dark gas in low metallicity galaxies, where the H_2 is not traced by CO (Grenier et al., 2005; Wolfire et al., 2010; Accurso et al., 2017a; Madden et al., 2020). This effect is competing with the fact that H_2 also has difficulties to form, as it preferentially forms on dust grains.

In more metal-rich galaxies, the observed CO is often used to estimate the total H_2 gas mass. The conversion factor used to infer H_2 column density from CO emission, X_{CO}, is also strongly affected by the decrease in metallicity in dwarf galaxies. As CO is easily photodissociated under metal-poor conditions, detection of CO in dwarf galaxies presents great challenges (Leroy et al., 2009, 2012; Cormier et al., 2014; Hunt et al., 2015; Grossi et al., 2016) and CO can not always be used to estimate the total molecular gas. The X_{CO} factor must be scaled up from the usual Galactic value at least according to the metallicity or higher (e.g., Wolfire et al., 2010; Feldmann et al., 2012; Schruba et al., 2012; Accurso et al., 2017b; Madden et al., 2020).

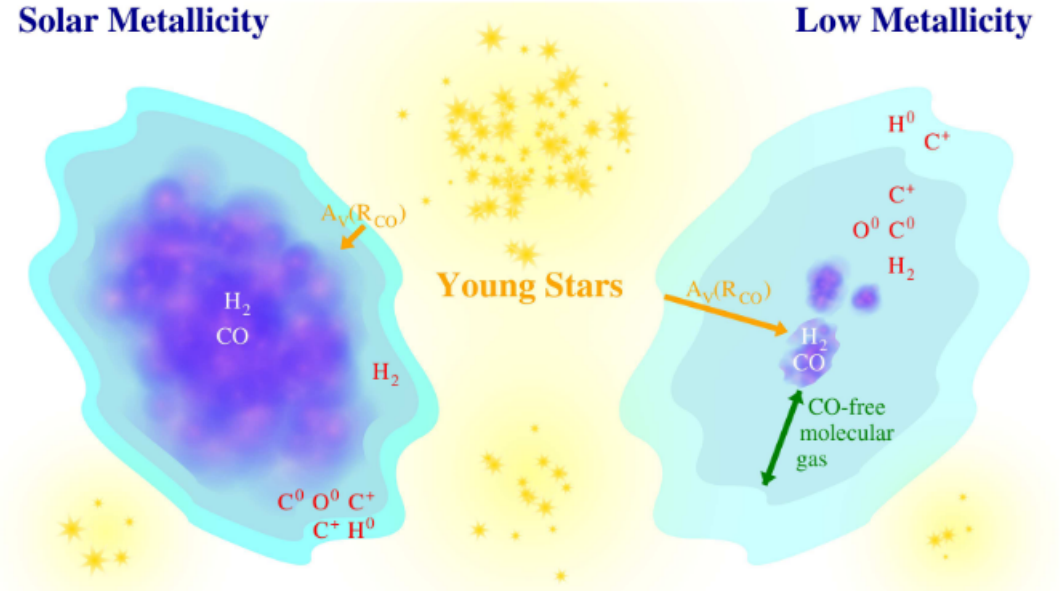

FIGURE 1.12: Comparison of a metal-rich (left) and a low metallicity (right) cloud, illuminated by the radiation field from nearby young stars. In the low-metallicity cloud, the dust shielding is decreased, and molecules are more easily dissociated. This leads to a layer of self-shielded H_2 gas that is not traced by CO, or CO-dark gas, and a much reduced CO core compared to the higher metallicity cloud. Figure from Madden et al. (2020).

Radiation field and SED On global scales, the overall interstellar radiation field is higher in star-forming dwarf galaxies compared to their metal-rich counterparts. This can be observed in the integrated SEDs of dwarf galaxies, where the peak of the IR SED can be shifted to shorter wavelengths, along with a steeply rising MIR continuum, all pointing to overall higher dust temperatures compared to more metal-rich galaxies (e.g., Hunter et al., 1989; Galliano et al., 2003, 2005; Engelbracht et al., 2008; Rémy-Ruyer et al., 2015; Madden et al., 2016, and see Figure 1.13). There have also been suggestions for an excess of sub-millimeter continuum (Galliano et al., 2003, 2005; Galametz et al., 2009; Rémy-Ruyer et al., 2015), which was tentatively explained by an additional cold dust component, spinning dust or a change in optical properties of the grains. The PAH emission is also decreased in low-metallicity galaxies, and may not be detected at all at metallicities lower than $\sim 1/5\ Z_\odot$ (e.g. Engelbracht et al., 2005). This effect, particularly evident in star-forming dwarf galaxies, could be due to the intense, less attenuated radiation field, permeating through a rather porous medium (Galliano et al., 2003, 2005; Madden et al., 2006) or through destruction of PAHs by shocks (O'Halloran et al., 2006).

Gas While evidence for molecular gas detected via CO is very limiting, the H I gas content is proportionally higher for many dwarf galaxies than for more metal-rich galaxies ($\geq$30% of the baryonic matter in blue compact dwarfs, e.g., Thuan & Martin, 1981, compared to $\leq$ 0.2% in the Milky Way), and extends much further than the optical size of the galaxy for many dwarf galaxies (e.g., Hunter et al., 2011). This large reservoir of neutral, atomic gas has not been converted into stars in dwarf galaxies; the precise conversion of H I gas into star formation is not clear. Moreover, the SFRs in dwarf galaxies have not been shown to be well correlated with H I gas (see e.g., Kennicutt & Evans, 2012; Cormier et al., 2014). Determining the total H_2 gas mass in star-forming dwarf galaxies from CO observations places them outside the Kennicutt-Schmidt relation (Cormier et al., 2014), suggesting that they could be more efficient with forming stars

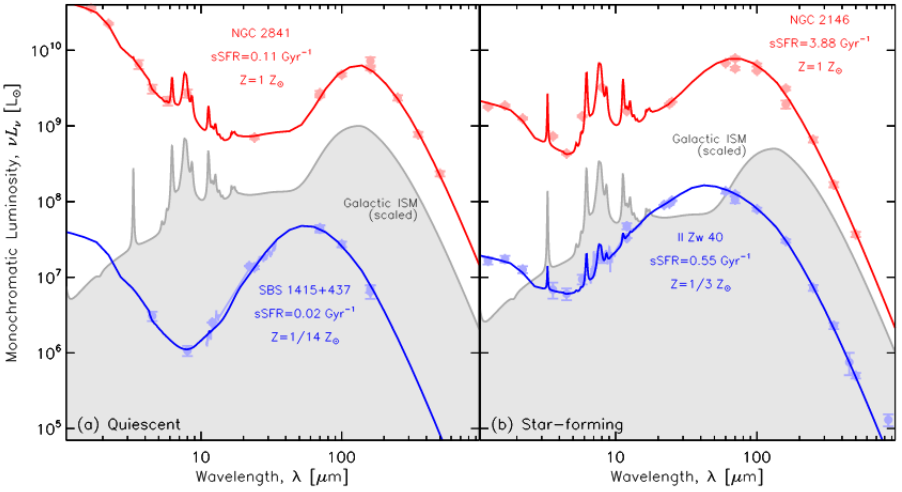

FIGURE 1.13: Comparison of the observed SEDs (and models) of local galaxies showing the effects of SFR and metallicity (Rémy-Ruyer et al., 2015). Left panel: quiescent galaxies; NGC 2841 has a metallicity similar to the Milky way, and SBS 1415+437 being an extremely metal-poor dwarf galaxy. Right panel: star-forming galaxies; NGC 2146 has a metallicity similar to the Milky Way, and II Zw 40 has a low metallicity, although not as extreme as SBS 1415+437. On both panels the scaled Milky Way ISM SED is represented for comparison. Figure from Galliano et al. (2018a)

with little H_2 (Figure 1.14), or more likely, that using CO to determine the total H_2 gas mass is not feasible (Schruba et al., 2012; Cormier et al., 2014; Galametz et al., 2009). Despite the lower metal abundance, the emission of some lines is boosted in dwarf galaxies compared to other tracers (Cormier et al., 2014, 2015, 2019). In particular, the [C II] 157μm and [O III] 88μm lines are often more prominent in low metallicity galaxies than in normal star-forming galaxies. Interestingly, these bright FIR lines have been shown to be valuable tracers of SFR overall in dwarf galaxies as well as in a wide range of local universe and high-z galaxies.

1.3.3 Relation with high-redshift galaxies

In the hierarchical model (Dekel & Silk, 1986), regular metal-rich galaxies were formed by merging and accretion of dwarf galaxies in the early universe. At this epoch, stars did not have time to enrich the ISM with metals, and the first galaxies would have been extremely metal-poor. However, due to the distances of the earliest possible galaxies we can detect today, only global values are accessible for the most part, and accessing valuable tracers is limited, leaving gaps in the our understanding of star-formation and galaxy evolution in the earliest epochs. Due to their low metallicity ISM, local dwarf galaxies can help us try to understand some aspects of star-formation and interaction with the ISM in environments that might be extremely metal-poor. They can be at least partly spatially resolved, and the closest ones have observations that are on parsec scale or lower (e.g., IC10, LMC and SMC). This provides us the possibility of disentangling the different phases and how they are effected by physical conditions and processes. Moreover, due to the high sensitivity of the Atacama Large Millimeter/submillimeter Array (ALMA), for example, it has been possible to observe the important FIR emission lines in galaxies out to very high redshift: [C II] 157μm was observed in a large sample of galaxies up to a redshift of 6 with the ALPINE survey (Le Fèvre et al., 2020, and associated studies), and even at higher redshift in galaxies (Hashimoto, 2020). [O III] 88μm was also observed at redshifts

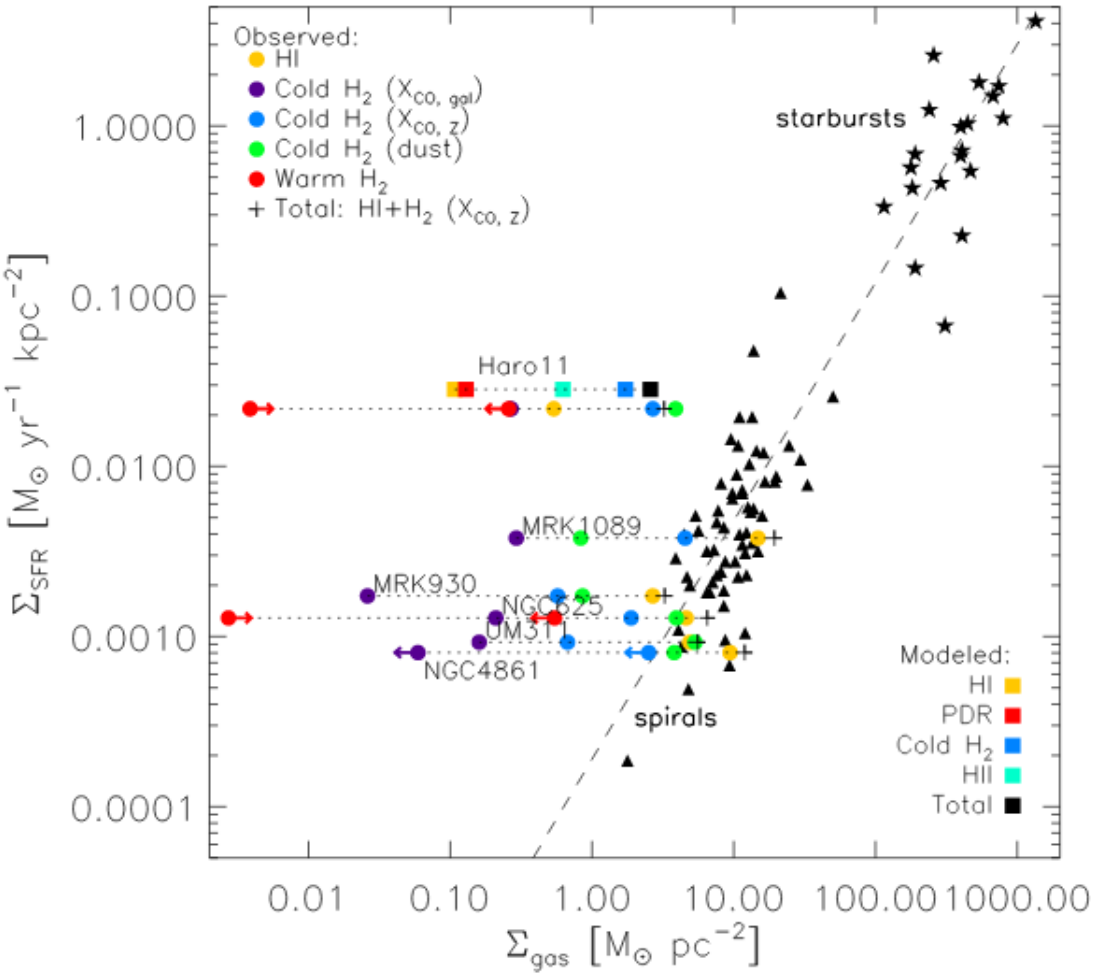

FIGURE 1.14: Kennicutt-Schmidt relation for normal and dwarf galaxies. The colors represent different ways to take into account the gas in dwarf galaxies. The total molecular gas is estimated through different methods, using a galactic conversion factor (purple), a conversion factor adapted according to metallicity of the galaxy (blue), estimating the molecular gas amount via dust emission, (green) or by direct measurements of the H_2 emission (red). The neutral atomic gas, H I, is also taken into account here (yellow), and modelled values are added for the galaxy Haro 11. We see that the method used to infer the gas quantity has a strong influence on the position of dwarf galaxies in the Kennicutt-Schmidt relation. Figure from Cormier et al. (2014).

of 7 or higher (Hashimoto, 2020). Thus, it should be possible to apply results of studies of the multi-phase ISM in local dwarf galaxies to high-redshift studies, to attempt to better understand more distant, early universe galaxies.

Some caveats have to be taken into account. Stars formed in early galaxies had a low metallicity, which is supposed to affect their radiation field (at high metallicity, there is an absorption of hard photons by metals in stellar atmosphere, see e.g., Kewley et al., 2001). On the other hand, local dwarf low metallicity galaxies often have a population of older and/or higher metallicity stars (see e.g., Thuan et al., 2008; Adamo et al., 2010, 2011; Doublier et al., 2000), indicating that their ISM underwent chemical enrichment, but the metals were ejected or diluted but accretion of pristine gas. Thus, the ISRF of dwarf galaxies may be different from what can be seen in early galaxies, with the addition of an older stellar component. Early galaxies also may have been more compact than local dwarf galaxies (e.g., Daddi et al., 2005). However, the

processes occurring in the ISM of star-forming regions are dominated by the radiation field of young, massive stars. The addition of an older stellar component thus is supposed to not have much influence until the most massive stars have disrupted their birth cloud. Moreover, the stars recently formed have the same metallicity than their surrounding ISM, and thus a radiation field that is close to what was found in early galaxies, when the average metallicity was similar to what is observed in the dwarf galaxies.

1.4 The Magellanic Clouds

In this study, we focus on our closest neighbors, the Magellanic Clouds. The Large Magellanic Cloud (LMC) and the Small Magellanic Cloud (SMC) are two dwarf satellite galaxies of the Milky Way at 50 kpc (Walker, 2012) and 61 kpc (Hilditch et al., 2005), respectively. Table 1.4 summarizes some characteristics of the Magellanic Clouds comparing them to the Milky Way.

The LMC shows clear signs of a bar structure, a flat disk and at least one spiral arm. Thus, it is sometime classified as a dwarf spiral (de Vaucouleurs, 1955; Ruiz-Lara et al., 2020). The metallicity of the LMC is 1/2 $Z_\odot$ (Pagel, 1997, 2003), which is similar to the ISM metallicity at the epoch of the peak of SFR in the universe (redshift of 1.5 - 2, Madau et al., 1996; Madau & Dickinson, 2014). A shallow metallicity gradient has been found in the LMC using iron abundances (Cioni, 2009; Feast et al., 2010), and for this study, we assume a homogeneous metallicity value of 1/2 $Z_\odot$. The lower metallicity of the LMC also lowers the dust-to-gas mass ratio by a factor of 2-4 compared to the Galaxy (Gordon et al., 2003; Galliano et al., 2011; Roman-Duval et al., 2014). From NIR surveys the older stellar population of the LMC seems smoothly distributed (e.g., van der Marel & Cioni, 2001), where the younger population is more concentrated on the arm and bar patterns (Moretti et al., 2014). The LMC also shows a variety of structures such as filaments, shells and holes at all scales in optical, IR, radio and H I wavelengths (see e.g., Kennicutt & Hodge, 1986; Dickel et al., 2005; Meixner et al., 2006, 2013, and Figure 1.15).

Physical properties	LMC	SMC	Milky Way
Morphological type	dIrr/dS	dIrr	barred spiral
Diameter (kpc)	8	3	~ 30
Metallicity ($Z_\odot$)	0.5	0.2	~ 1
Distance to MW (kpc)	50	61	-
Physical scale for $1''(pc)$	0.25	0.3	-
Inclination angle	23-37°	62°	-
M_{HI} ($M_\odot$)	$4.4 \times 10^{8\,(a)}$	$4.0 \times 10^{8\,(a)}$	4.5×10^9
M_{tot} ($M_\odot$) $^{(b)}$	$2 \times 10^{10\,(c)}$	$7 \times 10^{9\,(c)}$	$\sim 10^{12}$
Stellar mass ($M_\odot$)	1.7×10^9	3.7×10^8	1.8×10^{11}
Star formation rate ($M_\odot$ yr^{-1})	0.1 - 0.25	0.024 - 0.05	$\sim 1^{(d)}$
Dust-to-gas ratio	1.7×10^{-3}	$\sim 1 \times 10^{-4}$	$\sim 10^{-2}$

Unless specified otherwise, values are from Meixner et al. (2013) and references therein for the LMC, SMC and from Tielens (2005) for the Milky Way. (a): Brüns et al. (2005); (b): including dark matter; (c): Bekki & Stanimirović (2009); (d): Robitaille & Whitney (2010)

TABLE 1.4: Physical properties of the LMC and SMC. Milky Way is added for comparison.

FIGURE 1.15: Left: optical three-color image of the LMC, with red: hydrogen, blue: oxygen and yellow: sulfur. This image is made by the amateur astronomers from the Ciel Austral group. Right: *Herschel* Space Observatory and *Spitzer* Space Telescope observations in IR (credits to ESA/NASA/JPL-Caltech/STScI) blue: *Spitzer*/MIPS 24μm, green: *Herschel*/PACS 100μm and red: *Herschel*/SPIRE 250μm. We see that the ISM is structured with bubbles and filaments distributed throughout the galaxy.

The SMC is a dwarf gas-rich irregular galaxy (Westerlund et al., 1991; Stanimirovic et al., 1999), with scattered bright H II regions and a relatively constant metallicity of 1/5 $Z_\odot$ throughout (Russell & Dopita, 1992; Cioni, 2009). The older stellar population shows a regular spheroidal distribution in the SMC, while on the other hand, the younger population is widely asymmetric, and distributed between the main body, which contains the bar, and two very bright H II regions located to the north-east (N66 and N76, Henize, 1956). The wing, the more extended, rather diffuse ISM located toward the east of the main body, also contains some bright H II regions (e.g., N81, N83, N84, N88). This young stellar population is responsible for the characteristic clumpy morphology of the SMC, visible in Figure 1.16.

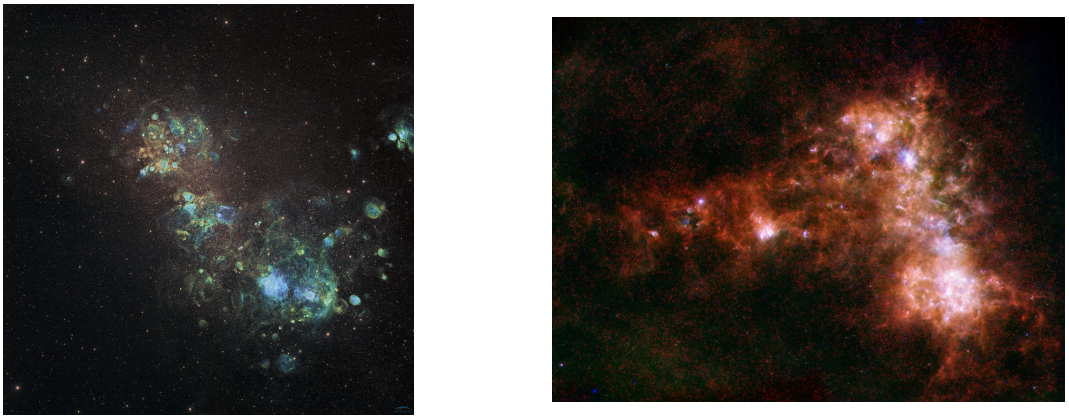

FIGURE 1.16: Similar to the Figure 1.15, for the SMC. Here again, the complexity of the irregular and clumpy ISM and the numerous structures are striking. Notice that, on the optical image, the diffuse ISM of the wing is not visible, nor are the H II regions inside (e.g., N83/84). There is also a bright optical source toward the west of the SMC (to the right of the optical image) that seems to have no or very little counterpart in IR.

The eastern wing of the SMC, as well as a structure in H I, called the Magellanic Bridge (Schmidt et al., 2020; Valdivia et al., 2019), which connects the Magellanic Clouds, show signs of interactions between the LMC and the SMC. Tidal interactions between the Magellanic Clouds and the Milky Way are also visible through the presence of the H I Magellanic Stream (Mathewson et al., 1974) and the Leading Arm (Putman et al., 1998). The Magellanic Clouds were probably

subject to a recent collision, that has led to asymmetries in the LMC disk and some low metallicity stars that have peculiar velocities (e.g., Cioni et al., 2000; van der Marel & Cioni, 2001; Kunkel et al., 1997; Olsen et al., 2011). According to theoretical models, those tidal encounters were probably repeated between the two Magellanic Cloud systems.

In this work, we aim to address the following questions: what are the physical conditions in star-forming regions? Which are the processes taking place in them? And how are the physical conditions and processes affected by the metallicity? We focus on a sample of star-forming regions in the Magellanic Clouds, presented in Chapter 2, which allows us to investigate the ISM impacted by vigorous star formation with the best possible spatial resolution at MIR and FIR wavelengths. We computed models to analyze our data, and present them in Chapter 3. In Chapter 4, we examine the physical conditions of the ionized phase, and attempt to disentangle the origin of the tracers observed in our sample. As our study of the Magellanic Clouds includes several bright FIR and MIR lines that are also more frequently detected at high redshifts, we developed a method with these diagnostics that may eventually help in the interpretation of high-redshift galaxies. We then focus on the photoelectric heating of the gas in Chapter 5, and compare different carriers of this process. Throughout this work, the effect of metallicity on the conditions and processes studied is addressed by the comparison between the LMC and SMC star-forming regions, as they have different metallicities.

CHAPTER 2

OBSERVATIONS

Contents

In this chapter we describe the sample of star-forming regions of the Magellanic Clouds we used, the observations, and the facilities with which observations were taken.

2.1 Telescopes and instruments

The *Spitzer* and *Herschel* space telescopes are the primary source of the MIR and FIR tracers we investigate in this study. Here we describe the instruments on board these telescopes.

2.1.1 Spitzer

The *Spitzer* Space Telescope (Werner et al., 2004) was an infrared observatory with three spectroscopy and photometry instruments, launched in 2003 by NASA, and completing observations by the end of 2019. Its 83 cm primary mirror was cooled to 5.5 K until 2009, with liquid helium supply, and continued after in a warm phase for ten years.

2.1.1.1 InfraRed Spectrograph

The InfraRed Spectrograph (IRS, Houck et al., 2004) was composed of four different modules: Short-Low, Short-High, Long-Low, Long-High. They were providing low resolution (R∼60-130) spectroscopic capabilities between 5.2 and 40 μm, and medium/high resolution (R∼600) spectroscopic capabilities between 9.9 and 37 μm. Table 2.1 summarizes basic characteristics of the IRS.

2.1.1.2 InfraRed Array Camera

The InfraRed Array Camera (IRAC, Fazio et al., 2004) was a four-channel imaging camera, simultaneously providing $5.2' \times 5.2'$ images at 3.6, 4.5, 5.8 and 8 μm. It had four detectors

Module	Wavelength range (μm)	Resolving power R	Plate scale (arcsec/pix)	Slit width (arcsec)	Slit length (arcsec)
SL1	7.46-14.29	61-120	1.8	3.7	57
SL2	5.13-7.60	60-127		3.6	
SL3	7.33-8.66				
LL1	19.91-39.90	58-112	5.1	10.7	168
LL2	13.90-21.27	57-126		10.5	
LL3	19.23-21.61				
SH	9.89-19.51	600	2.3	4.7	11.3
LH	18.83-37.14	600	4.5	11.1	22.3

TABLE 2.1: IRS module characteristics, from the IRS Instrument Handbook

with 256 × 256 pixels, each pixel being 1.2″ × 1.2″ in size. We also note that 2 of the IRAC channels can include a contribution from the major PAH features, namely at 6.2 μm, 7.7 μm and 8.6 μm. Table 2.2 summarizes the main characteristics of IRAC.

Channel	Central wavelength (μm)	Bandwidth (μm)	FWHM (arcsec)
1	3.6	0.750	1.66
2	4.5	1.015	1.72
3	5.8	1.425	1.88
4	7.9	2.905	1.98

TABLE 2.2: IRAC module characteristics, from the IRAC Instrument Handbook

2.1.1.3 Multiband Imaging Photometer for Spitzer

The Multiband Imaging Photometer for Spitzer (MIPS, Rieke et al., 2004) was designed for simultaneous broad-band photometry in three channels, with central wavelength at 24, 70 and 160 μm. Its main characteristics are given in Table 2.3.

Band	Central wavelength (μm)	Bandwidth (μm)	FOV (′ × ′)	FWHM (″)	Array size (pix × pix)	Pixel size (″ × ″)
1	24	4.7	5.4 × 5.4	6	128 × 128	2.5 × 2.6
2	70	19	5.2 × 2.6	18	32 × 16	9.9 × 10.1
3	160	35	5.3 × 2.1	38	20 × 2	16 × 18

TABLE 2.3: MIPS module characteristics, from the MIPS Instrument Handbook

2.1.2 Herschel

The *Herschel* Space Observatory (Pilbratt et al., 2010) was launched by NASA in 2009, containing three instruments, and designed to observe far-infrared to submillimeter emission. It was a 3.5 m telescope, cooled to 1.7 K with liquid helium, and it was decommissionned in 2013 when it ran out of cryogens.

2.1.2.1 Photodetector Array Camera and Spectrograph

The Photodetector Array Camera and Spectrograph (PACS, Poglitsch et al., 2010) was composed of two sub-instruments: the intregral-field spectrograph, with three bands of observations, with

a field of view of $47'' \times 47''$, divided into 5×5 pixels, and a three-bands photometer, where the short-wavelength (green or blue) band was observed at the same time as the long-wavelength (red) band, with a field of view of $1.75' \times 3.5'$. For the spectrometer, light from each pixel is separated by 1×25 pixels for spectral decomposition. Table 2.4 and 2.5 summarize the characteristics of the two instruments.

Order	Wavelength range (μm)	Resolving power R	FOV ($'' \times ''$)	FWHM ($'' \times ''$)	Array size (pix × pix)	Pixel size ($'' \times ''$)
1	102-210	1250	47 × 47	9.5	5 ×5	9.4 × 9.4
2	71-105	2500		9.5		
3	51-73	2700		12		

TABLE 2.4: PACS spectrograph characteristics

Band	Wavelength range (μm)	FOV ($' \times '$)	FWHM ($'' \times ''$)	Array size (pix × pix)
Blue	60-85	1.75 × 3.5	5.6	64 × 32
Green	85-125		6.8	
Red	125-250		11.4	32 × 32

TABLE 2.5: PACS photometer characteristics

2.1.2.2 Other *Herschel* instruments

Besides PACS, the *Herschel* telescope had two other instruments on board: the Spectral and Photometric Imaging REciever (SPIRE, Griffin et al., 2007) and the Heterodyne Instrument for the Far Infrared (HIFI, de Graauw et al., 2010). The SPIRE instrument was also subdivided into two instruments: a three-band (250 μm, 350 μm and 500 μm) imaging photometer composed of bolometer arrays, with a $4' \times 8'$ field of view, as well as a 194-670 μm Fourier Transform Spectrometer (FTS). HIFI was a heterodyne spectrometer with two observing bands from 157-625 μm with high spectral resolution (R $\sim 10^3$-10^7). As they are not used in the following work, HIFI and SPIRE will not be detailed further.

2.2 Data reduction

We describe the data reduction process, by first focusing on the spectroscopic data reduction, and then describing briefly the photometric data reatment.

2.2.1 *Spitzer*/IRS spectroscopy

We refer to Lebouteiller et al. (2012b) and Polles et al. (2019) for a more detailed description of the IRS spectroscopy treatment, and just note here the main steps of the procedure.

A first automatic cleaning of each exposure was made with IRSCLEAN, to remove pixels already flagged on the camera, and transients. A second cleaning was made by importing the data into CUBISM (Smith et al., 2007) and manually selecting bad pixels and artifacts for removing. The cleaning was made by S. Hony for the LMC sources and D. Hu for the SMC sources (private communications). Then a Monte-Carlo calculation was carried out to obtain the line fluxes and uncertainties from the spectral cubes. This calculation was done by creating

one hundred iterations of the cubes, in which each pixel value was varied within its uncertainty, following a normal distribution. For each pixel, the spectrum was divided into smaller windows to ease the estimation process of the continuum baseline. In each window, the atomic/ionic lines were fitted as Gaussians and the baseline was fitted by a polynomial at the same time. Specific features like PAHs bands were also fitted as Gaussians. The intensity of all the fitted lines was obtained by integrating along the line profile. The mean value of the 100 iterations was then taken to create the intensity map, and the uncertainty was taken as the absolute deviation.

2.2.2 *Herschel*/PACS spectroscopy

The treatment of *Herschel*/PACS spectroscopy is largely detailed in Lebouteiller et al. (2012a) and Cormier et al. (2015), so we again simply note the key elements of the data reduction.

The observations were downloaded from the *Herschel* Science Archive, and processed with the *Herschel* interactive processing environment (HIPE, Ott, 2010), user release 15. The pipeline first masks bad pixels and glitches, and applies a calibration. In the chop-nod observation mode, the chopper position observation is subtracted, and a spectral flat-field correction is applied. For the background subtraction, the OFF-spectra taken before and after the ON-spectrum time are smoothed and averaged, before being subtracted from the ON-frame. The data are then saved as spectral cubes, before being rebinned and projected onto a final grid. The spectral cubes are exported from HIPE, and we use the PACSman software (Lebouteiller et al., 2012a, , appendix A), version 3.63. Transients are automatically selected and removed. Then in each spatial position the spectra is fitted with two components: Gaussian profiles for the line along with a polynomial baseline. The width of the Gaussian is taken as the instrumental width, plus a broadening when the observed lines are found larger than the instrumental width. Similarly to the IRS data reduction, uncertainties on the fitted lines were estimated using a Monte-Carlo approach, with 100 iteration of the line fitting process made on data randomly perturbed within the error bars. The final fit results are taken as the median of the distribution, and the uncertainties as the standard deviation. Once flux values are calculated by integrating over the line profiles for each spatial position, the data are projected on a grid with pixel resolution of $3.1''$ with a drizzling scheme, and saved with the corresponding uncertainties. When different raster observations falls into the same final pixel, a fraction of each observation is taken and the uncertainties are added quadratically. We thank D. Cormier for the HIPE and PACSman reduction of the data.

Finally, the intensity maps of the lines were convolved to $12''$ and $18''$ resolution with a 2D Gaussian kernel, with $12''$ corresponding to the resolution of the longest wavelengths observed with PACS, and $18''$ to the resolution of the *Spitzer*/MIPS 70μm band resolution. To avoid oversampling of the beam, the maps were reprojected on a grid with pixels of $12''$ width.

2.2.3 Photometry

The photometric maps from the IRAC and MIPS instruments were observed with the SAGE project (Meixner et al., 2006) and have been retrieved from the *Spitzer* Heritage Archive for the entire LMC and SMC. The PACS and SPIRE photometric maps were taken from the NASA Infrared Science Archive, for the HERITAGE project (Meixner et al., 2010). Cutouts were selected around the regions studied, and convolved to $12''$ and $18''$ resolution, except for MIPS 70μm band which already has the limiting resolution of $18''$. The data were reprojected onto the $12''$ pixel grid constructed for the *Herschel*/PACS spectroscopic maps.

2.2.4 Point sources treatment in *Spitzer*/MIPS maps

We have made an effort to remove the obvious point sources (mostly tracers of recent star formation e.g., YSOs or masers) from the 24μm continuum maps to be able to use clean maps when we use the 24μm to compare with our emission line tracers. To this aim, we use an IDL procedure of V. Lebouteiller (see Lebouteiller et al., 2012a, for a detailed description). The principle is to fit a 2D PSF on different points indicated as point-sources; thus the algorithm is not choosing by itself which point can be a source to fit, this choice should be done before to prepare the fit. We relied on the point-source catalogs of previous studies of the Magellanic Clouds (Gruendl & Chu, 2009; Seale et al., 2012; Jones et al., 2017), and further selected point sources to remove corresponding to those also detected as point sources in the IRAC 8μm band. Then, the background is fitted and assumed to be flat on tiles, with an extent that depends on the size of the PSF and the intensity of the point-sources. The aim was to avoid degeneracy in the extraction of the sources, by not changing the background value drastically and the source value at the same time. This tiled background is one of the outputs of the software. Another output of this method is the "zoom background" which is based on the tiled fitted background, with an interpolation to obtain a resolution similar to that of the original map. This method eases the fitting procedure, but it creates an artificial reduction of the resolution, that can raise some issues. For our work, as the maps finally used are convolved and resampled at 12″, it does not pose a problem for most of the regions, because the flat tiles are roughly of the same size as the final pixels. However, there is an exception with 30 Doradus, for which the tiling is more extended, and its effect is still visible after convolution and resampling of the background map. Moreover, using this tiled background may erase some detailed spatial features, that can be important to evaluate the physical properties of the gas and dust in our sample.

The software also constructs a map with the result of the sources fitted. If there are two sources affecting a same point, they are simply co-added. This map is then subtracted from the original data. The N160 and N66 regions do not have point source correction, because it was not possible to fit point sources on those regions. For N160, there is saturation over a large part of the MIPS 24μm map, but unlike 30 Doradus, we do not have spectroscopic data on the same spectral range as the 24μm band, and thus cannot use a reconstructed continuum emission. We thus decided to simply mask the saturated zone, and all the point sources selected with the catalogs were inside the masked pixels. For N66, this SMC region raised different issues, the most important being that this area is very crowded with point sources, leading to artifacts of over-subtracted sources if we were to correct for the point sources.

2.3 Presentation of the samples

The different regions studied in this work consist of two samples, based respectively on *Spitzer* and *Herschel* spectroscopic observations. The first sample is a selection of H II regions observed with *Spitzer*/IRS, from the SAGE-Spec *Spitzer* Legacy Program (Kemper et al., 2010). Those observations are following the SAGE-LMC *Spitzer* Legacy Program (Meixner et al., 2006) that mapped the LMC with the broad bands available with the *Spitzer*/MIPS and IRAC instruments. We selected 6 of the 10 H II regions mapped with the IRS in SAGE-Spec with high detection rates at least for the main tracers we wanted to use: [S III] 18.7μm and 33.5μm, [S IV] 10.5μm, [Ne II] 12.8μm and [Ne III] 15.6μm. We completed this sample with two regions of the SMC, having photometric and spectroscopic observations from the SAGE-SMC *Spitzer* Legacy Program (Gordon et al., 2011). The 8 regions of the IRS sample are listed in Table 2.6.

Region	Center	Observed lines
LHA 120-N4	4h52′08″, -66°53′41″	[S III] 18.7μm, [Ar III] 9μm, [Ne II] 12.8μm [Ne III] 15.6μm, [S III] 33.5μm, [S IV] 10.5μm [Si II] 34.8μm
LHA 120-N11B	4h56′45″, -66°26′27″	[S III] 18.7μm, [Ar III] 9μm, [Ne II] 12.8μm [Ne III] 15.6μm, [S III] 33.5μm, [S IV] 10.5μm [Si II] 34.8μm
LHA 120-N63	5h35′38″, -66°01′04″	[S III] 18.7μm, [Ne II] 12.8μm, [Ne III] 15.6μm [S III] 33.5μm, [Si II] 34.8μm
LHA 120-N79E	4h52′02″, -66°19′12″	[S III] 18.7μm, [Ne II] 12.8μm, [Ne III] 15.6μm [S III] 33.5μm, [Si II] 34.8μm
LHA 120-N105A	5h09′56″, -68°52′19″	[S III] 18.7μm, [Ar II] 7μm, [Ar III] 9μm [Ne II] 12.8μm, [Ne III] 15.6μm, [S III] 33.5μm [S IV] 10.5μm, [Si II] 34.8μm
LHA 120-N180	5h48′47″, -70°02′07″	[S III] 18.7μm, [Ne II] 12.8μm, [Ne III] 15.6μm [S III] 33.5μm, [S IV] 10.5μm
LHA 115-N66	0h58′55″, -72°12′16″	[S III] 18.7μm, [Ne II] 12.8μm, [Ne III] 15.6μm [S III] 33.5μm, [S IV] 10.5μm, [Si II] 34.8μm
LHA 115-N76	1h03′14″, -72°03′56″	[S III] 18.7μm, [Ne II] 12.8μm, [Ne III] 15.6μm [S III] 33.5μm, [S IV] 10.5μm, [Si II] 34.8μm

TABLE 2.6: Regions of the MIR-selected sample with *Spitzer*/IRS observations. The regions beginning with LHA 120 are in the LMC, and the regions beginning with LHA 115 are from the SMC. Only the last part of the full name will be used in the rest of this work. The lines listed here are the infrared ionic emission lines with good signal-to-noise after full reduction of the data, at least on part of the mapped region. The centers indicated correspond to the observation of [S III] 18μm, which will be taken as a reference for the work using *Spitzer*/IRS data.

Another sample is based on *Herschel*/PACS observations as described in Cormier et al. (2015). The regions are listed in Table 2.7. There is little overlapping with the *Spitzer*/IRS sample, with only three regions in common. The different regions in the two samples are shown on three color images of the LMC and SMC in Figure 2.1.

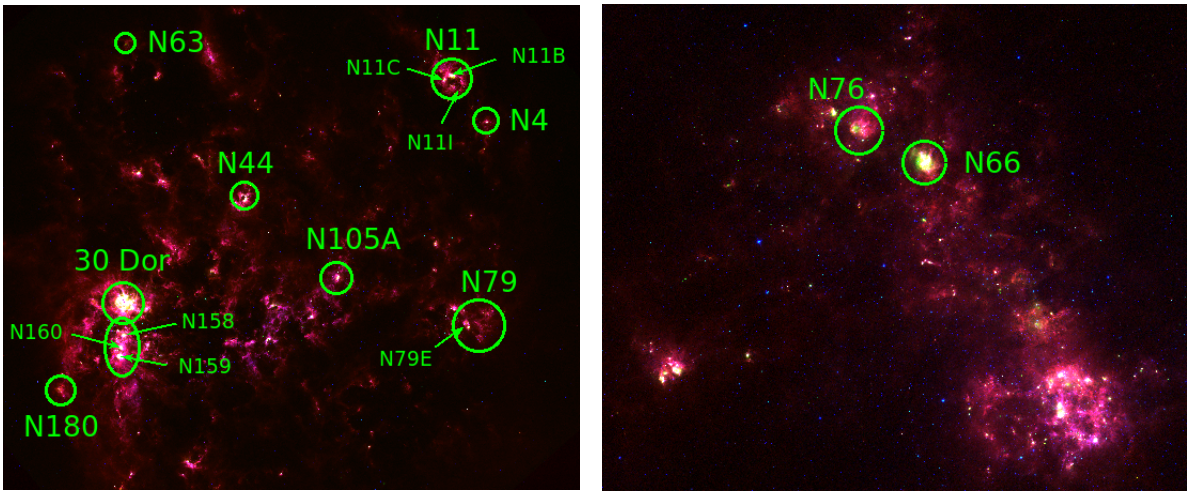

FIGURE 2.1: Three color image of the LMC (left panel) and SMC (right panel). The regions of our samples are indicated by circles, with subregions also specified. The colors are from MIR-FIR bands, red: *Herschel*/PACS 160μm, green: *Spitzer*/MIPS 24μm and blue: *Spitzer*/IRAC 8μm.

Region	Center	Observed lines
30 Doradus	5h38′43″, -69°05′48″	[O III] 88μm, [C II] 157μm, [O I] 63μm [O I] 145μm, [N II] 122μm
LHA 120-N11B	4h56′54″, -66°24′24″	[O III] 88μm, [C II] 157μm, [O I] 63μm [N III] 157μm
LHA 120-N11C	4h57′43″, -66°27′40″	[O III] 88μm, [C II] 157μm, [O I] 63μm
LHA 120-N11I	4h55′44″, -66°34′24″	[O III] 88μm, [C II] 157μm, [O I] 63μm
LHA 120-N44	5h22′03″, -67°57′52″	[O III] 88μm, [C II] 157μm, [O I] 63μm
LHA 120-N158	5h39′14″, -69°30′14″	[O III] 88μm, [C II] 157μm, [O I] 63μm
LHA 120-N159	5h39′54″, -69°45′18″	[O III] 88μm, [C II] 157μm, [O I] 63μm [O I] 145μm, [N II] 122μm
LHA 120-N160	5h39′42″, -69°38′52″	[O III] 88μm, [C II] 157μm, [O I] 63μm
LHA 120-N180	5h48′39″, -70°05′54″	[O III] 88μm, [C II] 157μm, [O I] 63μm
LHA 115-N66	0h59′09″, -72°10′46″	[O III] 88μm, [C II] 157μm, [O I] 63μm

TABLE 2.7: Regions of the sample with *Herschel*/PACS observations. The regions beginning with LHA 120 are in the LMC, and the regions beginning with LHA 115 are in the SMC. The names are used in the same way as in Table 2.6 - only the last part of the name. The lines listed are infrared atomic or ionic emission lines with good signal-to-noise after full reduction of the data. The centers indicated correspond to the [O III] 88μm map, which will be taken as reference for the work using *Herschel*/PACS data. It is thus normal that, for the common regions between the two samples, the centers indicated may not be the same, and the mapped areas of the overlapping sources are different sizes

We now describe with more detail the different regions and compile results from some studies from the literature, while highlighting the observations we use in our study.

2.3.1 Individual regions

30 Doradus This region is the brightest star-forming region in the Magellanic Clouds. A large zone at least as large as 5′, equivalent to 75 pc at the distance of the LMC, is ionized by the young stellar cluster R136 ($\leq$ 3 Myrs, Bestenlehner et al., 2020 and references therein). Also known as the Tarantula nebula, it is one of the most extreme and most studied star-forming regions in our neighbourghood (e.g., Kurt & Dufour, 1998; Tsamis et al., 2003; Indebetouw et al., 2013; Anderson et al., 2014; Chevance et al., 2016; Lee et al., 2019; Bestenlehner et al., 2020; Chevance et al., 2020b, among many others). Its interstellar radiation field (ISRF) is very intense (Anderson et al., 2014 found $\chi = 500\,\chi_0$ in units of Draine field[1], and Chevance et al., 2016, 2020b found G_{UV} between 10^2 and a few 10^4 in units of Mathis field[2]). Due to such high radiation field, and decreased dust abundance, we find the [O III] emission throughout the full mapped region (see Figure 2.4). However, denser clumps with size $\leq$1 to 3 pc are also detected toward this region with HCO^+ and HCN emission (Anderson et al., 2014; Galametz et al., 2020). These dense clumps are often spatially correlated with young stellar objects (YSOs) or

[1]Draine field is defined as the stellar radiation field between 91.2 and 200nm in Draine, 1978, with an integrated value of 3.03 10^{-3} erg cm^{-2} s^{-1}

[2]Mathis field is defined as the stellar radiation field between 9 and 800nm in Mathis et al., 1983, with an integrated value of 2.17 10^{-2} erg cm^{-2} s^{-1}

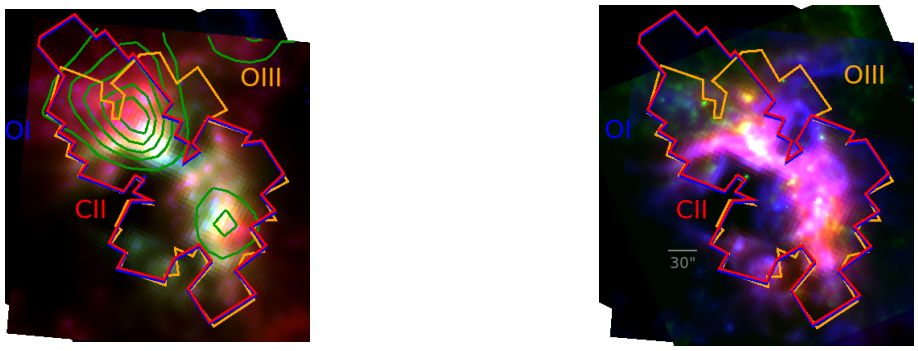

FIGURE 2.2: Three color images of the 30Dor region. Left panel: red: PACS 160μm (FWHM: 11″), green: MIPS 24μm (FWHM: 6″), blue: IRAC 8μm (FWHM: 2″). The green contours are the CO emission obtained from the MAGMA survey (Wong et al., 2011, , FWHM: 33″). Right panel: red: MIPS 24μm (FWHM: 6″), green: IRAC 8μm (FWHM: 2″), blue: Hα from MCELS (FWHM: 14″). On both images the fields of the *Herschel*/PACS spectroscopic maps are represented, with colors to differenciate the three emission lines we use: [C II] 157μm (red shape), [O I] 63μm (blue shape) and [O III] 88μm (orange shape). Note: the [C II] and [O I] map areas are identical and the outlines overlap.

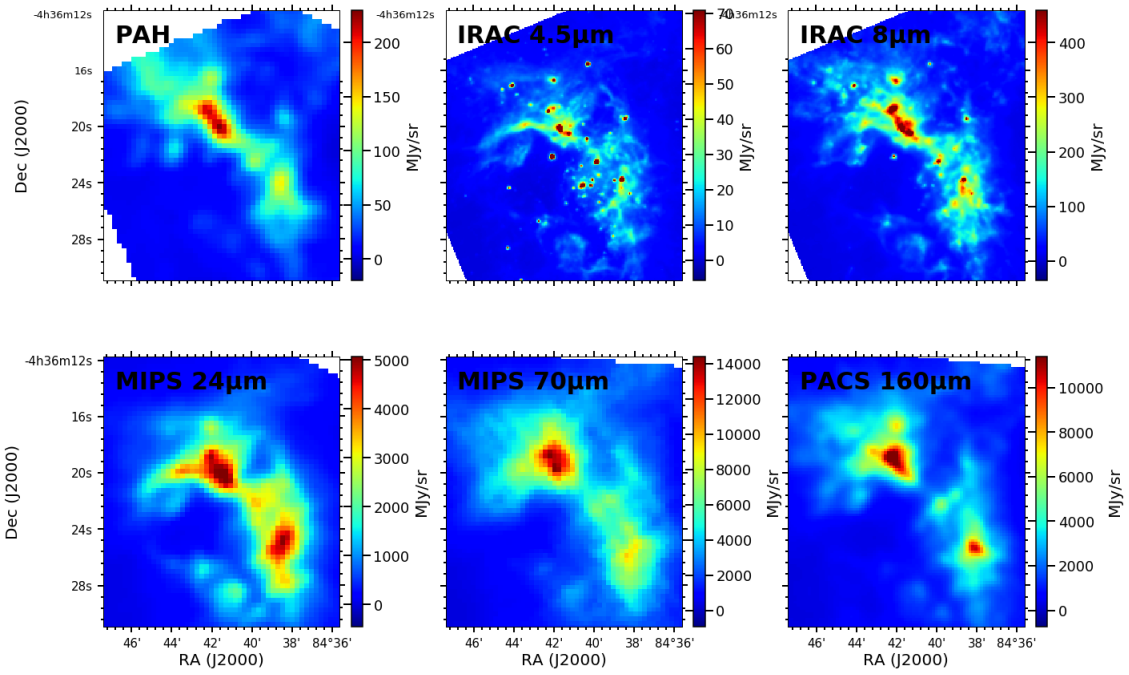

FIGURE 2.3: Continuum observations of the 30 Doradus region, from *Spitzer* and *Herschel* telescopes. The PAH emission is estimated from IRAC 8μm band with a method described in Chapter 5 (Seok et al., in prep.). The full 24μm band from MIPS was not usable, as there is a saturated area that creates artifacts through a vast part of the map. Thus, we replaced the saturated areas with a map obtained from the IRS spectroscopic observations, using the transmission function of the MIPS 24μm band.

are identical and the outlines overlap

H_2O masers (Gruendl & Chu, 2009). They are included in a larger molecular structure of $\sim$ 28 pc in diameter, which corresponds to the CO emission toward the northern structure of 30 Doradus (see green contours on Figure 2.2). The density of the region was shown to vary within the different phases, from a few 10 cm^{-3} in the ionized phase (Chevance et al., 2016) up to 600-650 cm^{-3} in PDRs (Kurt & Dufour, 1998; Tsamis et al., 2003; Chevance et al., 2020b). Those values

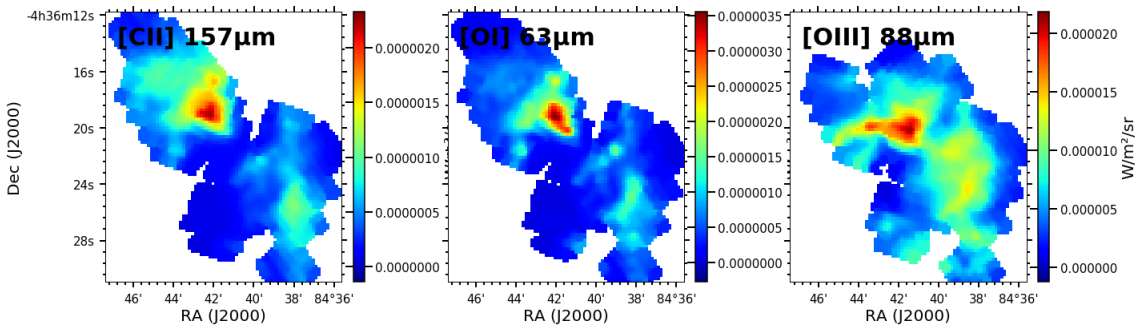

FIGURE 2.4: Observed PACS spectroscopic maps of 30 Doradus, for three IR lines we use. Observations are at the same position and with the same size as in Figure 2.3

are consistent with classical conditions in star-forming regions. The 30 Doradus region shows a bubble with almost no IR emission inside, surrounded by a partial circle of prominent MIR and FIR emission tracing layers of ionized gas and mixtures of warm and cool dust impacted by the massive stellar cluster, R136, located to the south-west part of this bubble. From Figures 2.3 and 2.4, we see that the spatial distribution of [O III] and 24μm band are very similar, with two major regions of emission, one to the north and the other to the west/south-west. The peaks of the neutral PDR tracers, [O I] and [C II] are at the same position, a bit offset to the east of the [O III] peak which is in close proximity to R136. The spatial distributions of [C II] and [O I] also resemble those of the longer wavelength continuum maps (e.g., PACS 160μm band, where it is especially striking). The CO emission, represented as green contours in Figure 2.2 (left panel), has two primary peaks in the region. The brightest peak is located to the north, where the PDR tracers peak; another CO peak is close to the bright region at the south-west of the bubble.

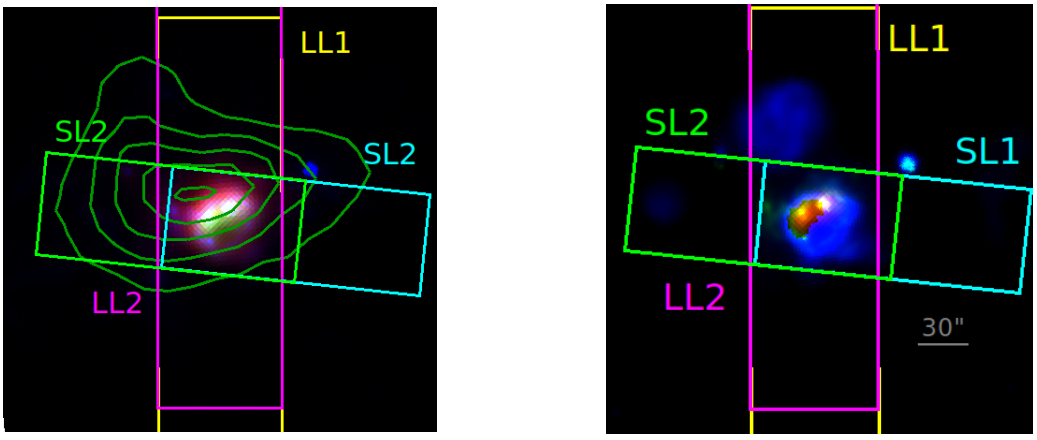

FIGURE 2.5: Three color image of the N4 region. Left panel, red: PACS 160μm (FWHM: 11″), green: MIPS 24μm (FWHM: 6″), blue: IRAC 8μm (FWHM: 2″). The green contours are the CO emission obtained from the MAGMA survey (FWHM: 33″). Right panel, red: MIPS 24μm (FWHM: 6″), green: IRAC 8μm (FWHM: 2″), blue: Hα from MCELS (FWHM: 14″). On both images the fields of observation from *Spitzer*/IRS are outlined in rectangles, with colors to differenciate the different IRS modules (SL1, SL2, LL1, LL2).

N4 This compact region (∼4′ in size) is located to the north-west of the LMC, just south of the bright N11 complex. It consists of two subregions, N4A and N4B, separated by a dark lane which corresponds to the peak of CO (J = 1 → 0) emission (Heydari-Malayeri & Lecavelier Des

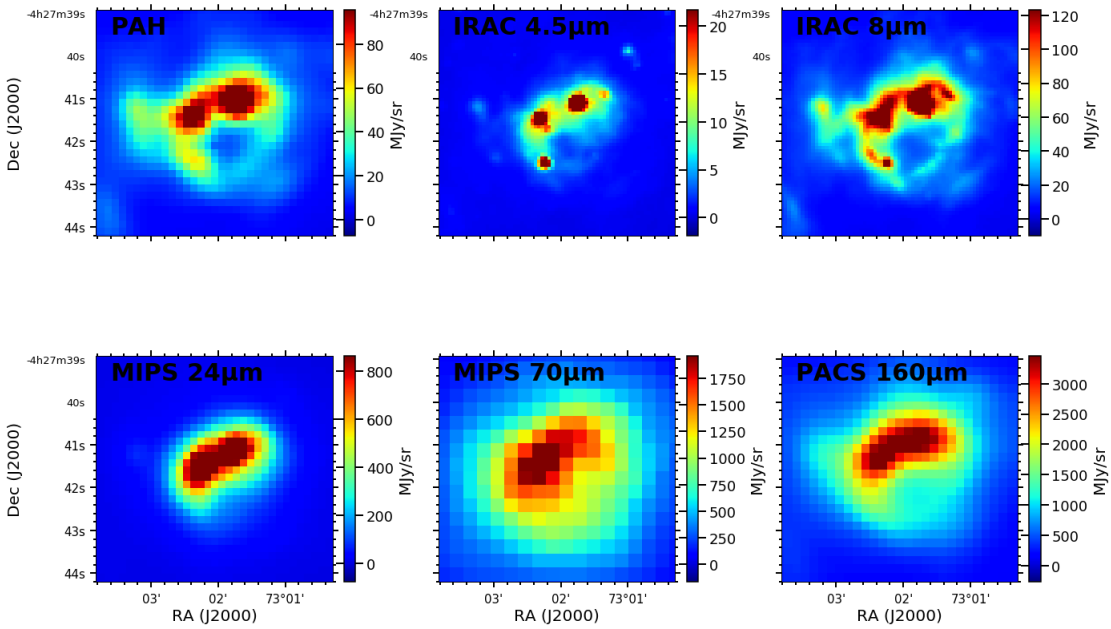

FIGURE 2.6: Continuum emission of the N4 region, from *Spitzer* and *Herschel* telescopes. The PAH emission is estimated from the IRAC 8μm band with a method described in Chapter 5 (Seok et al., in prep.).

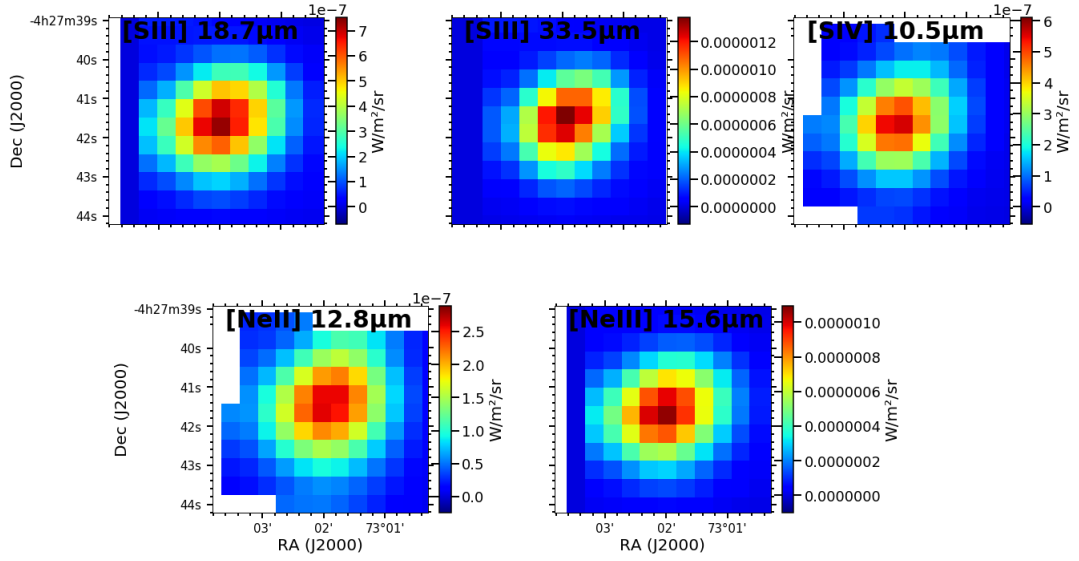

FIGURE 2.7: Emission lines from the IRS used in our study of the N4 region.

Etangs, 1994). N4A has two bright stars visible in Figure 2.5: N4B is the fainter blob north of N4A. The mean density of the region is reported from optical observations to be low, 70 to 80 cm^{-3} (Heydari-Malayeri & Lecavelier Des Etangs, 1994; Wilcots, 1994) and 45 cm^{-3} using radio tracers (Wilcots, 1994). However, higher densities can also be found: 250 to 900±300 cm^{-3} (Kurt & Dufour, 1998; Heydari-Malayeri & Lecavelier Des Etangs, 1994). Based on Hβ

observations, Heydari-Malayeri & Lecavelier Des Etangs (1994) estimated the age of the stellar cluster in N4 to be 4Myrs in N4A. This recent star formation burst was probably triggered by the development of N4B, which seems older, and has cleared its molecular cloud. We see in Figure 2.5 that IRS observations are centered on N4A. On the continuum maps (Figure 2.6), we see that emission is in a circular structure for most of the tracers (except maybe the 70μm band), with two brighter points that probably correspond to the stellar sources described in Heydari-Malayeri & Lecavelier Des Etangs (1994). The CO emission seems to peak a bit to the north-east of our observations, between N4A and N4B. The IRS ionic lines (Figure 2.7), however, do not show the annular observations as seen in the continuum band tracers. The emission is located roughly at the center of N4A, as a bright circular region with a smoothly decreasing extended component.

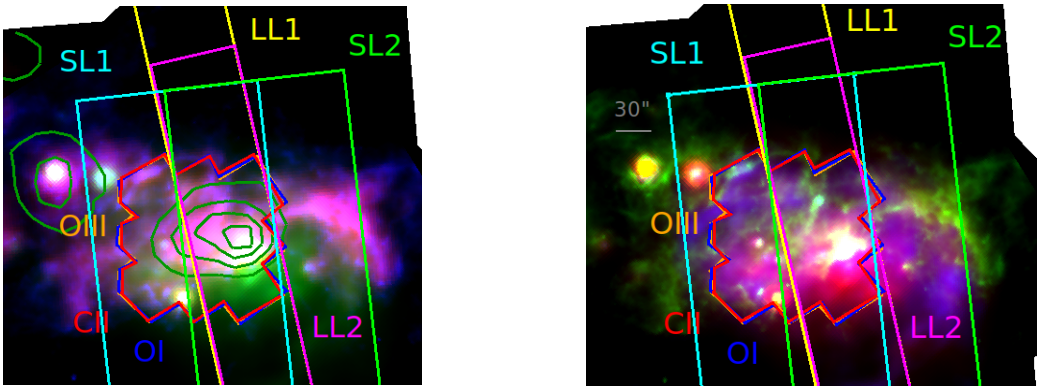

FIGURE 2.8: Three color image of the region N11B. Left panel, red: PACS 160μm (FWHM: 11″), green: MIPS 24μm (FWHM: 6″), blue: IRAC 8μm (FWHM: 2″). The green contours are the CO emission obtained from the MAGMA survey (FWHM: 33″). Right panel, red: MIPS 24μm (FWHM: 6″), green: IRAC 8μm (FWHM: 2″), blue: Hα from MCELS (FWHM: 14″). On both images the fields of observation from *Spitzer*/IRS are represented, with colors to differenciate the modules (SL1, SL2, LL1, LL2), and for the *Herschel*/PACS observations (red for [C II] 157μm, blue for [O I] 63μm and [O III] 88μm).

N11B N11B is one of the nine subregions of the superbubble N11 (N11A to N11I, Rosado et al., 1996), carved out by the stellar cluster LH9 (Lucke & Hodge, 1970; Parker et al., 1996). N11 is considered to be an older version of 30 Doradus (Walborn & Parker, 1992). N11B has an annular shape of ∼120 pc in diameter, with triggered star formation on the shell. N11B hosts the OB association LH10, and harbors signs of on-going star formation (pre-main sequence stars or ultracompact H II regions, Barbá et al., 2003; Hatano et al., 2006 or H_2O masers, Ellingsen et al., 1994). The morphology of the clouds is extensively described in Lebouteiller et al. (2012a). They underline the presence of multiple clouds with bright ionization fronts, including the bright region on the western part of N11B visible just south of the CO peak in Figure 2.8, left panel, which is even brighter on the right panel. The OB association LH10 is located on the south-west corner of the PACS observation field. The different tracers of ionized gas show a variety of possible densities throughout the region, varying from ∼10 cm^{-3} ([O III] 88μm extent in Lebouteiller et al., 2012a, optical [S II] and [O II] doublets in Tsamis et al., 2003, or in Nazé et al., 2001) to a few 10^2 cm^{-3} on the bright arcs in the clouds (Nazé et al., 2001; Lebouteiller et al., 2012a). A recent survey of HCO^+ and HCN in the Magellanic Clouds (Galametz et al., 2020) also found these tracers to be quite luminous in N11B, suggesting the presence of very dense gas. We see that the dust and gas (Figures 2.9 to 2.11) all show a peak at the bright Hα emission. There is also extended, more diffuse MIR and FIR continuum emission throughout the region. We see

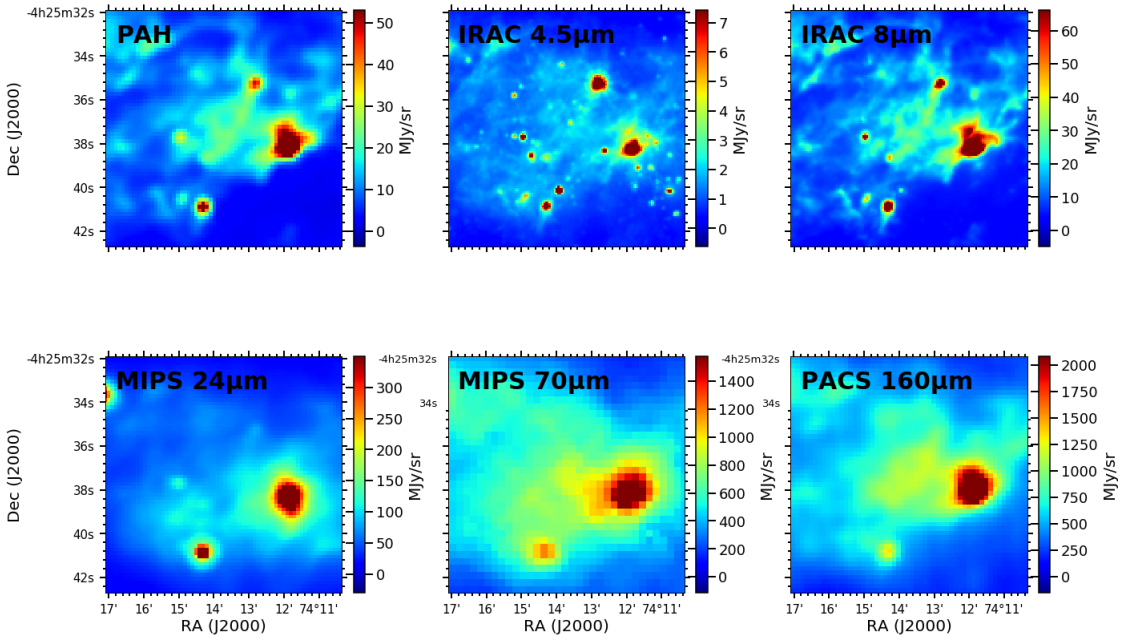

FIGURE 2.9: Continuum emission of the region N11B, similar to Figure 2.6. As the PACS observation field is smaller, the bands were centered and sized roughly to PACS observations, for comparison.

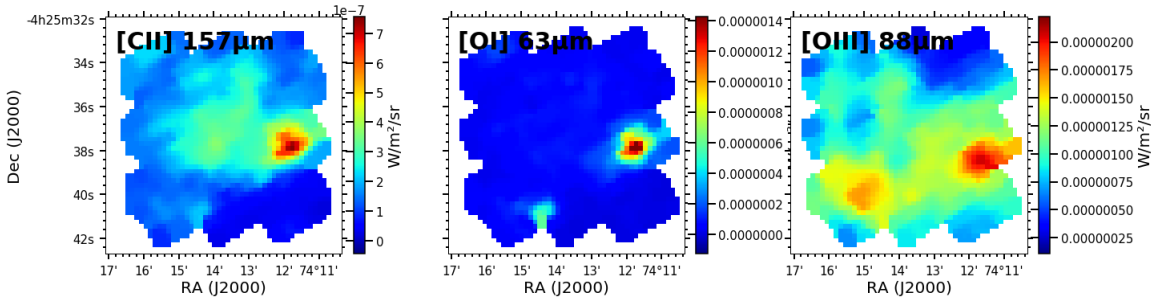

FIGURE 2.10: Similar to Figure 2.4, for the region N11B.

that all of the PACS FIR lines show peak emission corresponding to the Hα peak, with small offsets between them. [O I] does not show signs of extended diffuse emission, where extended emission is visible in the [C II] map, and even more so in the [O III] map. The extended emission encompasses almost the entire region, especially the [Ne II] emission, where three peaks span the full PACS field, from the bright Hα blob to the north-east of the PACS field. However, due to the mapping of the IRS LL module, only a small part of the diffuse component was observed with the IRS, and the maps are somewhat more centered on the brightest Hα peak. We also note that the [Ne II] peak is spatially aligned with peaks of the two [S III] lines, where the [Ne III] and [S IV] peaks are slightly offset to the south.

N11C This sub-region of N11 is located toward the eastern side of the bubble ridge. It hosts at least four early type O stars (Heydari-Malayeri et al., 1987, 2000), and most of the stars lie on the zero-age main sequence (ZAMS). The region itself is quite extended from the south-west

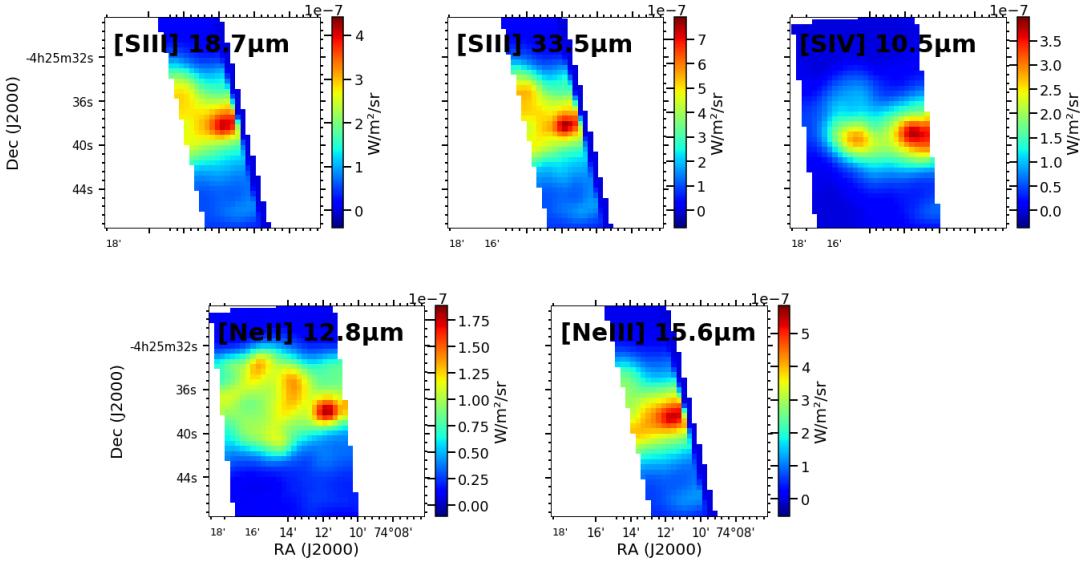

FIGURE 2.11: Similar to Figure 2.7, for the region N11B.

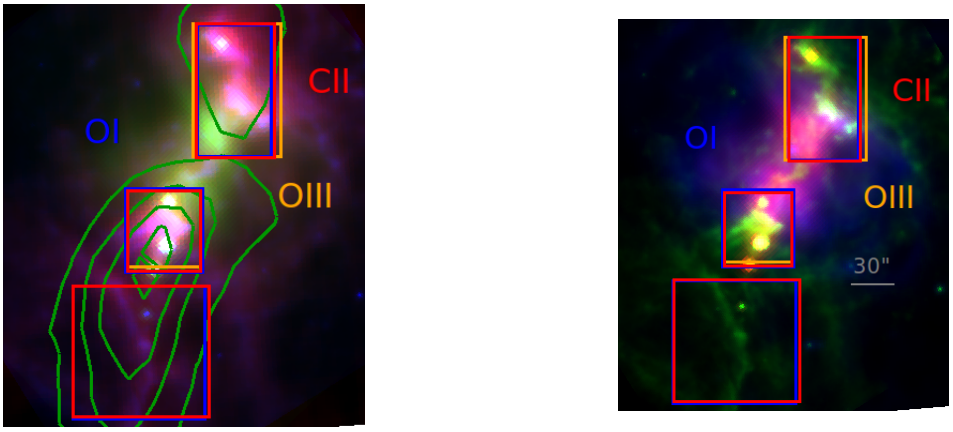

FIGURE 2.12: Similar to Figure 2.2 for N11C, with PACS observation fields.

to the north-east, with two bright IR zones at each end of the region, where the center shows bright Hα emission. Density determined from the [S II] doublet can be as high as 350 cm^{-3}, but more than half of the pointings have densities $\leq$50 cm^{-3} (Heydari-Malayeri et al., 1987). Using Hβ leads to even lower density estimates of $\sim$ 19 cm^{-3}. Thus the ISM is probably very clumpy. Heydari-Malayeri et al. (1987) also note that the large spread of [O III] 4363/Hβ and the fact that some O stars are visible, indicate that the region is probably density-bounded, especially toward the observer. The dense gas tracers, HCO^+ and HCN are associated with the southern IR emitting clump Galametz et al. (2020), where the MIR and FIR continuum bands and the PDR tracers, [C II] and [O I], peak (Figure 2.13 and Figure 2.14). The northern IR-emitting blob is associated with weaker but extended CO emission as well as weaker 24μm, 4.5μm and [C II] emission. The [O III] is more extended than the PDR tracers and also fills in between the 2 IR peaks. In retrospect, a larger PACS map would have captured the exceptionally full and far extent of the [O III].

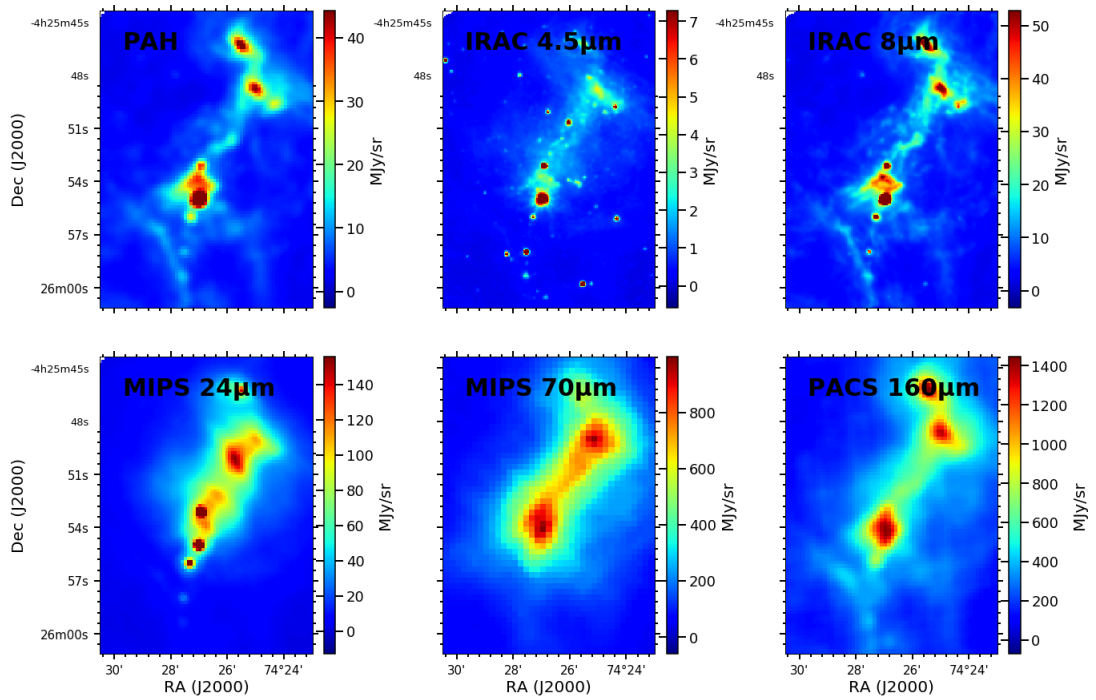

FIGURE 2.13: Continuum emission of the region N11C, similar to Figure 2.6.

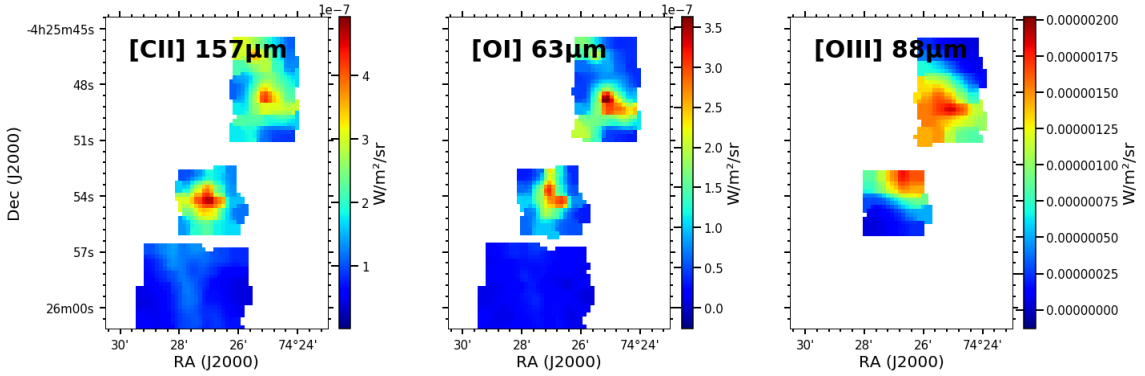

FIGURE 2.14: Similar to Figure 2.4, for the region N11C.

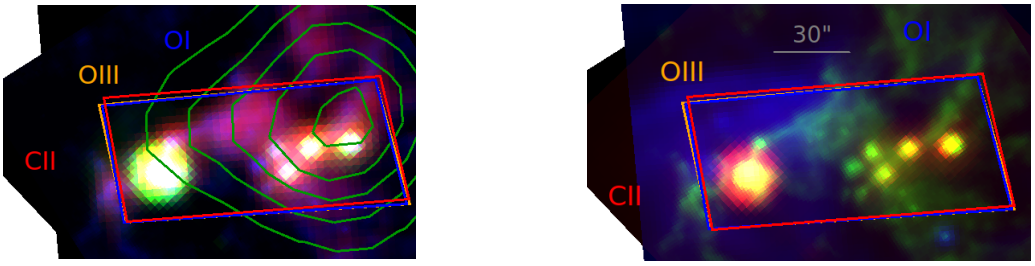

FIGURE 2.15: Similar to Figure 2.2 for N11I, with PACS observation fields.

N11I This region is relatively quiescent, having no H II regions nor any embedded OB sources. It shows discrete point sources with a CO cloud (Figure 2.15 peaking toward the western half of our *Herschel* maps. Fainter diffuse MIR and FIR emission exists, where CO peaks, in our photometry and spectroscopy maps, except for [O III] (Figures 2.16 and 2.17). The FIR continuum

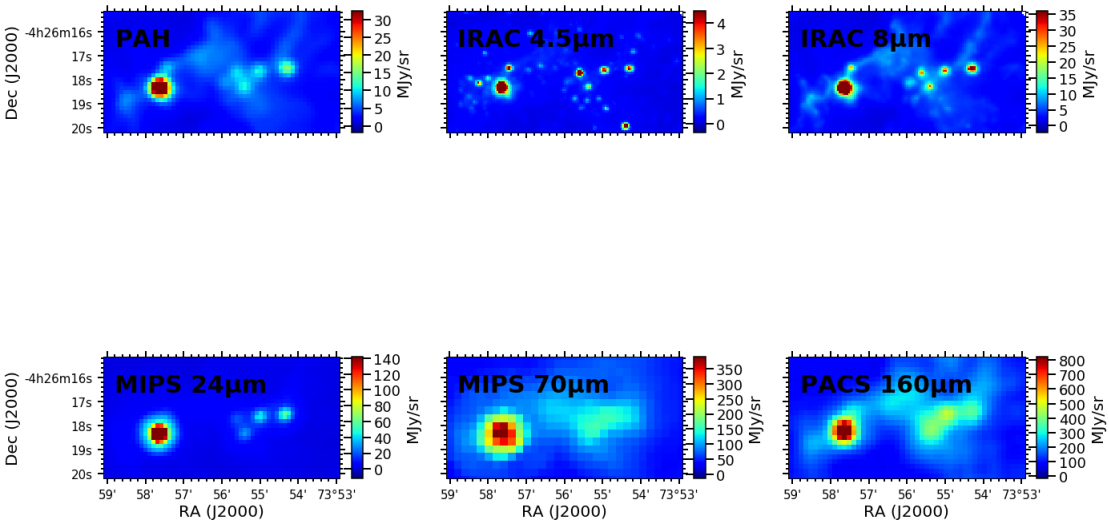

FIGURE 2.16: Continuum emission of the region N11I, similar to Figure 2.6.

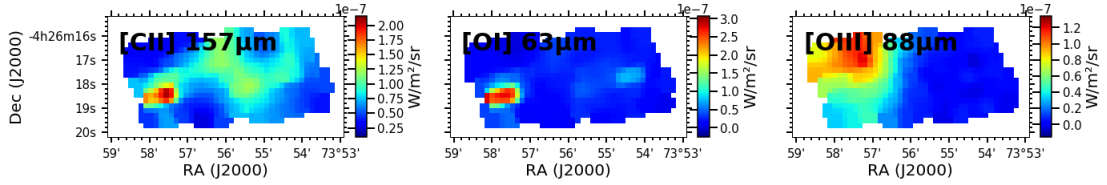

FIGURE 2.17: Similar to Figure 2.4, for the region N11I.

emission (Figure 2.16) is associated with the point sources seen in Hα and the MIR maps, with the source toward the east being the brightest and most extended. The [C II] and [O I] maps show a peak toward the same continuum peaks, but somewhat offset just to the south. [C II] and [O I] also have additional extended emission toward the west of the regions, where the CO peaks. On the other hand, the [O III] map is strikingly different, and shows a peak offset to the north of the brightest peak in the continuum, at the north-east edge of our observations. There is a sharp fall off in the [O III] distribution, avoiding any emission toward the west.

N44 This region is located roughly in the middle of the LMC. Oey & Massey (1995) find two episodes of star formation existing in N44: 10 Myrs ago in the main bubble, and 5 Myrs ago outside the main bubble. Our observations are located on the south-west side of the main bubble, between two subregions studied in McLeod et al. (2019), N44C and D, which are not visible in our IR observations. The gas density of the region, determined using optical lines, is found to range between roughly 100 and 200 cm^{-3} (McLeod et al., 2019; Toribio San Cipriano et al., 2017). This region also has molecular clumps, with sizes of ∼1.5 pc (Seale et al., 2012; Galametz

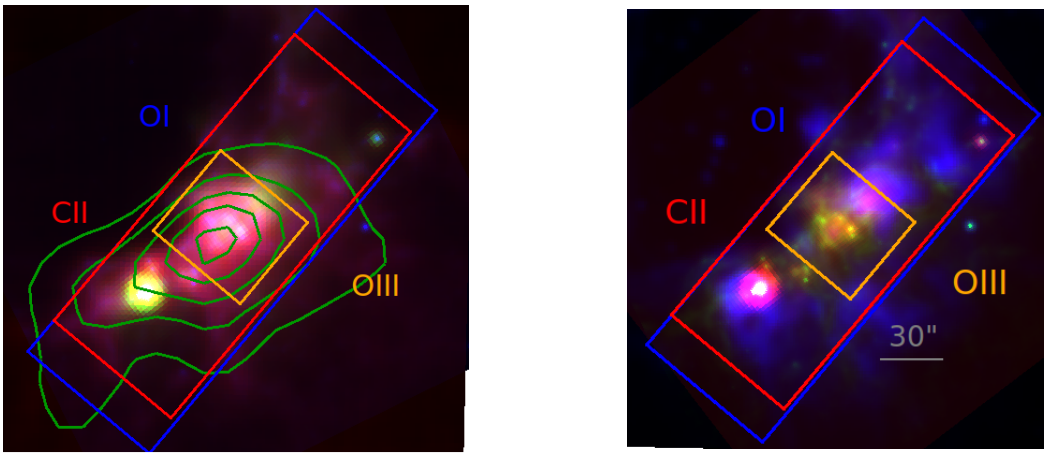

FIGURE 2.18: Similar to Figure 2.2 for N44, with PACS observation fields.

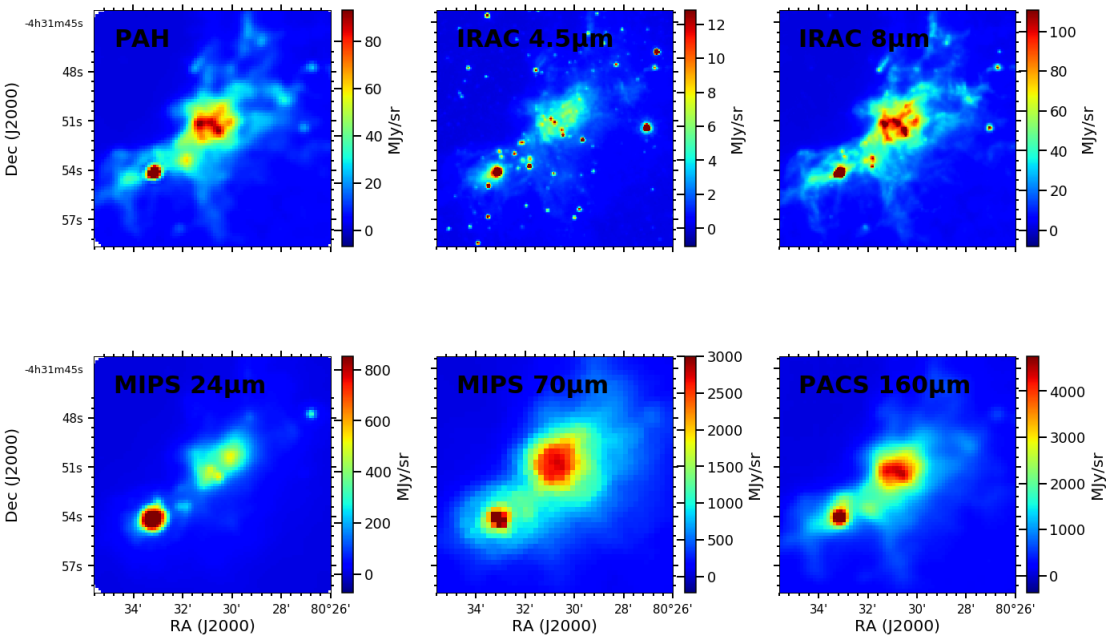

FIGURE 2.19: Continuum emission of the region N44, similar to Figure 2.6.

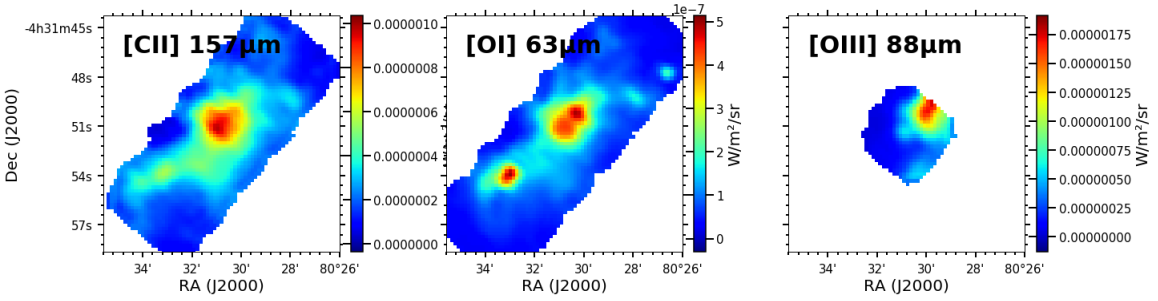

FIGURE 2.20: Similar to Figure 2.4, for the region N44.

et al., 2020). The ISRF is quite intense, and has been determined to be $\chi = 76\chi_0$ in units of the Draine field (Anderson et al., 2014). The bright IR emission on which the observations are centered, corresponds to several point sources, labeled as YSOs in the catalog of Gruendl & Chu (2009); Jones et al. (2017). The 70μm to 160μm and PAH and 8μm distribution all show similar relative peaks, with the largest concentrations toward the CO peak (Figure 2.18). The PACS PDR emission lines, [C II] and [O I], show a peak at the same spatial position as the continuum peaks, while the [O III] emission is offset to the north-west of that peak. There are signs of extended emission of [O III] toward the north-west, but not toward the south-east part of the region. The [O III] emission is spatially coherent with CO observations as well as part of the [C II] and [O I] emission. However, the PACS [O III] map is very limited in size and we can not say much about other possible emission in the N44 region.

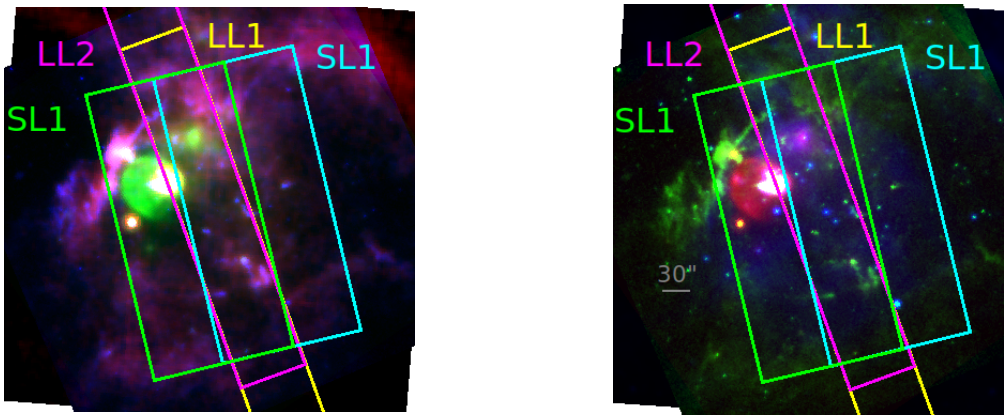

FIGURE 2.21: Similar to Figure 2.5 for N63. CO (1→0) contours are not displayed, as the region was not observed with the MAGMA survey. IRS observation fields are outlined.

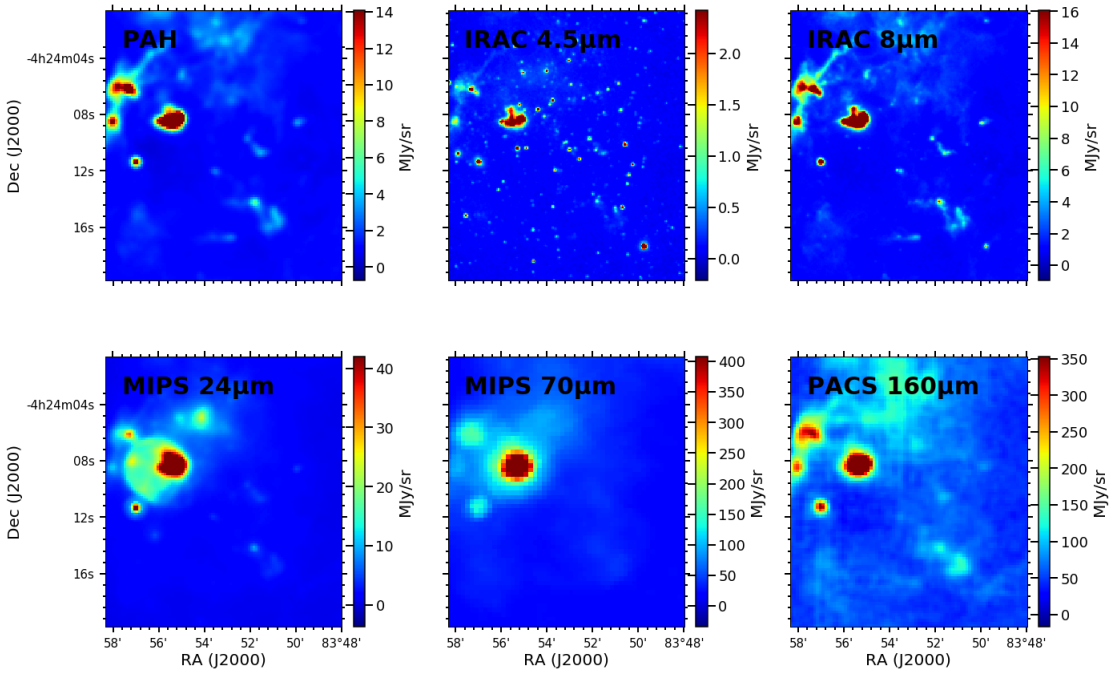

FIGURE 2.22: Continuum emission of the region N63, similar to Figure 2.6.

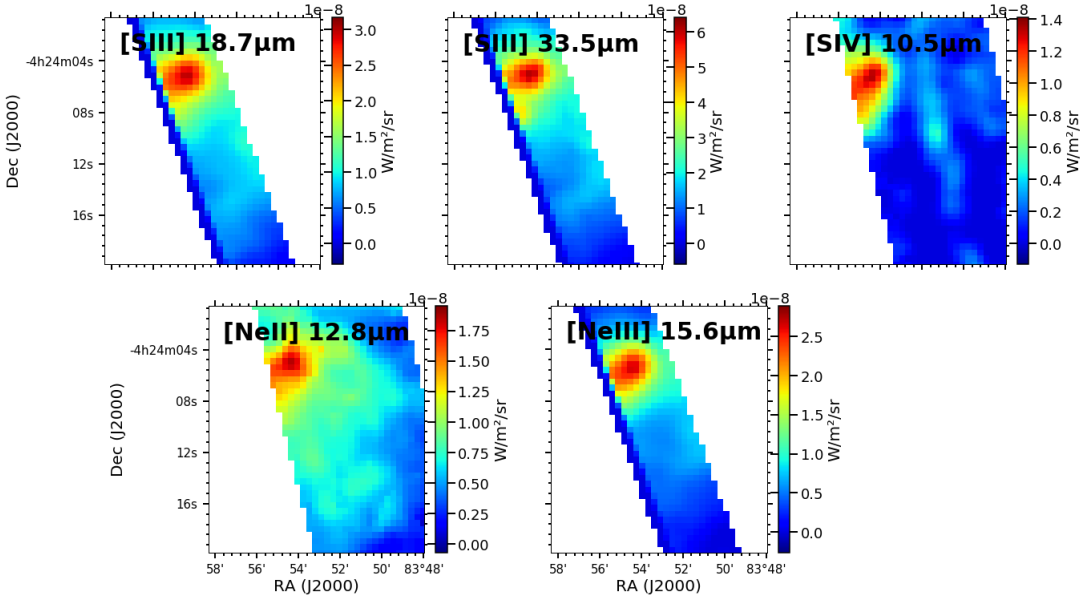

FIGURE 2.23: Similar to Figure 2.7, for the region N63.

N63 This region, located to the north-east of the LMC, hosts a bright supernovae remnant (SNR) with its associated H II region (Caulet & Williams, 2012), visible as the diffuse bubble in MIPS 24μm located toward the east in Figure 2.21 (green color on left panel, red color on right panel). It is also currently undergoing star formation with numerous YSOs that have been classified in Caulet et al. (2008). The density in the star-forming H II regions is found to be between 350 and 450 cm^{-3}, with an uncertainty of up to 200 cm^{-3} (Toribio San Cipriano et al., 2017). The continuum observations (Figure 2.22) show that the bubble in the east of the our observation field is the brightest zone of emission in all of the continuum bands. The IRS observations (Figure 2.23) also show a prominent bright source, but closer investigation shows that it is not at the same position as the brightest source in the continuum. It corresponds to a more diffuse emission spot at the north-west of the brightest source in the continuum images, and can be seen prominently in the 24μm image as well as at 70μm. It is spatially aligned with all of the IRS emission lines. We also notice that the diffuse emission associated with this source is quite extended in ionized gas, especially for [Ne II] and [S III] lines. PACS spectroscopic observations do not exist for N63.

N79E N79 (Ochsendorf et al., 2017) is considered to be a younger equivalent of 30 Doradus. It contains very young ($\leq$ 0.5 Myrs) and massive ($\geq$ 8 M$_\odot$) YSOs. It is one of the youngest sites of star-formation in the LMC, with highly embedded YSOs and a star formation efficiency higher by a factor 2-2.5 to that found in 30 Doradus. N79E is one of the three main sub-regions of N79 (N79 East, West and South). It corresponds to a bright knot in Hα and IR emission, but is optically darker than other regions like 30 Doradus or N11, suggestive of very embedded star formation (Ochsendorf et al., 2017). N79E has a bubble shape, partially open to the south, with the interior harboring some Hα emission (Figure 2.24), and an edge emitting prominently at all MIR and FIR continuum bands (Figure 2.25). Brighter emission knots can be seen along the edge of the bubble, at least three toward the west and two toward the south-east (see e.g., IRAC 8μm, upper right panel in Figure 2.25). At longer continuum wavelengths, only two of

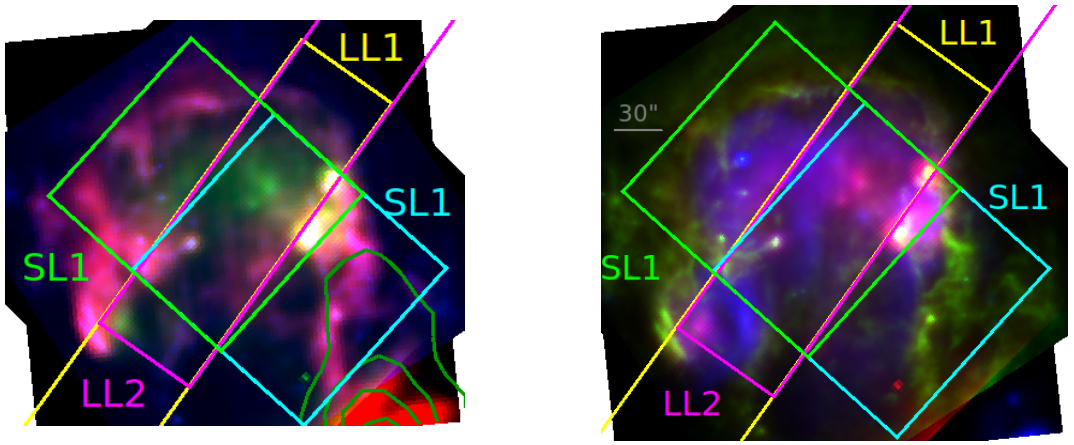

FIGURE 2.24: Similar to Figure 2.5 for N79E. IRS observation fields are displayed.

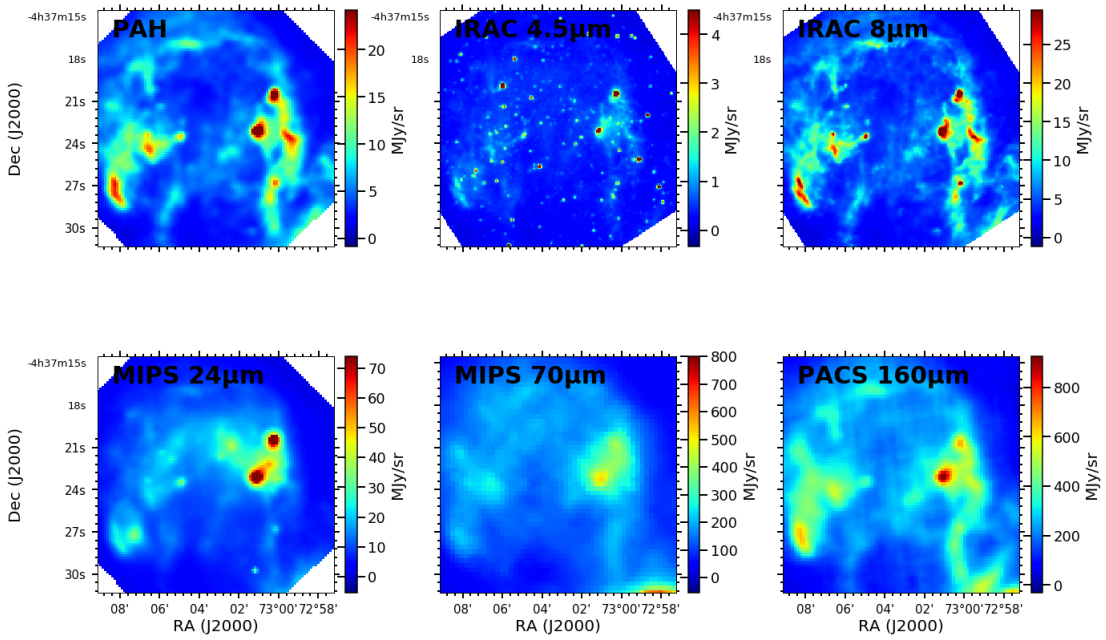

FIGURE 2.25: Continuum emission of the region N79E, similar to Figure 2.6.

the western knots are resolved, and south-east knots appear rather as diffuse emission. All of the IRS ionized lines show bright knots at the same spatial position as the continuum emission. Extended emission is evident along the edge of the bubble, with another bright knot roughly at the position of the south-east source seen in the IRAC 8μm image. The interior of the bubble also shows some diffuse extended emission for all the emission lines, although it is a bit fainter in the [Ne III] map. PACS spectroscopic observations do not exist for N79.

N105A This is the brightest subregion of the N105 complex. Study of the stellar content shows evidence of recent and on-going star formation, with the presence of OH and H_2O masers and YSOs (Bica et al., 1996; Ambrocio-Cruz et al., 1998; Massey et al., 2000; Carlson et al., 2012). Two Wolf-Rayet stars are detected in the associated stellar cluster, indicating that some of the star formation may be episodic. We see that this region shows bright compact emission, divided into two knots, on the north of our observation fields (Figures 2.27 and 2.28), with diffuse

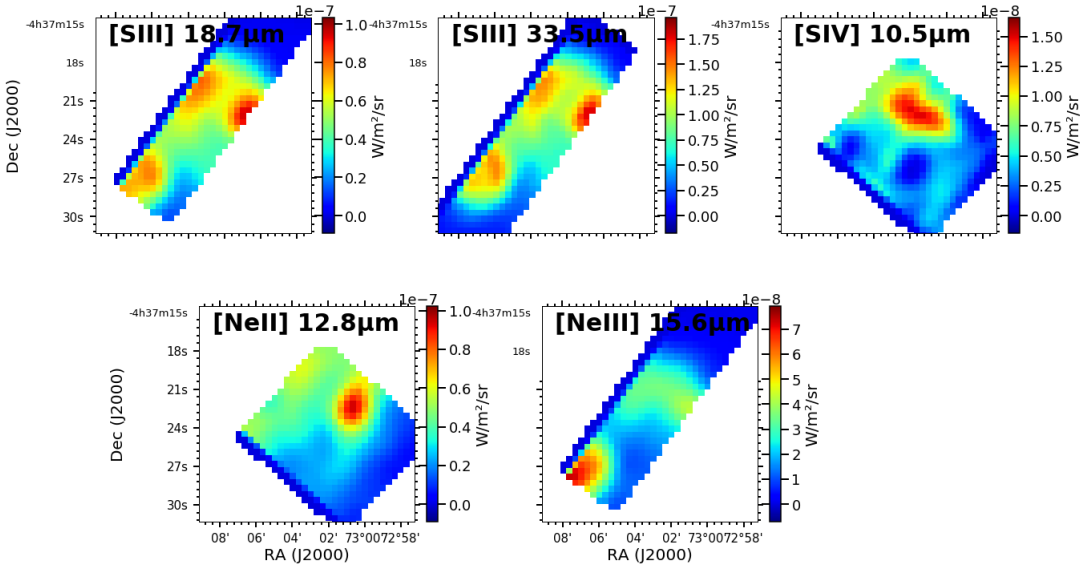

FIGURE 2.26: Similar to Figure 2.7, for the region N79E.

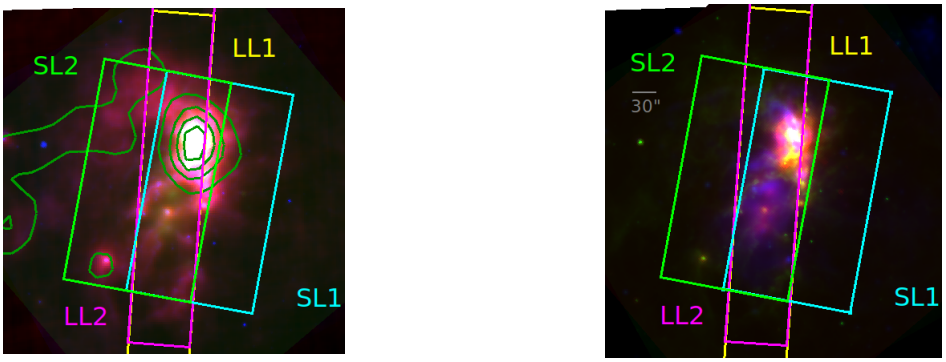

FIGURE 2.27: Similar to Figure 2.5 for N105A. IRS observation fields are displayed.

emission that extends toward the south. The continuum maps (Figure 2.28) and emission line maps (Figure 2.29) all peak at the same position. However, all of the lines show a second, more diffuse knot of emission toward the south-east of the peak where little FIR continuum emission exists, but where diffuse Hα emission can be seen (Figure 2.27). The detection of HCO^+ and HCN (Seale et al., 2012; Galametz et al., 2020) indicates the presence of dense gas clumps, with sizes of a few pc, bathed in an intense radiation field ($\chi = 83\chi_0$ in units of Draine field, Anderson et al., 2014). PACS spectroscopic observations do not exist for this source.

N158, N159, N160 These regions lie in the Molecular Ridge, a bright star-forming complex located south of 30 Doradus. The three brightest subregions are, from north to south, N158, N160 and N159 (see Figure 2.30, 2.33 and 2.36 for three color images of the subregions). Triggered star formation, that would have been initiated by 30 Doradus, and extending south (Fariña et al., 2009, and references therein) has been suggested. The whole Molecular Ridge is quite clumpy, with molecular emission in all subregions (e.g., Seale et al., 2012; Anderson et al., 2014; Galametz et al., 2020). The molecular detections are close to the peaks of the IR emission with clumps of high densities, up to a few 10^5 cm^{-3} (Martín-Hernández et al., 2008; Bolatto et al., 2000),

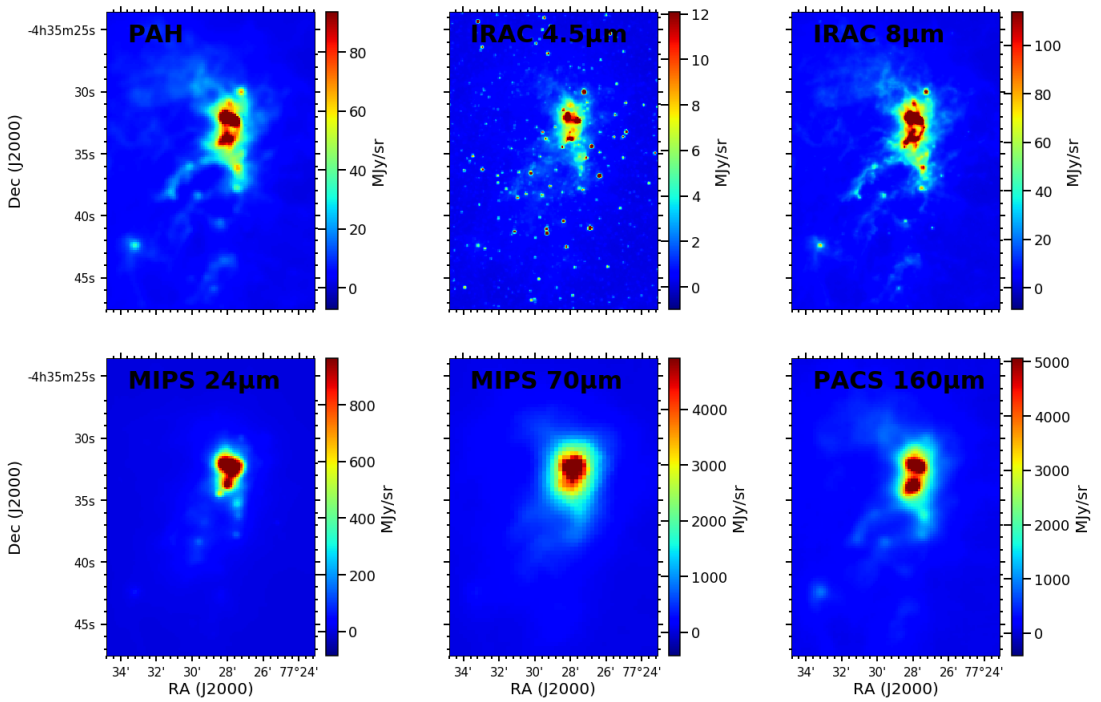

FIGURE 2.28: Continuum emission of the region N105A, similar to Figure 2.6.

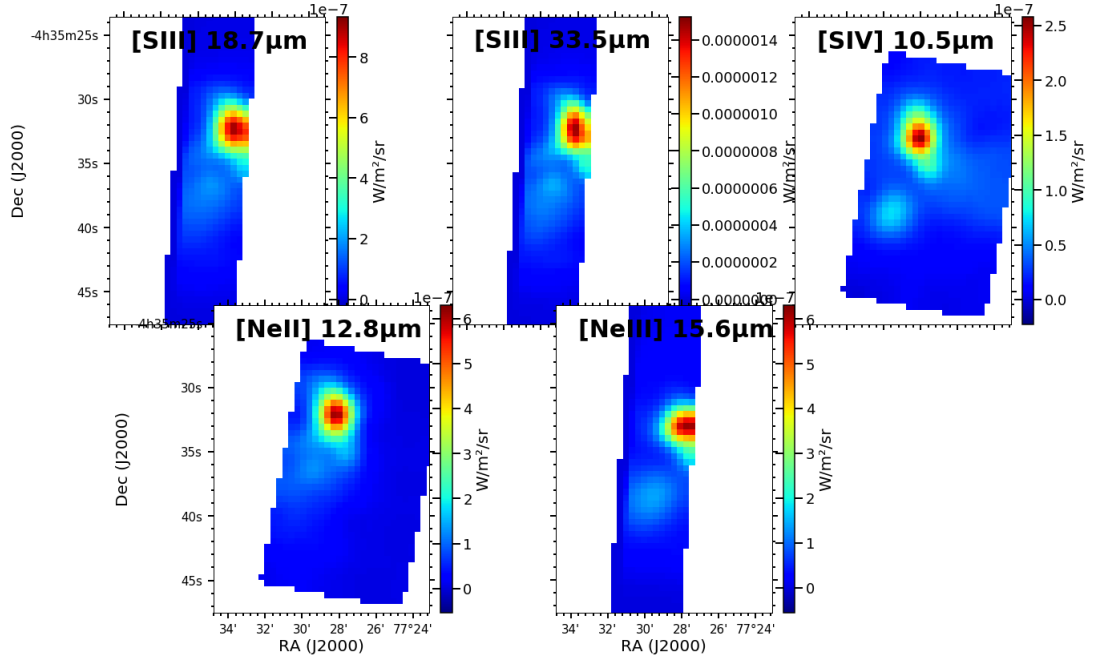

FIGURE 2.29: Similar to Figure 2.7, for the region N105A.

sitting in low density gas from a few 10^2 cm^{-3} to a few 10 cm^{-3} (Bolatto et al., 2000; Martín-Hernández et al., 2008; Heydari-Malayeri & Testor, 1986). Star formation is very active in all of the Molecular Ridge, and many YSOs are detected (e.g., Carlson et al., 2012). Although their global physical characteristics are similar throughout, the subregions of the Molecular Ridge show different spatial structure.

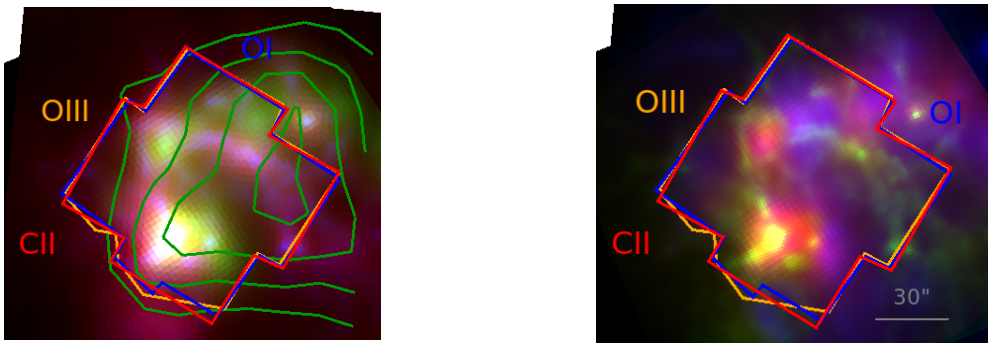

FIGURE 2.30: Similar to Figure 2.2, for the region N158. The boundaries of the PACS maps are overlaid with colors.

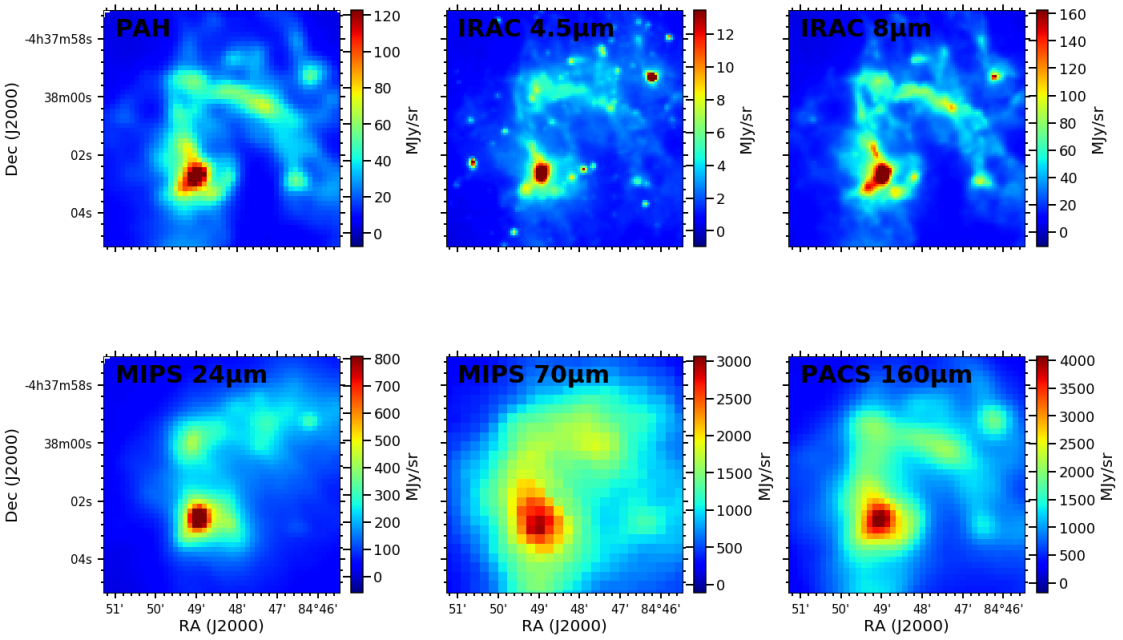

FIGURE 2.31: Continuum emission of the region N158, similar to Figure 2.6.

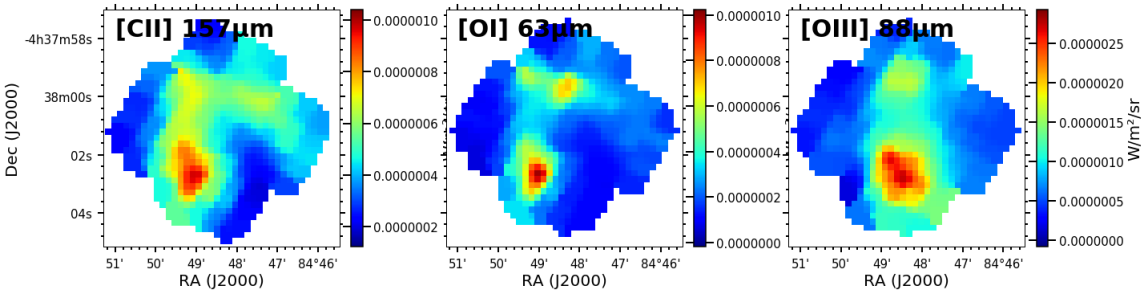

FIGURE 2.32: Similar to Figure 2.4, for the region N158.

N158 has an annular structure opened to the south and west, obvious in the IR continuum maps (Figure 2.31), with peaks along the arc-like ridge. The more diffuse emission of this arc at longer wavelengths fills in the annulus somewhat, and also extends toward the west of the

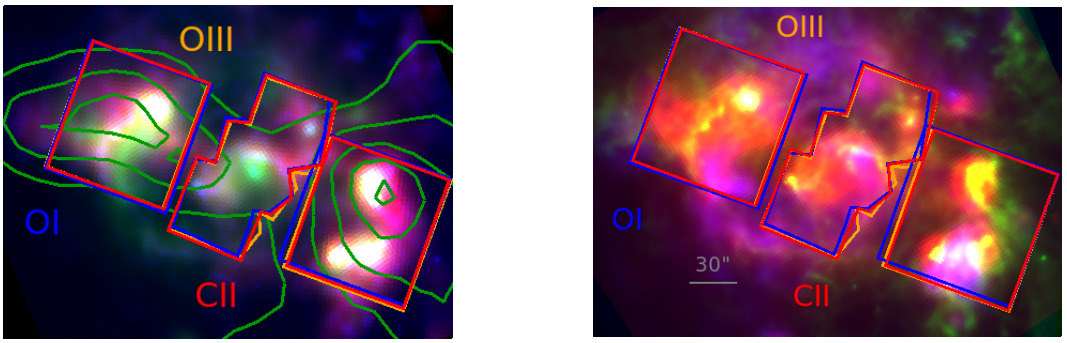

FIGURE 2.33: Similar to Figure 2.2, for the region N159. The boundaries of the PACS maps are overlaid with colors.

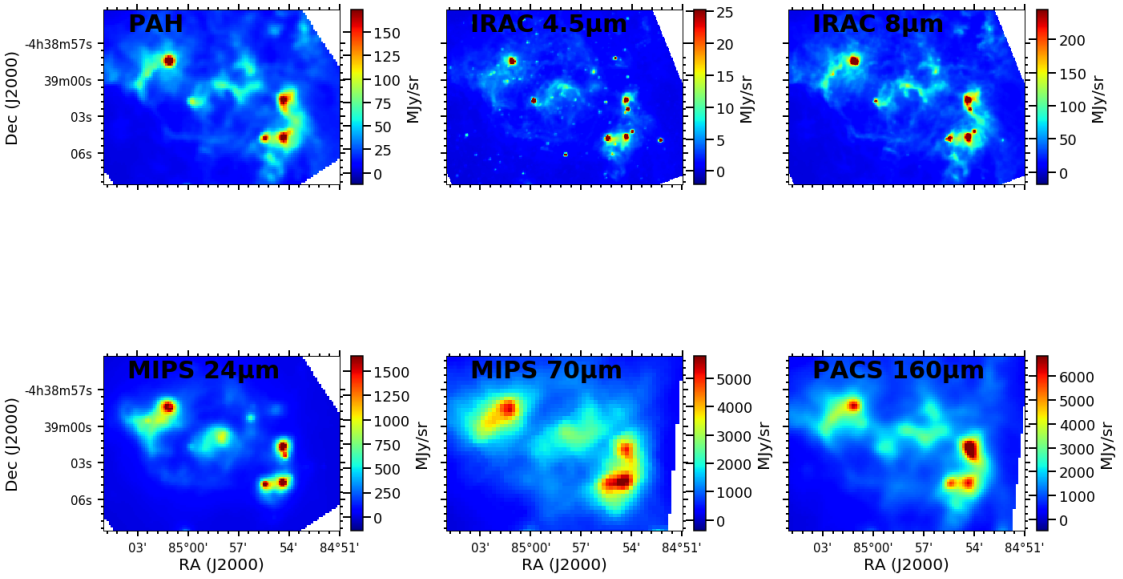

FIGURE 2.34: Continuum emission of the region N159, similar to Figure 2.6.

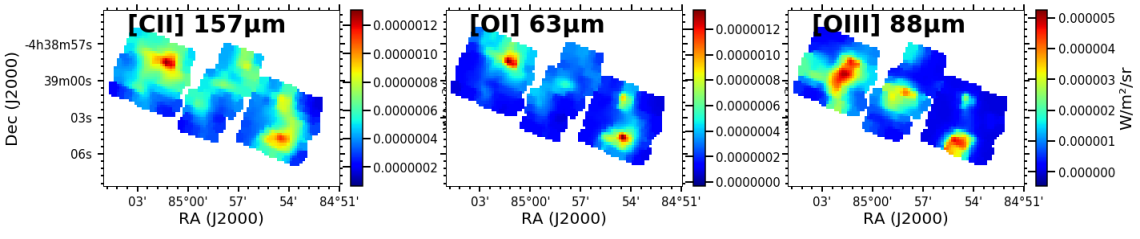

FIGURE 2.35: Similar to Figure 2.4, for the region N159.

region, where the CO emission is bright (Figure 2.30, left panel). The annular emission is visible the [C II] and [O I] maps (Figure 2.32). [O III] distribution differs from the PDR tracers, with a peak offset to the west compared to [C II] and [O I], filling in the bubble, and the diffuse

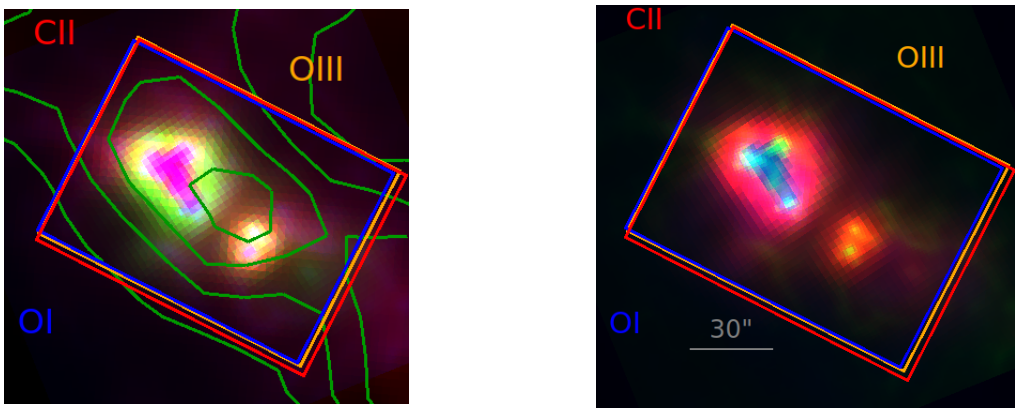

FIGURE 2.36: Similar to Figure 2.2 for the region N160. The boundaries of the PACS maps are overlaid with colors. The 24μm data (green in left panel, red in right panel) show a hole in the center of the star-forming bubble, due to saturation of the array. Contrary to 30 Doradus, we do not have a spectroscopic map to retrieve the missing 24μm continuum emission.

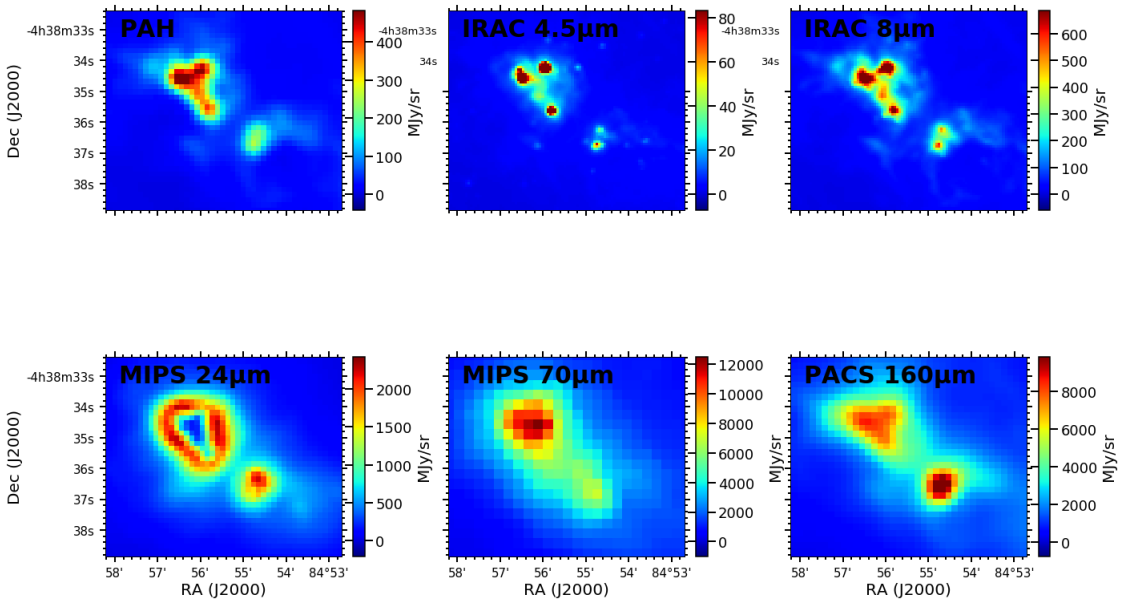

FIGURE 2.37: Continuum emission of the region N160, similar to Figure 2.6.

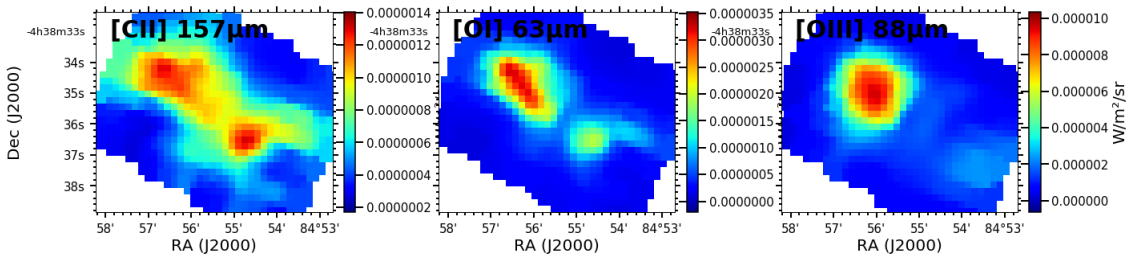

FIGURE 2.38: Similar to Figure 2.4, for the region N160.

[O III] emission extends almost vertically from south to north. Another prominent knot is visible toward the northern part of the ring for all of the FIR lines, again with the [O III] peak offset from the PDR emission lines.

N160, located just to the south of N158, shows quite a simple structure at FIR wavelengths, with two knots of bright emission visible in the PACS continuum maps: one to the north-east, which resolves into 4 sources at IRAC wavelengths and the one PACS source in the south-west which breaks up into 2 sources in the IRAC continuum maps (Figures 2.36 and 2.37). The two primary peaks can be seen in the [C II] and [O I] line maps, with an intense ridge between the two bright knots in [C II] emission (Figure 2.38). The [O III] line, on the other hand, is strikingly luminous, primarily in the north-eastern peak. We note that the CO emission peaks between the 2 primary peaks.

The southern ridge source, N159, shows 3 concentrations of star formation (Figures 2.33, 2.34 and 2.35) where there is emission from all of the continuum bands. Spectroscopic observations of the FIR lines focused on these three main zones of emission. The extent and relative intensities of the line emission varies throughout the 3 subregions. A cluster of several sources can be seen in all of the tracers toward the western side of the maps, with the relative intensities of the western sub-peaks in the different continuum tracers varying noticeably, suggesting important differences in the dust illumination and temperatures. The central concentration of the maps shows extended and more diffuse emission in all of the tracers, while [O III] shows a more compact source. As in most of the cases we study here, the distribution of the [O III] line while often associated with [C II] and [O I], is clearly offset. We also note that CO emission peaks toward the western and eastern concentrations where the PDR tracers also peak, and seems to avoid the central area.

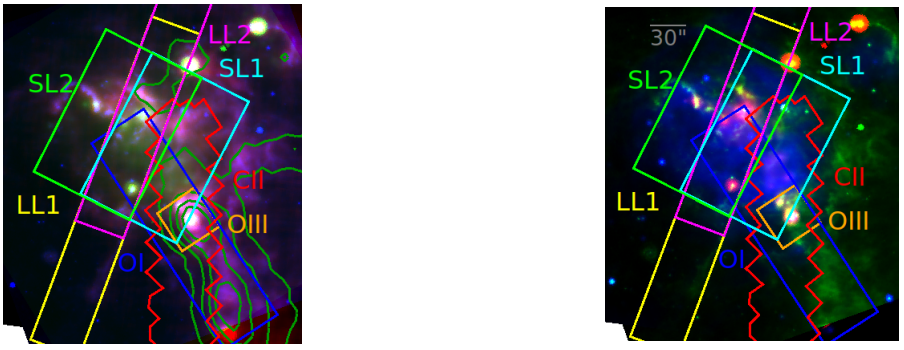

FIGURE 2.39: Similar to Figure 2.8 for N180. IRS and PACS observation fields are displayed.

N180 This region is located to the east of the Molecular Ridge. N180 harbors many YSOs (Caulet et al., 2008) and a SNR (Stephens et al., 2014). Stellar sources in this region, which include several O-type stars, are found to be younger than 10 Myrs (Bica et al., 1996). Gas densities, determined from optical observations, lie between 97 and 137 cm^{-3} for different subregions (Bica et al., 1996) with a more global value somewhat higher, around 250 cm^{-3}. The region as a whole, shows a large dusty extension toward the west, with arcs and bright peaks, and the center of the region has a prominent Hα peak (Figure 2.39) which corresponds to the peaks seen in most of the continuum and spectroscopic maps. The IRS and PACS spectroscopic observations do not center on the same position. Thus, two separate sets of continuum maps are presented: one set centered on the PACS spectroscopic map and another set of continuum maps centered on the IRS spectroscopic observations. The IRS spectroscopic observations are focused on the central star-forming bubble, which is bright in Hα (Figure 2.39), while the PACS observations

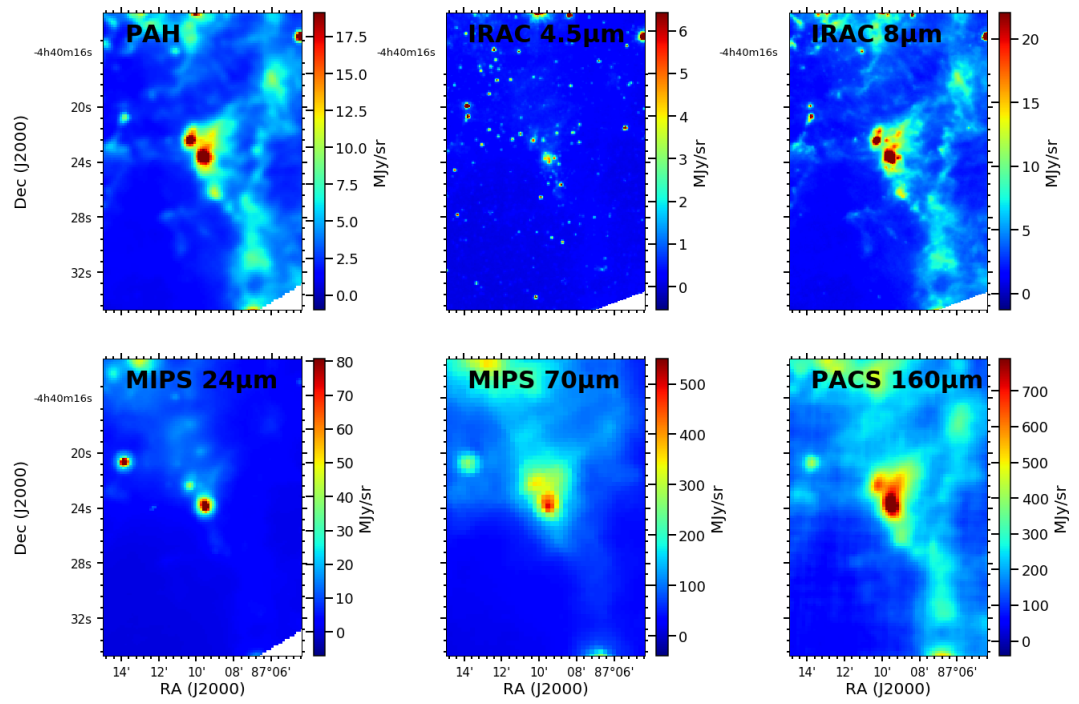

FIGURE 2.40: Continuum emission of the N180 region, similar to Figure 2.6. The continuum maps are centered on the PACS spectroscopic fields

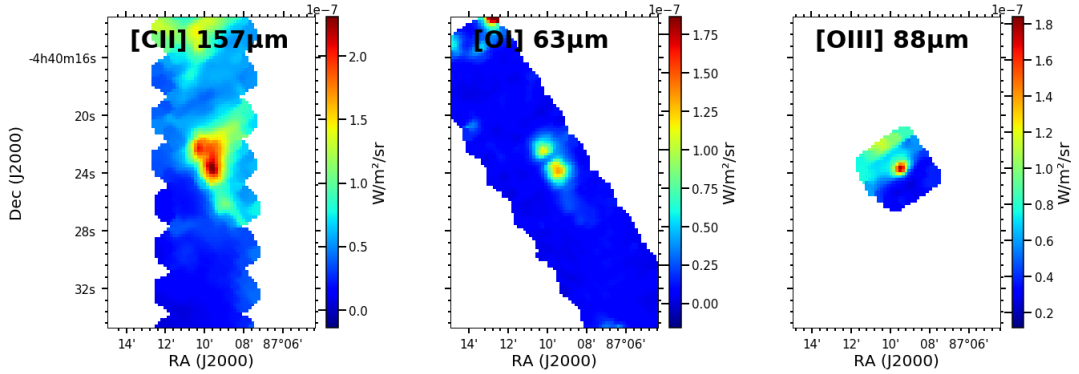

FIGURE 2.41: Similar to Figure 2.4, for the N180 region.

center on the region where the molecular emission peaks. PACS spectroscopic maps (Figure 2.41) exhibit a peak of the FIR emission at the same position as the sources in the continuum bands. [O I] shows compact emission while [C II] emission is quite extended toward the north and west. [O III] appears to also start to extend to the north, but the PACS [O III] map was limited to only one PACS footprint.

The IRS spectroscopic observations with *Spitzer* (Figure 2.43) focused on a more diffuse region of Hα emission, which also shows some extended PACS and IRAC continuum emission (Figure 2.42). The extended diffuse Hα emission corresponds to the peaks of [S IV] and [Ne III] as well as their extended emission. The two [S III] lines are extended with a peak a slightly shifted to the north-west compared to the [S IV] and [Ne III] peaks. The [Ne II] map shows two peaks: one at the same position as the [S III] line peaks, and the other located toward the south-west, just between the Hα-[S IV]-[Ne III] bubble and the PACS observations.

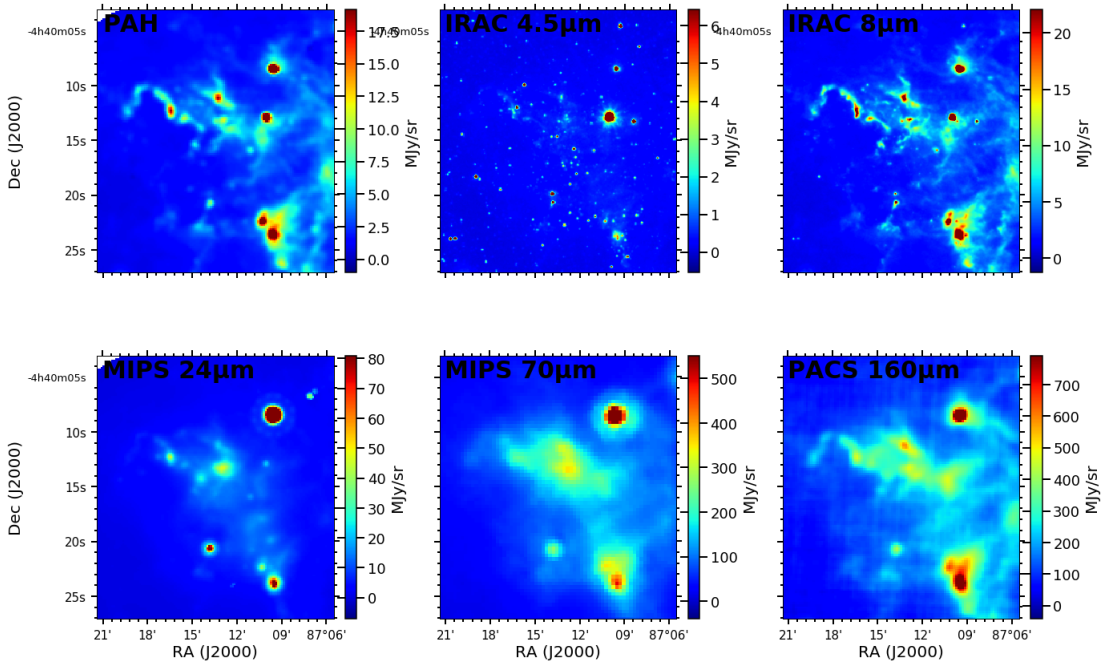

FIGURE 2.42: Continuum emission of the region N180, similar to Figure 2.6. Here, the continuum maps are centered on the IRS spectroscopic fields.

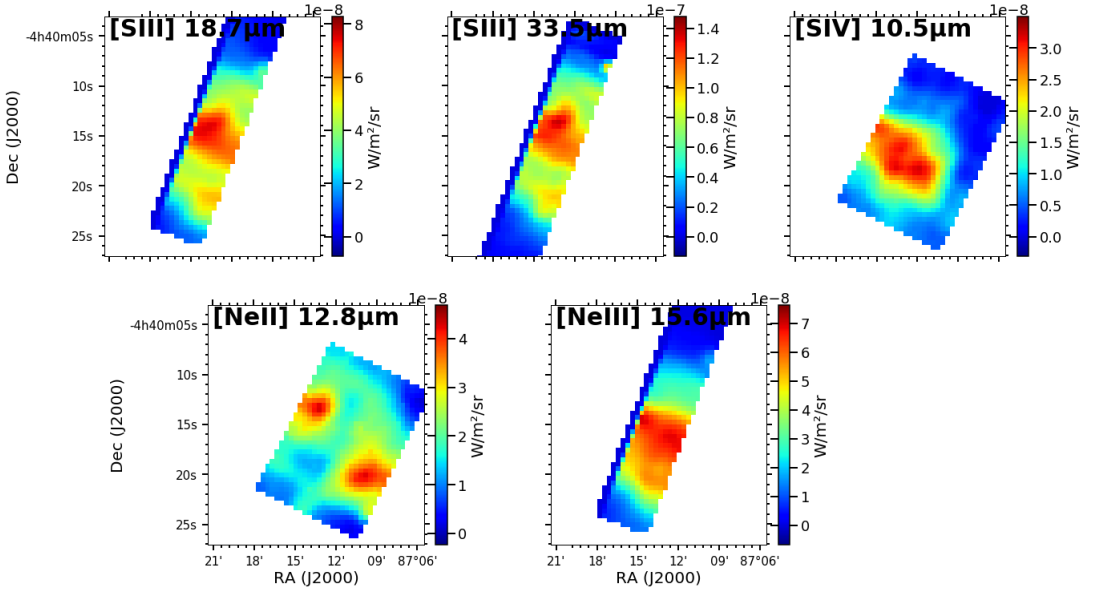

FIGURE 2.43: Similar to Figure 2.7, for the N180 region.

N66 This very active star-forming region is one of the two SMC regions in our sample. It is complex and shows evidences of multiple episodes of star-formation (Reid et al., 2006; Heydari-Malayeri & Selier, 2010), with the youngest being probably ∼3 Myrs old (Heydari-Malayeri & Selier, 2010; Rubio et al., 2018), resulting in an intense radiation field throughout the region - comparable to the values found within 30 Doradus (Lebouteiller et al., 2011; Whelan et al., 2013). The ISM of this region is also quite clumpy, with density peaks of a few 10^3 cm^{-3} in

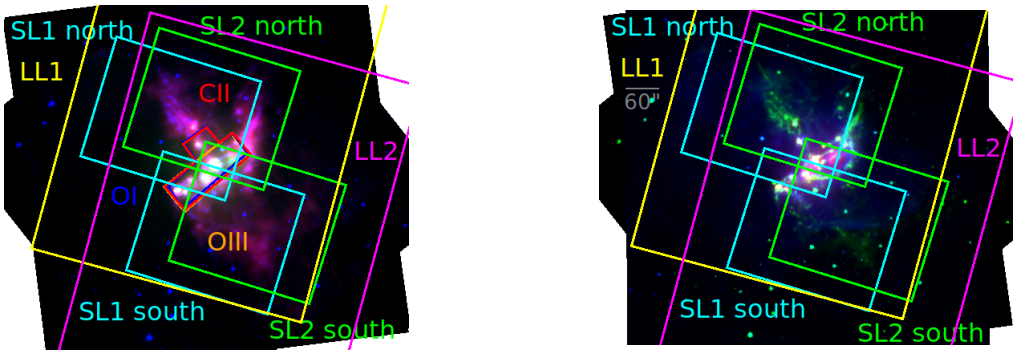

FIGURE 2.44: Similar to Figure 2.8 for the region N66. IRS and PACS observation fields are displayed. As we do not have access to CO (1→0) observations, molecular emission contours are not represented on left panel.

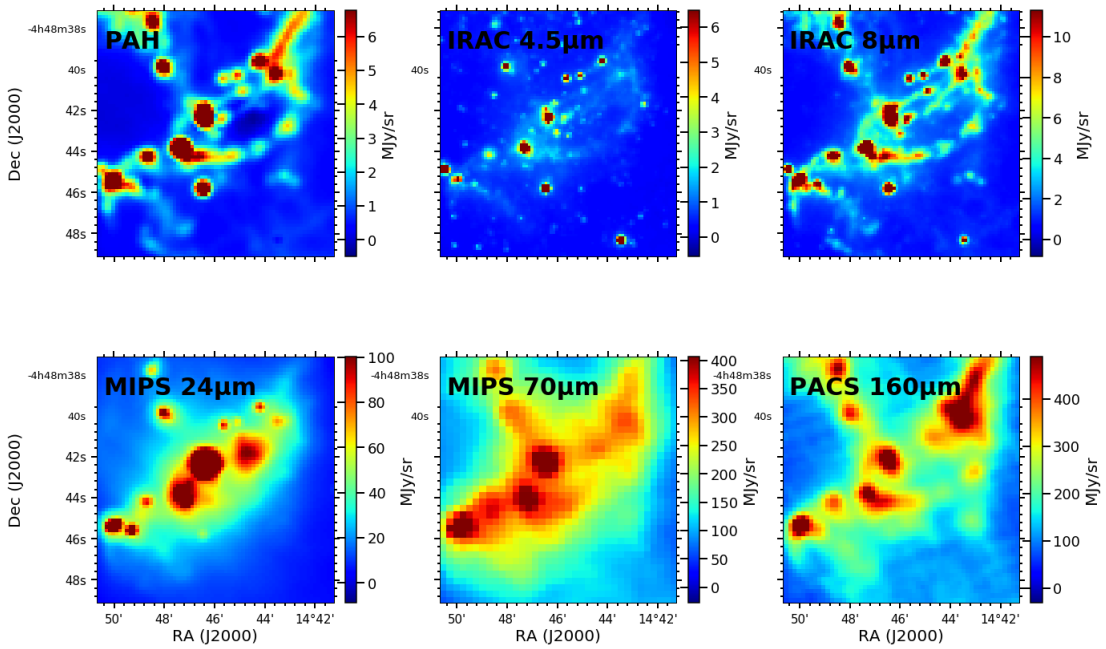

FIGURE 2.45: Continuum emission of the N66 region, similar to Figure 2.6. The bands are centered on the PACS spectroscopic observations.

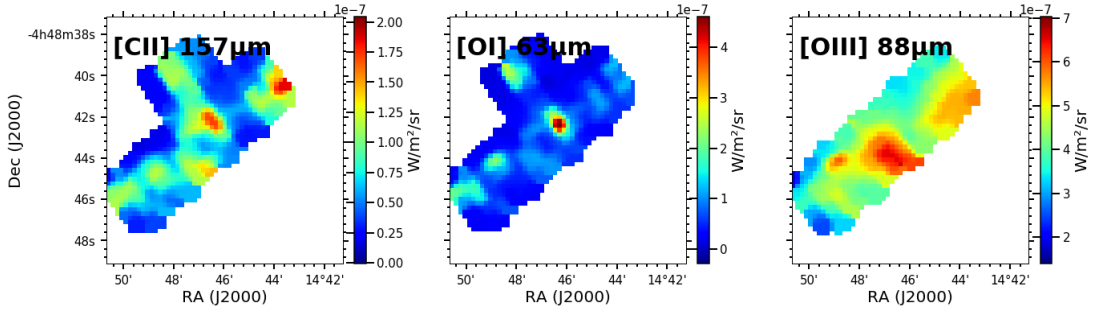

FIGURE 2.46: Similar to Figure 2.4, for the region N66.

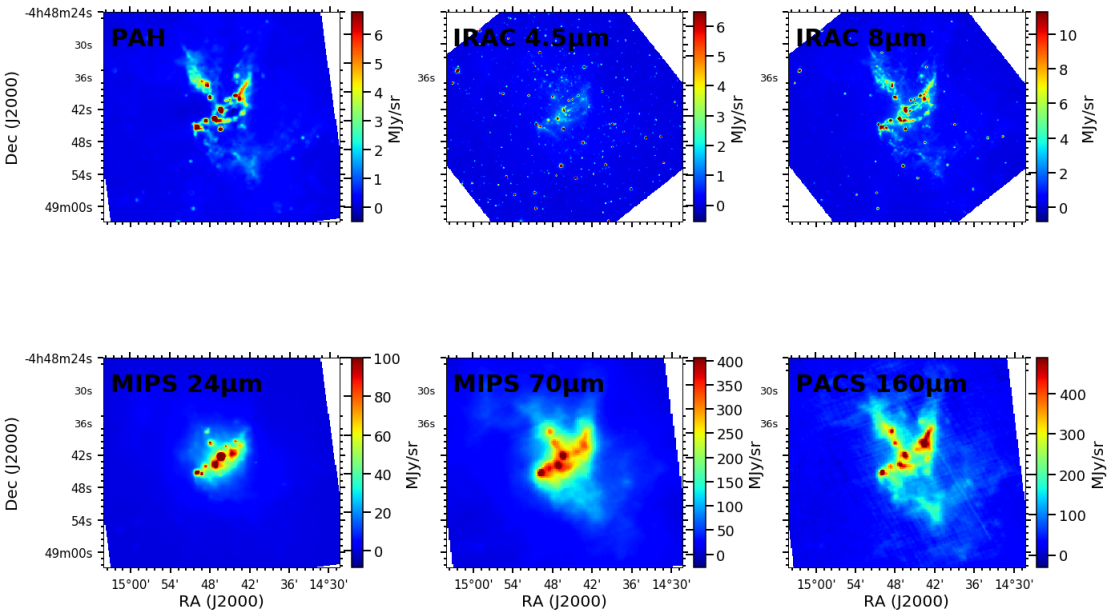

FIGURE 2.47: Continuum emission of the N66 region, similar to Figure 2.6. The bands are centered on the IRS spectroscopic observations.

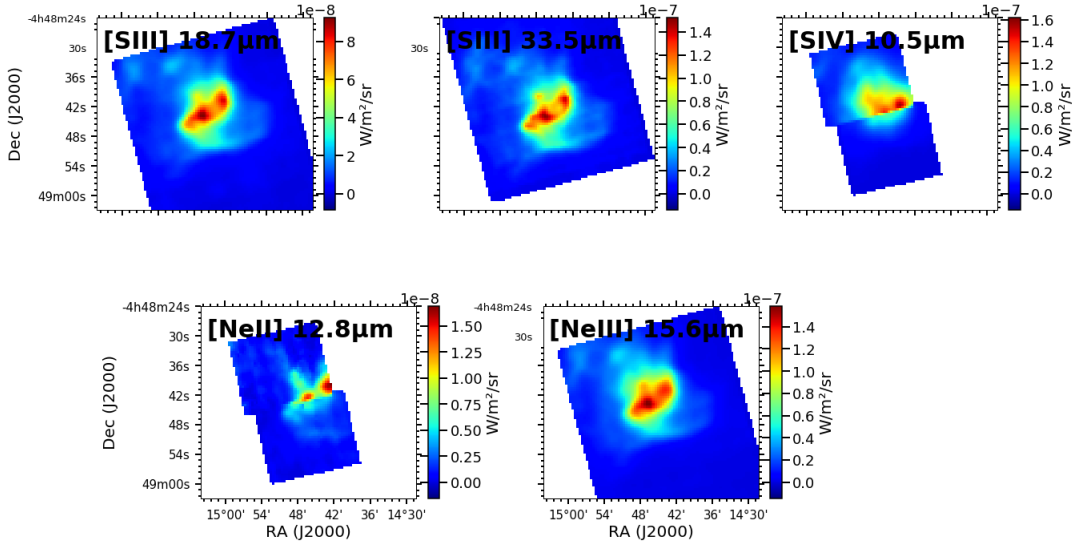

FIGURE 2.48: Similar to Figure 2.7, for the N66 region. The [S IV] and [Ne II] lines were observed with the SL module in IRS but the full region was observed at different times. Calibration differences cause the breaks in the map reconstruction.

small clumps (Rubio et al., 2000; Tsamis et al., 2003; Requena-Torres et al., 2016) bathing in a less dense medium, of a few 10 cm^{-3} to a few 10^2 cm^{-3} (Tsamis et al., 2003; Reid et al., 2006; Heydari-Malayeri & Selier, 2010), with an overall average density of $\sim 10^2$ cm^{-3} (Kurt & Dufour, 1998; Toribio San Cipriano et al., 2017). IRS observations are much more extended than those of PACS (Figure 2.44), one field covering a large region around the main star-forming zone,

separated into two fields for the SL module, while another field focuses on the brightest part of the region. The continuum observations (Figure 2.45) centered on the PACS spectroscopic fields, show a very clumpy distribution, with more diffuse emission flowing from the clumpy region (see Figure 2.44). The PACS spectroscopic observations focus on the clumpy central part. We see that the [C II] emission is extended and follows the continuum emission quite closely, with peaks that follow the 70μm distribution particularly well (Figure 2.46). The [O I] emission is much less extended, with one particularly prominent peak roughly at the center of the map, and more diffuse sources located toward the [C II] peaks. The [O III] line, however, shows a different distribution, being much less clumpy, with extended emission all over the map. The IRS observations (Figure 2.48), show a central cluster with only two extended peaks of emission. The [Ne III], [Ne II] and [S III] lines show an interesting diffuse arc extended from the central cluster to the south and west, also corresponding to faint emission in the PACS 160μm map (Figure 2.44).

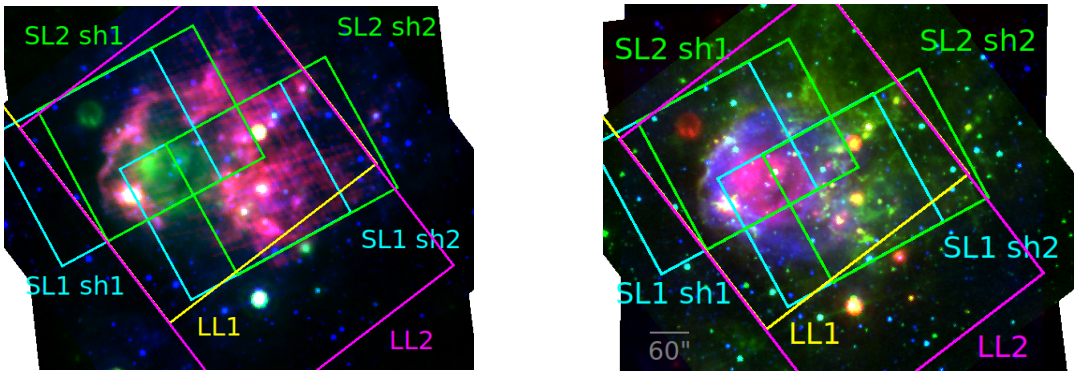

FIGURE 2.49: Similar to Figure 2.5 for N76. IRS observation fields are displayed. As we do not have access to CO (1→0) observations, molecular emission contours are not represented in the left panel.

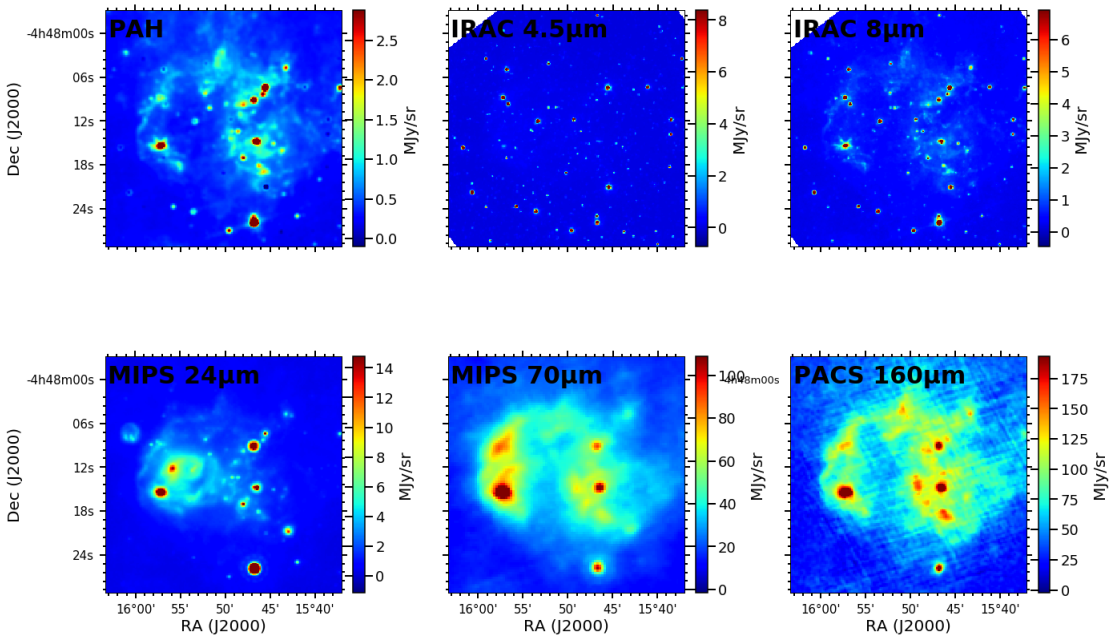

FIGURE 2.50: Continuum emission of the N76 region, similar to Figure 2.6.

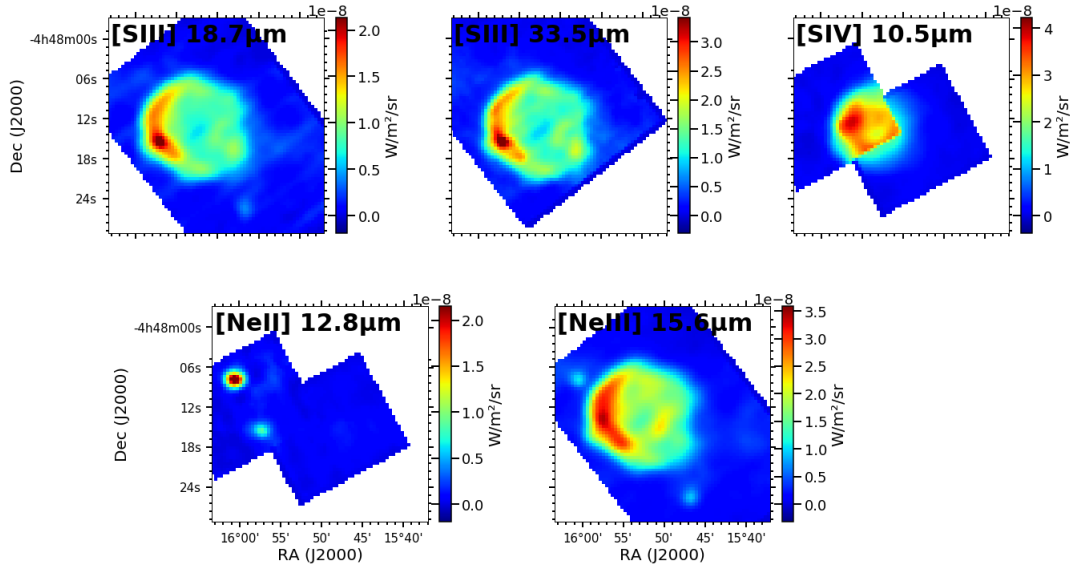

FIGURE 2.51: Similar to Figure 2.48, for the region N76.

N76 Located to the north of N66, N76 has been little studied (Garnett et al., 1991). It hosts a SNR, and signs of recent star formation, although the radiation field is partly supported by an older stellar population. We see in Figure 2.49 that this region contains a large bubble, visible in Hα emission (blue, right panel), with a less extended 24μm emission in the center (red in left panel, green in right panel). The edges of this bubble are visible in the continuum maps, especially in 70μm and 160μm bands (Figure 2.50). The IRS lines, [Ne III] and the [S III] lines, cover the extent of the Hα bubble (Figure 2.51). The [S IV] line distribution also has circular emission, but is less extended, and basically located at the center of the Hα bubble. Only the [Ne II] distribution does not resemble the Hα bubble, with only two emission peaks of emission and no extended emission. PACS spectroscopic observations do not exist for this source.

2.3.2 Global picture

To have a more global view of the sample, we attempt to organize the different star-forming regions on an evolutionary sequence. The main challenge in that attempt of classification is that star formation is not a simple and linear process. There may have been multiple episodes of star formation in a same region, with some of them triggered, for example, by the expansion of an H IIbubble, or supernovae events, or different subregions that are not at the same evolutionary stage. Moreover, there is different evidence that can help to understand the evolutionary stage: the presence of SNRs, or other tracers of stellar winds (e.g., Wolf-Rayet stars), measures of the age of some stars if they can be resolved individually, etc. Each of those tracers have uncertainties, and they do not always agree. Thus, the organization presented here is a very preliminary attempt to have a qualitative view on the evolution of star-forming regions, and we do not aim to have a quantitative estimation of the "evolutionary time scale" between two regions, nor of the age of individual regions.

We created two classifications: one for large regions, by considering the union of different subregions (e.g., N11), the other for sub-regions taken separately (e.g, considering individually N11B, N11C and N11I). The two organizations are presented in Figures 2.52 and 2.53.

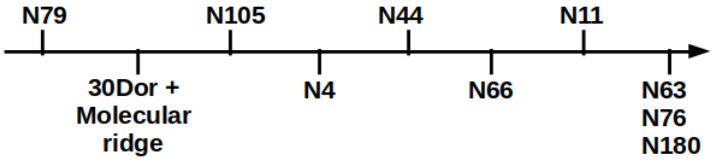

FIGURE 2.52: Attempt of a qualitative classification of the relative evolutionary stage of the global star-forming regions in this study.

For global regions, we decided to consider the three sub-regions of the Molecular Ridge together with 30 Doradus, as 30 Doradus is thought to have triggered the star formation of the Molecular Ridge. N79 is considered to be a younger version of the 30 Doradus complex (Ochsendorf et al., 2017). N11, on the other hand, is similar to an older version of 30 Doradus (Walborn & Parker, 1992). The complex N105 contains evolved stars, and thus is probably older than 30 Doradus. The region N4 is composed of two sub-regions, and it seems that the sub-region N4B triggered star-formation in N4A. Considering the fact that the stellar age in N4A is similar to that found in 30 Doradus (Heydari-Malayeri & Lecavelier Des Etangs, 1994), the complete region N4 is probably older than 30 Doradus. However, as we do not have signs of triggered star formation in N105, the region N4 is also probably older than N105. The two complexes N44 and N66 contain both evolved stars, and evidences of triggered star formation. However, they do not present a stellar cluster as evolved as the central cluster LH9 in N11, and are thus between N4 and N11. We based the respective positions of N44 and N66 on some indications of stellar age, but this organisation has to be taken with caution. Finally, the regions N63, N180 and N76 were placed at later stages than the N11 complex. Indeed, they present signs of an old stellar population, especially through the presence of SNRs. However, we lack more detailed investigation of the absolute age or evolutionary stage of those regions to be able to separate them on this evolutionary path.

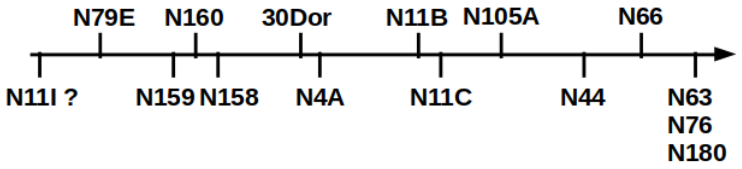

FIGURE 2.53: Attempt of a qualitative classification of the relative evolutionary stage of the star-forming regions, taking into account the individual sub-regions.

We now focus on individual sub-regions, when they are observed separately. Here again, the region N79E is probably younger than 30 Doradus and the three subregions of the Molecular Ridge (N158, N159 and N160). The star formation in the Molecular ridge was probably triggered from north to south, leading to the respective evolutionary positions of N158, N159 and N160. 30 Doradus is also logically a bit more evolved than those three subregions. N4A shows stellar ages close to those found in 30 Doradus, and thus this region is probably a bit more evolved, but close to 30 Doradus. On the contrary to the organisation of the larger regions, the two subregions

N11B and N11C are less evolved than N105A, N44 and N66, with younger star clusters, that have less disrupted the star-forming initial cloud. The respective positions of the other regions (N105A, N44, N66, N76, N63, N180) are similar to that made for the organization of the global regions.

The N11I region is a special case, as it is the only one with no clear signs of ongoing star formation. It contains a cloud with CO emission, but is much more quiescent than the other regions. We suggest that this region is less evolved than N79E, before the first star forming event, but it is not possible to clearly identify if it is a region just about to form new stars.

2.4 Other data used

For the point source correction, we relied on a few catalogs: Gruendl & Chu (2009), which focused on YSOs in the Magellanic Clouds; Jones et al. (2017), where a systematic classification of the point sources in the Magellanic Clouds is made; and Carlson et al. (2012), where they focus on YSOs in some star-forming regions of the Magellanic Clouds. The use of these three catalogs allowed us to construct a complete list of point sources for all of our regions.

To put our Magellanic Cloud regions in a larger context we compare our results to full, unresolved galaxies of the Dwarf Galaxy Sample described in Madden et al. (2013). This survey is a collection of 48 dwarf galaxies in the Local universe, chosen to cover a wide range of physical parameters (e.g., metallicity: 1/50 $Z_\odot$ to 1/3 $Z_\odot$, stellar mass: $\sim 10^6$ $M_\odot$ to a few 10^{10} $M_\odot$, total IR luminosity: 6.6 10^7 $L_\odot$ to 1.6 10^{11} $L_\odot$), observed with the *Herschel* photometry and spectroscopy as well as MIR photometry from *Spitzer* (Bendo et al., 2012).

CHAPTER 3

MODELS

Contents

3.1 Modeling strategy

As we have seen in Chapter 1, the ISM is complex and characterized by numerous parameters: density, elemental abundances, radiation fields, metallicity, among many others. We will restrict our focus to some of them: the metallicity, the effect of which can be seen by comparing the LMC and SMC (see Chapter 1, Section 1.4 for details), the density, which can be traced with combinations of MIR emission lines detected by *Spitzer*/IRS and FIR lines detected by *Herschel*/PACS in the Magellanic Clouds (see Chapter 2, Section 2.3), and the ionization parameter (U), which is linked to both the distribution of matter and the ionization properties of the source. U is the dimensionless ratio of the hydrogen-ionizing photons to the total hydrogen density, defined as follows:

$$U = \frac{Q(\mathrm{H}^0)}{4\pi\, r^2\, n_{\mathrm{H}}\, c} \tag{3.1}$$

where $Q(\mathrm{H}^0)$ is the number of hydrogen-ionizing photons emitted by the source per second, n_{H} is the total hydrogen density, c is the speed of light and r is the distance from the ionizing source to the cloud inner edge.

Various models can be used to describe the ISM, depending on the objective of the study. For example, the Meudon photodissociation region code (Le Petit et al., 2006) concentrates on the detailed physics of the PDR and molecular region and MOCASSIN (Ercolano et al., 2003), which is a 3D Monte-Carlo photoionization code. However, since our aim is to have a model

of the multiphase ISM, we use a code that allows us to compute both the ionized and neutral phases self-consistently. We prefer a 1D model to reduce computation time and to allow a large variation in the parameters.

For this study we use Cloudy (version 17.01; Ferland et al., 2017), which is a 1D photodissociation and photoionization code that self-consistently solves the thermal, chemical and radiation equilibrium of a multi-phase medium exposed to a radiation source. The user provides the spectrum of an ionizing source, that can be either a prescription included in Cloudy (e.g., a blackbody or a power law) or a spectrum from another prescription (e.g., a stellar atmosphere, AGN, stellar population), and sets the parameters to define the media ionized by the source. Those parameters can include many features, such as the distribution of the matter (e.g., density, distance from the ionizing source), the composition of the media (e.g., elemental abundances, dust quantity and composition) or other radiation sources (e.g., Cosmic Microwave Background (CMB) or cosmic rays (CR)).

To calculate the opacity of the emission lines, it is possible to give the number of iterations or to iterate to full convergence. As one iteration after the first calculation is often sufficient to compute coherent opacities for the lines, we use a single iteration for all of our models. The calculation is stopped based on criteria set by the user (e.g., reaching a given temperature, a given opacity), and warnings are given in the case of aborted models. We assume static(no global motion, e.g., flows or collision) and steady-state conditions (i.e., we assume that the medium reached physical, chemical and thermal equilibrium) in the modeled ISM and do not include turbulence. In principle, the addition of some dynamic behaviour can have a significant effect on observations. For instance, in an expanding shell the opacity of the medium for a line will decrease, while the central wavelength of the line shifts as the material expands. Dynamical effects are complex and are still under development in Cloudy (e.g., winds, flows, time-dependant variation of the ionizing source, non-equilibrium medium).

3.2 Description of the model parameters

A simple approximation of the ISM physical conditions is to suppose that the density is constant throughout the cloud. Such a hypothesis has the advantage of being fast to compute, and the model outputs can be linked more easily to the parameters used. However, there is also evidence of the ISM being in pressure equilibrium (e.g. Field et al., 1969; Wolfire et al., 1995), instead of having a constant density. Thus we ran 2 sets of models: one with constant density and another with constant pressure to evaluate the effects on the model solutions. Table 3.1 summarizes the model input parameters.

3.2.1 Radiation source

In star forming regions, the main ionizing sources are the massive O and B-type stars, but there is a distribution of masses of stars, the most numerous being the less massive stars, which can also influence the ISM, by heating the dust, for example. The ionizing source used in our models is a full stellar evolutionary synthesis of the stellar population, the PopStar models (Mollá et al., 2009), with the Chabrier initial mass function (Chabrier, 2003). We assume a single burst of star formation. The effective temperature is no longer a relevant parameter, and we chose to vary the age of the burst. In a first set of models, we varied the age across a very broad range, from 0.1 to 100 Myrs, with steps of 0.2 dex. After a first comparison of the constant density model outputs with the data (see Section 4.4.2), we noticed that models with burst ages of 10 Myrs or more cannot reproduce some observation (e.g., [O III] 88μm), independently of the other parameters.

Moreover, at ages younger than 1 Myrs, the new stellar cluster is probably too embedded in the initial birth cloud to be observed with our tracers. Thus, the probable age of the star cluster is between 1 and 10 Myrs for all of our sources, and constant pressure models only concentrate on this range of ages, with the same step (0.2 dex).

There are additional radiation sources that can influence the ISM conditions. We chose to include two additional radiation fields included in Cloudy database: the Cosmic Microwave Background at redshift 0, and included cosmic rays assuming the Galactic rate (see Ferland & Mushotzky, 1984, for details). Cosmic rays are necessary to sustain the chemistry observed in neutral gas, as well as in the molecular core (e.g. Dyson & Williams, 1997).

3.2.2 Structure of the gas

The ionizing source is linked to the gas structure through the ionization parameter (see Equation 3.1 for definition), as this parameter links the quantity of ionizing photons and the inner radius of the cloud. The ionization parameter is varied in log from -5 to 0, by steps of 1 dex for the constant density models. A first comparison with our observations (see Chapter 4, Section 4.4.2) shows that the two extreme value, log(U)= -5 and log(U)=0, are unable to reproduce the observations. Thus, the constant pressure models were run with a smaller range, between log(U) of -4 and -1 with steps of 1 dex.

The initial density is also set in the models. For the constant density models, the density is fixed at its initial value, varied in $\log(n_{\rm H}) = 1$ to 6 in steps of 0.5 dex. The initial density is also a parameter for the constant pressure model. Indeed, the pressure in the models is self-consistently calculated by the model with $P = n_{\rm H}.k_{\rm B}.T$, where P is the pressure, $n_{\rm H}$ is the total hydrogen density, $k_{\rm B}$ is the Boltzmann constant and T is the temperature. The pressure can be set by itself in Cloudy, but for consistency and comparison between constant pressure and constant density models we always give an initial density as input. For the constant pressure models, we decided to change the range of the initial density. The first comparison with our data (see Section 4.4.2) showed that the highest values of the initial density, at 10^3 cm^{-3} and more, were not able to reproduce the emission of the ionized gas. It also gave a hint toward a possible need of densities below our lower bound, which was set to 10 cm^{-3}. Thus, the initial density in the constant pressure models is varied from $\log(n_{\rm H}) = 0$ to 3 in steps of 0.5 dex.

Another important aspect of the structure of the gas in the model is the criterion used to stop the calculation. It can be based on physical parameters (e.g., a temperature, a distance from the ionizing source, a density, a mass), on the composition of the gas (e.g., the quantity of a molecule, an ion, an atom) or on properties of the output radiation (e.g., the intensity of a line, an optical depth). There is also a stopping criterion based on the number of zones used for the calculation. We decided to use a stopping criterion of $A_{\rm V}$=2.5. This prescription ensures us to reach into the PDR for all the models of our grid (Tielens & Hollenbach, 1985; Hollenbach & Tielens, 1999). An inspection of the model outputs showed that the region where molecular hydrogen is formed is always reached.

3.2.3 Properties of the gas and dust

The relative elemental abundances are chosen according to a Galactic template in Cloudy, based on Cowie & Songaila (1986); Savage & Sembach (1996); Meyer et al. (1998). The grain distributions are also set using this template, and based on Mathis et al. (1977). Considering that PAHs can play an important role in the thermal balance of the ISM (e.g. Watson, 1972; Tielens & Hollenbach, 1985; Wolfire et al., 1995; Draine & Li, 2000), we include PAHs in our models. The

Parameters	Constant density models	Constant pressure models
Metallicity	1/2 $Z_\odot$, 1/5 $Z_\odot$	1/2 $Z_\odot$, 1/5 $Z_\odot$
Log of burst age (Myrs)	5−8, steps 0.2	6−7, steps 0.2
Log(n_H) (cm^{-3})	1 − 6, steps 0.5	0 − 3, steps 0.5
Log(U)[a]	-5 − 0, steps 1	-4 − -1, steps 1
Stopping criterion	A_V=2.5	A_V=2.5

(a) The ionization parameter (U) is defined in equation 3.1

TABLE 3.1: Main parameters and their range of values used to compute Cloudy model grids for this study.

Feature (μm)	Center (μm)	Wavelength range (μm)	Continuum range (μm)
PAH 3.3	3.30	3.25−3.35	3.20−3.25, 3.35−3.40 [a]
PAH 6.2	6.2	5.9−6.4	5.4−5.9
PAH 7.9	7.9	7.4−8.4	6.4−7.4
PAH 11.3	11.3	11.1−11.5	10.7−11.1
PAH 11.8	11.8	11.6−12.3	12.3−13.0
PAH 13.3	13.3	12.9−13.7	13.7−14.5

(a) The continuum for the this feature is split into two parts, as the surrounding of this features does not allow an estimation of the continuum on only one side of the feature (*refer to the PAH spectrum when I'll have inserted it*). The sum of the two continuum widths corresponds to the full width of the feature.

TABLE 3.2: Characteristics of the PAH features available in Cloudy, along with the associated continuum bands.

default prescription for PAH size distributions in Cloudy is from Abel et al. (2008). Because the Magellanic Clouds have lower metallicity than the Galaxy, we scaled the elemental abundances by 0.5 $Z_\odot$ and 0.2 $Z_\odot$ (LMC and SMC, respectively) and the grain and PAH relative abundances similarly, for the Magellanic Clouds conditions. To mimic the destruction of PAHs in ionized regions and their decrease in molecular regions, the PAH abundance is scaled in Cloudy with the abundance of neutral atomic hydrogen.

3.2.4 Output tracers and conditions of the gas and dust

A wide variety of information can be saved at the end of the Cloudy computation of the model. We chose to save information of atomic lines that match the spectral range of *Spitzer* and *Herschel* telescopes, along with some other lines that may be observed with other facilities (see Chapter 1, Table 1.3 for the list of lines and additional information). We also saved continuum emission to compare with the continuum bands used in our study: IRAC 3.6μm, IRAC 4.5μm, IRAC 5.8μm, IRAC 8.0μm, MIPS 24μm and MIPS 70μm for the *Spitzer* telescope, and PACS 70μm, PACS 100μm and PAC 160μm for the *Herschel* telescope (for more information about the observation bands, see Table 2.2, 2.3 and 2.5 in Chapter 2).

The PAH emission is composed of several complex features (Figure 1.13 in Chapter 1, or Figure 5.1 in Chapter 5). It is possible to save the Cloudy output for PAH emission on the six main features between 3μm and 15μm (Table 3.2). The output is the complete emission of PAH plus the continuum. To allow the user to obtain the PAH emission alone, the continuum value is saved around each PAH feature, with the same width as the feature itself. The widths of the individual features are small enough to consider the continuum to be constant, and subtracting the surrounding continuum is enough to recover the PAH emission (Table 3.2).

We also saved the total infrared luminosity (TIR), defined as the total emission between 3μm and 1100μm in Dale & Helou (2002).

3.3 Description of the model diagnostics

Here we investigate the evolution of various outputs from the models. We have saved global values of the emission lines for the full model, and cumulative intensity of the emission as a function of depth into the cloud. This depth dependency will be represented with the extinction, A_V, which is also computed by the model for each zone.

To investigate further dependencies based on the proportions of PDRs and H II regions toward a line of sight, we created models for different cases based on the full cumulative models: the H II region only and PDR only. According to the classical definition of the ionization front, the split between the two regions is chosen as the point at which the electron density has dropped to half of its maximum value. The H II region emission is then the cumulative emission at this limit, and the PDR emission is the total emission with the H II emission subtracted. The precise limit between H II region and PDR can be discussed, but changing our limit on the electron density, e.g., from 50% of its maximum to 10% of its maximum, would not have a strong effect on our result. For all the models, it would only change the distribution of the tracers between H II region and PDR by a few percent. This potential effect was thus not studied in this work.

3.3.1 Description of the evolution of the tracers with depth

We show the behaviour of different outputs computed by the model as a function of depth into the cloud, represented by the extinction in A_V, for metallicities of 1/2 $Z_\odot$ and 1/5 $Z_\odot$, stellar ages of 4 Myrs and 10 Myrs, log(U) of -4 to -1 in steps of 1 dex and densities of 10 cm^{-3}, 100 cm^{-3} and 1,000 cm^3 (Figures 3.1 and 3.2). The electron density illustrates the difference between the ionized H II region, and the neutral PDR. The temperature is displayed to have a general idea of the physical conditions in the modeled ISM. The other plotted values are the cumulative emission of some diagnostic lines and bands[1]. These include [O III] 88μm, considered to be a good tracer of H II regions, [C II] 157μm and [O I] 63μm, that are major coolants of the atomic PDR gas, and two *Spitzer*/MIPS bands, at 24 and 70μm. The plotted values are normalized to 1 in order to facilitate comparison. However, the maximum temperature (T_{max}), which is approximately the value reached at the ionization front, is indicated above each subplot.

Physical conditions In the first set of models, with half solar metallicity (Figure 3.1), we see that the electron density and temperature are at their maximum values at the beginning of the cloud, stay roughly constant, and suddenly drop. The exact cloud depth (A_V) at which this drop occurs depends strongly on the ionization parameter. It also seems steeper for higher ionization parameter values, but this is due to the logarithmic representation. Another noticeable behaviour is the small discrepancy between the depth of the ionization front and the drop of the temperature, which leads to a small part of the PDR being heated to more than 1 000 K, although the PDR is usually considered to have a temperature lower than 1 000 K (see e.g., Tielens & Hollenbach, 1985). We will come back to this point in Section 3.3.2.

[1] A rigorous account of the band flux would require integrating the modeled SED within the filter transmission of each instrument. This integration requires the knowledge of the assumed flux convention used to estimate the flux at the nominal wavelength of the band. These conventions are well documented, but are not the same for every instrument. In practice, the rigorous color-corrected flux is never significantly far away from the SED model interpolated at the nominal wavelength of the filter (Galliano et al., 2021).

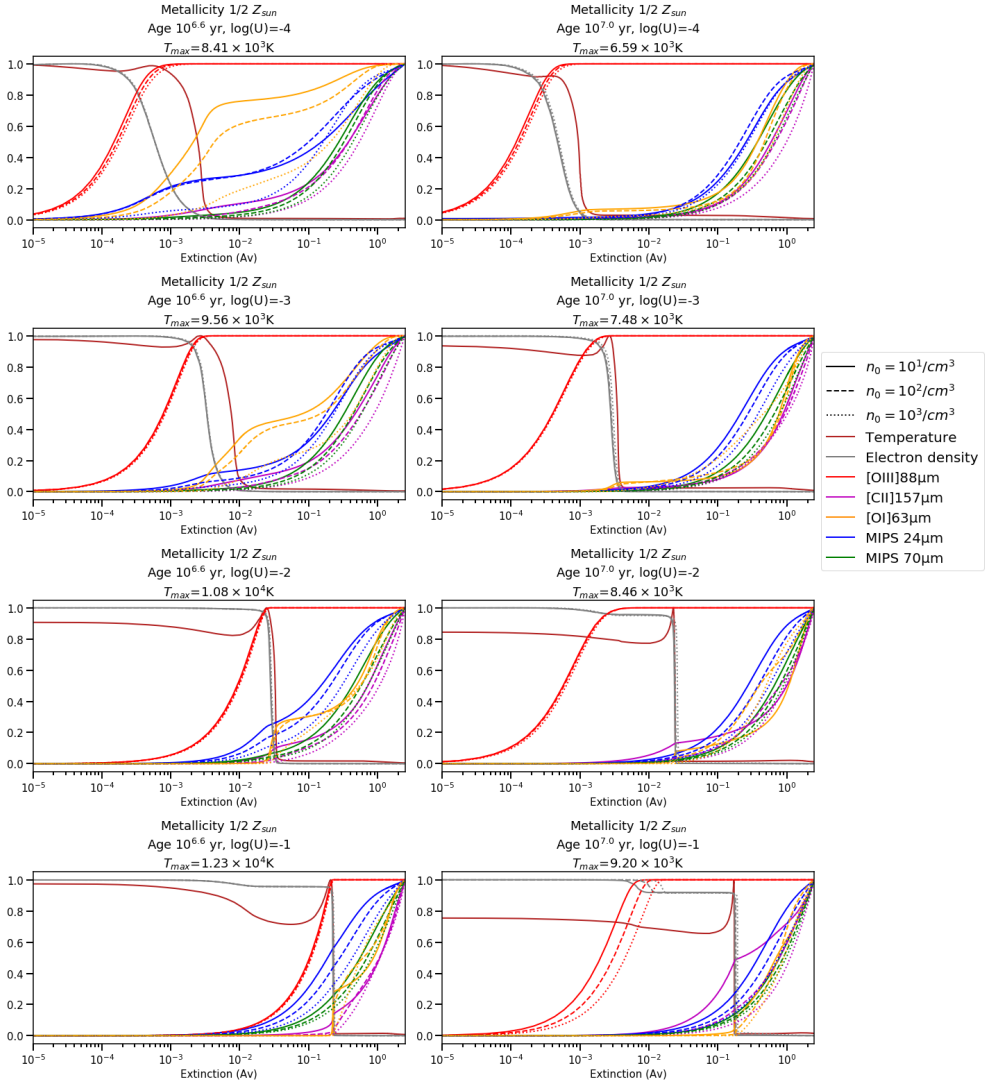

FIGURE 3.1: Results of constant density models with half solar metallicity, for FIR line and band intensities and gas temperatures (normalized to 1) for densities between 10 and 1,000 cm^{-3} as a function of A_V. (line color and type legend on the right of the figure). Tmax is indicated above each subplot. Results are displayed for two ages, ∼4 Myrs (left) and 10 Myrs (right), four log(U) values between -4 and -1, increasing from top to bottom.

[O III] 88μm We see that the [O III] line is a very good tracer of the H II region, as it is always fully emitted by the time the ionization front is reached. This is due to the high energy needed to create the O III ion, 35.12 eV (see Table 1.3). Since the ionization front is the place where most of the photons capable of ionizing hydrogen have been absorbed, only photons with energy lower than 13.6 eV are left beyond the H II region. The density and ionization parameter do not significantly influence the [O III] behaviour.

[C II] 157μm Understanding the [C II] line is relatively straightforward, being almost totally emitted beyond the ionization front, in the neutral PDR. In principle, the [C II] emission can arise from the H II region as the energy required to ionize C^+ is 11.26 eV (see Table 1.3). However, the critical densities are not the same when considering the electrons versus the hydrogen atoms as collision partners (see Table 1.3), which makes an important difference for the [C II] excitation. The fact that the excitation temperature of the fine-structure line is low (91K) also has a

significant influence on the region where the [C II] 157μm line is emitted. At higher temperature gas, as in H II regions, higher ionization levels of the carbon atom will be populated, thus other transitions will be observed. In the range of conditions we are considering here the [C II] line thus can be used as a good tracer of PDRs, with little contamination from ionized regions, if any. This situation is unusual for metal-rich galaxies, where only a small part of [C II] comes from PDRs. However, it is common in low metallicity galaxies to have a large contribution of PDRs to the [C II] line emission, with only a small part arising from H II region ($\leq$30% in DGS sample, e.g., Cormier et al., 2015).

[O I] 63μm As the energy required to ionize the oxygen atom is 13.62 eV (see Table 1.3), which is very close to that required to ionize hydrogen, in principle the [O I] line can be emitted in both H II regions close to the ionization front as well as the neutral PDRs. So the [O I] emission that can, in principle, originate from H II regions can only be emitted close to the ionization front, where the most energetic photons were absorbed. However, only a small fraction of the [O I] is emitted at the ionization front, up to 20% at most. The density has little influence on that quantity, although very high densities (around 10^3 cm^{-3}) tend to reduce the contamination by the H II region. It is coherent with the critical density of [O I], 5×10^5 cm^{-3}, for collisions with hydrogen atoms. When the density of the model increases toward this critical density, the emission of the [O I] in the PDR increases, and the relative contribution from the atomic gas at the ionization front decreases. The ionization parameter also has a small influence on the emission of [O I] close to the ionization front. When the ionization parameter increases, the proportion of the [O I] line emission arising from the gas at the ionization front decreases and drops to a few percent. It can be understood by the increase of ionizing photons, that creates higher ionization levels of the O ion deeper into the cloud, decreasing the [O I] emission at low A_V.

MIPS 70μm band We see in Figure 3.1 that the 70μm band emission is associated with PDRs. At low ionization parameters, the possible 70μm emission in the H II region is less than 10%, but this percentage increases with ionization parameter, and for the highest densities (over 10^3 cm^{-3}). At the value log(U)=-1, up to 30% of the 70μm emission can be emitted by the H II region very close to the ionization front. Still, the majority of the band emission typically traces PDRs.

MIPS 24μm band The 24μm band is clearly the most ambiguous tracer. It is often used to trace warm dust and is implicitly considered typical of the dust emission in H II regions close to the ionization source. However, for some cases there can be a strong contamination from the PDRs. For example, with an intermediate ionization parameter (log(U)= -3) only $\sim$10% of the band intensity is emitted before the ionization front is reached, despite the lower temperature of the gas in the PDRs. At higher ionization parameters, we see an increase of the 24μm emission from the H II region. This can be explained by the increase of the temperature, especially at the ionization front (8,400K for log(U)= -4, compared to 12,300K for log(U)= -1). The increase we see at the highest cloud depths, however, has to be linked to another heating mechanism. In the model output, we see that this increase corresponds to regions where the dominant heating mechanisms are the cosmic rays and the formation of the H_2 molecule. The combination of these two effects results in heating of the gas in the PDR, thus a production of emission at 24μm.

For the higher age, at 10 Myrs, we see that 24μm is emitted only in the PDRs. This is explained by the fact that, at this burst age, the most massive stars have already died, and only less massive, cooler stars remain. Thus, the energy of the photons is not sufficient to heat the

dust to temperatures to emit 24μm from the H II region. As the heating deep into the PDR is linked to processes that are not dependent on the temperature in the H II region, namely H_2 molecule creation and interaction with cosmic rays, the 24μm emission in the PDR remains.

3.3.2 Effect of metallicity

We consider a similar set of models now setting the metallicity to that of the SMC value, 1/5 $Z_\odot$ (Figure 3.2). We notice that the global behaviour of the plotted quantities does not differ overall compared to the models at 1/2 $Z_\odot$.

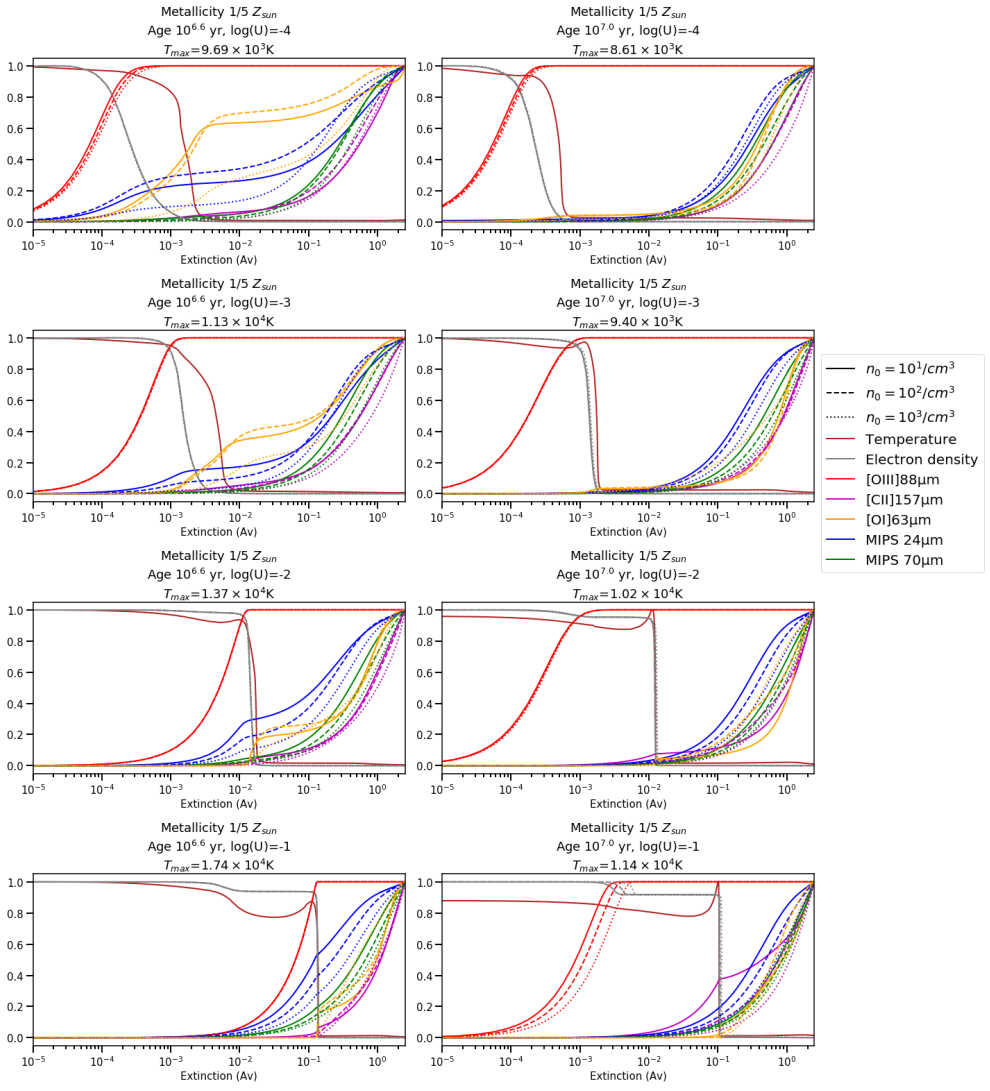

FIGURE 3.2: Similar to Figure 3.1, but with metallicity scaled to 1/5 $Z_\odot$.

Physical conditions One of the most important differences is that the part of the PDR with a temperature over 1 000K is slightly more extended than for the 1/2 $Z_\odot$ models, this region being at A_V between 5 10^{-4} and 3 10^{-3} at 1/2 $Z_\odot$, and between 2.5 10^{-4} and 2 10^{-3} at 1/5 $Z_\odot$. This can be explained by the lower amount of dust in these models, allowing the penetration of heating photons even deeper into the cloud at 1/5 $Z_\odot$ than at 1/2 $Z_\odot$. As a consequence, the transition of the ionizing front (i.e., the sharp decrease of the electron density) occurs at slightly lower depths in the case of 1/5 $Z_\odot$ compared to 1/2 $Z_\odot$, but this effect is very small.

Line and continuum band emission The behaviour of the [O III] 88μm, [C II] 157μm and the MIPS 70μm band emission does not differ strongly from the case of 1/2 $Z_\odot$. The [O I] 63μm emission also has a very similar behaviour at 1/5 $Z_\odot$ compared to 1/2 $Z_\odot$. However, the emission from [O I] 63μm at the ionization front is a bit lower, but only by a few percent. For the 24μm emission, we also have a behaviour very similar to the 1/2 $Z_\odot$ models. The 24μm band is emitted by both the H II region and PDR, with a fraction of the 24μm band arising from the H II region that increases from 10-20% for log(U)= -4 to roughly 60% for log(U)= -1, where values are very similar to those of 1/2 $Z_\odot$ models.

We thus see that in general, for constant density models, there is no striking difference between 1/2 $Z_\odot$ and 1/5 $Z_\odot$ when considering the behaviour of the cumulative emission of lines and bands, and the respective proportion arising from the H II region and the PDR. This indicates that those tracers are not affected by the change of metallicity between the LMC and SMC, and thus can be used to better understand the other physical conditions. We will now have a look at the constant pressure models, for which density is allowed to vary throughout the cloud.

3.3.3 Effect of the physical prescription - constant pressure models

The constant density models are used as a first approximation for the ISM conditions, but it is thought that the ISM is more probably in pressure equilibrium (e.g. Field et al., 1969; Tielens, 2005; Osterbrock & Ferland, 2006). A first comparison of the constant density models with observed data also indicates that a constant density representation of the ISM may not represent accurately the ISM conditions (see Chapter 4, Section 4.4.3). Thus, we ran models with constant total pressure instead of constant density. The range of parameters was also slightly shifted and restricted, as a first comparison of the models with our data showed that very high initial densities were unable to reproduce the observations, and densities below our lower bound could be useful. For a detailed range and explanations, see Table 3.1 and Section 3.2. For these constant pressure models, we consider the same tracers as we did for the constant density models, but now also track the behaviour of density through the cloud.

Hydrogen density variation We see that hydrogen density (simply referred to as density hereon) stays roughly constant, at the initial value, throughout the H II region, before increasing in the PDR (Figure 3.3). The increase of density is linked to the sharp decrease of temperature that we observe, in this case of constant pressure. The density value at the end of the cloud is roughly three orders of magnitude higher than the initial value, for all of the models, without a clear dependency of this final value on the other parameters, leading to final densities between a few 10^4 cm^{-3} and a few 10^6 cm^{-3}. Those very high densities can sometimes be observed in very dense molecular regions (e.g., Bolatto et al., 2000; Anderson et al., 2014; Galametz et al., 2020). However, in our observations, the clouds embedding young star clusters are bathing in an external diffuse radiation field, emitted by other stellar sources in the galaxy. Adding an additional diffuse radiation field can be an interesting improvement of our models, and would help to understand the behaviour at the external edges of the cloud.

At young ages, the density in our models always increases in two steps: once just after the ionization front, and a second time around $A_V \sim 1$. At 10 Myrs, those two steps are only visible at very low ionization parameter, and the first increase is always negligible compared to the increase at high A_V. The initial density does not play an important role in the relative strength of the two density increases, except at low ionization parameter. For a value of log(U)= -4, the effect of the initial density is strong, the first increase of density after the ionization front representing 60% of the final density for an initial density of 10^1 cm^3, while it is only 10% of

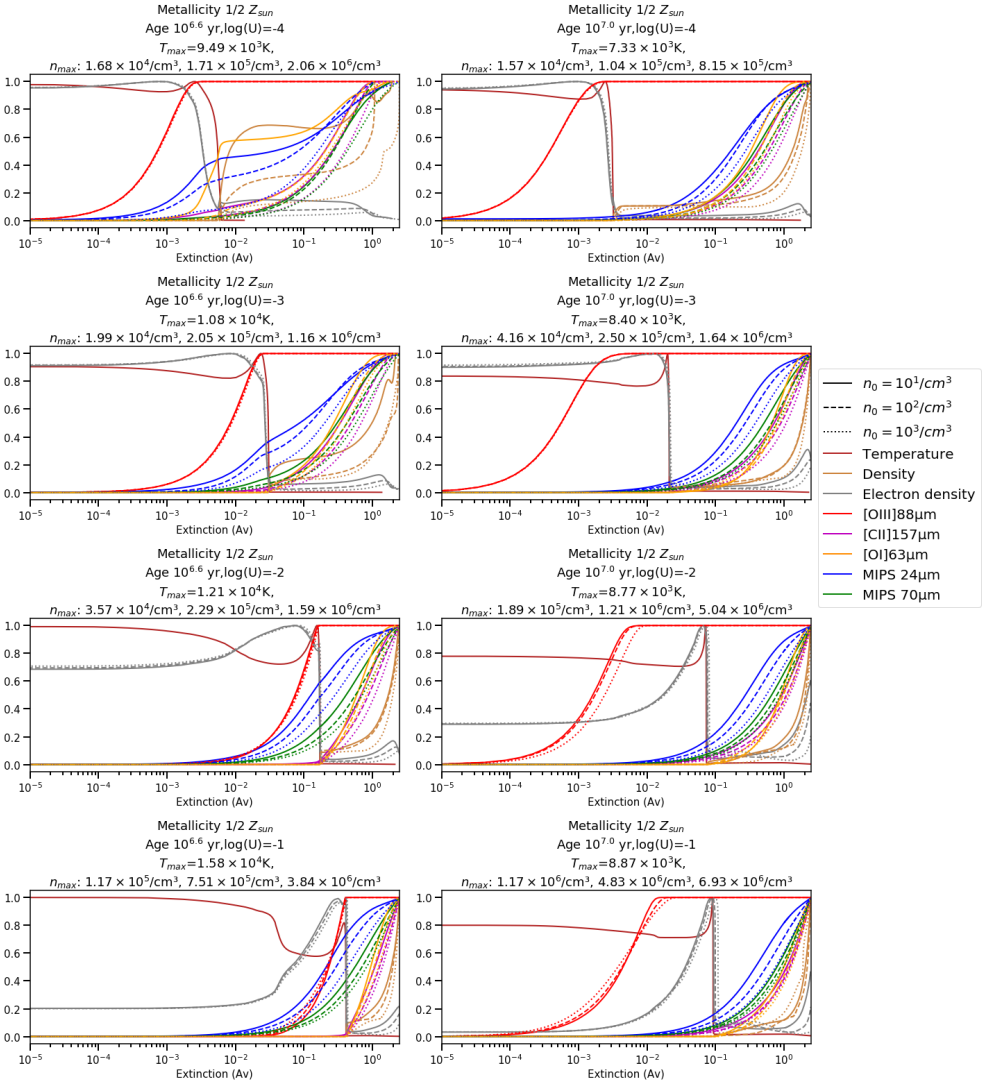

FIGURE 3.3: Similar to Figure 3.1, but for the constant pressure, 1/2 $Z_\odot$ metallicity models. We added the full hydrogen density, the final maximum value being displayed above each subplot, for the three initial densities represented. The maximum value of the electron density is not shown, as it can be deduced from the initial density value. The other outputs are shown in the same way as in Figures 3.1 and 3.2.

the total increase for an initial density of 10^3 cm^3. At a value of log(U)= -3, the first increase represent only ∼20% to ∼10% of the total increase, and for a higher ionization parameter it is 10% of the total increase, independent of the initial density.

Other physical conditions The temperature and electron density also have different behaviours from those of constant density models. At low ionization parameter (log(U)= -4 and log(U)= -3), their evolution is similar to that of constant density models, staying constant and roughly at the maximum values throughout the H II region, and the drop of temperature occurs slightly deeper than the location of the ionization front. The first noticeable change is an increase of the electron density, well correlated with the first increase of global density in the PDR.

However, for the case of high ionization parameter (log(U)=-2 and log(U)=-1), the electron density at the beginning of the cloud starts with 20% of the maximum electron density at log(U)=-1. When approaching the ionization front, the electron density increases to attain its

maximum value, which corresponds to a drop in temperature, and both attain a peak just before they drop off. When looking at the detail of the output, this increase of the electron density in the ionized region, close to the ionization front, corresponds to an increase in hydrogen density. This increase, however, is not evident in Figures 3.3 and 3.4, as it corresponds to a factor of 5 at most, being thus negligible compared to the increase by three orders of magnitude we see in the PDR. The behaviour of the temperature just before the ionization front is also linked to the increase of hydrogen density.

[O III] 88μm and [C II] 157μm Considering the tracers that are examined here, the [O III] and [C II] emission lines have behaviours that are consistent with the descriptions above. The [O III] line is fully emitted by the H II region, although it is a bit closer to the ionization front than in constant density models. The [C II] line is also emitted almost fully by the PDR, with a possible small component emitted from within the H II region at low ionization parameter, but never reaching more than a few percent.

MIPS 70μm band Similarly to the constant pressure models, the MIPS 70μm band emission also has straightforward behaviour, but there is more contamination from the H II region. Indeed, with the constant density models, the contribution of 70μm emission from H II regions is not over 20%, and is the highest in very high ionization parameters, with log(U)=-1. With constant pressure models, this H II region component contributes even at lower ionization parameters, log(U)=-3, and can reach 40% at log(U)=-1. Thus, in a constant pressure model, with high ionization, a significant contribution to the 70μm band emission may come from the H II region.

[O I] 63μm At low ionization parameter (log(U)=-4), the initial density has an important impact on the depth of emission of the bulk of the [O I] 63μm line. Around 60% of the emission is emitted close to the ionization front at low ionization parameter, for a density of 10 cm^{-3}, when only a few percent arises from the H II region for a density of 10^2 cm^{-3} or higher. The remaining emission of the line arises beyond A_V=10^{-1}. However, at higher ionization parameter, the majority of the [O I] 63μm emission, if not the totality, arises from deep within the PDR, beyond A_V of 10^{-1}. This can be understood through the evolution of the density with the depth: when the total density increases toward values close to the critical density of the line, the line emission increases. The temperature of the medium and the strength of the radiation field can also have an influence, but weaker than the influence of density.

In our constant density models, we imposed the initial density values throughout the cloud. As the initial density values in Figures 3.1 and 3.2 remain much lower than the critical density of the line (5×10^5 cm^{-3}, see Table 1.3), the temperature of the gas was playing a bigger role, and then the evolution of the temperature of the gas with the depth was the origin of the complex behaviour of the [O I] 63μm line. In this constant pressure case, the bulk of the emission is corresponding to higher densities, close to the critical density. The line can show a small emission level at lower depths, but the global behaviour is straightforward.

MIPS 24μm band As in the constant density models, the MIPS 24μm band emission is emitted by both the H II region and PDR, but in these constant pressure models the fraction of the emission arising from H II regions is higher: in the low density, low ionization parameter models (log(U)=-4, n_0=10 cm^{-3}), at least 40% of the 24μm emission arises from the H II region, but this fraction decreases with increasing initial density, being as low as 10% when the initial density is 10^3 cm^{-3}. On the other hand, the fraction of 24μm emission originating from H II regions tends to increase with increasing ionization parameter. The cluster age has a similar

effect in constant pressure models as in constant density models: at 10 Myrs, most of the 24μm emission arises from PDRs, starting at A_V=10^{-1}, almost independently of the other parameters. We notice that this depth is similar to that of the constant pressure models here, indicating that the processes at play at high ages are the same or very similar for both the constant density and constant pressure cases.

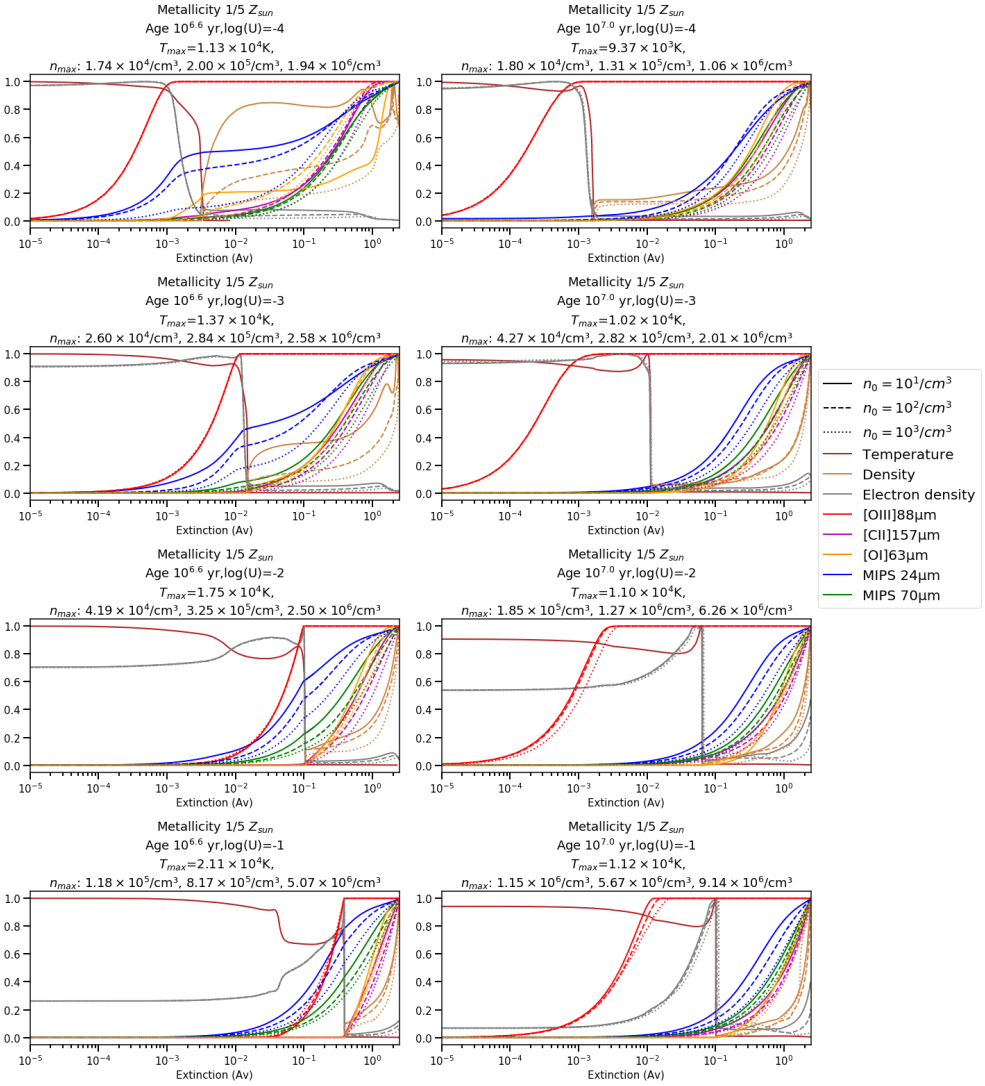

FIGURE 3.4: Similar to Figure 3.3, but with 1/5 $Z_\odot$.

The effect of metallicity, that can be investigated through the comparison of Figure 3.3 and Figure 3.4, is similar to that discussed in Section 3.3.2 for all the outputs that were presented in the constant density models. For the hydrogen density, we notice that for the lowest ionization parameter, log(U)=-4, and the lowest initial density, 10 cm^{-3}, the first increase of hydrogen density just after the ionization front represents a greater fraction of the total density increase, with 80% instead of 65%, as in the constant density case.

3.3.4 *Spitzer*/IRS MIR lines

We inspected the behaviour of some important diagnostic mid-infrared lines (Figure 3.5), which are often used to trace a wide range of properties of the ionized ISM, such as density and ionization parameter, and were observable with the IRS spectrometer onboard the *Spitzer* telescope.

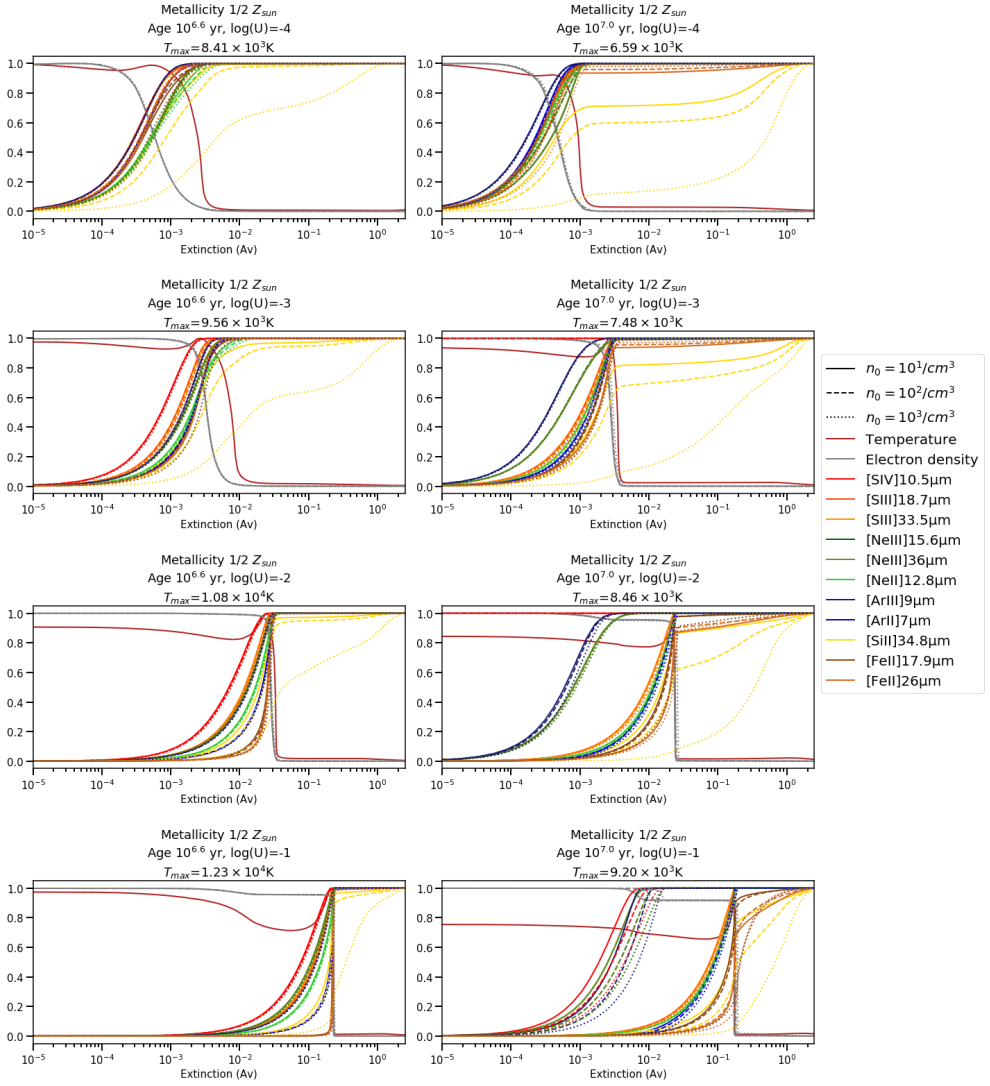

FIGURE 3.5: Mid-infrared tracers of the gas in the ISM, that were observed by the *Spitzer*/IRS instrument. The cumulative line intensities normalized to 1 are plotted against the extinction in A_V, and the temperature and electron density were represented for comparison with other tracers seen in Figures 3.1 and 3.2.

The chosen lines are well detected in star forming regions of the Magellanic Clouds, and especially in the sample we study here. We use only outputs from the 1/2 $Z_\odot$, constant density models, as there is no significant difference between 1/2 $Z_\odot$ and 1/5 $Z_\odot$ models, nor between constant density and constant pressure models.

Almost all of the lines are emitted in the ionized region, close to the ionization front, independently of the age, ionization parameter, or density (Figure 3.5). This is in good agreement with the fact that most of these ions require energies greater than 13.6 eV to be created, except [Fe II] 26μm and [Si II] 34μm. Thus, the ionized gas lines cannot be used to probe PDR conditions, or to discriminate between PDR and H II region emission. The only exception is the [Si II] 34.8μm line, which can be emitted from both regions.

For all of the lines except [Si II] 34.8μm, we see that both the density and ionization parameter have little to no effect on the behaviour of the lines at 4 Myrs. At 10 Myrs, when the ionization parameter increases, the lines with the highest ionization ([S IV] 10.5μm, [N III] 15.6μm and 36μm, and [Ar III] 9μm) are emitted at lower depths.

The [Si II] 34.8μm line can be emitted by both H II regions and PDRs, with a proportion varying with the parameters of the model. We see that increasing the density tends to decrease the fraction of the line emission arising from the H II region, from 50-90% at low density (10 cm^{-3}) down to 10-30% at high density (10^3 cm^{-3}). This corresponds well to the critical densities of this line, 1×10^3 cm^{-3} for collisions with electrons, thus in the H II region, and 3×10^5 cm^{-3} for collisions with hydrogen atoms, thus in the PDR. Indeed, at the lowest densities, the line can be emitted mostly by the H II region, due to the large difference between the density and the critical density of the line in the PDR. When the density increases, both H II-emitted and PDR-emitted intensities are boosted, but emission from the PDR rises more than that from the H II region, because the maximum density displayed corresponds to the H II region critical density of the line. The fraction of the line emitted in the H II region then saturates at this density, and the rate of the increase of the line intensity is lower when approaching the critical density. Thus, the balance between the fraction of the line emitted by the PDR and H II region changes, giving more weight to the PDR emission.

We also see that the ionization parameter has the opposite effect on the [Si II] 34.8μm emission: when U increases, the proportion of the emission arising from the H II region tends to increase, but with an effect less prominent than that of the evolution with the density. The H II-emitted proportion of the [Si II] line is between 50% and more than 90% at the highest ionization parameters, and between ∼10% and almost 30% at the lowest ionization parameter. We also notice that increasing age tends to somewhat decrease the fraction of the line emitted in the H II region. Those changes may be explained by differences of the distribution of the silicon element between its possible ionization states, which is affected by the strength of the radiation field, i.e. by the age and the ionization parameter here. We do not investigate this further here, since our study does not include other [Si II] lines.

3.4 Construction and use of Cloudy grids

Here we focus on the use of the grids with the *Spitzer*/IRS data. The investigation of the *Herschel*/PACS data will be done differently and described and investigated in detail in Chapter 4.

3.4.1 Construction of the grids and solution search

The *Spitzer*/IRS observations produced maps of emission lines with detailed spatial resolution, with pixel size of 7", which correspond to 1.75 pc at the distance of the LMC (see Chapter 1, Section 1.4). With the use of some specific MIR lines, it is thus possible to obtain detailed maps of some physical conditions. To this end, we chose some well-detected lines in most of the IRS sample.

When the models reach high depth into the cloud, the computation of Cloudy models can take a long time. Thus, our models are sparse, with rather coarse steps of 1 or 0.5 in log space. Using only those calculated values would have an effect similar to decreasing the spatial resolution of the final parameter maps. We decided then to create a finer grid of density and ionization parameter a posteriori, with steps of 0.1 dex for the two parameters and the same limits as the Cloudy models (we will refer to this denser grid as the interpolated grid of models or simply the interpolated models). We carried out cubic interpolation on the sparse grid calculated by Cloudy to populate the dense grid with the value of the diagnostic ratios. The interpolation was done on the ratios themselves rather than on individual emission lines, in order to minimize the uncertainties due to the approximations used by the interpolation methods. The values of

the observed ratios are then compared to the ratios in the interpolated grid of models. As the two parameters, density and ionization parameter, are linked (see equation 3.1), we decided to determine the two parameters simultaneously. To this aim, we need at least two observed ratios to compare with the interpolated models.

When the interpolated grid of models is created, for each pixel of the map, the value of the observed diagnostic ratios is used to compute a weighted χ^2 for each point of the grid. The χ^2 is then used to compute a probability density function (PDF) for each parameter, by calculating the value of $\exp(\chi^2)$ and collapsing the grid on the dimension of the researched parameter. After some investigation of different pixels of the maps, we saw that the PDF can be approximated by a Gaussian. In this case, the final value for the parameter is the maximum of the PDF, and the uncertainty is the full width at half maximum (FWHM). This is how we computed the parameters and corresponding uncertainties on all of the maps.

This simple method bears some caveats. First, it does not take into account the possibility of degeneracy between the parameters, which often leads to multiple possible solutions. Our simple method does not handle multiple solutions, but it is possible to include a test to identify multiple peaks. Then, we assume the shape of the PDFs to be a Gaussian. If the shape obtained is very different, the derived value for the parameters and/or the associated uncertainties can be inaccurate. We inspected our results to be certain that those cases are not found in our sample, allowing us to use this simple determination method.

3.4.2 Effect of interpolation

We have seen that the computation time for models that reach high depth and with fine grids with Cloudy can be very long. However, interpolation can introduce uncertainties on the values of ratios. Thus, in order to characterise potential discrepancies between the fully modeled values and interpolated values, we computed a sub-model with a smaller grid. We decided to choose edge values inside the typical range of ISM conditions: log(U) is between -2 and -3, the density between 10 and 10^3 cm^{-3}, and we use steps of 0.1 dex for both parameters. We computed a model for one typical burst age of ∼4 Myrs ($10^{6.6}$ yrs), and included the two metallicity cases, 1/2 and 1/5 $Z_\odot$.

We also computed those models for constant pressure as well as for constant density. Constant pressure models seem more representative of the physical conditions, but the density does not really increase much in the H II region, with at most an increase of a factor of a few (see Section 3.3.3). On the other hand, constant density models are faster to compute, and the interpretation of the spatially resolved density is easier, as we can directly link the initial density to the effective density. This is not possible with constant pressure models in which the density varies with the depth.

We show in the Figures 3.6 and 3.7 the value of the ratios used in our analysis in the interpolated models and in the finer grid models calculated with Cloudy, and we investigate the uncertainty introduced by the interpolation with the ratio of the interpolated value and the finer grid value calculated with Cloudy.

For the ratios of [S III] 18μm/[S III] 33μm the uncertainty induced by the interpolation is of a few percents at most (Figure 3.6). As the calibration uncertainty for the IRS module is around 15%, it is possible to use the interpolation for those two ratios while neglecting the additional uncertainty.

For the ratios [S IV] 10μm/[S III] 18μm and [Ne III] 15μm/[Ne II] 12μm, the uncertainties of the interpolation reaches 40% and a bit more than 20%, respectively. For the [S IV] 10μm/[S III] 18μm the uncertainty introduced by the interpolation is larger than the calibration uncertainty

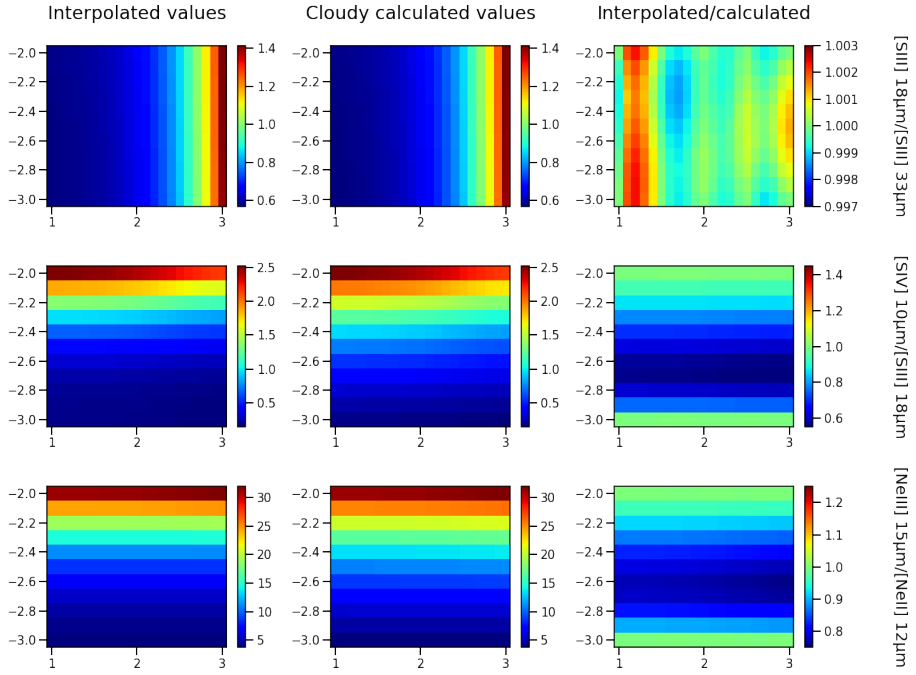

FIGURE 3.6: Value of the ratios used in the analysis of IRS data, with the values of interpolated models in the left column, and the values calculated by Cloudy in the middle column. The right column contains the ratio of interpolated models and Cloudy calculated models, to quantify the uncertainty induced by the interpolation. The models used, for both the finer Cloudy grid and the interpolated models, use 1/2 $Z_\odot$ metallicity and constant density case.

for lower ionization parameter values, with log(U) between -2.3 and -2.9. For the ratio [Ne III] 15μm/[Ne II] 12μm the uncertainty introduced by the interpolation is larger than the calibration uncertainty for log(U) between -2.5 and -2.8. In this range of ionization parameters, it is necessary to take into account the uncertainty of the models to accurately infer the value used to create the maps of parameters, or to use another diagnostic to infer the value of the parameters in this range of ionization parameter.

The comparison of Figures 3.6 and 3.7 indicates that changing metallicity between 1/2 and 1/5 $Z_\odot$ does not introduce significant differences in the uncertainty due to the interpolation, for all of the ratios studied. Figures 3.8 and 3.9 show the interpolated values, the Cloudy calculated values and the ratio of the two models for the constant pressure models. We see in Figure 3.8 that the uncertainty due to the interpolation of the ratios [S III] 18μm/[S III] 33μm is a bit higher that that of the constant density models, but still always smaller than the calibration uncertainty of 15%.

For the ratios [S IV] 10μm/[S III] 18μm and [Ne III] 15μm/[Ne II] 12μm the uncertainties derived at 1/2 $Z_\odot$ metallicity are similar in constant pressure models to those found for constant density models (up to 40% for [S IV] 10μm/[S III] 18μm and up to 20% for [Ne III] 15μm/[Ne II] 12μm). For 1/5 $Z_\odot$ metallicity, however, the uncertainties derived on ratios [S IV] 10μm/[S III] 18μm and [Ne III] 15μm/[Ne II] 12μm are much smaller for constant pressure models than for constant density models, with uncertainties up to 10% for the two ratios.

We see that interpolating on the model grids introduces some uncertainties on the ratios we used compared to values computed by a more precise Cloudy model. For [S III] 18μm/[S III] 33μm the uncertainties on the models are much lower than the 15% calibration uncertainties of the observations, thus they can be neglected in a first approximation. For [S IV] 10μm/[S III] 18μm

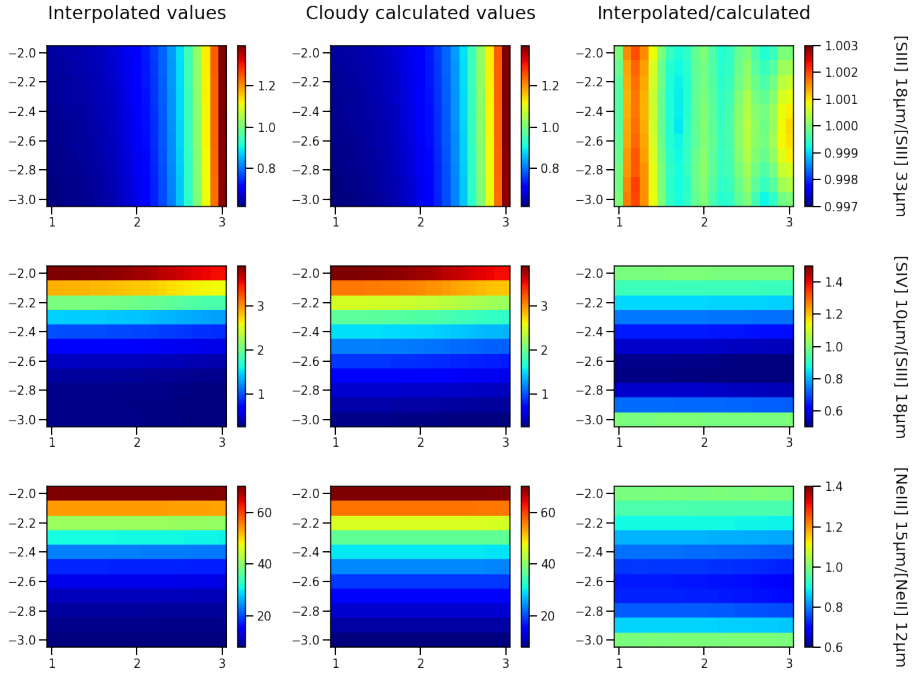

FIGURE 3.7: Similar to Figure 3.6, but with 1/5 $Z_{\odot}$ and constant density case.

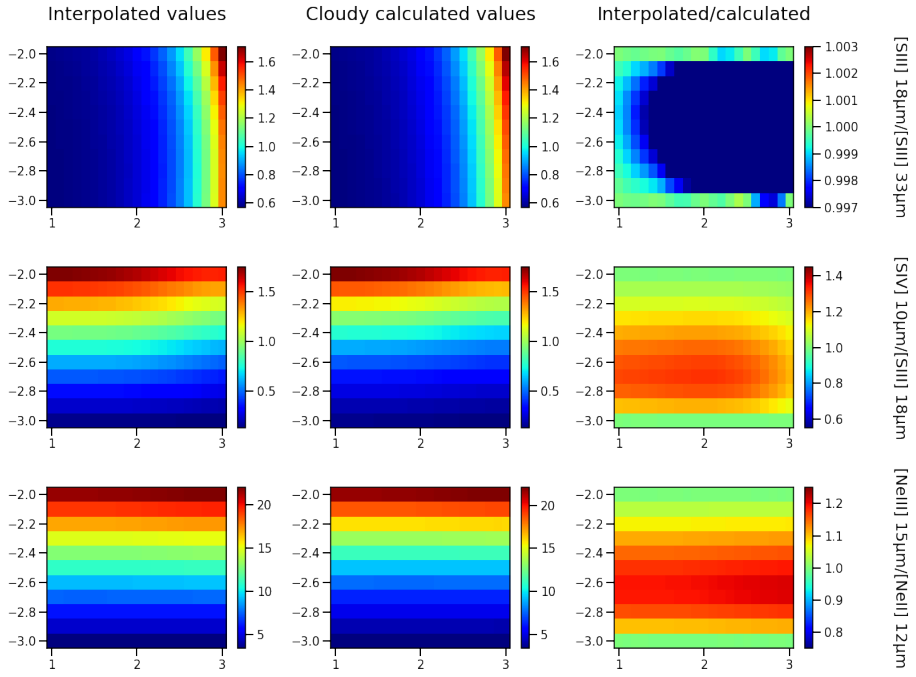

FIGURE 3.8: Similar to the Figure 3.6, but with 1/2 $Z_{\odot}$ and constant pressure case.

and [Ne III] 15μm/[Ne II] 12μm the uncertainties reach 40% and 20% respectively on part of the parameter space. For a metallicity of 1/2 $Z_{\odot}$, there is not much difference between constant density and constant pressure models, and the uncertainties due to the interpolation are similar for all of the ratios we selected. However, for a metallicity of 1/5 $Z_{\odot}$, the uncertainties due to interpolation on constant pressure models are smaller than on constant density models. Constant pressure and constant density models will both be used and compared in further analyses, in

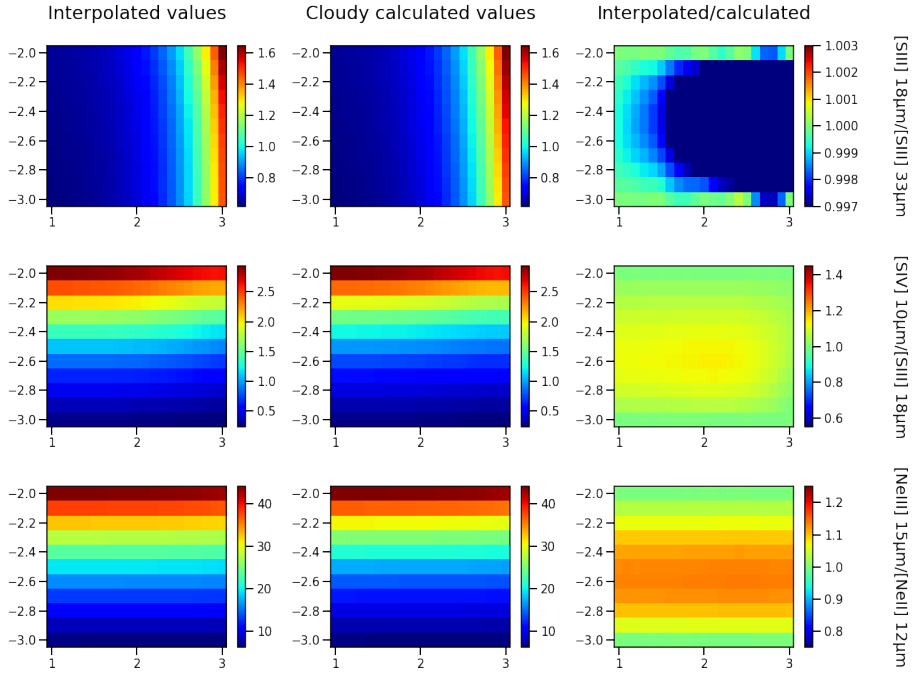

FIGURE 3.9: Similar to the Figure 3.6, but with 1/5 $Z_{\odot}$ and constant pressure case.

order to constrain the best hypothesis for the modelling.

3.5 Summary

In this chapter, we presented a grid of models that we computed to study the physical conditions of the iSM in star-forming regions. Those models are simple, 1D, and they are based on classical physical assumptions. We prepared two sets of models with different hypothesis: one for which the density is kept constant through the cloud, and the other for which the total pressure is kept constant through the cloud, in order to verify if the constant pressure model is indeed more representative of the ISM conditions. We did not attached importance to the luminosity of our models: as we have different star-forming regions in our observed sample (see Chapter 2), each region would require a different scaling of the models, and it is unclear on which tracers we should base this scaling (for an example of tests on scaling this sort of models, see e.g., Polles et al., 2019). Thus, we decided to keep general models, and use mostly ratios of tracers to investigate the physical conditions of the different regions in our sample.

We examined the evolution of the tracers with A_V, which increase with depth into the cloud, and with the different physical parameters varied in the grid, namely the density and the ionization parameter. This investigation will allow us, in the following chapters, to have a better understanding of our tracers, and to select which ones are appropriate for the conditions we want to study (e.g., [O III] 88μm is always fully emitted before the ionization front, thus it can be used to trace the presence of ionized gas).

In the following chapters, the output of the models presented here will be compared to observed tracers from each of the star-forming regions in our sample, in order to disentangle the physical conditions of the ISM in those regions, and to investigate some of the processes at play in the different phases.

CHAPTER 4

DISENTANGLING GAS AND DUST EMISSION IN STAR-FORMING REGIONS OF THE MAGELLANIC CLOUDS

Contents

When observing the ISM in galaxies, different phases will be mixed within the telescope beam. Examining the properties of the different tracers observed can help to disentangle the different phases along the line of sight and their properties. Here, we use MIR and FIR spectroscopic and photometric data to investigate the different phases in the Magellanic Cloud regions we observed. The [O III] emission line is a tracer of diffuse ionized gas (energy potential of 35 eV and critical density n_{crit}=5×10^2 cm^{-3}), and it is also a tracer of the presence of young, massive stars, thus recent star formation (e.g., Cormier et al., 2015; De Looze et al., 2014). The [C II] emission line can arise from both ionized and neutral gas, requiring 11.3 eV to ionize C^0. Thus, in principle, the [C II] line can exist in both H II regions and PDRs in classical star-forming galaxies. However, in low-metallicity galaxies, the contribution of the ionized gas to the [C II] line is often small (∼30% or less, see e.g., Cormier et al., 2019 this hypothesis is also consitent with the models used in this study, and presented in Chapter 3). The [O I] emission line is also a tracer of PDRs (13.62 eV to ionize O^0), but is typical of ISM with high UV radiation fields and/or high density (the [C II] line has a lower critical density than the [O I] 63μm line, n_{crit}=5×10^5 cm^{-3} for [O I] 63μm line and n_{crit}=3×10^3 cm^{-3} for [C II] Tielens & Hollenbach 1985). To complement these spectroscopic data, we use the *Spitzer*/MIPS 24μm band, which is often used as a star-formation tracer as it is emitted by hot dust and often associated with compact emission of star-formation sites (see e.g. Kennicutt & Evans, 2012 for a review on different star formation tracers), and *Spitzer*/MIPS 70μm band, which traces cooler dust, often associated with PDRs, but, in principle, can also arise from an ionized phase. We investigate relationships between all

of these different tracers in our sample of Magellanic Cloud star-forming regions to study the physical properties they reveal, and to investigate the potential predictive power of some tracers. The emission line [O III] 88μm and the MIPS 24μm band, especially, should be strongly linked as they are both tracers of recent star formation in star-forming galaxies.

To this aim we use the spectroscopic maps of *Herschel*/PACS and the photometric maps from *Spitzer*/MIPS (see Chapter 2) convolved to 12" (resolution of [C II] 157μm maps with PACS) or 18" (resolution of MIPS 70μm maps), and resampled to 12" pixel width to avoid oversampling of the beam.

4.1 Spatially-resolved relation between the [O III] 88μm line and the 24μm continuum band

The proximity of the Magellanic Clouds, together with the capability of recent spatial telescopes (high spatial resolution and sensitivity), allows us to study the physical properties of the ISM with excellent spatial resolution (∼1 to 4 pc with *Herschel*/PACS). With our sample of star-forming regions we take full advantage of that resolution, and investigate the relation between the [O III] 88μm emission line and the MIPS 24μm band. Such a comparison can be done for any tracer of the H II region, but the [O III] 88μm was observed in many different surveys covering a wide range of galaxy type and conditions (e.g., DGS, Madden et al., 2013, KINGFISH, Kennicutt et al., 2011, among many others), allowing to test this relation on a large panel of conditions in future studies.

Figure 4.1 shows the correlation between the MIPS 24μm band and the [O III] 88μm for all 12" pixels in all of our sources for which the [O III] line detection is more than 5σ. We see that the different sources together exhibit a wide range of values, spanning around 3 orders of magnitude in 24μm and four orders of magnitude in [O III]. We find a very clear linear relation between those two tracers in log-log space. This correlation is fitted with a weighted χ^2 method, leading to the following relation:

$$\log(\Sigma_{[\mathrm{OIII}]\,88}) = 0.857(\pm0.013) \times \log(\Sigma_{24}) - 1.57(\pm0.066) \tag{4.1}$$

where the surface brightness, Σ, is expressed in $\mathrm{W\,m^{-2}}sr^{-1}$. We see that the spread varies significantly with the flux. It is tight (around 0.5 dex) for the brightest regions, especially 30 Doradus, but can reach almost 2 dex spread, especially with N159 and N11I. This spread is partly due to differences between the local physical properties of the regions (e.g. between N44 and N11C), and intrinsic variations within each region (e.g., N159).

If we consider each region separately (Figure 4.2), we can see that the slopes of the individual regions resemble the global slope for most of the regions, although some regions exhibit an offset compared to the global relation. 30Dor seems to drive the global slope while N11B, N160 and N158 follow similarly the global slope but fall slightly shifted above or below it. All but some positions in N44, N11I and N159 fall within the 95% confidence level found from the global relation. For N11C, N44 and N159 the pixels that exhibit an offset or a difference in behaviour to the global relation are the low brightness pixels. Taking the example of N11C (see Figure 4.3), the steeper slope is seen for pixels on the left of the points of the regions, which have a 24μm surface brightness around or lower than 10^{-6} $\mathrm{Wm^{-2}}sr^{-1}$. Thus, we see that the strength of emission affects the ratio [O III]/24μm, and that low brightness regions can have a ratio different from high brightness regions.

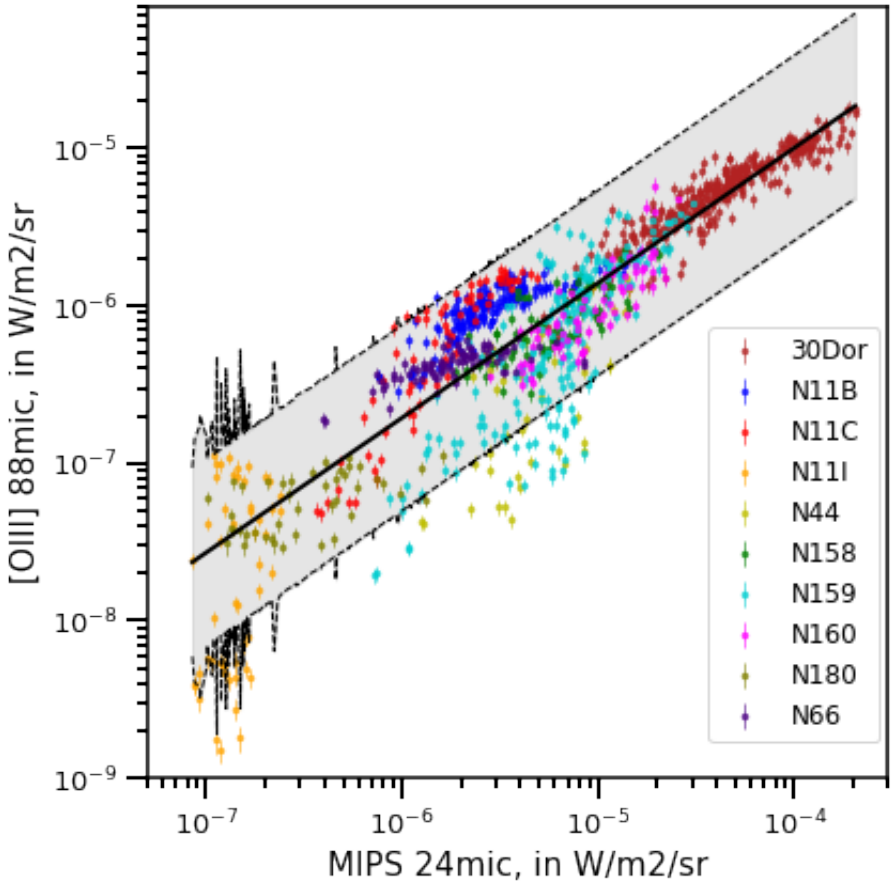

FIGURE 4.1: Relation between [O III] 88μm and MIPS 24μm in all of the pixels in all of our star-forming regions for those pixels above 5σ in the [O III] line. The black solid line represents the fitted linear relation in log-log space, and the dashed lines and grey filling represent the 95% confidence interval on the fit. The colored symbols refer to the individual regions labeled in the legend to the right of the plot.

N66 is the only region from the SMC we study here. Due to the difference in metallicities between the two galaxies (Z_{LMC}=1/2 $Z_\odot$ and Z_{SMC}=1/5 $Z_\odot$), both [O III] and 24μm are affected: there are less oxygen atoms, thus a decreased [O III] emission; the quantity of dust is also lowered which decreases the 24μm emission, but on the other hand the ISM in low metallicity galaxies, such as the SMC, experience an overall harder radiation field than high metallicity galaxies, which should increase the 24μm emission, shifting the peak of the SED to shorter wavelengths. Despite those effects, N66 does not differ much from the LMC regions. However, the slope of the region appears flatter than the slope of the global relation pointing to the possibility that [O III] and 24μm are are not as well linked in the LMC regions. Perhaps the [O III] in N66 originates from a more extended, diffuse component and not well associated with compact star-forming regions from which the 24μm is emitted. More studies on other regions in the SMC would be necessary to conclude on this point.

Note that the fits to the [O III] and MIPS 24μm correlations were made using convolved and resampled maps. Moreover, the MIPS 24μm maps were treated to remove contamination from point sources, and thus have a 'clean' view of the ISM emission. However, this treatment and the method to remove the point sources could have had an influence on the fitting results. The

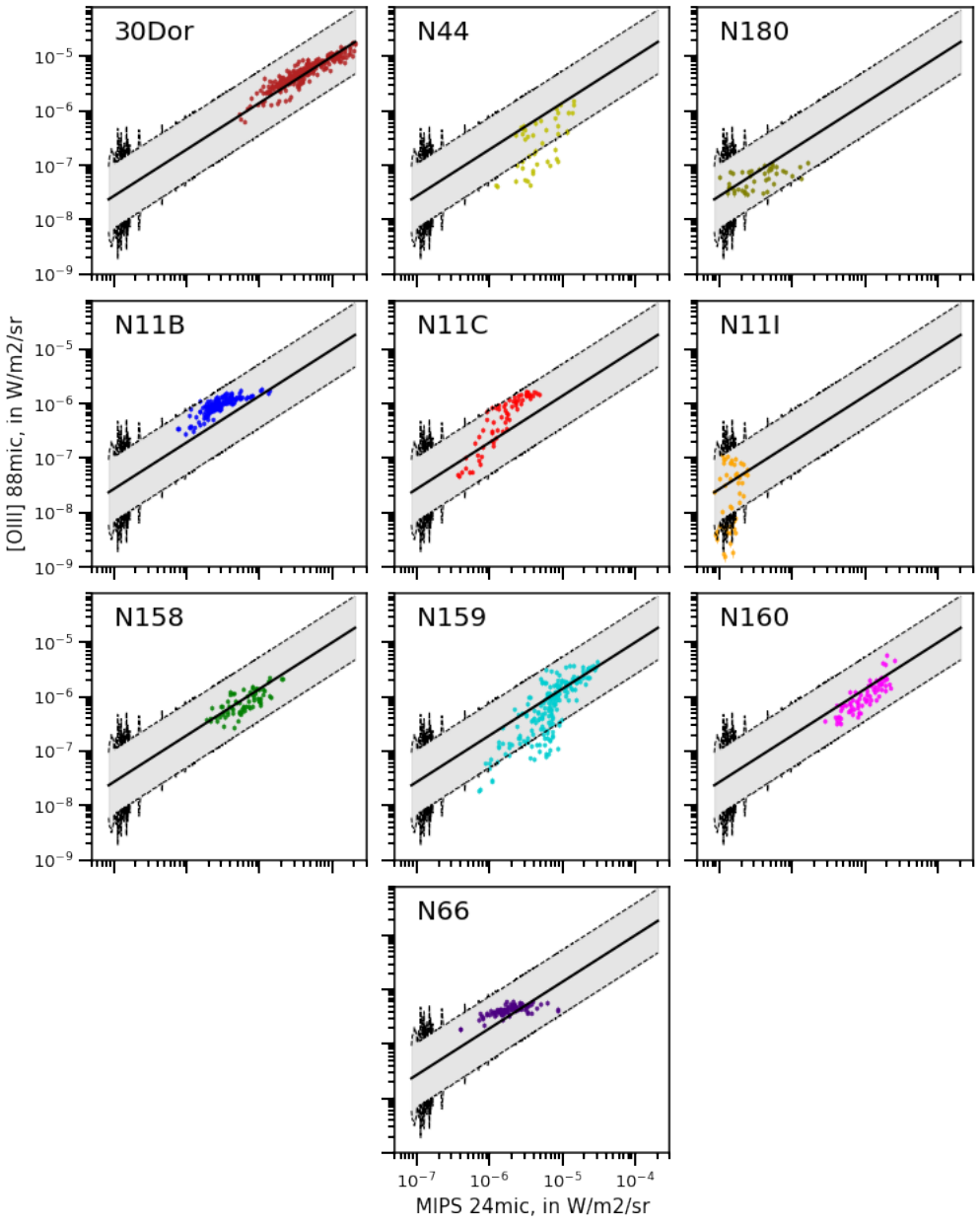

FIGURE 4.2: Relation between [O III] 88μm and MIPS 24μm in all of the pixels of our individual star-forming regions. The black solid line represent the fitted linear relation in log-log space for the total sample, and the dashed lines and grey filling represents the 95% confidence interval on the fit.

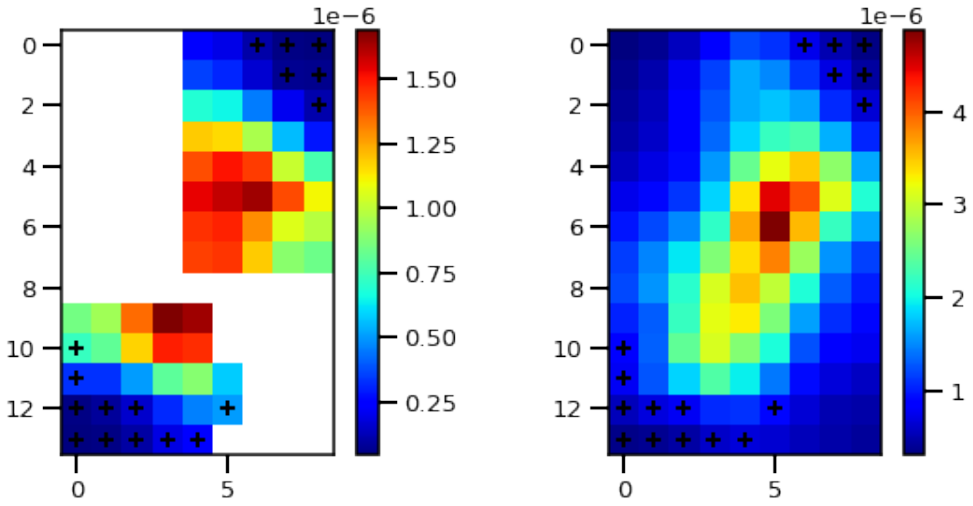

FIGURE 4.3: Left panel: [O III] map for N11C; right panel: MIPS 24μm map for N11C. Both maps are convolved to 12″and resampled to 12″pixels size. The black crosses correspond to pixels that have low surface brightness (on the left of the bulk of the regions in Figures 4.1 and 4.2) showing a behaviour different from the global relation.

effect of different treatments of the data and fitting methods are detailed in Appendix A. We see from the different tests made that the fit remains robust in these cases.

4.2 Integrated relation and comparison with DGS data

The correlation we find between 24μm and [O III] stands for resolved star-forming regions. However, the predictive power of this relation could be of a great interest to prepare observations of low metallicity galaxies beyond the Magellanic Clouds. However, it is rare to have such high spatial resolution for other galaxies, and observations are often integrated over entire, more distant galaxies, which could lead to deviations from the results of our sample of well-resolved star-forming regions. To test our procedure, we compare our findings on the Magellanic Clouds sample to other observations. We chose to use the DGS targets, a sample of dwarf low metallicity galaxies, from a few hundreds of kpc to a few hundreds of Mpc in distance.

4.2.1 Calculation of surface brightness and fluxes

The *Spitzer* 24μm broad band emission was efficiently mapped on much larger scales than MIR or FIR spectroscopic lines. For example, the full LMC and SMC were mapped with *Spitzer*/MIPS 24μm, but only a handful of small star-forming regions were mapped in the PACS [O III] line. Thus, the relation between [O III] and 24μm described in Section 4.1 can be used to predict [O III] emission where 24μm was observed and to estimate fluxes for potential future IR spectroscopic missions. In order to verify if this relation can be used on a large range of environments, we compare our sample from the Magellanic Clouds to observations from other dwarf galaxies, using the DGS data (see Chapter 2). To be able to make this comparison, we compute integrated flux and surface brightness for the Magellanic Cloud star-forming regions in our sample. The total surface brightness and the total flux are computed for all the regions, according to the equations 4.2 and 4.3.

$$\begin{aligned} \Sigma_{\rm total} &= F_{\rm total}/s_{\rm total} \\ &= \sum F_{\rm pix}/\sum s_{\rm pix} \\ &= \sum \Sigma_{\rm pix}\, s_{\rm pix}/s_{\rm pix}\, nb_{\rm pix} \\ &= \sum \Sigma_{\rm pix}/nb_{\rm pix} \end{aligned} \tag{4.2}$$

$$\begin{aligned} F_{\rm total} &= \Sigma_{\rm total}\, s_{\rm total} \\ &= \frac{\sum \Sigma_{\rm pix}}{nb_{\rm pix}}\, nb_{\rm pix}\, s_{\rm pix} \\ &= \sum \Sigma_{\rm pix}\, s_{\rm pix} \end{aligned} \tag{4.3}$$

where Σ is the surface brightness in W/m^2/sr, F the flux in W/m^2, s the size in arcsec and nb is for number of pixels in the map. The calculations were made on the maps with the original resolution and sampling.

4.2.2 Fit of the relation with integrated values

To take into account the different distances of the Magellanic Clouds and the DGS galaxies, we convert the flux into luminosity and normalize them to solar luminosity.

In Table 4.1, we present the values and uncertainties of the different fits, and in Figure 4.4, we show the fitted relation with the corresponding confidence intervals for the integrated surface brightness, the flux and the luminosity. We see that the slope and intercept obtained for the surface brightness of integrated and spatially resolved data are very close, and agreeing with each other within the uncertainties. The slopes fitted for the fluxes and luminosities are a bit steeper than for the surface brightness, but they are still coherent with surface brightness results within the uncertainties.

Method	Slope	Intercept	R^2
Resolved data			
Surface brightness (non corrected)	0.844±0.012	-1.628±0.065	0.803
Integrated data			
Surface brightness	0.845±0.108	-1.653±0.578	0.884
Flux	0.910±0.076	-1.866±0.87	0.947
Normalized luminosity	0.910±0.077	-0.447±0.343	0.946

TABLE 4.1: Fitted parameters of the relation between [O III] 88μm and MIPS 24μm for the different integrated values, and the resolved surface brightness for comparison purposes. The R^2 parameter is added as an estimation of the goodness-of-fit. As DGS 24μm observations are not corrected from point sources we used non-corrected 24μm data in all of the fits for fair comparison.

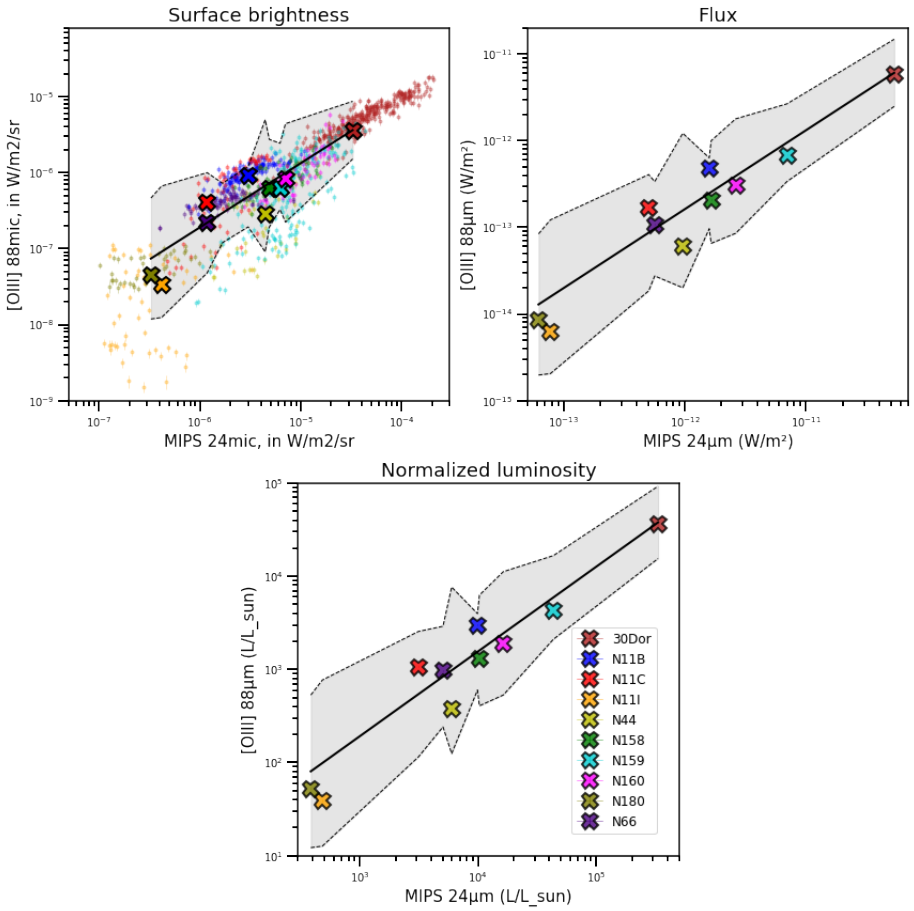

FIGURE 4.4: A linear relation is fitted between [O III] 88μm and MIPS 24μm for the integrated surface brightness (upper left panel), the fluxes (upper right panel) and the normalized luminosity (lower panel). The 95% confidence intervals are represented with dashed lines and grey filling, the fitted relation is represented with the back solid line. In the upper left panel, the spatially resolved data are also represented for comparison, but they are not taken into account for the fitting on integrated surface brightness.

4.2.3 Comparing between DGS and the Magellanic Cloud regions

We compare the [O III] 88μm and 24μm luminosities of the integrated Magellanic Cloud regions with those of the DGS targets in Figure 4.5. We emphasize that the fit of the relation is computed

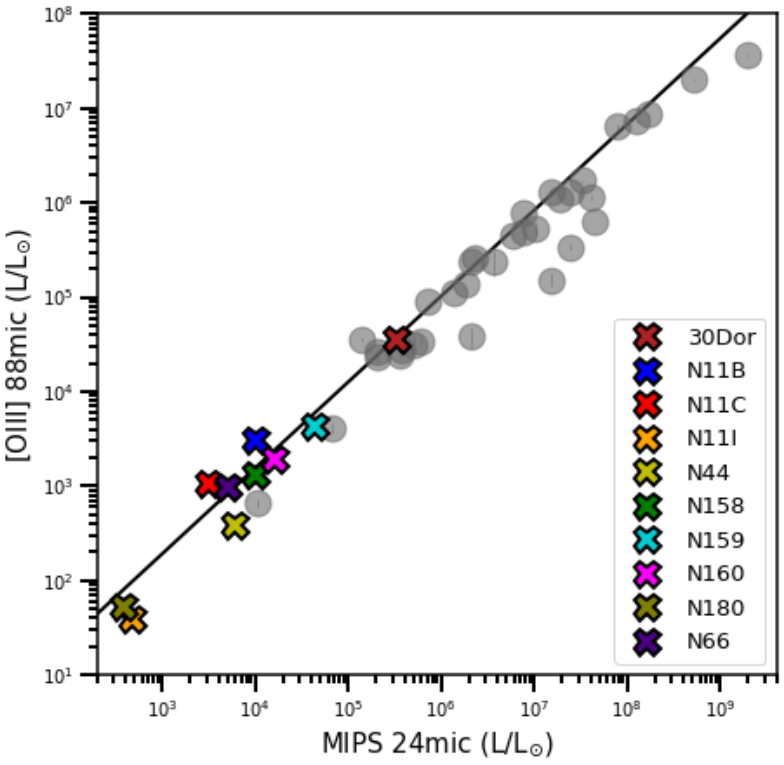

FIGURE 4.5: Relation between the [O III] 88μm line and 24μm luminosity. The DGS sample corresponds to the grey circles, and the region from the Magellanic Cloud sample are coded with colors, as indicated in the inserted box. The black solid line is the relation fitted on the Magellanic Cloud star-forming regions only.

with our Magellanic Clouds sample alone, and DGS targets lie just slightly below this relation. This behaviour can be explained by a small enhancement of 24μm emission compared to the [O III] 88μm line. Indeed, [O III] 88μm arises from energetic ionized media (35 eV needed to create the specie) heated by young O and B stars, where 24μm emission can be powered by other stellar types. Thus some 24μm may not arise from only O and B stars when integrating over full galaxy scales, thus increasing slightly the 24μm emission compared to the limited resolved star-forming sample we use for the Magellanic Clouds. However, this difference is small, suggesting that most of the 24μm emission is still coming from the star forming regions, even when considering the full emission of a galaxy (e.g., Contursi et al., 2002). The part of 24μm not arising from star-forming regions is thus linked to the presence of other phases in the beam. Our small Magellanic Cloud maps are centered on the brightest zones of star formation, largely filled by ionized gas, as we saw in Section 4.4.4. Thus if we extend our beam to larger regions, or to full galaxy scales, we may collect more PDR gas in our beam (with possibly low-excitation PDR) and possibly some 24μm emission from PDRs which would then account for enhanced 24μm compared to [O III] emission, which is only rises close to recent star formation. Thus, the integrated galaxies show a similar correlation of [O III] with 24μm compared to our sample zooming into star-forming regions only, but with the 24μm being slightly increased.

Despite this caveat, we have seen that this relation holds over more than three orders of magnitude for both [O III] 88μm and 24μm, and is still valid for numerous galaxies at different

distances from the Milky Way, giving our calibration a powerful predictive possibility, that we demonstrate below in Section 4.3

4.3 Summary of the fitted parameter and predictive use

We use two of our calibrations to explore the predictive potential of the observed correlation between 24μm and [O III]: one with the surface brightness of spatially resolved observations, and the other with luminosity, normalized to solar luminosity to compare with the DGS sample.

We recall the two calibrations we derived:

$$\begin{aligned} \log(\Sigma_{[\mathrm{OIII}]\,88}) &= 0.857(\pm0.013) \times \log(\Sigma_{24}) - 1.57(\pm0.068) \\ \log(L_{[\mathrm{OIII}]\,88}) &= 0.910(\pm0.077) \times \log(L_{24}) - 0.447(\pm0.343) \end{aligned} \tag{4.4}$$

with the first calibration for surface brightness, Σ, in units of W/m^2/sr for the tracers, and the second calibration for luminosity, L, in units of L$_\odot$.

We also compare the difference between the predicted values and the observations of the [O III] to the predicted uncertainties. The uncertainties were calculated using a Monte Carlo simulation based on the uncertainties of the fitted parameters, and we investigate if they are able to reproduce the variations between the observations and predictions. We investigate similarly the predictions for the luminosity by comparing to the observed values for the DGS data.

4.3.1 Comparing predictions and observations in our sample

We first compare the predictions of [O III] we derive with Equation 4.4 based on the observed 24μm emission for the sample of star forming regions, to the observed maps of [O III] emission in Figures 4.6 to 4.15.

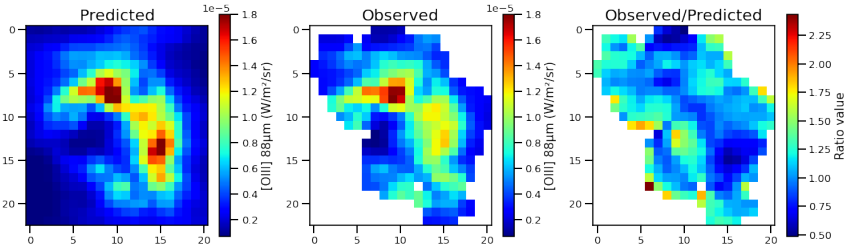

FIGURE 4.6: The predicted map of [O III], given the observed 24μm (left panel) is compared to the actual map of [O III] observed with *Herschel*/PACS (middle panel), and the ratio of observed over predicted emission (right panel). The two maps of [O III] are represented on the same scale, based on the extreme values of the observation, and are displayed in W/m^2/sr.

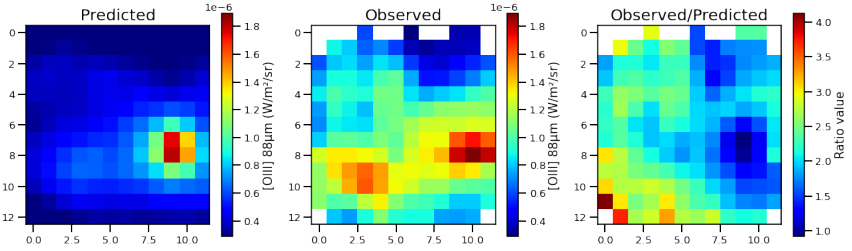

FIGURE 4.7: Similar to Figure 4.6, but for N11B.

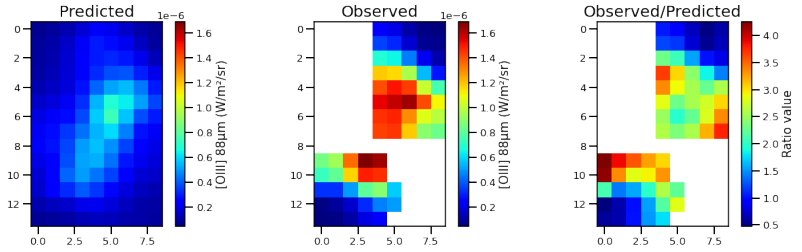

FIGURE 4.8: Similar to Figure 4.6, but for N11C.

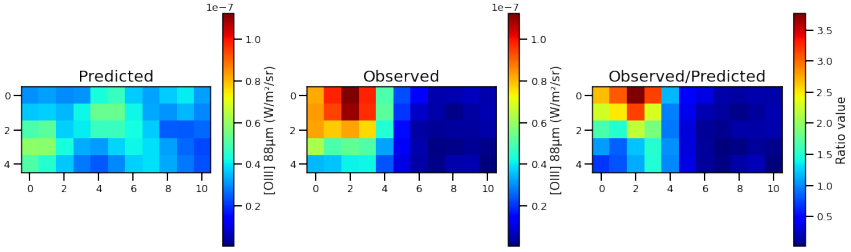

FIGURE 4.9: Similar to Figure 4.6, but for N11I.

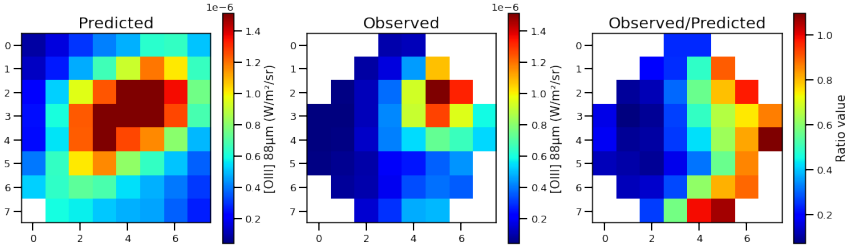

FIGURE 4.10: Similar to Figure 4.6, but for N44.

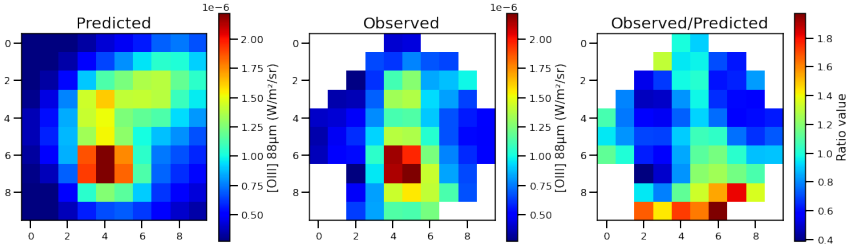

FIGURE 4.11: Similar to Figure 4.6, but for N158.

For almost all of the regions, the spatial distribution of the predicted and observed [O III] 88μm emission (Figures 4.6 to 4.15 and Figure 4.16) are in good agreement, within a factor 3 for most of the pixels. The only exception is N11I. Indeed, this region shows a large discrepancy between the spatial distributions of [O III] and 24μm. Moreover, it is one of the two faintest regions in both 24μm and [O III] emission. With that in mind, the line emission is only underestimated by a factor 3.5 at most.

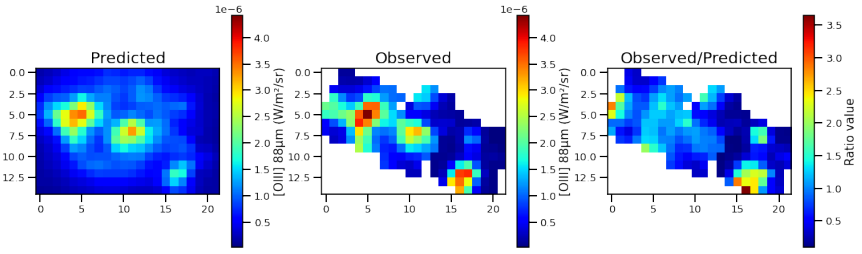

FIGURE 4.12: Similar to Figure 4.6, but for N159.

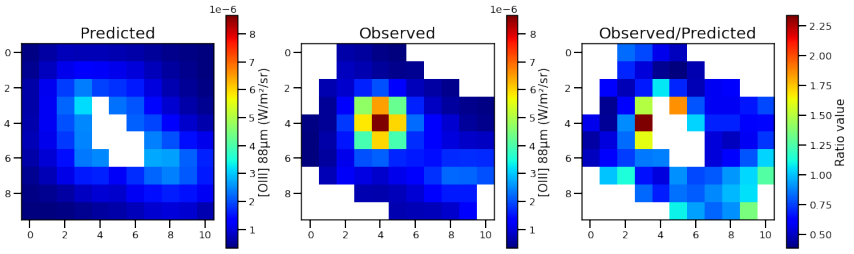

FIGURE 4.13: Similar to Figure 4.6, but for N160.

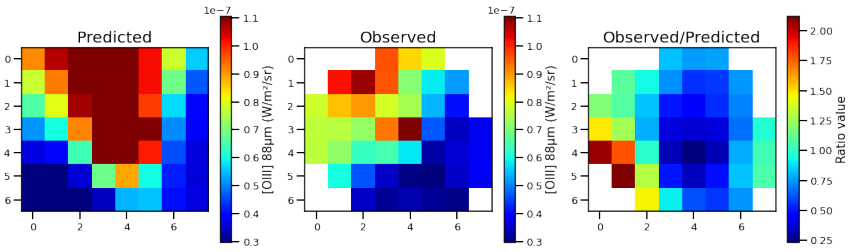

FIGURE 4.14: Similar to Figure 4.6, but for N180.

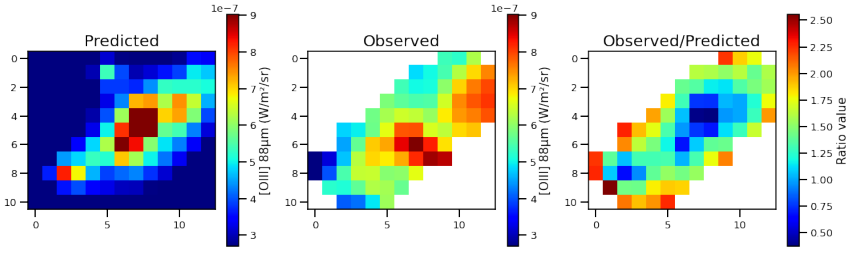

FIGURE 4.15: Similar to Figure 4.6, but for N66.

Other regions with important differences between the predictions and the observations are N11B and N11C. Those two regions lie slightly above the global relation, although they have the same slope. This offset from the global correlation is visible in the predicted values, which underestimate the [O III] emission by a factor of 2-3 over a large zone. For all of the other regions, the predicted [O III] emission is quite similar to the observed values over large areas of the maps, and only a few individual pixels shows a discrepancy that is never higher than a factor of a few.

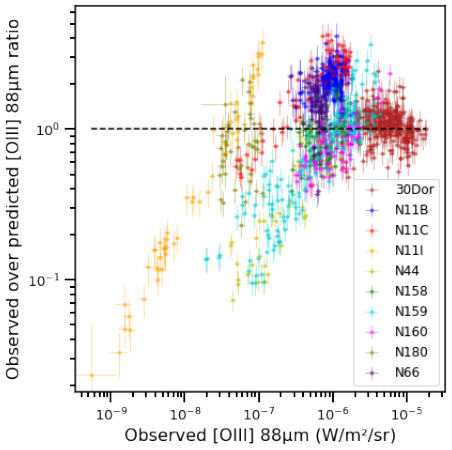

FIGURE 4.16: Ratio of observed over predicted emission of [O III]. The value of 1, corresponding to a one-to-one agreement of the prediction sand the observations, is indicated with a horizontal dashed line.

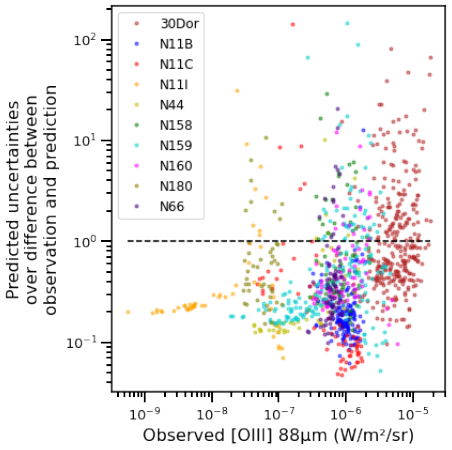

FIGURE 4.17: Uncertainties calculated on the predicted [O III] based on 1σ uncertainties on the fitted parameters, compared to the difference between the observation and the prediction.

The ratio of observed to predicted emission of [O III] (see Figure 4.16, and right panel of Figures 4.6 to 4.15) also shows that the predicted and observed [O III] emission are in good agreement. The ratio of the two is around unity, with a spread of 1 dex or less for most of the regions. Only N159 and N11I exhibit larger differences, with predicted values up to ten times higher than the observations, and a few pixels of N11I at even greater difference. Thus, our correlation allows us to make predictions of [O III] from the observed 24μm which are accurate up to a factor of a few, and can be used to prepare future observations even if the physical conditions of the ISM are not known a priori.

We also compared the uncertainties on the prediction to the actual difference between predictions and observations (Figure 4.17). We see that predicted uncertainties are not able to account for the full discrepancies between observed and predicted values of [O III]. Thus, it is better to use the correlation directly, and not to try to predict uncertainties.

For completeness, we also investigate the predictions made on the luminosity, for the integrated values on our sample and the DGS values. The predicted and observed [O III] luminosity are

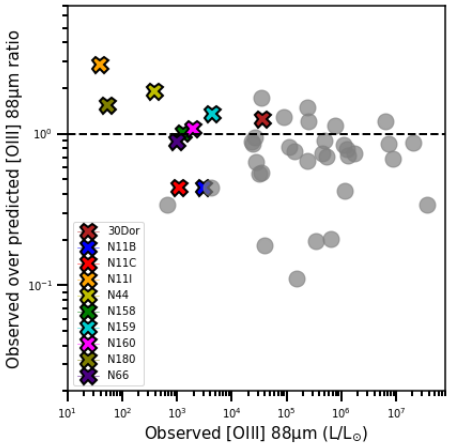

FIGURE 4.18: Predicted [O III] emission, from observed 24μm for integrated luminosity for the Magellanic Clouds sample and the DGS compared to the observed luminosity. The horizontal dashed line indicates when predicted and observed values are equal.

in good agreement for the Magellanic Cloud sample and for DGS targets (Figure 4.18). The discrepancy between predictions and observations is similar to those found for the resolved data, with a factor of a few most of the time, and some extreme galaxies for which the disagreement can be up to 1 dex at most. As the estimated uncertainties were not significant for the resolved data, we did not try to see if uncertainties on the predictions derived from the fitting uncertainties were relevant here.

4.3.2 Predictions for other regions of interest

As an example of the predictive power of the relation between [O III] and 24μm, we display here the predicted [O III] maps for some regions of the Magellanic Clouds which are not yet mapped in [O III], but which have been mapped in 24μm. We choose to make this estimation for the regions of the sample observed with *Spitzer*/IRS, in Figures 4.19 to 4.23.

We also show the estimation for the Molecular Ridge, the bright star-forming arc located south of 30 Doradus, which contains the regions N158, N159 and N160 (Figure 4.24). This molecular ridge region is selected here as it is the target of a proposed Joint Legacy Program with the instrument FIFI-LS (Fischer et al., 2018), onboard the airborne telescope, SOFIA (Erickson & Davidson, 1993): LMC+ (PIs: S. Madden and A. Krabbe). The program targets a large region, of 1°×0.5°, to observe the [C II] 157μm, [O III] 88μm, [O III] 52μm and [O I] 63μm lines. These observations would provide the largest maps observed with SOFIA in the Magellanic Clouds, which will be compared with the voluminous archival data available, including molecular CO emission, H I emission and FIR maps. This program also brings synergies with other planned or possible observations of the region, with ALMA, JWST or other instruments onboard SOFIA.

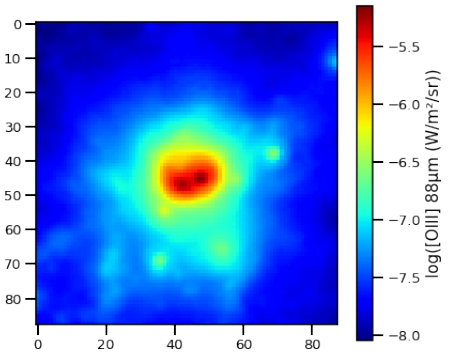

FIGURE 4.19: Predicted observations of [O III] 88μm in the region N4, based onthe observed 24μm maps, calculated with our derived the calibration. The predicted emission is represented in $\log_{10}$ value to highlight the diffuse component of the predicted [O III] emission.

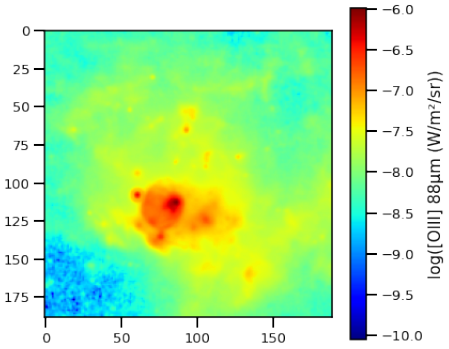

FIGURE 4.20: Similar to Figure 4.19, for the region N63.

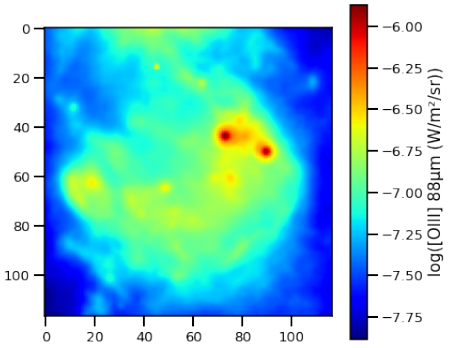

FIGURE 4.21: Similar to Figure 4.19, for the region N79E.

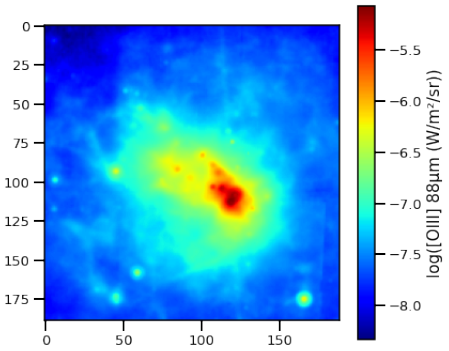

FIGURE 4.22: Similar to Figure 4.19, for the region N105A.

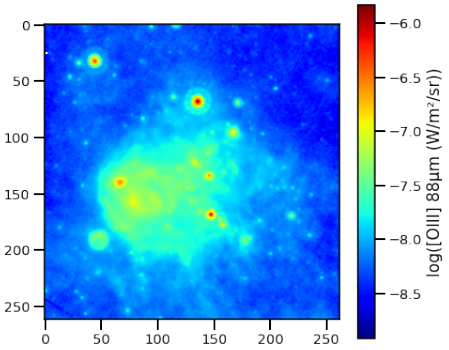

FIGURE 4.23: Similar to Figure 4.19, for the region N76.

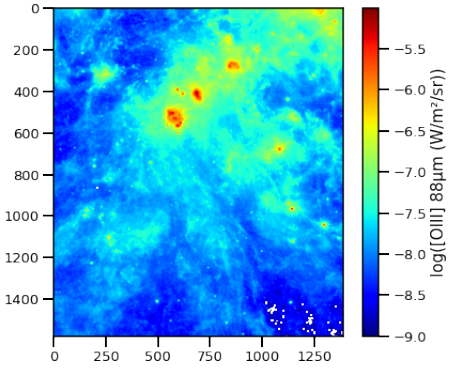

FIGURE 4.24: Similar to Figure 4.19, for the molecular ridge south to 30 Doradus.

4.4 Disentangling dust emission from ionized regions and PDRs

Now that we have studied the direct observed correlation between the [O III] emission line and MIPS 24μm band and its predictive capability, we will investigate the data with the help of the models described in Chapter 3, and try to understand the physical parameters that control the relation between [O III] and 24μm. We aim to understand the spread of the data around the relation that we calibrated, and see if it is linked to the physical conditions of the ISM in the star-forming regoins of our sample. In particular, we suspect that the 24μm emission, which is often considered to be a characteristic tracer of the H II region, may include a contamination by PDR emission. The method we developed is based on a non classical use of the Cloudy models, so we will first describe the modeling strategy. We will then describe the evolution of [O III]/24μm with relevant physical parameters, and we will examine the possibility of deriving these through a comparison between model and observations. We will investigate in particular the distribution of matter along the line of sight with the use of our new method.

4.4.1 Modelling strategy

We base our study on the Cloudy models described in Chapter 3. The ISM corresponds to a mixture of different regions in our telescope beam (diffuse ionized regions, PDRs, H II regions, etc.), and can not always be modeled by a single Cloudy simulation (i.e., 1D model simultaneously solving one H II region plus one PDR). Thus, we investigate the effect of distribution of the ionized and neutral material in our observations. To this aim, we used the Cloudy output option to save the cumulative emission as a function of the depth within the illuminated cloud. Based on this emission and the electron density, also saved as a function of depth in our Cloudy calculation, we separated the emission into two parts: one arising from the H II region, before the ionization front, and the other arising from the PDR[1], after the ionization front, defined as the depth where the electron density drops to half its maximal value. We consider the total emission from the H II region as a pure H II region model and the total emission from the PDRs as a pure PDR model. We then mix the two components to mimic a physical mixture of ionized region and PDR along the line of sight, for a given pixel in the map, with the equation 4.5:

$$\begin{cases} I_{\text{mixed model}} &= c_{\text{H II}}\, I_{\text{H II}} + c_{\text{PDR}}\, I_{\text{PDR}} \\ &= c_{\text{H II}}\, I_{\text{H II+PDR}} + (c_{\text{PDR}} - c_{\text{H II}})\, I_{\text{PDR}} \\ c_{\text{H II}} + c_{\text{PDR}} &= 1 \end{cases} \tag{4.5}$$

where $I_{\text{mixed model}}$ is the total intensity of a tracer for the mixed model, in W m$^{-2}sr^{-1}$; $I_{\text{H II}}$ the intensity of the tracer in the H II region only; I_{PDR} the intensity of the tracer in the PDR only. $c_{\text{H II}}$ and c_{PDR} are the scaling factors of the H II region and PDR respectively.

With this method, we represent different physical configurations for the distribution of H II region and PDR by changing the proportions of PDR (and by construct, H II regions) in Equation 4.5. We underline that this mixture is made only between models having the same initial (at the illuminated edge of the cloud) density and ionization parameter. We use this simple approach to avoid degeneracy between the parameters, as a first step.

Some of the cases that can be described by Equation 4.5 are illustrated in Figure 4.25 which describes different cases linked to the proportion of PDRs in the mixed models. For example, when there is 0% of PDR, the model resembles that of a naked H II region. Similarly, a proportion

[1]Here we refer to the PDRs as the H I region including the PDR

of 100% PDR corresponds to a model of an isolated PDR. We underline that in reality, the model of an isolated PDR corresponds to an observation with only PDR emission along the line of sight, but the PDR can be a part of a larger structure that contains also H II regions, but is not seen along this line of sight. A proportion of 50% corresponds to a single Cloudy model (1D connected H II region and PDR). The multiplicative factor for the full model, is similar to a luminosity scaling but we preferred to use ratios between lines and continuum bands to construct a more general use of the models.

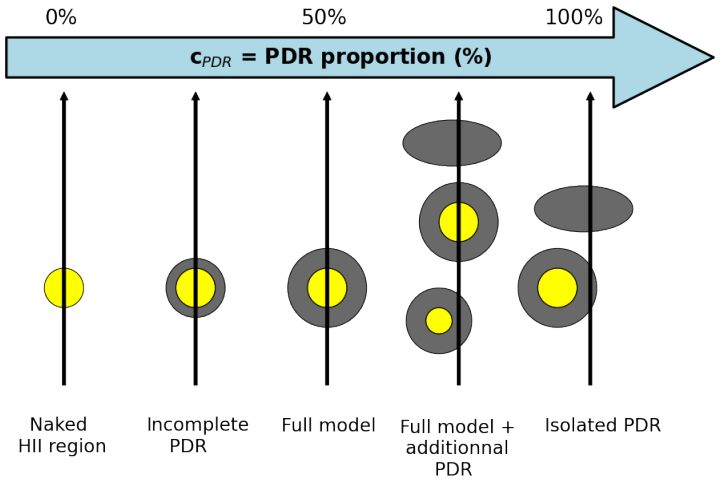

FIGURE 4.25: Sketch of different PDR proportions in our mixed models. The yellow regions designate H II regions, and PDRs are represented in grey. The blue arrow indicates the direction of increasing PDR proportion. The black arrows show the lines of sight through the represented clouds (each line of sight representing a given pixel in our maps). As per Equation 4.5, the 0% PDR proportion case corresponds to no PDR in the model, hence fully ionized gas; the 50% corresponds to single Cloudy model, with a connected H II region and PDR (Equation 4.7); and 100% signals a full PDR model, without an H II region contribution. Note that 50% of PDR does not correspond to a medium with half of the volume being filled by PDR, but corresponds to a mix that can be modeled by a Cloudy model with a full PDR layer.

The extreme cases of 0% and 100% of PDR are easy to represent, and all the other cases are based on the interpretation of Equations 4.6 to 4.8. The percentage of PDR we use here is not corresponding to the amount of PDRs in the medium, but to the amount of PDR emission from the model we use. A percentage of PDRs superior to 50% corresponds to a covering factor of the PDR on the H II region greater than 1, with more PDRs along the line of sight than a simple model, or in other words there is more than one cloud along the line of sight, with potentially different intercepts between the cloud and the line of sight. Thus, it can be a way of interpreting the distribution of matter in the third dimension. The method we developed here and describe in Section 4.4.3 is seen as a first step toward a more detailed model of the matter along the lines of sight (with different conditions between H II regions and PDRs) and its cumulative observed emission.

Since this is a relatively non-standard approach, we will investigate three examples with different proportions of H II regions and PDRs to illustrate the corresponding physical configurations. To understand what these cases represent in terms of the classical single H II region plus PDR Cloudy model, we rewrite Equation 4.6 in terms of $I_{\rm single}$, which denotes a single full Cloudy

model. We then scale the full single Cloudy model along with the fraction of PDR intensity (I_{PDR}) necessary to match the balance of H II region plus PDR.

4.4.1.1 Example: 90% H II region and 10% PDR

For a mixed line of sight dominated by H II region, Equation 4.5 gives:

$$\begin{cases} I_{\rm single} & = & I_{\rm HII+PDR} \\ 0.9\,I_{\rm H\,II} + 0.1\,I_{\rm PDR} & = & 0.9\,I_{\rm H\,II} + 0.9\,I_{\rm PDR} - 0.8\,I_{\rm PDR} \\ & = & 0.9\,I_{\rm single} - 0.8\,I_{\rm PDR} \\ & = & 0.9\left(I_{\rm single} - \frac{0.8}{0.9} \times I_{\rm PDR}\right) \end{cases} \tag{4.6}$$

In Equation 4.6, we see that a proportion of 10% of PDR can be simulated as a full Cloudy model with part of the PDR suppressed, assuming all of the modeled ISM have identical conditions (same ionizing sources, same initial density and same initial ionization parameter). The physical interpretation of a single Cloudy model, with part of the PDR removed, may represent a matter-bounded region, where the PDR is decreased due to lack of gas and dust.

4.4.1.2 Example: 50% H II region and 50% PDR

For a balanced mix of H II region and PDR, Equation 4.5 gives:

$$0.5\,I_{\rm H\,II} + 0.5\,I_{\rm PDR} \;=\; 0.5\,I_{\rm single} \tag{4.7}$$

As we have noticed before, we see in Equation 4.7 that a mixture with 50% of PDR corresponds to a single Cloudy model, with all of the PDR emission taken into account, still under the assumption that the H II region and the PDR component have the same initial density and ionization parameter. We highlight the point that 50% of PDR does not correspond to a medium with half of the volume being filled by PDR, but corresponds to a mix that can be modeled by a Cloudy model with a full PDR layer. This configuration can be physically interpreted as lines of sight through the different zones of a star-forming cloud with a young star cluster, and may represent a radiation-bounded cloud.

4.4.1.3 Example: 10% H II region and 90% PDR

For a mix dominated by PDR region, Equation 4.5 gives:

$$\begin{aligned} 0.1\,I_{\rm H\,II} + 0.9\,I_{\rm PDR} &= 0.1\,I_{\rm H\,II} + 0.1\,I_{\rm PDR} + 0.8\,I_{\rm PDR} \\ &= 0.1\,I_{\rm single} + 0.8\,I_{\rm PDR} \\ &= 0.1\,(I_{\rm single} + 8\,I_{\rm PDR}) \end{aligned} \tag{4.8}$$

In Equation 4.8, we see that a proportion of 90% of PDR in the mixture can be represented by a full Cloudy model with a further addition of eight times more PDR in this case. We underline that those PDR are connected to H II regions lying outside the line of sight. Such a model also represents a radiation-bounded case along the corresponding line of sight between the cluster and the cloud. Physically, this configuration can not be modeled by a single Cloudy model, as it would overestimate the emission of tracers emitted by the H II region.

Note that these illustrations are made considering that we model our observations with a single Cloudy model (i.e., same initial density and ionization parameter). In reality, the distribution of the matter in the ISM can be much more complex. Around a young star, neither the H II region nor the PDR may fully cover the stellar source. The H II region can be reduced to a blob of

ionized gas near the star, and the covering factor of the PDR can be lower than unity, leading to a configuration with part of the cloud surrounding the star being matter-bounded (no or little PDR beyond the ionized gas), and part of it being radiation bounded (with a full PDR beyond the ionized gas). However, we keep the assumption that a simple Cloudy model can be used. This means that if along the line of sight there is a thick PDR covering only a part of the H II region, we will model it as a thinner PDR which is fully covering the H II region. Higher spatial resolution observations, of course, would help to constrain a more detailed modeling scheme.

The method developed in Section 4.4.3 allows us to constrain the physical parameters used as input in our Cloudy models: the age, the initial density and the ionization parameter. Based on those parameters, it is possible to determine the PDR proportion for each pixel in the map. To constrain our mixed model, we use a ratio of observed PDR and H II region tracers, such as ([C II]+[O I])/[O III], to determine the fraction of PDR, c_{PDR}, needed in the model to reproduce the observed ratio, using Equation 4.9. This approach will be used in Section 4.4.4 when we apply this to each pixel in our maps.

$$\begin{cases} R_{\rm obs} &= \frac{I_{\rm CII,\,obs}+I_{\rm OI,\,obs}}{I_{\rm OIII,\,obs}} \\ &= \frac{(c_{\rm HII}\,I_{\rm CII,\,HII}+c_{\rm PDR}\,I_{\rm CII,\,PDR})+(c_{\rm HII}\,I_{\rm OI,\,HII}+c_{\rm PDR}\,I_{\rm OI,\,PDR})}{c_{\rm HII}\,I_{\rm OIII,\,HII}+c_{\rm PDR}\,I_{\rm OIII,\,PDR}} \\ c_{PDR} &= \left(1-\frac{I_{\rm CII,\,PDR}+I_{\rm OI,\,PDR}-R_{\rm obs}\,I_{\rm OIII,\,PDR}}{I_{\rm CII,\,HII}+I_{\rm OI,\,HII}-R_{obs}\times I_{\rm OIII,\,HII}}\right)^{-1} \end{cases} \tag{4.9}$$

In Equation 4.9, $R_{\rm obs}$ is the observed ratio, with $I_{\rm CII,\,obs}$ the observed line intensity of [C II] $I_{\rm OI,\,obs}$ the observed line intensity of [O I] and $I_{\rm OIII,\,obs}$ the observed line intensity of [O III]; $R_{\rm obs}$ is reformulated by using Equation 4.5 for each tracer in order to compare the models to the observations, where $I_{\rm CII,\,HII}$ is the intensity of the [C II] line in the H II region model, with similar definitions for the other lines, and $I_{\rm CII,\,PDR}$ is the intensity of the [C II] lines in the PDR model, with similar definitions for the other lines. Equation 4.9 provides $c_{\rm PDR}$ which gives the final formula for the PDR proportion.

4.4.2 Evolution of [O III]/24μm with physical parameters

We created grids of models (Chapter 3) by varying three parameters: the age of the burst ionizing the cloud, the initial density of the cloud at its illuminated edge and the ionization parameter, again at the illuminated edge. A separation of the model values around the ionization front, as described in the first part of Section 4.4.1, allows us to investigate a new parameter, that we call PDR proportion and that we note as $c_{\rm PDR}$. As the luminosity was not used in our models, it is not possible to directly compare the modeled to observed values. Thus, we will investigate the evolution of the ratio [O III]/24μm with the different parameters, namely the initial density, the ionization parameter, the age of the ionizing burst of star formation and the PDR proportion.

Figure 4.26 shows the evolution of the ratio [O III]/24μm as a function of the age of the burst ionizing the cloud, the initial density of the cloud at its illuminated edge, the ionization parameter and the PDR % for each pixel from all of our maps. The observed values are represented with the median, the median absolute deviation, and the distribution of the observed ratio with a histogram displayed on the side of each panel. The upper left panel shows the evolution of the ratio with the proportion of PDR emission within the line of sight. While it is clear that, when the full distribution of all regions is taken into account, the models favor young ages and low density in particular, they do not allow us to constrain right away the PDR proportion.

The upper right panel in Figure 4.26 shows the evolution of [O III]/24μm with the age of the burst of star formation which plummets between ∼4 and 10 Myrs: models with burst ages greater than 4-5 Myrs are not able to reproduce the observed ratio. Older ages, such as 10 Myrs,

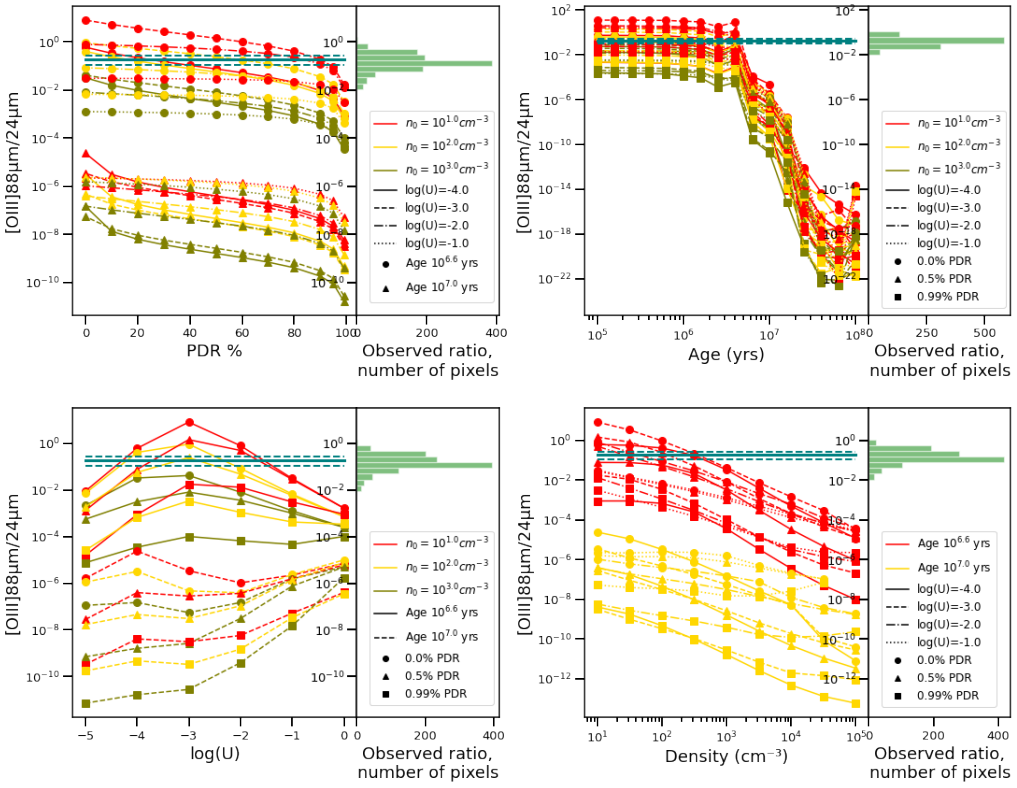

FIGURE 4.26: Evolution of the ratio [O III]/24μm with the four parameters varied in the models: the proportion of PDR in the line of sight (*upper left panel*), the age of the star formation burst (*upper right panel*), the ionization parameter at the illuminated surface of the cloud (*lower left panel*) and the initial density at the illuminated edge of the cloud (*lower right panel*). The models used are set with constant density, and a metallicity of 1/2 $Z_\odot$. The blue solid line is the median of the observed ratio, the blue dashed lines are representing the variation of the median absolute deviation, and the histogram on the right side of each plot shows the distribution of the observed ratio value. Note that the legend symbols and colors are different for each panel.

are also eliminated based on the evolution of ratio with PDR fraction (upper left panel). This can be explained by considering the lifetime of the O and B type stars, which is about a few Myrs and is consistent with the age determined by studies of the stellar content of the different Magellanic Cloud regions (Parker et al., 1996; Gruendl & Chu, 2009; Heydari-Malayeri et al., 1987; Oey & Massey, 1995; Seale et al., 2012; Bica et al., 1996, among many others). The death of O and B stars induces a drop in the emission of high-ionization species, including [O III]. Meanwhile, other stars continue to heat the dust, which continues to emit at 24μm. Thus, the ratio [O III]/24μm tends to decrease after the age when most of the O and B stars have died. By comparing the observations to the models the most likely maximal age for the burst is 4 Myrs. It is difficult to constrain a lower limit because the ratio is not evolving much until 1 Myr. Thus, we will limit further studies to ages in our grid of models that are within to those limits: 1 Myr, 1.6 Myr, 2.5 Myrs and 4 Myrs.

The evolution of the ionization parameter with the ratio of [O III]/24μm, does not help to isolate the range of possible values of PDR fraction (Figure 4.26, lower left panel). However,

by comparing the observed median and median absolute deviation of the ratio to the model, we can see that the most extreme values of the ionization parameter in the models, log(U)=-5 and log(U)=-1, are not probable. Thus we will limit our study to models within log(U)=-4 and log(U)=-2.

The lower right panel of Figure 4.26 shows the evolution of [O III]/24μm with the initial density. We see that the ratio decreases with increasing initial density. This can be understood due to the critical density of the [O III] line: 5×10^2 cm^{-3}. Thus, when the density increases beyond this value, the emission line saturates. The 24μm emission, however, continues to increase with the density, resulting in a decrease of the ratio [O III]/24μm. The models fitting the data all have densities lower than $\sim 1000\,\mathrm{cm}^{-3}$.

4.4.3 Determining the ISM conditions

According to the models, the emission of 24μm can also arise from PDRs, while the [O III] emission can only originate from the ionized gas (see Chapter 3). Thus, we will include the [C II] emission line as a typical tracer to constrain PDRs. It will be completed by the [O I] 63μm line which is often used to trace PDRs with high UV illumination and/or high density (see Chapter 3, and Tielens, 2005; Osterbrock & Ferland, 2006; Tielens & Hollenbach, 1985).

To trace the ISM physical conditions, we inspect the ratio [O III]/24μm as a function of ([C II]+[O I])/[O III]. As the [O III] line is emitted by the H II regions only, and [C II] and [O I] lines are emitted mostly from PDRs in low metallicity galaxies, we can consider the ratio as a tracer of the proportion of PDR emission within the line-of-sight. A high value of ([C II]+[O I])/[O III] indicates that the proportion of emission arising from PDR is important. As the MIPS 70μm band emission generally traces cooler dust than that of the 24μm band, and is emitted mainly by PDRs in our models, we decided to also compare the ratio [O III]/70μm to ([C II]+[O I])/[O III].

4.4.3.1 Global results for the sample

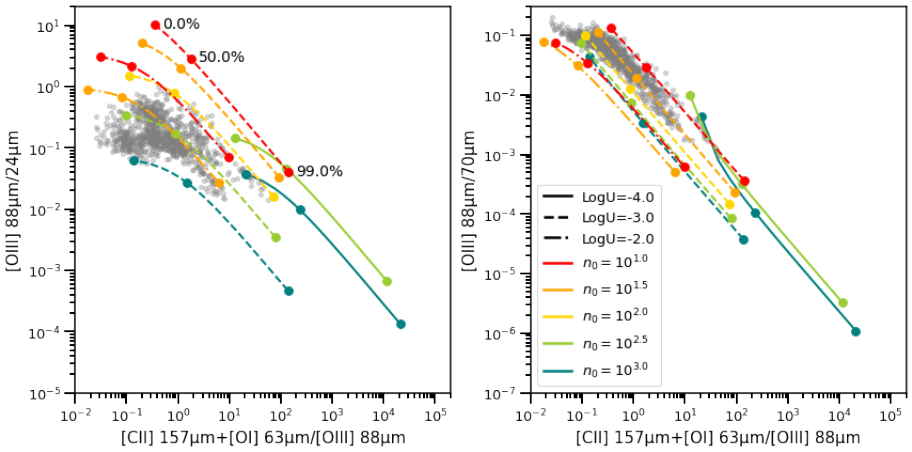

FIGURE 4.27: *Left panel:* The ratio [O III]/24μm as a function of ([C II]+[O I])/[O III]. The grey points are the observed data, and the lines are the Cloudy models with constant density. The proportion of PDR emission for the total emission varies along the line of each models, from 0% to 99%, and markers indicates some reference proportions, at 0%, 50% and 99%. Those proportions are indicated for one of the models, as the PDR proportion markers are the same for all models. *Right panel:* Similarly to the left panel, the ratio of [O III]/70μm as a function of ([C II]+[O I])/[O III]. The legend is common for the two panels, and the proportion of PDR emission has the same representation as that for the representation of the ratio [O III]/24μm. The age of the starburst is 1 Myrs for both panels.

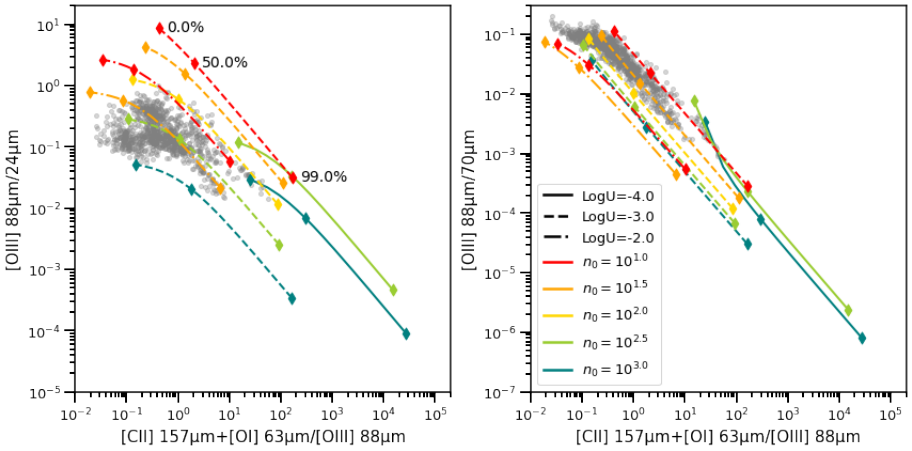

FIGURE 4.28: Similar to Figure 4.27, for an age of the star formation burst of 1.6 Myrs.

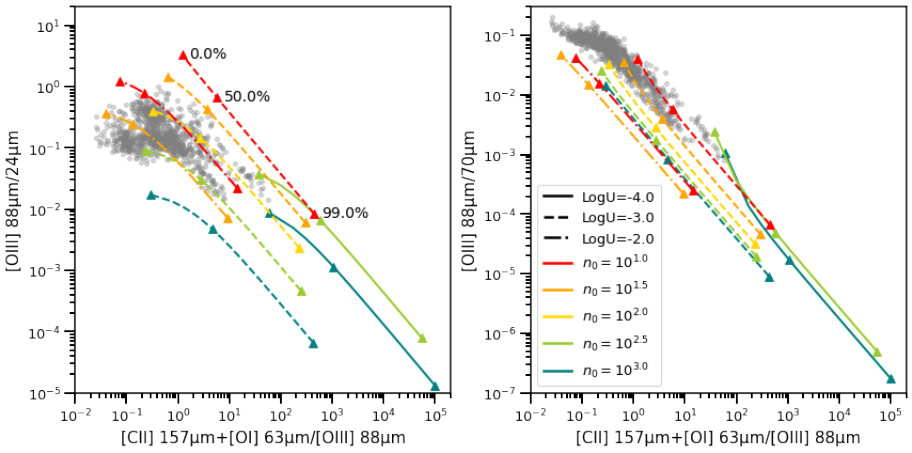

FIGURE 4.29: Similar to Figure 4.27, for an age of the star formation burst of 2.5 Myrs.

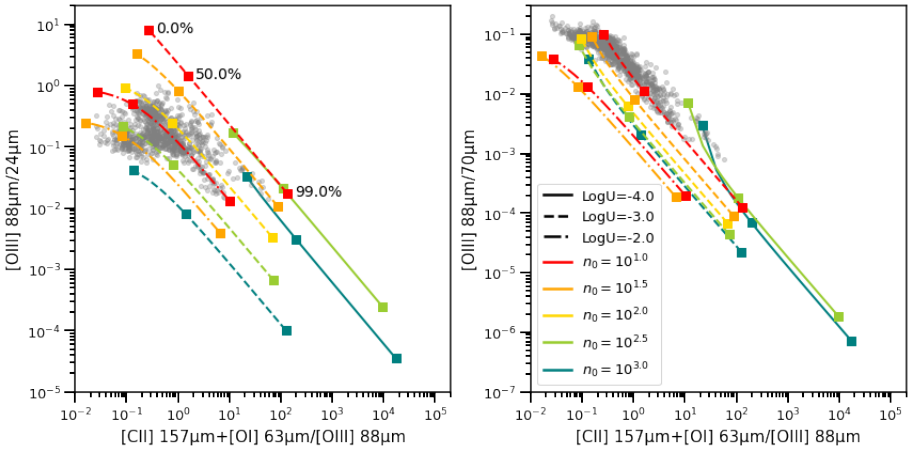

FIGURE 4.30: Similar to Figure 4.27, for an age of the star formation burst of 4 Myrs.

Figures 4.27 to 4.30 show the ratios of observed [O III]/24μm and [O III]/70μm as a function of the ratio intended to trace the proportion of PDR emission, namely ([C II]+[O I])/[O III]. Constant density models are overlaid, each of them being plotted for a range of PDR proportions in the model from 0% to 99%. The different figures are for different ages of the initial star

formation burst, at 1 Myr, 1.6 Myrs, 2.5 Myrs and 4 Myrs, the most likely burst ages for the observed regions (Section 4.4.2).

We see that the observed ratio [O III]/24μm shows a possible bimodal behavior, depending on the value of the PDR proportion (Figures 4.27 to 4.30, left panels): for low values of the ratio ([C II]+[O I])/[O III], up to ∼1, a relatively flat trend is seen, albeit with a wide spread of values, while for higher values of ([C II]+[O I])/[O III] beyond ∼1 there is a decrease of the [O III]/24μm ratio with increasing values of ([C II]+[O I])/[O III]. The flat trend can be interpreted as having both the [O III] and the 24μm arising from ionized gas, while the subsequent decrease in [O III]/24μm corresponds to an increasing proportion of the emission coming from PDRs, where the 24μm also contributes, but with little emission from the [O III] line. On the other hand, the ratio [O III]/70μm, (Figures 4.27 to 4.30, right panels) only shows a relatively tight decreasing trend with ([C II]+[O I])/[O III]. Considering that most of the 70μm is usually expected to arise from PDRs, it reinforces the idea that the decrease seen in [O III] corresponds indeed to an increase of PDR proportion.

The range of parameters for which the models reproduce the observations does not seem to depend much on the age (Figure 4.27 to 4.30, left panels). We see that observations show an elbow in the ratio [O III]/24μm, which corresponds to the evolution of the models with the PDR proportion, c_{PDR}. Thus, this parameter seems to be an important driver of the behaviour of the data. We then search for models with values of ionization parameter and density, with c_{PDR} varying between 0 and 99%, which closely match the data. With those conditions, the models that are the closest to the data have intermediate ionization parameters, log(U) of -2 and -3, and low to intermediate densities, from 10^1 to $10^{2.5}$ cm^{-3}. Some models with low ionization parameter (log(U)=-4) and intermediate to high densities ($10^{2.5}$ to 10^3 cm^{-3}) can fit part of the data. However, the global behaviour of those models is not representative of the data. Thus, this low ionization parameter value is highly improbable.

If we wish to derive a single set of physical parameters that reproduces the [O III]/24μm observations with varying PDR proportions, this would be for models with log(U)=-3 and densities between 10^2 and $10^{2.5}$ cm^{-3}, or to models with log(U)=-2 and densities between 10 and $10^{1.5}$ cm^{-3}.

On the other hand, the [O III]/70μm as a function of ([C II]+[O I])/[O III] (Figures 4.27 to 4.30, right panels), indicates that the best models prefer low ionization parameter (log(U)=-3) and low densities (10 to $10^{1.5}$ cm^{-3}). Considering physical models of PDRs (e.g., Tielens & Hollenbach, 1985 and references within), it is not plausible that it should be interpreted as a need for low density in PDRs, while keeping a low ionization parameter of log(U)=-3. This may be pointing to the fact that the models we use here may not be accurate, and we need to have other hypotheses. The ionization parameter is linked to the density, and a decrease of the ionization parameter may correspond to an increase of the density. Thus, a possible explanation is that the models point to an increase of density in PDRs compared to H II regions in order to fit the [O III]/24μm and [O III]/70μm at the same time. This corresponds well to the idea that the ISM is considered to be in pressure equilibrium, and thus that density increases in the PDRs. To explore this possibility, we will compare the data with constant pressure models.

The ratios [O III]/24μm and [O III]/70μm are represented as a function of ([C II]+[O I])/[O III] in Figures 4.31 to 4.34 with constant pressure models overlaid, for ages from 1 to 4 Myrs. We see that the evolution of the modeled ratio with the PDR proportion agrees with the data better than the constant density models, with a flatter trend at low PDR proportions (50% or less), and a decreasing trend for higher proportions (over 50%). Most importantly, it is also possible to find models that are fitting well the ratios of [O III]/24μm and [O III]/70μm simultaneously.

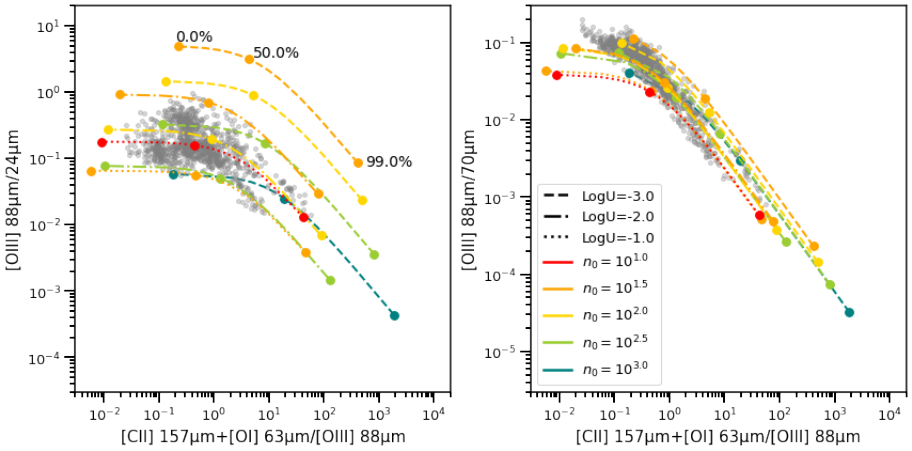

FIGURE 4.31: Similar to Figure 4.27, for constant pressure models. The legend in the right panel stand for the whole figure.

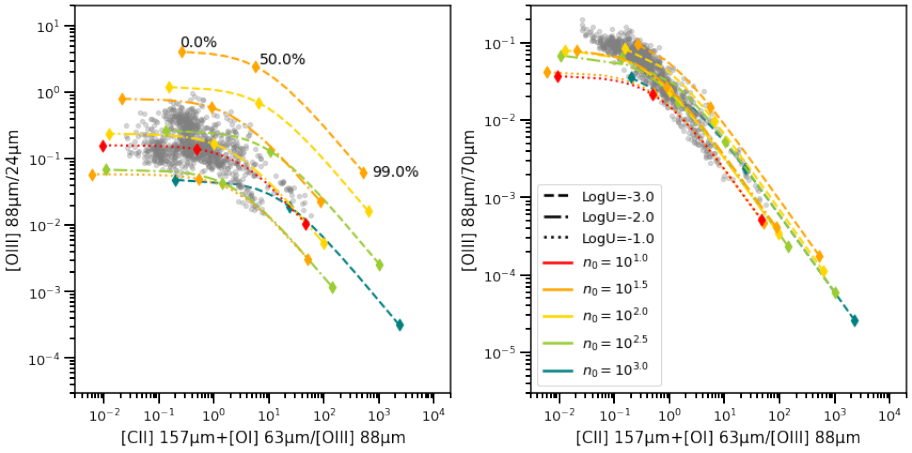

FIGURE 4.32: Similar to Figure 4.31, for an age of the star formation burst of 1.6 Myrs.

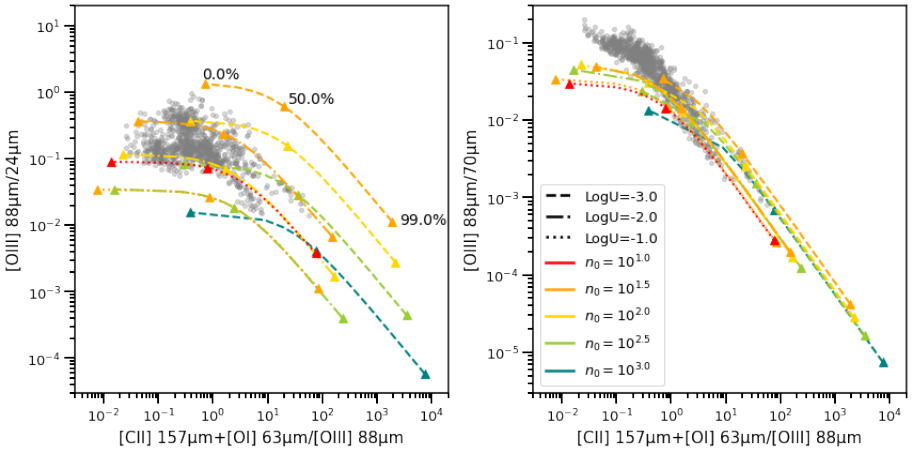

FIGURE 4.33: Similar to Figure 4.31, for an age of the star formation burst of 2.5 Myrs.

The models that are best agreeing for the entire data set have an initial density of $10^{2.5}$ cm^{-3}, an ionization parameter of log(U)=-3 and various proportions of PDRs. Notice that the PDR proportion fitting the data is below 50% most of the time. This means that the emission can be

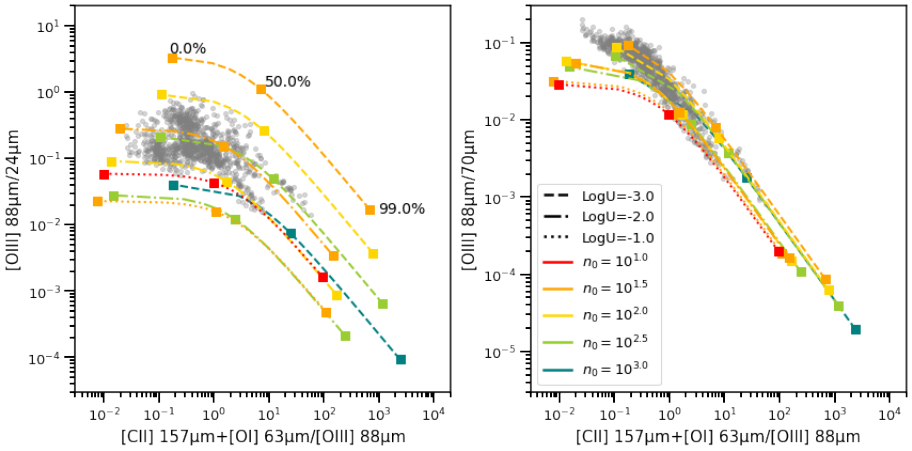

FIGURE 4.34: Similar to Figure 4.31, for an age of the star formation burst of 4 Myrs.

modeled with a single connected H II region and PDR model and a covering factor of the PDR between 0 and 1[2].

4.4.3.2 Individual regions

We investigated individual regions in the same way than for the global behaviour. The figures are shown in Appendix B (Figures B.1 to B.10). We see for each region that the models that are best fitting the data are close to the best model found for the whole sample, but differences can be seen from one region to another. We summarize the best fitting models for the total sample and the individual regions in Table 4.2. Some other models that can be agreeing for part of the data inside the regions are also indicated.

We see that when multiple models are agreeing, an increase of ionization parameter corresponds to a decrease of the initial density. In most of the cases, our results are coherent with previous studies (see references in Table 4.2 and Section 2.3). It is probable that the density we report here corresponds to a rather diffuse ionized gas, that is ubiquitous in our maps. Although there are dense clumps observed in almost all the regions in our sample, the highest densities are hidden by two effects: the dilution of dense clumps by the surrounding lower density medium, due to the resolution and sampling of our data, and the fact that we report the initial densities, where the actual densities in our models can rise to a few 10^5-10^6 cm^{-3} at high A_V, corresponding to the high-density clumps observed.

N44 (Appendix B, Figure B.5) is the region that deviates most from the global distribution of the parameters, being the only region with a higher ionization parameter (log(U)=-2, where all of the other regions and the global value show log(U)=-3), and having a lower initial density. McLeod et al. (2019) found that a large bubble was carved out in the region by the central star cluster, leading to a large zone with very low density. This morphological observation may explain the low global density we find, which directly leads to a higher ionization parameter. It is a condition unique to this region, as the other regions in our sample do not show such a large excavation of the ISM.

While the PDR tracers, [O I] and [C II], are prominently emitting in all of the star forming regions studied, most regions have quite low proportions of PDR components along the lines of sight throughout their regions. All but 4 regions have less than 12% PDR proportion anywhere within their map.The N11C region shows pixels with at least 30% PDR proportions along their

[2]A PDR proportion lower than 50% corresponds to a covering factor between 0 and 1, where a PDR proportion higher than 50% corresponds to a covering factor greater than 1.

	Best model $\log(U)$, density	Other agreeing models $\log(U)$, density	References
Global sample	-3, 2.5	-2, 1.5 to 2	
		-3, 2 to 2.5	
30 Doradus	-3, 2.5	-3, 1.5 to 2	(1) (2) (3) (4)
		-2, 1.5 to 2	
N11B	-3, 2 to 2.5	-	(5) (6)
N11C	-3, 2	-3, 2.5	(7)
N11I	-3, 2	-3, 2.5	
N44	-2, 1.5	-2, 2	(8) (9) (12)
		-3, 2.5 to 3	
N158	-3, 2.5	-2, 1.5	(10) (11)
N159	-3, 2.5	-2, 1.5 to 2	(10) (11) (12)
N160	-3, 2.5	-2, 1.5 to 2	(10) (11) (13) (14) (15)
N180	-3, 2 to 2.5	-2, 1.5	(8)
N66	-3, 2	-	(3) (4) (9) (16) (17)

(1)Anderson et al. (2014), (2)Gruendl & Chu (2009), (3)Tsamis et al. (2003), (4)Kurt & Dufour (1998), (5)Lebouteiller et al. (2012a), (6)Nazé et al. (2001), (7)Heydari-Malayeri et al. (1987), (8)McLeod et al. (2019), (9)Toribio San Cipriano et al. (2017), (10)Bolatto et al. (2000), (11)Okada et al. (2019), (12)Seale et al. (2012), (13)Heydari-Malayeri & Testor (1986), (14)Heydari-Malayeri et al. (2002), (15)Martín-Hernández et al. (2008), (16)Heydari-Malayeri & Selier (2010), (17)Requena-Torres et al. (2016)

TABLE 4.2: Ionization parameters and initial densities of the constant pressure models that reproduce the full global data set of all regions together as well as the individual regions. The fourth column indicates a few references about the different regions that can be interesting for comparison. We refer to Chapter 2 for further details and descriptions about the regions.

lines of sight and only three regions exhibit PDR proportions higher than 50% for some of the pixels of the regions: N44, N11I and N159. Both N159 and N44 show complex morphology, with arcs, bubbles, and clumps. They also show ongoing star formation, with associated molecular clumps. On the other hand, N11I shows a more quiescent and extended molecular clump. Those three regions exhibit a higher PDR proportion on part of the maps which could be linked to the stellar formation activity, as the regions N44 and N159 present recent star formation, and the birth cloud may not be totally dispersed. For N11I, it could be linked to ongoing star formation inside the quiescent molecular cloud. A comparison with CO observations, and point source catalogs would be useful to understand the properties of those regions. As most of the regions have low PDR proportions, this implies that most of the pixels are largely dominated by H II regions, and there is little neutral gas that can be observed along the line of sight compared to the ionized gas. On the other hand, pixels where the PDR proportion is higher than 50% correspond to a covering factor higher than 1, or to an excess of PDRs considering a simple model with a connected H II region and PDR. This can mean that we have multiple clouds along the line of sight, or that we are looking through the external part of a cloud that is spatially resolved. In all the cases here, we see that the PDR proportion varies significantly within a region. We will thus investigate the spatially resolved distribution of PDR proportion, to have a better understanding of how it can be linked to physical interpretation.

4.4.4 Insights on the distribution of ionized and neutral gas

For each region, assuming the best fitting model determined in Section 4.4.3, we calculate the PDR proportion needed to match the observed ([C II]+[O I])/[O III] ratio (Equation 4.9). Those

maps are presented in Figure 4.35 to 4.44, along with other emission and ratio maps for comparison.

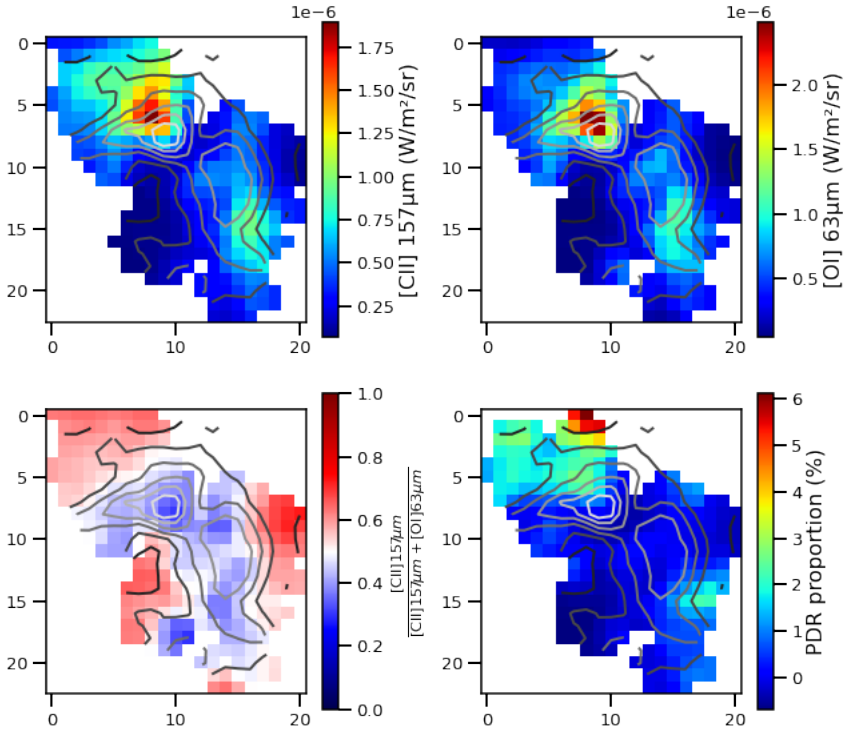

FIGURE 4.35: The distribution of [C II] 157μm and [O I] 63μm emission (upper left and right panels respectively); the ratio of [C II] 157μm/([C II] 157μm+[O I] 63μm) (lower left panel) and the distribution of the PDR proportion (lower right panel) in 30 Doradus. The contours of the [O III] 88μm emission line are overlaid on the four panels for comparison, with color going from light gray for higher emission to dark gray for lower emission.

From the comparison of the [C II], [O I] and [O III] emission (Figures 4.35 to 4.44), we see that the distribution of the PDR proportion is not spatially correlated with that of the PDR tracers, [C II] and [O I]. The spatial distribution of the two PDR tracers is quite similar while they peak somewhat offset from the [O III] emission. The lines of sight for the peak PDR proportions are often found in close proximity of the peaks of the H II tracers, yet offset from them. Significant [O III] emission can be found toward the [C II] and [O I] peaks. Thus substantial ionized gas is also present in those pixels and mixed with the PDR tracers. Note that strong emission of PDR tracers in one line of sight does not mean that PDRs are dominant along the line of sight.

We also tentatively tried to link the PDR proportion with the physical conditions in the PDRs. According to Tielens & Hollenbach (1985), the cooling of the gas is dominated by the [O I] emission line in PDRs that are dense and strongly illuminated, thus more often PDRs that are close to the illumination source. On the other hand, [C II] is the dominant coolant in PDRs that can be less dense, or less irradiated. Projection effects can be misleading, and it is difficult to access the 3D distribution of matter. This problem arises in addition to the determination of the physical parameters, in particular the density which is a key parameter for a study using [O I]. In that vein, Chevance et al. (2016) applied PDR models to FIR lines in 30 Doradus, including [C II] and [O I] and continuum emission to constrain the density of the different clouds and investigate the 3D matter distribution.

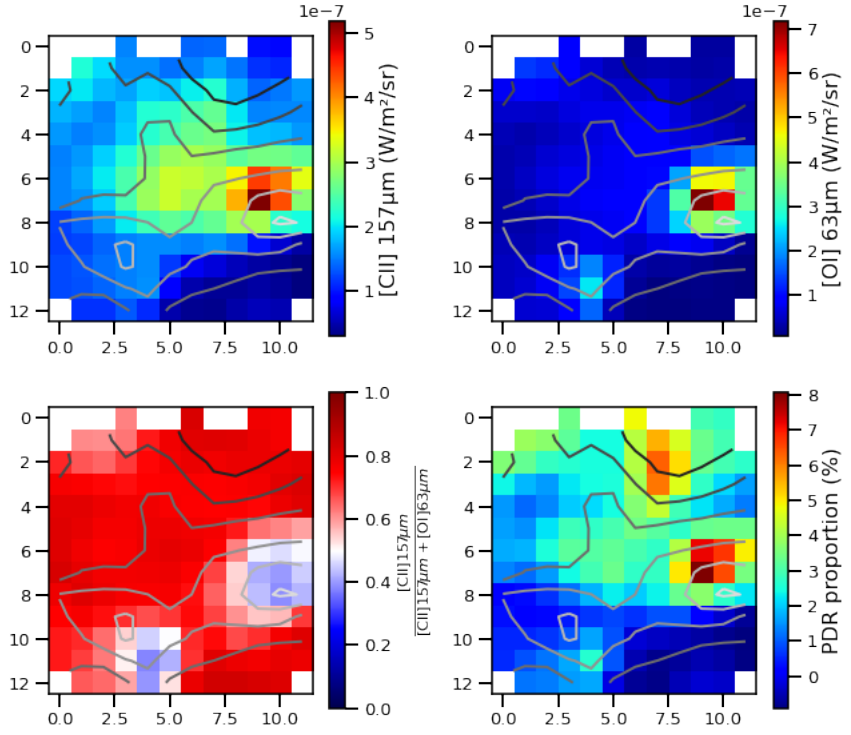

FIGURE 4.36: Similar to Figure 4.35, for the region N11B.

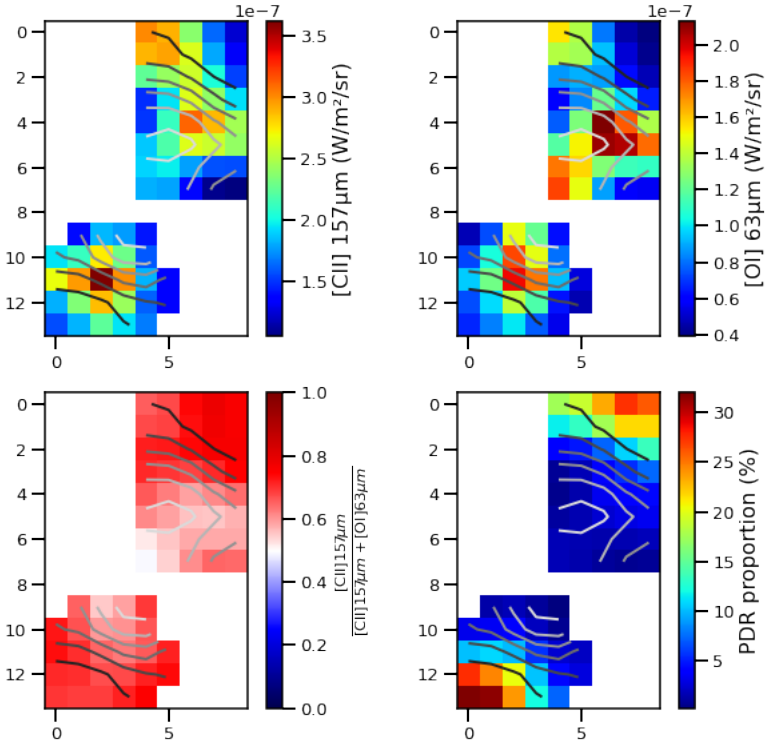

FIGURE 4.37: Similar to Figure 4.35, for the region N11C.

We also compare the PDR proportion maps to the ratio [C II]/([C II]+[O I]) (Figures 4.35 to 4.44, two lower panels). Regions with ratios lower than 0.5 are dominated by [O I], and

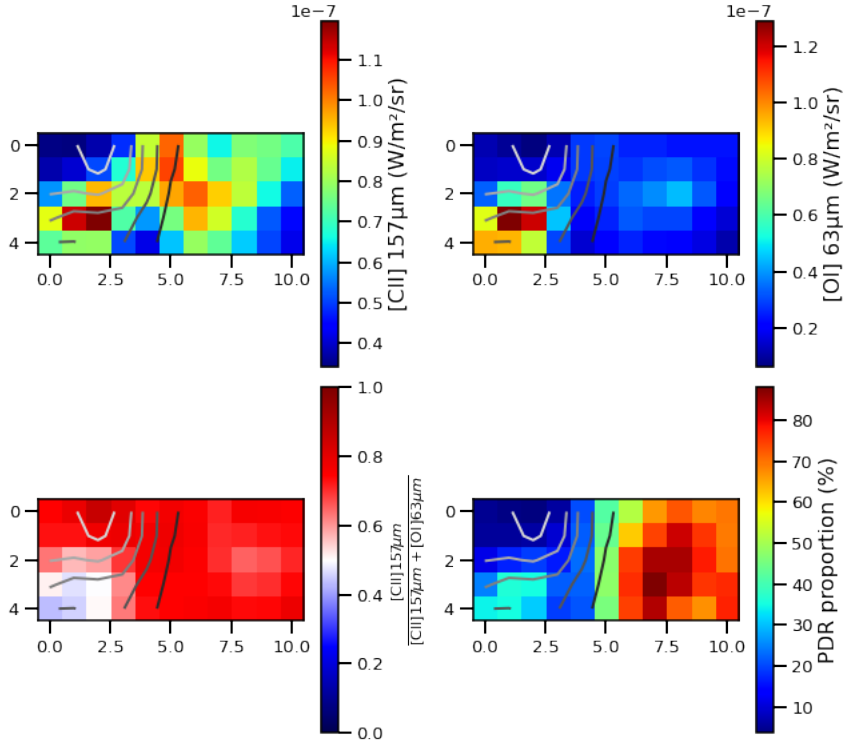

FIGURE 4.38: Similar to Figure 4.35, for the region N11I.

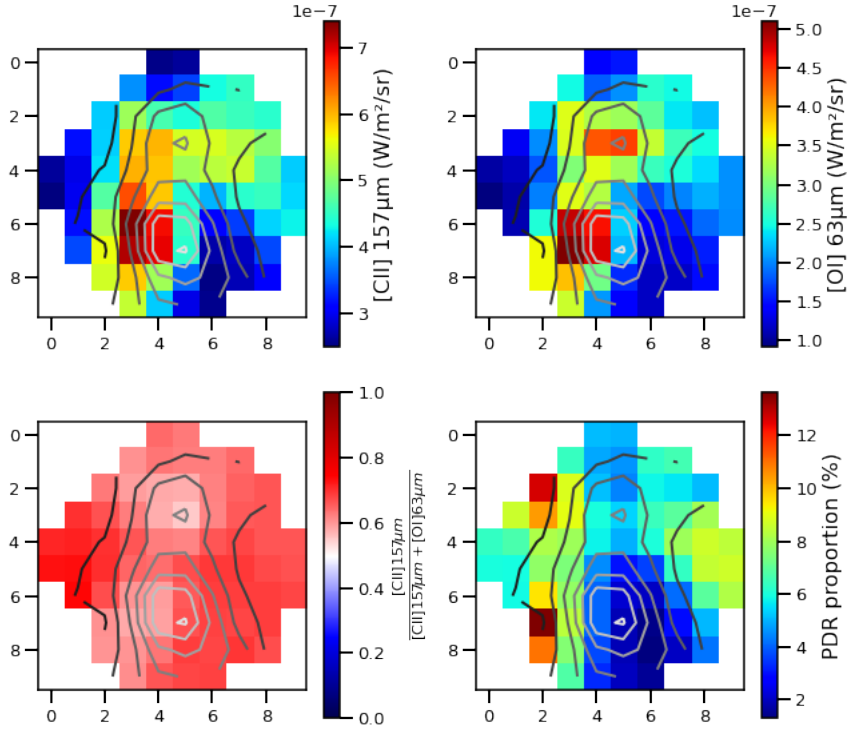

FIGURE 4.39: Similar to Figure 4.35, for the region N158.

regions with a ratio value higher than 0.5 are dominated by [C II]. We see that the ratio [C II]/([C II]+[O I]) is correlated with c_{PDR} considering the ionization parameter and density

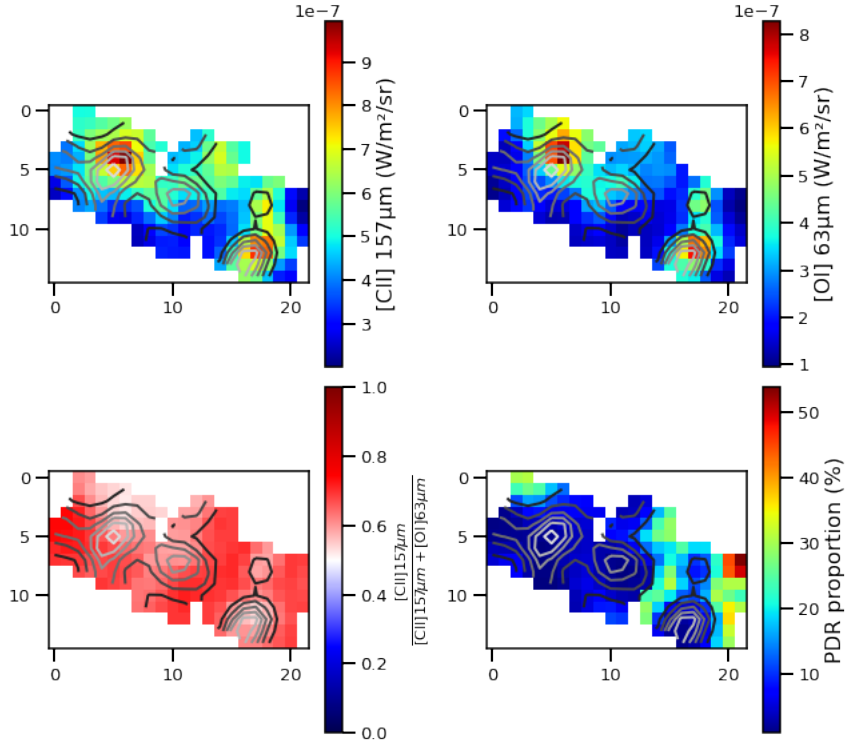

FIGURE 4.40: Similar to Figure 4.35, for the region N159.

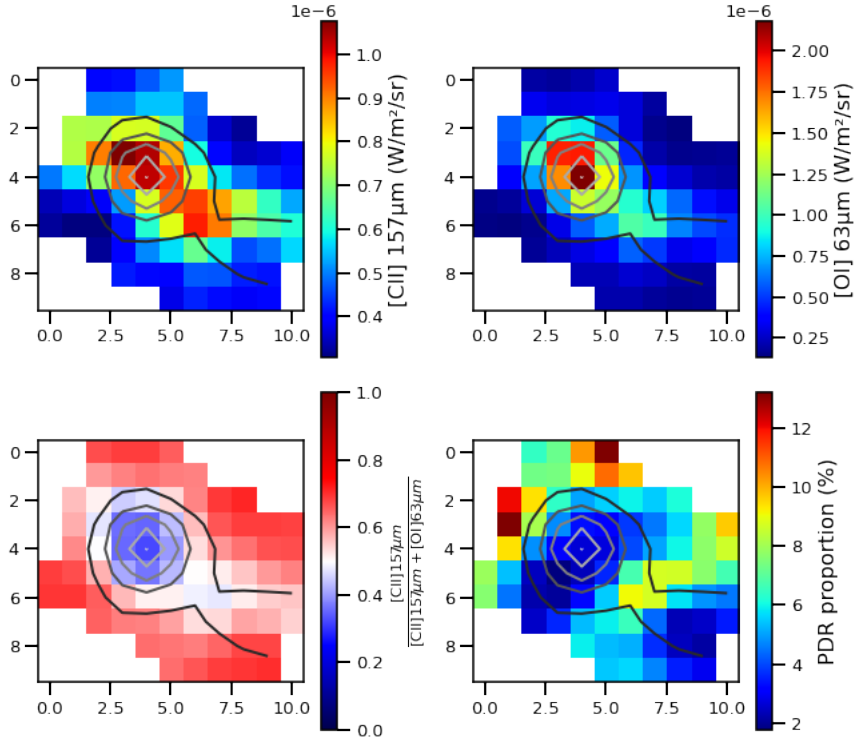

FIGURE 4.41: Similar to Figure 4.35, for the region N160.

(see also Figure 4.45, that compare directly the values of those two ratios for all the regions). When the ratio is low, the PDR proportion is also low, and the H II region is dominates (see

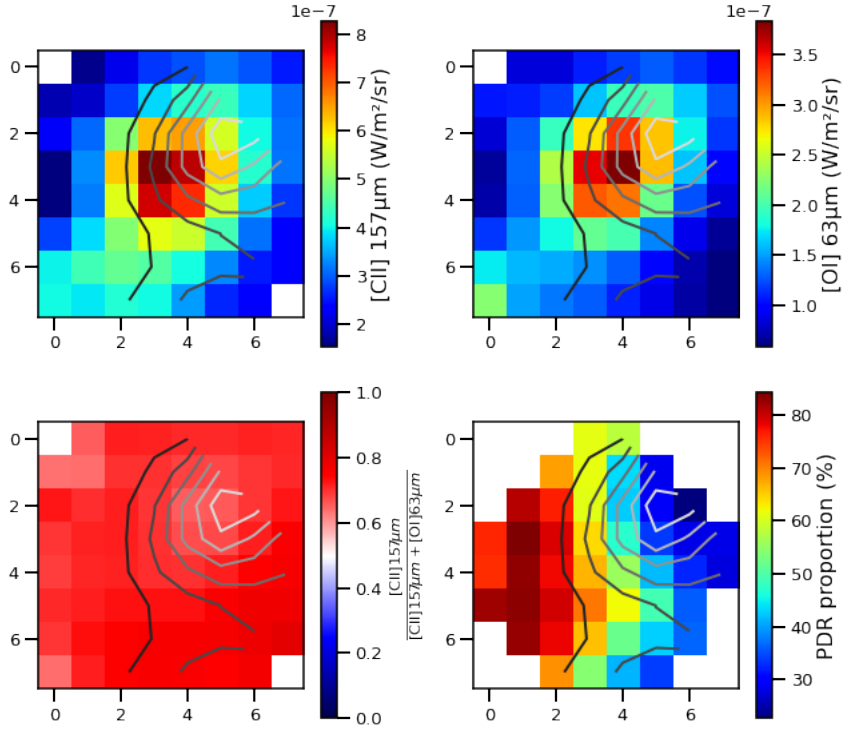

FIGURE 4.42: Similar to Figure 4.35, for the region N44.

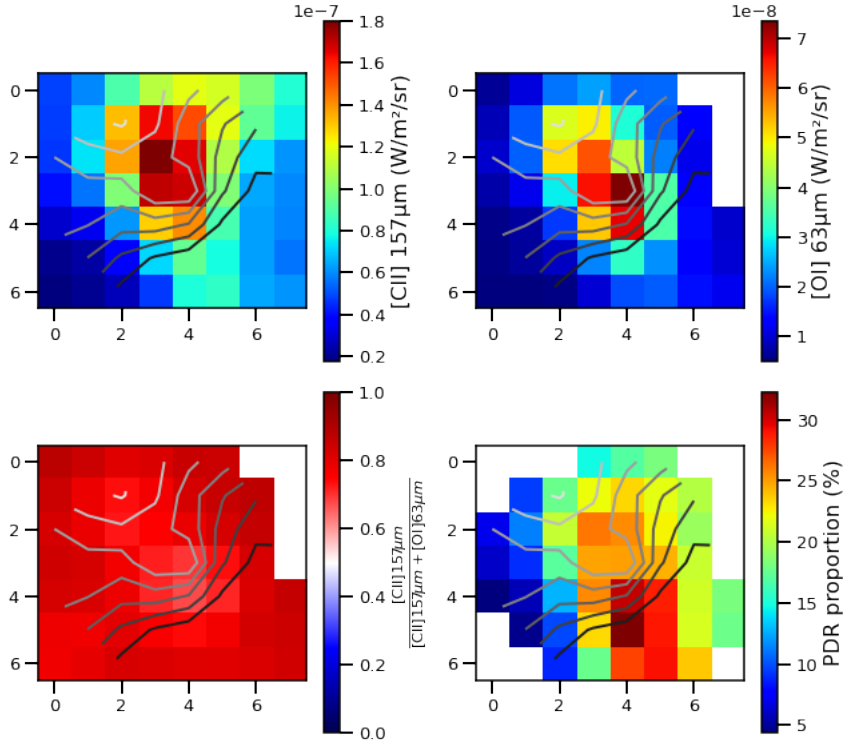

FIGURE 4.43: Similar to Figure 4.35, for the region N180.

e.g., Figure 4.35). When the ratio is high, the PDR proportion is higher and tends toward PDRs dominating (see e.g., Figure 4.38 or 4.42). However we see that even in cases close to those limits,

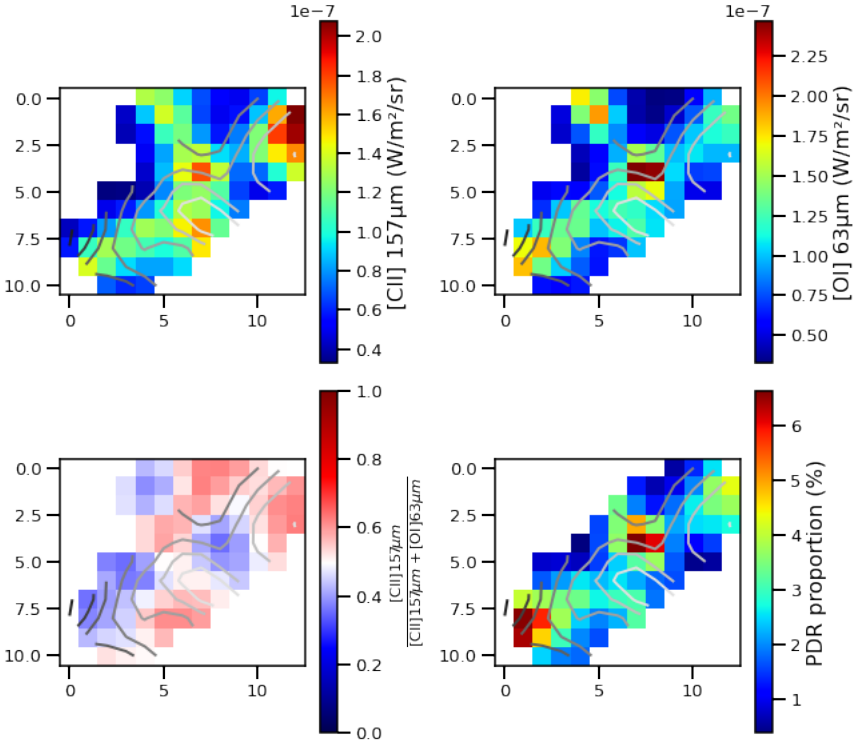

FIGURE 4.44: Similar to Figure 4.35, for the region N66.

the actual interpretation of the ratio [C II]/([C II]+[O I]), and constraining the PDR proportion still needs the use 24μm and 70μm. A more detailed study on the possibility to link that ratio to a fraction of dense and highly illuminated PDRs is made in Section 5.3.

We also see that an increased ratio of [C II] 157μm/([C II] 157μm+[O I] 63μm) can be linked to an increased PDR proportion with Figure 4.45. There is a clear positive correlation between the [C II]/([C II]+[O I]) ratio and the proportion of PDR derived with our method. There is also a spatial correlation of [C II]/([C II]+[O I]) ratio with [O III] (e.g., Figure 4.35, comparing the ratio on lower left panel and the contours). This suggests that PDRs dominated by [O I] emission are spatially associated with ionized gas emission, and with areas where the PDR proportion is low. On the other hand, the pixels with the highest PDR proportion are associated with low emission of [O III] and PDR cooling is dominated by [C II]. Physically, it corresponds to different ways to look through a cloud: pixels that are close to the ionizing source are dominated by the H II region emission, and associated PDRs have very intense UV illumination, thus the [O I] line dominates the cooling of PDRs. When we look further from the sources, there is less and less ionized gas along the line of sight, so the PDR proportion increases, and in the meantime the cooling of PDR gas becomes dominated by [C II] emission.

These results show that this original approach is useful in investigating the spatial distribution of the gas in 3D. It may provide a rough idea of the proximity of the cloud to the ionizing sources, by combining the [O III], [C II] and [O I] lines with the MIPS bands at 24μm and 70μm.

4.4.5 Discussion and caveats

In the previous section, we presented a new method to provide a sense of the distribution of the ISM phases along sight lines in the studied regions. This method is based on a few tracers only: [O III] to trace the ionized gas, [C II] and [O I] to trace PDR gas, and MIPS 24μm and

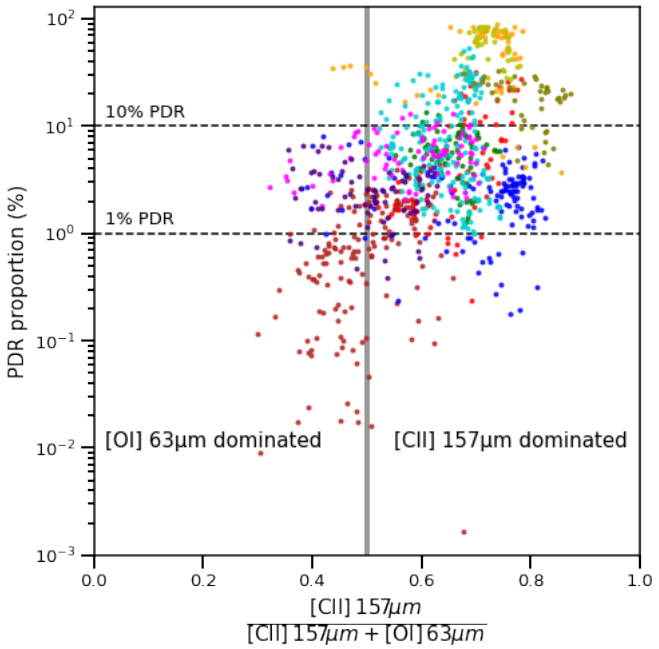

FIGURE 4.45: The relation between the PDR proportion and the ratio [C II]/([C II]+[O I]), for all of the pixels in all of the regions studied here, with the same region color code as Figure 4.1. The 1% and 10% PDR proportions are indicated by the two dashed horizontal lines. The vertical gray line separates regions where cooling is dominated by [C II] (left) and regions where the cooling is dominated by [O I] 63μm (right).

70μm tracing the warm and cooler dust emission. We first demonstrated that 24μm can have a significant contribution from PDR components, not only from the H II regions, as is normally assumed in the literature. The possible 24μm from PDRs can not be neglected. Then, we determined some properties of the star-forming regions, such as the ionization parameter and the density at the illuminated edge of the cloud, which is important to constrain the age of the burst of star formation. Our method also gives access to a new parameter, c_{PDR}, which is described in Section 4.4.1. This parameter allows us to investigate the distribution of gas between H II regions and PDRs along the line of sight in a new and original way.

It is always difficult to investigate the distribution of matter, whether it is spatial distribution or contribution from the different phases of the ISM. A number of studies have been done during the past decades to try to disentangle the geometry and distribution effects. These include, but are not limited to, multi-sector models with different densities, ionization parameters or radiation fields (Cormier et al., 2015); the combination of radiation-bounded and matter-bounded models (Cormier et al., 2015; Polles et al., 2019); the addition of other sources of excitation beyond optical/UV stellar light, such as X-rays (Lebouteiller et al., 2017); as well as the use of a PDR covering factor parameter applied to a standard simulation with H II regions and PDRs (Cormier et al., 2019). Other works attempted to make 3D simulations of turbulent star-forming clouds with a chemical network and self-consistend physical calculations, sometimes by coupling different codes (Röllig et al., 2007; Glover & Mac Low, 2011; Glover et al., 2015; Glover & Clark, 2016; Offner et al., 2014; Accurso et al., 2017a). Despite all these efforts, and many more, there are still degeneracies related to the conditions of star-forming regions. Detailed observations with increased spatial and spectroscopic resolution indeed reveal very high levels of complexity in galactic ISM regions. It helps to understand the global picture when the different phases are studied as an ensemble. However, the tracers used raise different issues, like absorption

(optical/UV, but also self-absorption in some conditions, when viewed through the Milky Way disk, or edge-on galaxies), and extinction effects. The possibility that a single tracer can arise from multiple phases, such as [C II] potentially originating in both PDRs and H II regions, also needs to be accounted for.

The origin of 24μm emission can also lead to ambiguous interpretation as we have seen. As it is usually associated with star-forming regions, the 24μm band is often used directly as a tracer of star-formation regions and of the star-formation rate (e.g., Hao et al., 2011; Kennicutt & Evans, 2012). It is then often implicitly considered as coming from the ionized phase only. Our study demonstrates that it is not the case, and that the origin of the 24μm emission from PDRs should also be considered for a more accurate interpretation. Although 24μm is always associated with star formation (whether because it originates from H II regions and/or PDRs), it is important to keep in mind that significant 24μm emission can arise from PDRs when tackling empirical diagnostic relationships. By comparing the ratios [O III]/24μm and ([C II]+[O I])/[O III], it should be possible to calibrate the relation and derive a correction factor (which would depend on multiple parameters, e.g., the density) to apply to 24μm to separate the contribution of H II regions and PDRs.

One of the interests of this work is that our method relies on IR tracers, that are not normally extinguished nor absorbed in most of the cases (except when there is a Galactic cloud along the line of sight). In particular [C II] and [O III], are among the brightest emission lines for low metallicity dwarf galaxies, and are popular tracers being observed in high-redshift galaxies with ALMA. [C II] 157μm observations have been carried out up to a redshift of z$\sim$6 in the large ALPINE sample of Le Fèvre et al., 2020 and associated studies, Carniani et al., 2020, or even at z$\sim$7 or higher with Hashimoto, 2020. Likewise, the [O III] 88μm line has been detected at z$\sim$7 (e.g. Hashimoto, 2020).

The origin of the [C II] 157μm line can be uncertain, more so in high metallicity galaxies. It can be emitted by both neutral and ionized gas as it requires 11.3 eV to create [C II] and 24 eV to ionize it, but particularly in low metallicity galaxies the contribution of ionized gas is often small (typically less than 30%, Cormier et al., 2019). Thus, our models are consistent with that found in low-metallicity galaxies, and our new method would certainly be convenient to derive a picture of the physical conditions in distant low-metallicity galaxies, where these few tracers already exist.

In particular, our method gives an insight into the distribution of the different phases, allowing us to estimate physical conditions on a global scale and potentially on smaller scale, and it gives a preliminary indication of the geometry of the regions, and models that can represent it (matter-bounded, radiation bounded or the presence of additional PDRs). There are, however, caveats to keep in mind when using this method to probe PDR distributions, that we detail here.

First, we assume that in a given pixel the different phases (H II regions, PDR and neutral gas) have the same physical conditions, in particular the same density at the illuminated edge of the cloud and the same ionization parameter. Considering that the ISM is clumpy, it is not highly probable that all of the clumps along the line of sight have the same density, or the same illumination conditions. The assumption of constant pressure through all the models can also be criticized. The density profile may be more complex than these simple assumptions, and other effects can disturb the assumed equilibrium (winds, steps in pressure, turbulence, flows, etc.).

Another caveat is that our models are computed up to A_V of 2.5. This leads to very high densities (up to a few 10^6 cm^{-3}) in the PDR, which induce strong [C II] and [O I] emission. It is probable that not all of the PDRs attain those high depths, and an investigation of different final cuts of the model have to be taken into account eventually.

Bringing more diagnostic tracers into the modeling scheme may also help to refine the results and make them more robust. *Spitzer* has observed numerous MIR H II region tracers such as [Ne II] and [Ne III], [Si II], iron lines and molecular hydrogen lines, potentially helping further to constrain the conditions in PDRs and H II regions mixed within the telescope beam. *JWST* will eventually bring us a rich array of these tracers, hopefully, also in the Magellanic Clouds. Additionally, velocity resolved observations to separate different clumps and phases, would also bring further information on the phase distributions.

Despite all of these challenges, the method presented here brings a new angle to study and disentangle the emission from the ionized and neutral gas in star-forming regions, with the possibility of application to other unresolved low metallicity galaxies, even at high redshift.

4.5 Summary

In this chapter, we investigated the ionized gas in the resolved Magellanic Cloud sources, and tried to link its gas emission to dust emission by comparing [O III] line to the 24μm continuum band. We found a clear linear correlation in log -log space, which we demonstrated to be a useful tool to make predictions of the [O III] emission to prepare for future observations. This correlation holds on many orders of magnitude, for both spatially resolved and integrated observations. By comparing the fitted correlation of the resolved Magellanic Cloud regions to the DGS observation, we showed that it can be used on unresolved galaxy scales and for wide range of metallicities and distances.

We also created and explored a new diagnostic tool based on the ratio of [O III]/24μm and a ratio that we used to disentangle PDR and H II region emission, namely ([C II]+[O I])/[O III]. This comparison allowed us to estimate some of the physical parameters of the gas, with the use of a grid of Cloudy models with constant pressure, and to obtain new insight into the ISM phase distribution of the gas along the line of sight, which is a common issue in observations, especially those without velocity resolution. Although our approach to estimate the contribution of PDRs and H II regions is very crude, it shows an interesting qualitative agreement with previous studies on some regions in our sample. The use of a new parameter, that we call PDR proportion, gives access to estimations of the matter distribution along the line of sight, and can effectively be linked to a covering factor of PDR.

There are many developments that can be build onto this method. For instance, it would be interesting to see how this comparison behaves on a larger scale than our sample, and on more diffuse emission. To this end, one can rely on observations of more extended regions (like the LMC+ SOFIA program), or on other tracers that show similar behaviour as those we use here. Perhaps the Hα line, if corrected for extinction, could play the role of [O III] here. Estimations of PAHs via broad band emission can give an approximation of the PDR emission but a spectroscopic map would be most useful.

Another interesting path to explore would be the possibility to precisely link the PDR proportion used here in the models to a more physical parameter, like the volume or the mass filling factor of PDRs, through the transformation of the line emission into column density of the different phases.

Having better estimates of the physical conditions or access to diagnostics with higher spatial and velocity resolution to probe the different clouds and clumps along the line of sight, would also be very useful. This could be done by using more spectroscopic tracers, and/or velocity resolved observations.

CHAPTER 5

STUDY OF THE PHOTOELECTRIC EFFECT HEATING PROXIES

Contents

As we now have a better understanding of the distribution of PDRs and H II regions in the Magellanic Clouds, we turn to investigate the properties of the heating and cooling of the PDRs. Determining tracers of the thermal properties of the star-forming gas brings insight into the ISM conditions necessary to form stars, one of which requires cooling of the dense gas. As we have already seen in Chapter 1, IR fine structure lines are often important gas coolants, with the two principal coolants in PDRs being the [C II] 157μm and [O I] 63μm lines. Table 5.1 lists some characteristics of these important FIR cooling lines in PDRs, as well as other MIR lines that may contribute to but not necessarily dominate the cooling. Due to its ionization potential, we see that [C II] 157μm can be emitted in both neutral and ionized gas (11.3 eV to create the specie, 24 eV to ionize it). However, multiple studies show that in low metallicity environment, this line is mostly emitted by neutral gas, with little contribution from the ionized gas, especially at the scale of star forming regions ($\leq$ 30%, with most cases on the order of $\sim$ 10% Cormier et al., 2019). The star-forming gas is the dense gas and the main coolants in the dense gas are CO and dust. However, it is also important to study [CII] and [OI] to understand the heating mechanism in the H I region in order to understand the relationship with SFR and getting the right ingredients when inferring the CO-dark gas.

Here we aim to investigate the properties of the carriers playing major roles in the photoelectric (PE) heating - the primary heating mechanism in PDRs. The primary agents involved in the PE are electrons ejected by UV radiation from PAHs, or dust grains, especially the smallest ones, the very small grains (VSGs). These electrons then heat the gas through collisions of atoms or molecules in dense or diffuse gas (see e.g., Bakes & Tielens, 1994; Weingartner & Draine, 2001b,c;

Line	Wavelength	E.P.	I.P.	ΔE/k	Critical density
	(μm)	(eV)	(eV)	(K)	(cm^{-3})
[C II]	157.64	11.26	24.38	91	50 [e]; 3×10^3 [H]
[O I]	63	–	13.62	228	5×10^5 [H]
[O I]	145	–	13.62	99	1×10^5 [H]
[Si II]	34.81	8.15	16.35	413	1×10^3 [e]; 3×10^5 [H]
[Fe II]	26.55	7.90	16.19	554	1×10^4 [e]; 2×10^6 [H]

TABLE 5.1: Characteristics of the main FIR and MIR cooling lines of the PDRs. E.P. is the excitation potential, i.e., the energy needed to create the specie, where I.P. is the ionization potential, i.e., the energy needed to ionize the specie. For the critical density, the collision partner is indicated (e: electron or H: hydrogen atom) after the value of density.

Tielens, 2008; Croxall et al., 2012). The grain PE heating efficiency is defined as the ratio of the heating of the gas by photoelectrons over the total dust heating (normally via absorption of UV and optical photons). It is usually considered to be the ratio of the FIR line cooling and the dust cooling, defined by the ratio of ([C II]+[O I])/TIR, (Croxall et al., 2012) is an observational measure of the PE efficiency, with the other neutral gas coolants being relatively negligible in normal galaxies. However, this ratio is observed to decrease in galaxies undergoing extreme star formation, such as ULIRGs or starburst galaxies (e.g. Malhotra et al., 2001). Some studies also point out that PAH abundance can have a significant effect on the photoelectric efficiency of the neutral gas, thus explaining part of the decrease of ([C II]+[O I])/TIR, also called the line deficit problem (Rubin et al., 2009; Malhotra et al., 2001; Habart et al., 2001; Brauher et al., 2008). In addition to the interest in PAHs in the role of gas heating, shorter wavelengths, such as 24μm trace warm dust, especially small grains stochastically heated. Longer wavelengths, such as 70μm and 100μm, are better tracers of large grains in thermal equilibrium but can also trace colder dust.

In this work, we will compare the cooling of gas traced by the [C II] and [O I] emission to the PE heating tracers. As we do not have access to spectroscopic observations over the range of the brightest PAH features, we will estimate PAH emission through a photometric calibration (Section 5.1). We will then investigate the PE efficiency proxies, ([C II]+[O I])/PAH and ([C II]+[O I])/TIR, that we will respectively name $\epsilon_{\rm PAH}$ and $\epsilon_{\rm TIR}$ (Section 5.2). Motivated by our results of our observed $\epsilon_{\rm PAH}$, we will then explore the spread of the $\epsilon_{\rm PAH}$ with the ratio of [O I]/([C II]+[O I]) (Section 5.3), and investigate the potential contamination of TIR by other phases than PDRs (Section 5.5.1). Finally, we discuss the different results (Section 5.5) and conclude (Section 5.6).

5.1 Tracers of gas heating

The multiple tracers for the gas heating that we investigate include PAH emission as well as the continuum in three bands, 24μm, which is normally emitted by small grains stochastically heated and large warm grains, 70μm, which is related to dust in PDRs at intermediate temperatures (see Section 4.4.3) and 100μm, which arises from cooler dust grains in thermal equilibrium. We also examine the effect of the carriers traced by TIR emission for the PE efficiency.

5.1.1 Estimating PAH emission from photometric bands

Using the IRS spectroscopic observations to quantify PAHs was not possible since these only exist in small fields within a few of the regions in our sample. In order to have a consistent

measurement in all of our samples, we use the photometric method calibrated by Seok et al. (*in prep*), which uses the limited spatially and spectroscopically resolved observations to calibrate the broad bands from which the PAH bands can be extracted. The spectral range of the IRS spectra were selected so that the integrated value corresponds to the emission in the *Spitzer*/IRAC 8μm band which hosts the two prominent PAH features, at 7.7μm and 8.6 μm (see Figure 5.1). These features represent 25 to 50% of the total PAH emission, depending on the ionization state of the PAHs (Draine & Li, 2000, 2007).

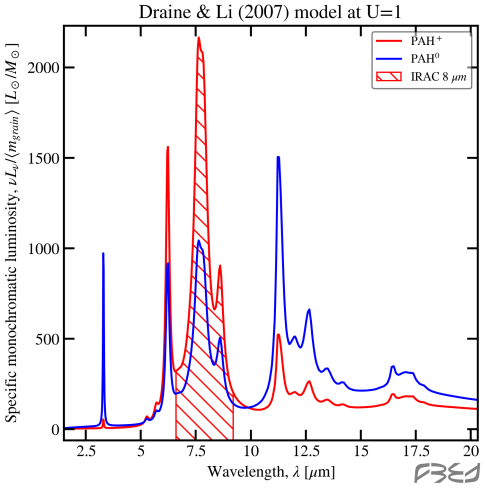

FIGURE 5.1: Spectral PAH features in the NIR-MIR wavelength range, using models from Draine & Li (2007) with an interstellar radiation field of 1 in units of Mathis field (Mathis et al., 1983). The red curve corresponds to charged PAHs, and the blue curve to neutral PAHs. The red hatched area is the emission inside the IRAC 8μm band. Credit of the figure: F. Galliano.

The wavelength range of the spectra is then decomposed with the Bayesian fitting code HerBIE (Galliano, 2018; Galliano et al., 2018b) into four components:

$$I_{8,\mathrm{S}} = I_{8,\mathrm{S}}^{\mathrm{star}} + I_{8,\mathrm{S}}^{\mathrm{dust}} + I_{8,\mathrm{S}}^{\mathrm{lines}} + I_{8,\mathrm{S}}^{\mathrm{PAH}} \tag{5.1}$$

where $I_{8,\mathrm{S}}$ is the spectroscopic equivalent of the 8μm band emission, $I_{8,\mathrm{S}}^{\mathrm{star}}$ is the stellar component of $I_{8,\mathrm{S}}$, $I_{8,\mathrm{S}}^{\mathrm{dust}}$ its dust component, $I_{8,\mathrm{S}}^{\mathrm{lines}}$ its ionic lines component and $I_{8,\mathrm{S}}^{\mathrm{PAH}}$ its PAH component. The first result obtained by Seok et al. (*in prep.*) is that the contribution of lines to the 8μm band is negligible ($I_{8,\mathrm{S}}^{\mathrm{lines}} \sim 0$). This decomposition was applied to six star-forming regions in the LMC (details on Table 5.2) that have both spectroscopic and photometric observations, which are necessary for calibration of the photometric determination of the PAH bands.

To avoid contamination of stellar contribution in the wavelength range of the PAHs, the IRAC 4.5μm band is used to trace the stellar emission instead of the IRAC 3.6μm band used in Marble et al. (2010). The 3.6μm band contains a bright PAH feature, at 3.3μm, which thus can contaminate the estimated stellar emission. The dust contribution to the longer wavelength range of the IRAC 8μm band was estimated with the MIPS 24μm band. A linear fit of the relation between the spectroscopically estimated components and the tracers chosen gives:

$$\begin{cases} I_{8,\mathrm{S}}^{\mathrm{star}} &= \alpha \times I_{4.5} \\ I_{8,\mathrm{S}}^{\mathrm{dust}} &= \beta \times I_{24} \\ \alpha &= 0.392 \pm 0.001 \\ \beta &= 0.0241 \pm 0.0005 \end{cases} \tag{5.2}$$

No.	Region	Center
1	DEM L8 (N4)	04h52′06.31”, −66°55′27.1”
2	DEM L10 (N79)	04h52’11.90”, -69°20’43.1”
3	DEM L34 (N11)	04h56’50.09”, -66°24’50.0”
6	DEM L86 (N105)	05h09’55.99”, -68°54’03.2”
8	DEM L243 (N63)	05h35’31.10”, -66°02’38.8”
10	DEM L323 (N180)	05h48’52.39”, -70°03’51.5”

TABLE 5.2: LMC regions sample used to calibrate the photometric estimation of PAH emission. The missing numbers in the first column correspond to regions that have no usable spectroscopic data, but are used to verify if the integration of spectroscopic data to mimic the IRAC 8μm band is corresponding well to the real IRAC observations.

with $I_{4.5}$ and I_{24} the band emission of IRAC 4.5μm and MIPS 24μm respectively. The fits made on the data for those two components are represented in Figure 5.2. We see that the relation between $I_{4.5}$ and $I_{8,\mathrm{S}}^{\mathrm{star}}$ (left panel) is very tight, where the relation between I_{24} and $I_{8,\mathrm{S}}^{\mathrm{dust}}$ (right panel) exhibits more scatter.

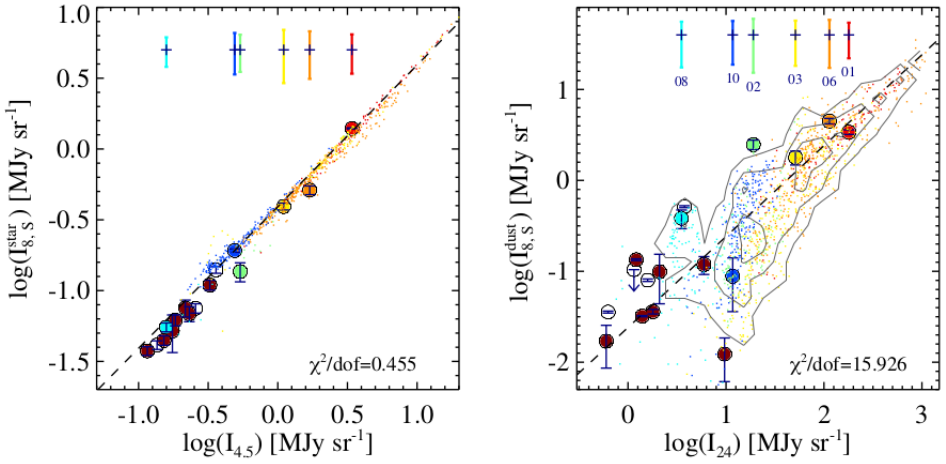

FIGURE 5.2: Left panel: the correlation of the fitted stellar light ($I_{8,\mathrm{S}}^{\mathrm{star}}$) with IRAC 4.5$\mu$m band ($\mathrm{I}_{4.5}$); right panel: the correlation of fitted dust emission ($\mathrm{I}_{8,S}^{dust}$) with MIPS 24μm band (I_{24}). The color coding corresponds to the different regions of the Magellanic Clouds where the limiting IRS spectra exist, with their corresponding typical error bars on the top of the figure. The dashed lines are linear fits between the two values. Small points correspond to values for each pixel separately, and larger circles correspond to values integrated over each region. Figure from Seok et al. (*in prep.*)

Using the fitting results, the calibration to obtain the PAH emission is then:

$$I_{8,\mathrm{P}}^{\mathrm{PAH+lines}} = I_8 - \alpha \times I_{4.5} - \beta \times I_{24} \tag{5.3}$$

Comparison of the fitted PAH bands from photometry with the spectroscopically determined values is represented in Figure 5.3. The smaller points are the values for each pixel separately, and larger circles are the values for the integrated emission for each region. We notice that the calibration gives slightly different results when applied to each pixel separately from when applied to value integrated on the whole region.

This method has allowed us to create a map of the PAH estimation in the IRAC 8μm band for the whole of the LMC and SMC, using the SAGE observations (Meixner et al., 2006). We then

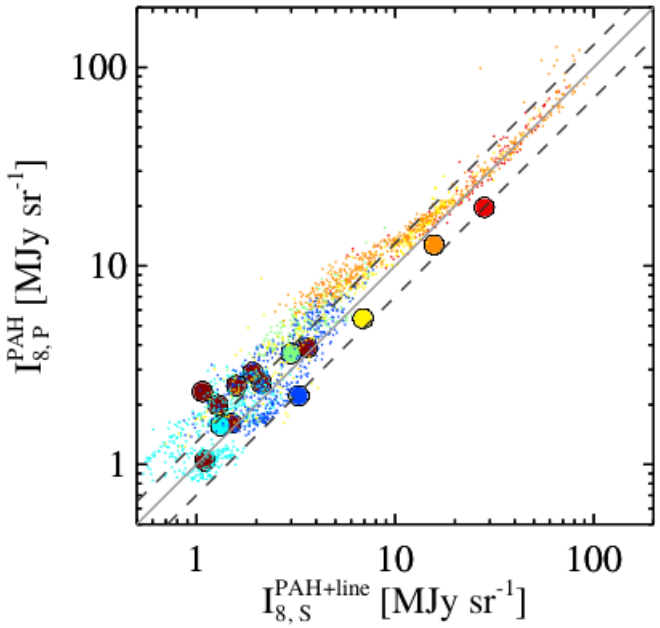

FIGURE 5.3: Correlation between the PAH emission derived from photometric data ($I^{PAH}_{8,P}$) and the emission obtained by fitting the spectroscopic data ($I^{PAH+line}_{8,S}$). The solid line corresponds to the one to one relation, and the dashed lines to a 30% variation. Color and size coding are similar to Figure 5.2. Figure from Seok et al. (*in prep.*)

took cutouts of the full maps to obtain the spatial distribution of PAHs for the different regions in our sample. The PAH maps were then convolved to 12" and 18" to match the resolution of [C II] 157μm and MIPS 70μm respectively, and reprojected on a grid of 12" pixel size, in order compare with other observations.

5.1.2 Estimating TIR from MIR to FIR broad bands

In addition to investigating PAHs as a source of gas heating, we look into the carriers of TIR emission as another potentially important source. TIR emission is the total flux integrated from 3μm to 1100μm (Helou et al., 1988). However, using the integrated value on such a large range requires numerous observations, so TIR is often approximated by using continuum band emission. Calibrating the use of multiple MIR to FIR bands together Galametz et al. (2013) constructed estimators of the TIR flux for many combinations of the different observational bands available with *Spitzer* and *Herschel* telescopes. In the following work we use their calibration based on MIPS 24μm, MIPS 70μm and PACS 100μm fluxes:

$$F_{\rm TIR} = (2.162 \pm 0.113)\ F_{24} + (0.185 \pm 0.035)\ F_{70} + (1.319 \pm 0.016)\ F_{100} \qquad (5.4)$$

with F the flux values (W/m^2) for the individual bands. We will attempt to estimate the fraction of each band and TIR arising from PDRs, in order to use them as PE heating tracers. Since we know that the 24μm band is partly emitted by the H II regions (see Chapter 4), we will use it to determine the effect of contamination from the ionized gas, and compare with other tracers that are expected to be mainly emitted in PDRs.

Now that we have described the tracers we use for the heating of the gas, and the way they were obtained, we will compare their emission to the emission lines of the two main coolants, the [C II]

and [O I] to determine if PE is the dominant heating mechanism and, under the assumption that the ISM has reached thermal equilibrium, to investigate the PE heating efficiency from PAHs and VSGs (Croxall et al., 2012).

5.2 Test of the different heating tracers

We examine the behaviour of the ratio of the cooling line emission over the different tracers of heating in our individual sources. Lebouteiller et al. (2012a, 2019) found that PAHs are a better tracer for heating in N11B than TIR. The ratio of ([C II] 157μm+[O I] 63μm)/PAH was flat with PAH, while the ratio of ([C II] 157μm+[O I] 63μm)/TIR decreased with increasing TIR. However, this study focused only on one region in the LMC. Thus, here we expand it to our larger LMC and SMC sample.

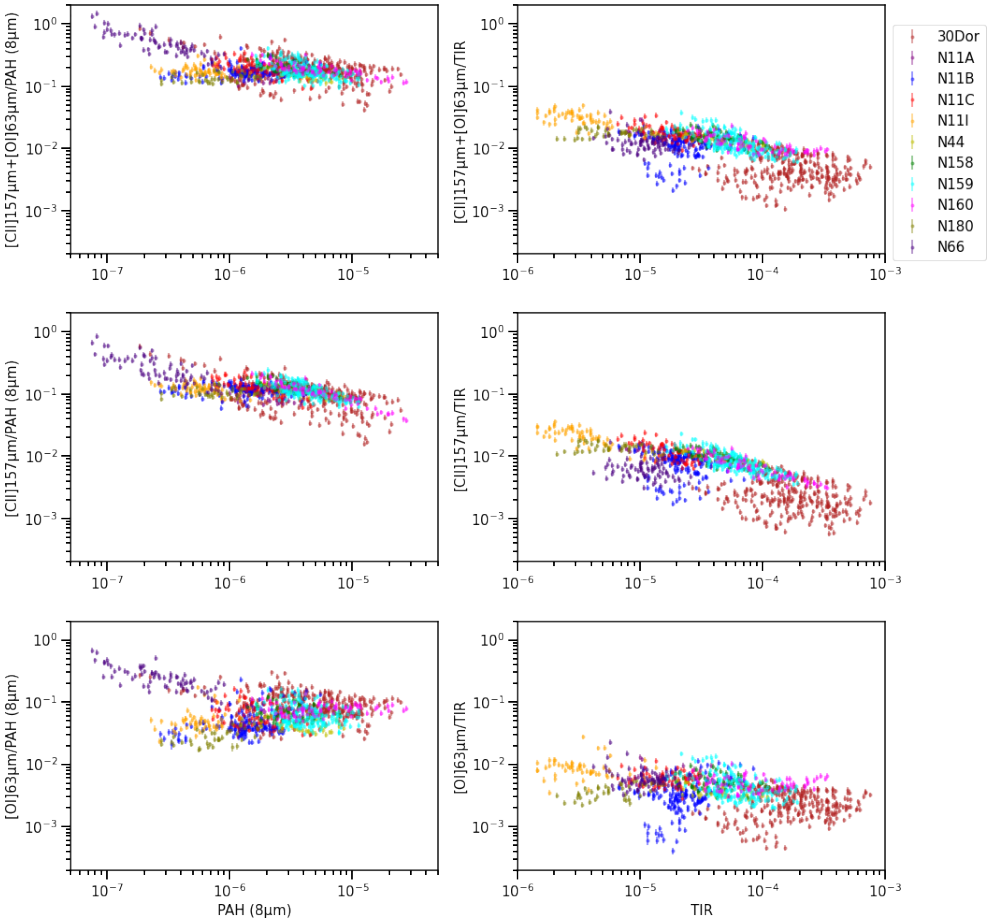

FIGURE 5.4: The ratio of the cooling lines over the two main tracers of gas heating: PAHs as the main tracer of gas heating (left) and the TIR emission (right) as the main tracer of the gas heating. When PAHs are considered the dominant gas heating, the SMC region N66 (the lowest values of PAH fluxes) appears to exhibit different behaviour from the LMC regions, that otherwise have a relatively flat ratio of $\epsilon_{\rm PAH}$ as a function of PAH emission over 2 dex in PAH emission.

Total gas cooling ([C II]+[O I]) We see in Figure 5.4 (upper left panel) that the ratio of $\epsilon_{\rm PAH}$ is flat over almost two orders of magnitude of PAH emission for all our LMC regions (that

is, not including the SMC N66 region), with a value of the ratio of ∼0.2. Considering that the PAH emission in the IRAC 8μm band accounts for around half of the total PAH emission, this value is in very good agreement with Lebouteiller et al. (2012a) where they find a global value for the ratio $\epsilon_{\rm PAH}$ around 0.1, and the global behaviour is coherent with findings from Croxall et al. (2012), Sutter et al. (2019) and Lebouteiller et al. (2012a, 2019), where they compare the [C II] emission arising from neutral gas with the PAH emission. N66, which is the only SMC region in our sample, however, shows a low emission of PAHs and is offset from the LMC sources with a clear decrease of the ratio $\epsilon_{\rm PAH}$ with increasing PAH emission. However, a careful investigation reveals that some pixels in 30 Doradus that exhibit values for $\epsilon_{\rm PAH}$ similar to that found in N66, having a similar decrease of PE proxy with increasing PAH intensities. Thus, the global differences (e.g., the metallicity) between the LMC and the SMC are probably not the only cause of the difference between N66 and the other regions in our sample.

The generally low PAH emission throughout N66 can be partially due to the SMC metallicity, which is lower than LMC metallicity ($Z_{\rm SMC}$=1/5$Z_\odot$, $Z_{\rm LMC}$=1/2$Z_\odot$): lower metals can mean a lower abundance of PAHs, and thus a decreased emission from those molecules. However, this effect alone can not explain the behaviour of $\epsilon_{\rm PAH}$ with PAH emission, as a decrease in metal abundances would also affect the emission of [C II] and [O I] emission. The hard radiation field in N66, comparable to that found in 30 Doradus, can also destroy PAH molecules, reducing their emission (Tielens, 2008; Rubin et al., 2009; Lebouteiller et al., 2011; Whelan et al., 2013). The production of the PAH molecules can also be affected by many factors, like the global temperature or the quantity and size distribution of dust. Thus, PAHs may not be the main carriers of heating mechanism in N66, and the heating may be involving other processes. There can be PE heating linked to VSGs, or even to larger grains, that would enhance the temperature of the gas, and the cooling by [C II] and [O I] lines without affecting PAHs. As the N66 region is actively star-forming and very complex, other heating processes could be investigated, such as the presence of shocks.

On the other hand, the ratio $\epsilon_{\rm TIR}$ (upper right panel) shows a systematic decrease with increasing TIR for all of the regions overall. We deduce that TIR, in our sample, is not as good as PAH emission in tracing the heating of the gas. This decrease could be linked to a classical issue raised when tracing the PE efficiency; numerous studies have used the [C II] 157μm line as a probe of the gas cooling, and TIR as a proxy for the gas heating, also finding a systematic decrease of the ratio with increasing TIR (e.g., Malhotra et al., 2001; Croxall et al., 2017; Herrera-Camus et al., 2018; Sutter et al., 2019). Different explanations have been raised, including:

1. [C II] is optically thick or absorbed by dust in galaxies with high IR emission
2. an increased radiation field would ionize C^+ into C^{++}; this explanation is often associated with AGN activity, but the energy needed is only 24.4 eV, which can be attained in star-forming regions
3. the thermalization and saturation of [C II] in warm and dense PDRs, where [O I] dominates the heating
4. in highly irradiated regions, FUV emission from young stars is absorbed before escaping through the PDR
5. VSGs become charged, and thus the energy needed to photo-eject an electron is higher, diminishing the heating of the gas

6. the TIR emission is coming from a mixture of different phases, including the PDRs, inducing a contamination of the TIR emission by the other phases

In our case, we take into account the [O I] emission in the cooling tracers, thus ruling out the possibility of (3) (this consideration, however, will be interesting to look into, later). The possibility of extinction or absorption (1) is also not probable, considering that such an attenuation is not seen in the ratio with PAH (upper left panel). The same reason would also dismiss the possibility that C^+ is ionized into C^{++} (2), or that the FUV emission does not reach through the PDR (4). The possible contamination (6) will be studied in Section 5.4. The last possibility left (5), that VSGs could loose efficiency at heating the gas due to increased charge, can not be tested here. If PAHs are dominated by neutral molecules, we may see a different behaviour with VSGs, but it would need more detailed observations of the PAHs to investigate this possibility, with spectroscopically resolved observations and studies of the different PAH bands.

Individual cooling lines We now consider the two main PDR cooling lines separately. Ratios using [C II] and [O I] relative to the gas heating by PAHs or TIR are displayed in Figure 5.4 (middle panels and lower panels, respectively). We see that [C II]/PAH decreases with increasing PAH flux, where [O I]/PAH, aside from N66, increases somewhat as PAH flux increases. The two ratios show an important scatter, but in the LMC sources only, the [C II] emission dominates up to a PAH flux of a few 10^{-6} W/m^2/sr, beyond which [O I] becomes dominant. All of the N66 region deviates from the main relation, especially in the [O I]/PAH behavior. Moreover, the slope of N66 data is similar for all of the three ratios: ([C II]+[O I])/PAH, [C II]/PAH and [O I]/PAH. The behaviour of the ratios [C II]/PAH and [O I]/PAH in our LMC sample is similar to that found in Lebouteiller et al. (2012a, 2019). This behaviour is coherent with one of the reasons above proposed to explain the [C II] deficit, in which the [C II] line thermalizes and saturates, leading to the dominance of [O I] for the cooling: conditions in the PDRs are not fully homogeneous, and the [O I] is dominant in dense and warm PDRs, highly illuminated and thus close to the ionizing source (Kaufman et al., 1999, 2006), while [C II] dominates the cooling in less dense and/or less illuminated PDRs, located further away from the source (Wolfire et al., 1995, 1990). In Figure 5.4, we see that the ratio [C II]/TIR shows a strong decrease, which is even steeper than that for the ratio ([C II]+[O I])/TIR. On the other hand, the ratio [O I]/TIR is almost flat, showing only a very shallow decrease, a bit hidden by the scatter. These behaviours are coherent with both the ratios of individual cooling lines with PAH emission, and the global decrease of the ratio ([C II]+[O I])/TIR. We can interpret the steeper decrease of [C II]/TIR as a combination of the global decrease of the ratio with the two cooling lines, plus the fact that [O I] is the dominant cooling line for higher TIR values. The shallower slope for [O I]/TIR is also pointing toward the same explanation.

We have seen two interesting effects in our data. Judging from the spread and the slopes of the plots in Figure 5.4, we think that $\epsilon_{\rm TIR}$ is not a good proxy for PE heating, and considering the possible explanations mentioned earlier, the contamination of TIR by phases other than PDRs is the most probable. There is also a difference in behaviour between our two main cooling lines, which could be linked to the prominence of dense and highly illuminated PDRs in some places of our spatially resolved maps. We will further investigate those two possibilities.

5.3 Spread of the $\epsilon_{\rm PAH}$ ratio

The spread of the $\epsilon_{\rm PAH}$ ratios we see in Figure 5.4 can hold important insights into the gas heating and cooling story. It can be due to observation uncertainties, or to some physical effects,

among which can be the PE efficiency of PAHs. Positively charged PAHs are less efficient in PE heating, as it becomes more difficult to eject an electron (Weingartner & Draine, 2001c). On the other hand, the two cooling lines do not dominate the cooling process under the same conditions, with [O I] tracing dense and/or intense UV-illuminated PDRs while [C II] can trace less dense and/or less illuminated PDRs. However, in those dense and highly illuminated PDRs, the PAH molecules are more easily charged, and thus the PE efficiency is lower in those PDRs. To facilitate discussion, we will call PDR* the denser and/or highly UV-illuminated PDRs and PDR$^\circ$ the less dense and/or less illuminated PDRs. Naively, if [O I] traces well PDR*, the ratio [O I]/([C II]+[O I]) should trace the proportion of PDR* of the total PDRs, and thus the PE efficency proxy, $\epsilon_{\rm PAH}$, should decrease with this ratio.

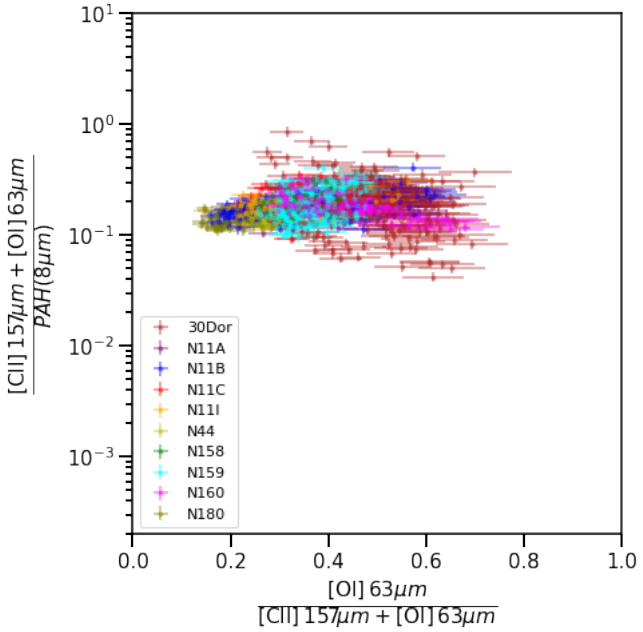

FIGURE 5.5: The ratio of ([C II]+[O I])/PAH, which is a proxy for the PE efficiency, $\epsilon_{\rm PAH}$, as a function of [O I]/([C II]+[O I]).

As we see in Figure 5.5, the PE efficiency proxy, $\epsilon_{\rm PAH}$, is somewhat flat with respect to [O I]/([C II]+[O I]). This behavior could indicate that the dispersion is dominated by observational uncertainties and uncertainties from the PAH emission estimation method, or that [O I]/([C II]+[O I]) is not tracing the proportion of PDR*. We will investigate this last possibility.

We call f* the volume proportion of PDR*, which is the fraction of the volume along the line of sight containing dense PDRs. It is illustrated in Figure 5.6, with an f* value of 0.3 for an example. If we note $F_{\rm OI}$ the total emission of [O I] observed, we can divide it into the part coming from PDR*, noted $F^\star_{\rm OI}$, and the part coming from PDR$^\circ$, noted $F^\circ_{\rm OI}$. If we want to retrieve the fraction f*, we can use a model with two components, describing respectively the dense and/or highly UV-illuminated PDRs, dominated by [O I] emission, and the less excited and/or less dense PDRs, dominated by [C II] emission. It would be necessary to have a precise idea of what can be applied to make the difference between the two types of PDRs, and which limits have to be considered. The emission of the two cooling lines obtained from the models would depend on many other parameters, like the density, the intensity of the radiation field, the pressure, or the magnetic fields. Considering that, the emission of cooling lines from the PDR*, $F^\star_{\rm OI}$ and $F^\star_{\rm CII}$, will be computed on a grid of values for the different parameters within

the limits decided for the dense and/or illuminated PDRs. The emission of the cooling lines for the less excited and/or less dense PDRs, $F^{\circ}_{\rm OI}$ and $F^{\circ}_{\rm CII}$, will be computed on a grid of the same parameters, but with different limits. It would then be possible to search all of the combinations agreeing with the observations :

$$\begin{cases} F_{\rm OI,\,obs} &= F^{\star}_{\rm OI}\, f^{\star} + F^{\circ}_{\rm OI}\,(1-f^{\star}) \\ F_{\rm CII,\,obs} &= F^{\star}_{\rm CII}\, f^{\star} + F^{\circ}_{\rm CII}\,(1-f^{\star}) \end{cases} \tag{5.5}$$

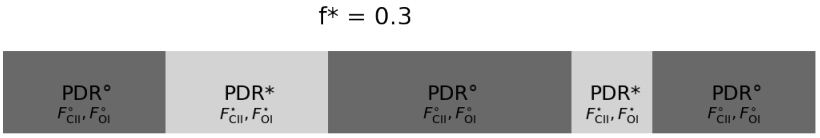

FIGURE 5.6: This figure is an illustration of the proportion in volume filled by dense and/or highly UV illuminated PDRs, that we name PDR*. This fraction is called f*. The more diffuse and/or less illuminated PDR is called PDR$^{\circ}$. The emission from each type of PDR is noted for the first zones defined. $F^{\circ}_{\rm CII}$ and $F^{\circ}_{\rm OI}$ are the emission of [C II] 157μm and [O I] 63μm respectively, arising from PDR$^{\circ}$. The same notations are used for PDR*.

As some parameters may be degenerate, there could be many potential solutions, with different values for f*. The proportion of PDR* can not be directly constrained, except if all of the other physical parameters of the ISM are separately determined, which would require many different tracers. Could the ratio of [O I] 63μm/([C II] 157μm+[O I] 63μm) be a tracer of f*? We will link this fraction to the ratio of observed values with the possible models described earlier.

$$\frac{F_{\rm OI,\,obs}}{F_{\rm CII,\,obs}+F_{\rm OI,\,obs}} = \frac{F^{\star}_{\rm OI}\, f^{\star} + F^{\circ}_{\rm OI}\,(1-f^{\star})}{(F^{\star}_{\rm CII}\, f^{\star} + F^{\circ}_{\rm CII}\,(1-f^{\star})) + (F^{\star}_{\rm OI}\, f^{\star} + F^{\circ}_{\rm OI}\,(1-f^{\star}))} \tag{5.6}$$

If we suppose that $F^{\circ}_{\rm OI} \ll F^{\star}_{\rm OI}$ and $F^{\star}_{\rm CII} \ll F^{\circ}_{\rm CII}$, we obtain:

$$\begin{aligned} \frac{F_{\rm OI,\,obs}}{F_{\rm CII,\,obs}+F_{\rm OI,\,obs}} &\simeq \frac{F^{\star}_{\rm OI}\, f^{\star}}{F^{\circ}_{\rm CII}\,(1-f^{\star})+F^{\star}_{\rm OI}\, f^{\star}} \\ &\simeq \left(1+\frac{F^{\circ}_{\rm CII}}{F^{\star}_{\rm OI}}\left(\frac{1}{f^{\star}}-1\right)\right)^{-1} \end{aligned} \tag{5.7}$$

We see from Equation 5.7 that the ratio we study is much more complicated than a simple probe of the fraction of PDR*. In fact, the [O I] 63μm/([C II] 157μm+[O I] 63μm) would be a tracer of f* if there is a conspiracy to have $F^{\star}_{\rm OI} \simeq F^{\circ}_{\rm CII}$, considering that $F^{\star}_{\rm OI}$ and $F^{\circ}_{\rm CII}$ are the emission from the models with different physical conditions, and those condition vary when

considering different observations. It is thus highly improbable to have a direct tracer of f* with this ratio.

As an example of the degeneracy of f* with the other parameters, we will take two values of f*, and see under which conditions the observed ratios of [O I]/([C II]+[O I]) would be the same. We consider $f^\star_1 = 0.2$ and $f^\star_2 = 0.8$. We give an illustration of those cases in Figure 5.7. Equation 5.7 then gives:

the case 1: $f^\star_1 = 0.2$

$$\begin{aligned} \frac{F_{\mathrm{OI,\,obs,\,1}}}{F_{\mathrm{CII,\,obs,\,1}}+F_{\mathrm{OI,\,obs,\,1}}} &\simeq \left(1+\frac{F^\circ_{\mathrm{CII,\,1}}}{F^\star_{\mathrm{OI,\,1}}}\left(\frac{1}{f^\star_1}-1\right)\right)^{-1} \\ &= \left(1+\frac{F^\circ_{\mathrm{CII,\,1}}}{F^\star_{\mathrm{OI,\,1}}}\left(\frac{1}{0.2}-1\right)\right)^{-1} \\ &= \left(1+\frac{F^\circ_{\mathrm{CII,\,1}}}{F^\star_{\mathrm{OI,\,1}}}(5-1)\right)^{-1} \\ &= \left(1+\frac{4\,F^\circ_{\mathrm{CII,\,1}}}{F^\star_{\mathrm{OI,\,1}}}\right)^{-1} \end{aligned} \tag{5.8}$$

and the case 2: $f^\star_1 = 0.8$

$$\begin{aligned} \frac{F_{\mathrm{OI,\,obs,\,2}}}{F_{\mathrm{CII,\,obs,\,2}}+F_{\mathrm{OI,\,obs,\,2}}} &\simeq \left(1+\frac{F^\circ_{\mathrm{CII,\,2}}}{F^\star_{\mathrm{OI,\,2}}}\left(\frac{1}{f^\star_2}-1\right)\right)^{-1} \\ &= \left(1+\frac{F^\circ_{\mathrm{CII,\,2}}}{F^\star_{\mathrm{OI,\,2}}}\left(\frac{1}{0.8}-1\right)\right)^{-1} \\ &= \left(1+\frac{F^\circ_{\mathrm{CII,\,2}}}{F^\star_{\mathrm{OI,\,2}}}\frac{10-8}{8}\right)^{-1} \\ &= \left(1+\frac{F^\circ_{\mathrm{CII,\,2}}}{4\,F^\star_{\mathrm{OI,\,2}}}\right)^{-1} \end{aligned} \tag{5.9}$$

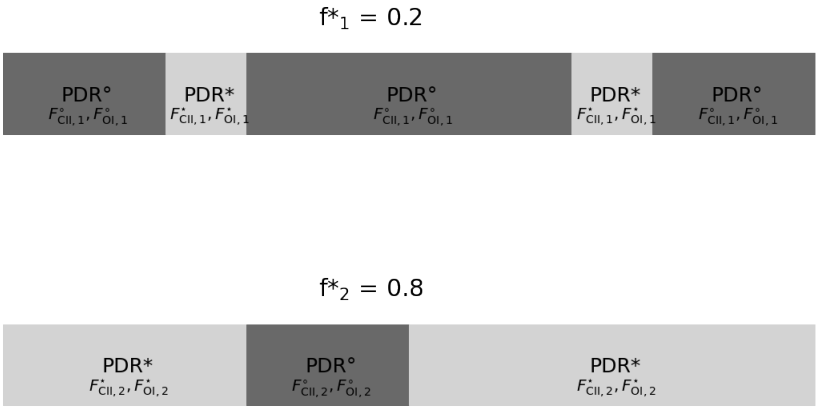

FIGURE 5.7: Similar to Figure 5.6, with two other cases of f*. We chose those values to illustrate possible distributions of PDR* and PDR$^\circ$.

In the two cases detailed in equations above, we can have the same value of [O I]/([C II]+[O I]) ratio if the physical conditions between the two cases change the values of the fluxes of the lines modelled, by a factor of a few. A variation of f* from one extreme to the other can be compensated by a moderate variation of the emissivity of the lines, thus by moderate variations of the physical parameters of PDRs. This indicates that the ratio [O I]/([C II]+[O I]), taken at the scale of a full star-forming region, does not trace well the proportion of PDR*.

We also emphasize that these calculations use the simple assumption that PDRs with the same types also have the same physical conditions. In a more realistic star-forming region, the clouds along the line of sight are probably not sharing exactly the same physical conditions, which further complicates the determination of f*.

5.4 Potential contamination of the PDR tracers with ionized gas phase emission - comparison with models

As we saw in Section 5.2, the emission of the different heating tracers may originate from different phases. To look closer into this possibility, we will compare the PE heating efficiency proxies to the ratio we used to trace the proportion of PDR and H II region, the ratio ([C II]+[O I])/[O III]. We will also use our models with mixed PDR and H II components as described in Section 4.4.1. We examine the range of proportions of PDR in our mix, from 0% to 99%. At a value of 0%, however, the emission of the PDR cooling lines, [C II] and [O I], is very low, as there is little emission before the ionization front. So the behaviour of the modeled ratios of cooling lines with heating tracers shows a strong evolution for the lowest PDR proportion, that can be strongly affected by the hypothesis of the models. Thus, we expect to have a clearly different behaviour that will allow us to discriminate between the constant pressure and constant density models.

5.4.1 Individual broad bands and PDR gas heating

We now inspect the possibility of the individual bands, 24μm, 70μm and 100μm, to trace the PDR gas heating. We display the ratio of the cooling lines over 24μm as a function of the ratio ([C II]+[O I])/[O III] (Figure 5.8). We know from our previous study in Chapter 4 that the 24μm band is mostly emitted by ionized regions. The behaviour of this ratio should then provide indications of ionized gas contamination in the PDR tracers. There are two trends in the data, one with an increase of cooling lines over 24μm up to ([C II]+[O I])/[O III]$\sim$ 1, and a flatter trend for values greater than 1. This behaviour is in good agreement with constant pressure models, on the left panels. We see that the increasing trend corresponds to PDR proportions that are lower than 50% (middle marker of the lines), thus to models that are similar to a cloud with incomplete PDR. Those are models where the H II region emission is dominant, thus the increasing trend at low values of ([C II]+[O I])/[O III] is a sign of contamination of the band emission by ionized gas. If we have a look at the right panels of Figure 5.8, we see that the constant density models are also agreeing with data, although some of them do not show the increase at low ([C II]+[O I])/[O III] ratio, and are globally flat. From this figure with 24μm as a tracer, we can not distinguish between constant pressure and constant density models, although the constant pressure models seem to correspond a bit better to the data behaviour.

We inspect the ratio of the cooling lines over 70μm as a function of the ratio ([C II]+[O I])/[O III] in Figure 5.9. The first striking result is that the constant density models, displayed in the right panels, are not coherent with all of the data. Thus, the use of MIPS 70μm band is important to discriminate between our models, as we have already seen in Chapter 4. From the constant pressure models (left panels of Figure 5.9), we notice that the data shows a small rise of cooling lines over 70μm at low values of ([C II]+[O I])/[O III]. As noted at the beginning of the section, this corresponds to models with low PDR proportions. Thus it indicates that the 70μm band also contains contamination from ionized gas, although it is much less significant than for the 24μm band, which is largely emitted by H II regions. Another noticeable result is that models to constrain [O I]/70μm and ([C II]+[O I])/70μm are much more densely packed than models

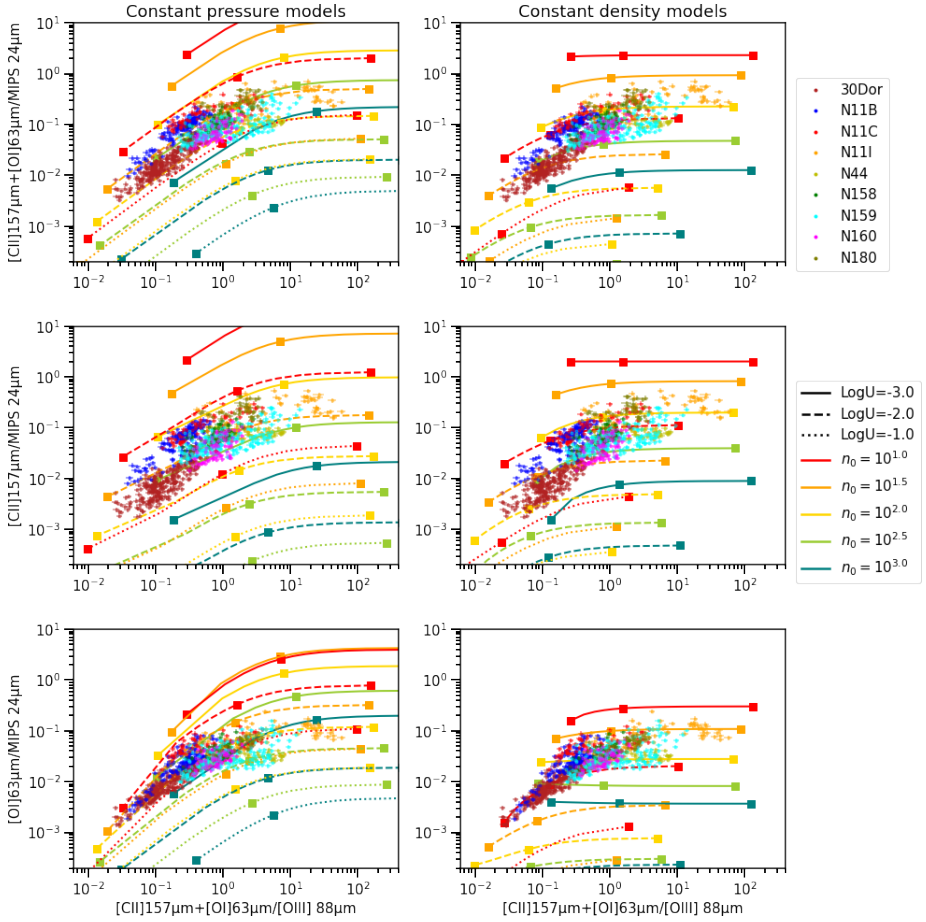

FIGURE 5.8: The ratio of ([C II]+[O I])/24μm as a function of the ratio we use to disentangle the PDR emission from the ionized region emission, namely ([C II]+[O I])/[O III] (upper panels), and the ratio of each cooling line over MIPS 24μm separately, in middle and lower panel. On the left panels, data are superimposed with the constant pressure models, and on the right panel with constant density models. Models are represented with different proportions of PDR along each line, with the markers to indicate some specific values: 0%, 50% and 99% from lower to higher values of ([C II]+[O I])/[O III].The line colors designate different densities and the line types different log(U), all described in the legend to the right of the plots.

for [C II]/70μm, making it more difficult to discriminate between models. Most of the displayed models can at least partly fit the data. These results demonstrate that investigations involving the [C II] line alone are thus necessary to be able to discriminate some of the models.

In Figure 5.10, we investigate the potential contamination of the PACS 100μm band by ionized region emission. When attempting to constrain the TIR with only one band, the 100μm band has been shown to most closely define the TIR (Lebouteiller et al., 2012a; Galametz et al., 2013). As is also evident in Figure 5.9, we see that the constant density models are not able to fit the data (right panels of Figure 5.10). In some of the constant density models, especially at intermediate values of ionization parameter (log(U)=-3), there is even a drop in the cooling lines over 100μm for increasing ([C II]+[O I])/[O III] until ([C II]+[O I])/[O III] ~1,where it levels off and remains flat. This difference in behaviours between constant pressure and constant density models was expected, as we noted in the beginning of the section. The constant pressure models seem to explain the data better (left panels of Figure 5.10), and there is again an increase of the cooling lines over the PACS 100μm band for low values of ([C II]+[O I])/[O III]. This increase

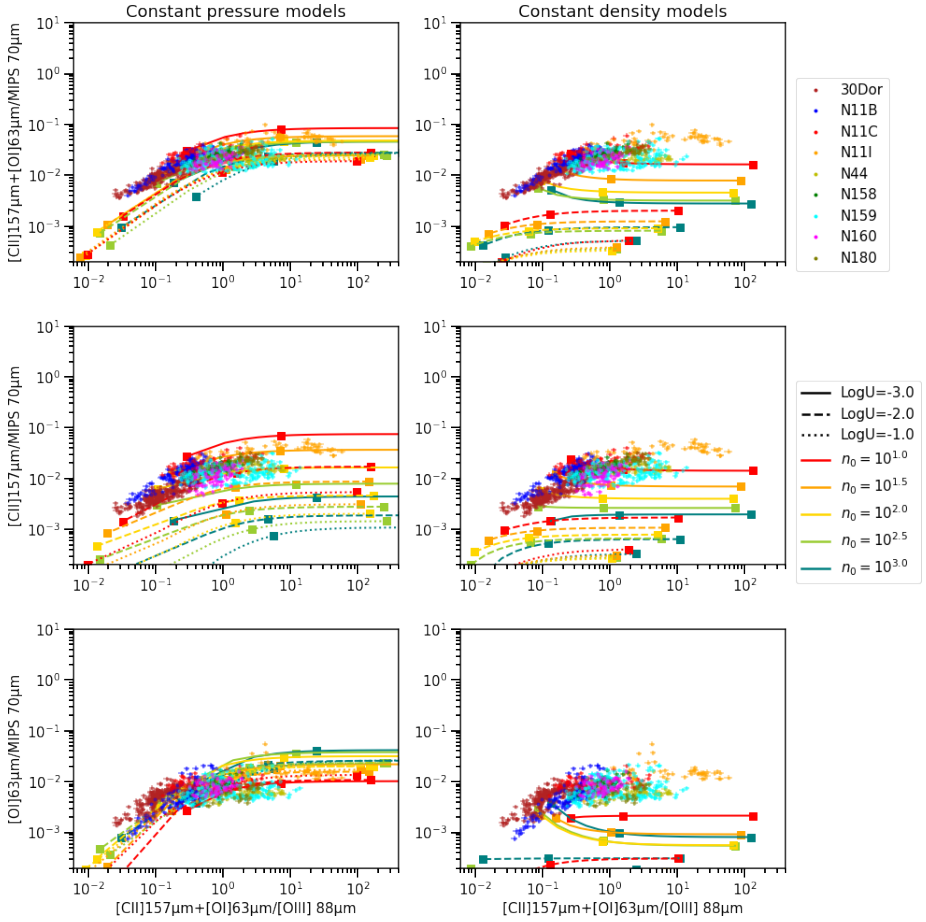

FIGURE 5.9: Similar to Figure 5.8, by replacing the band MIPS 24μm by the MIPS 70μm band.

is also seen in the models at low proportions of PDRs. The PACS 100μm band is thus also contaminated by emission from the H II regions, although this contamination is lower than for all of the other bands. We also notice that models for the ratio ([C II]+[O I])/PACS 100μm are tighter than for the ratios using one of the cooling lines separately, thus it is difficult to discriminate between some of the models.

5.4.2 Use of TIR to trace PDR gas heating

In Figure 5.11, we show the ratio of cooling lines over TIR, as a function of the ratio ([C II]+[O I])/[O III]. The TIR of the data was calculated in Section 5.1.2 by using the MIR and FIR broad bands. We see that there is a contamination of TIR by emission from the ionized phase. Moreover, this contamination is stronger than that found with PACS 100μm band alone, which was the less affected tracer. We also notice this trend in the behaviour of the models. We note that the TIR of the models is not calculated in the same way we do with the formula of Galametz et al. (2013), but is obtained by integrating the IR emission in the models between 3μm and 1100μm. By comparing the TIR calculated on the whole range of IR emission to the TIR approximated with the different bands for our data, we ensure that the behaviour we see, especially at low value of ([C II]+[O I])/[O III], is not an artifact due to the estimation of TIR from incomplete observation of the wavelength range.

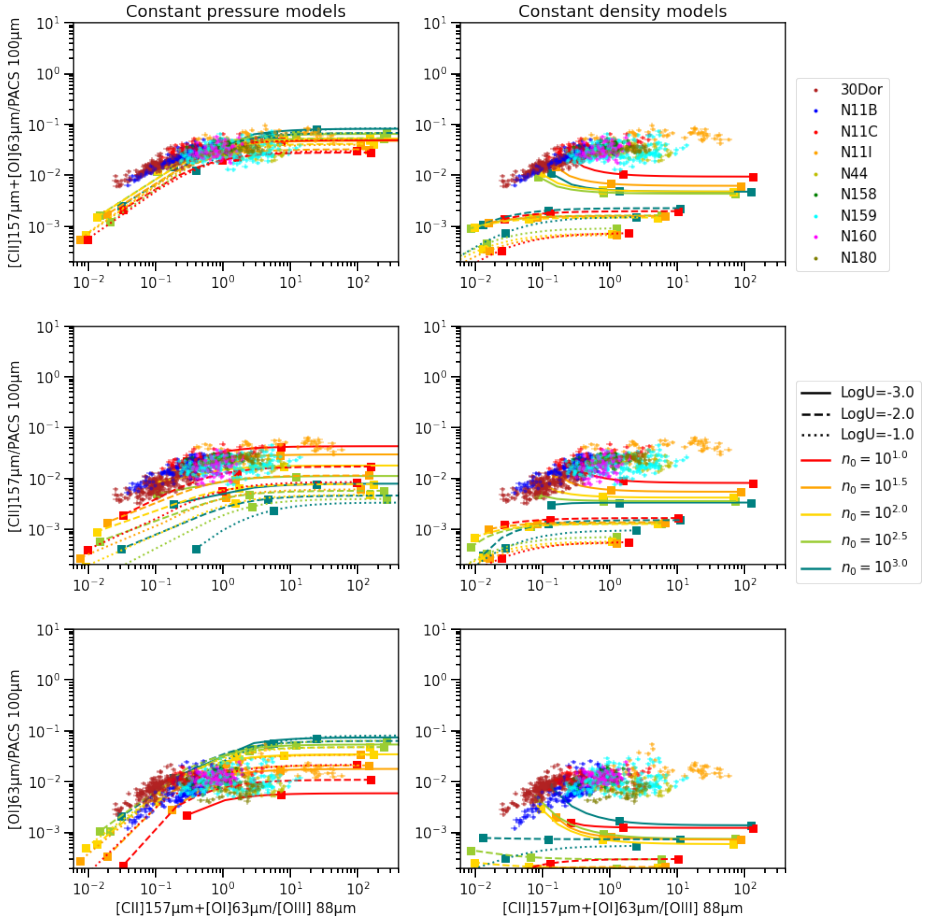

FIGURE 5.10: Similar to Figure 5.8, by replacing the band MIPS 24μm with the PACS 100μm band.

Taking into account the contamination of TIR by the ionized gas is important to be able to compare to the PDR cooling lines. An interesting development of this study would be to identify the part of the TIR that is emitted from PDRs exclusively, in order to remove the contamination of other phases. We attempt to make such a correction here. We see that emission is dominated by PDRs where the data present a plateau in $\epsilon_{\rm TIR}$. Thus, this plateau value can be taken in order to estimate the part of TIR emission arising from PDRs, and the turning point in the data can be used to differentiate pixels that are dominated by PDR emission from pixels that are dominated by H II region emission. We roughly estimate the turning point to be at a value of x_0=4×10^{-1} for the ratio ([C II]+[O I])/[O III].

We see in Figure 5.12, that the relation between $\epsilon_{\rm TIR}$ and TIR is much tighter when considering only the pixels dominated by PDR emission. Thus, when no selection is applied, the dispersion is dominated by the contamination of TIR by ionized phase emission. However, there is still a decrease of $\epsilon_{\rm TIR}$ with increasing TIR suggesting that another process may be at play or that there is still some low level comtamination from the ionized phase. It could be a contamination of TIR by phases other than H II regions, or linked to the fact that TIR covers the emission of all types of grains, while the PE heating is due to small grains, for example, or that a physical effect may enhance dust emission, but not affecting the heating of the gas. However, it is not possible for us to push the analysis further here and explore the other possible causes of this

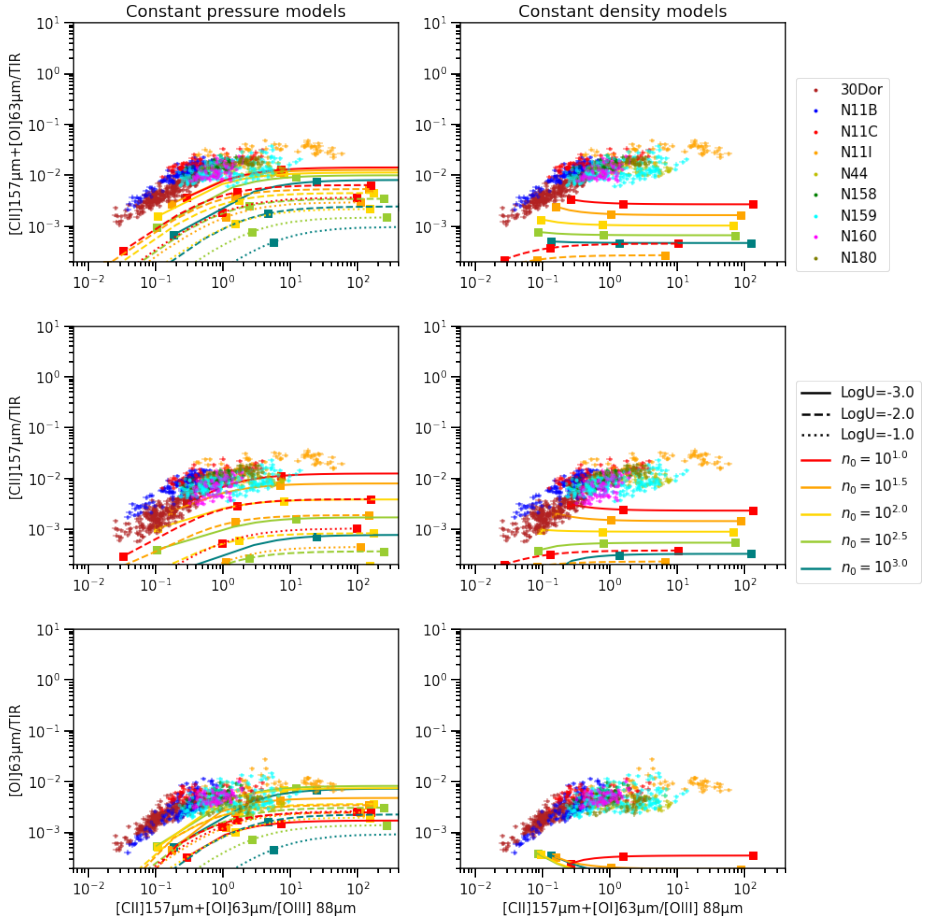

FIGURE 5.11: Similar to Figure 5.8, by replacing the band MIPS 24μm with the TIR emission. The observed TIR is calculated as explained in Section 5.1.2, and the TIR of the models is the emission integrated between 3 and 1100μm.

decrease. Further study on this subject is left for future follow-up.

5.4.3 Use of PAHs to trace PDR gas heating

For completeness, we investigate the relation of the ratio of cooling lines over PAHs with the ratio of ([C II]+[O I])/[O III] (Figure 5.13), using the PAH calibration method described earlier in Section 5.1.1. We notice that the data are globally much flatter than when using the other tracers of gas heating with somewhat of an increase in the spread at low values of ([C II]+[O I])/[O III]. We notice that for the ratios with [O I] only, the constant pressure models do not agree for the full data set whereas global solutions exist for constant density models. The constant pressure models do show characteristic flat profiles, but the plateaus for most of the models lie higher than most of the data. The ratio of [C II]/PAH shows a better agreement between models and data, and the ratio calculated with the modelled values is much flatter, even for low proportion of PDR. The fact that models and data are not in agreement for this ratio can be linked to different reasons. First, the method used to estimate the PAH emission in the IRAC 8μm band is known to result in quite a large spread, and uncertainties in both the method to calculate PAH emission and the bands used have not been taken into account in our study. Moreover, the model calculation of PAH emission may be uncertain: Cloudy assumes that the quantity of PAH

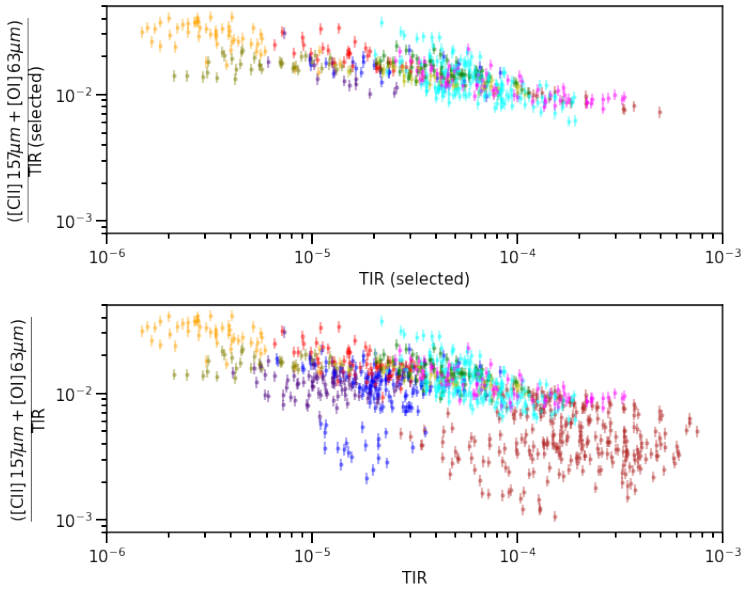

FIGURE 5.12: Upper panel: relation between ([C II]+[O I])/TIR and TIR without pixels dominated by H II region emission. Lower panel: relation between ([C II]+[O I])/TIR and TIR without selection.

molecules directly scales with the column density of H I gas but this is likely more complex (e.g. Rémy-Ruyer et al., 2015). The emission from the two cooling lines, and especially the behaviour before the ionization front, are also strongly affected by the initial conditions and hypotheses, especially if we use constant density or constant pressure models. Despite all of these possible issues, we see that the models still roughly agree with our observations, and we are able to give interesting indications about the physical processes at play in these regions of different gas phases.

By studying the possible contamination by ionized gas emission of all the bands used to construct TIR from our data, the TIR itself and the PAH emission, we first noticed that the models we use do follow the overall observational trends. In some cases, it would even be possible to deduce a range of possible values for the physical parameters. We also notice that the observed ratio of ([C II]+[O I])/[O III] shows little contamination from PAH emission (Figure 5.13), making the PAHs, in principle, excellent tracers of gas heating in PDRs.

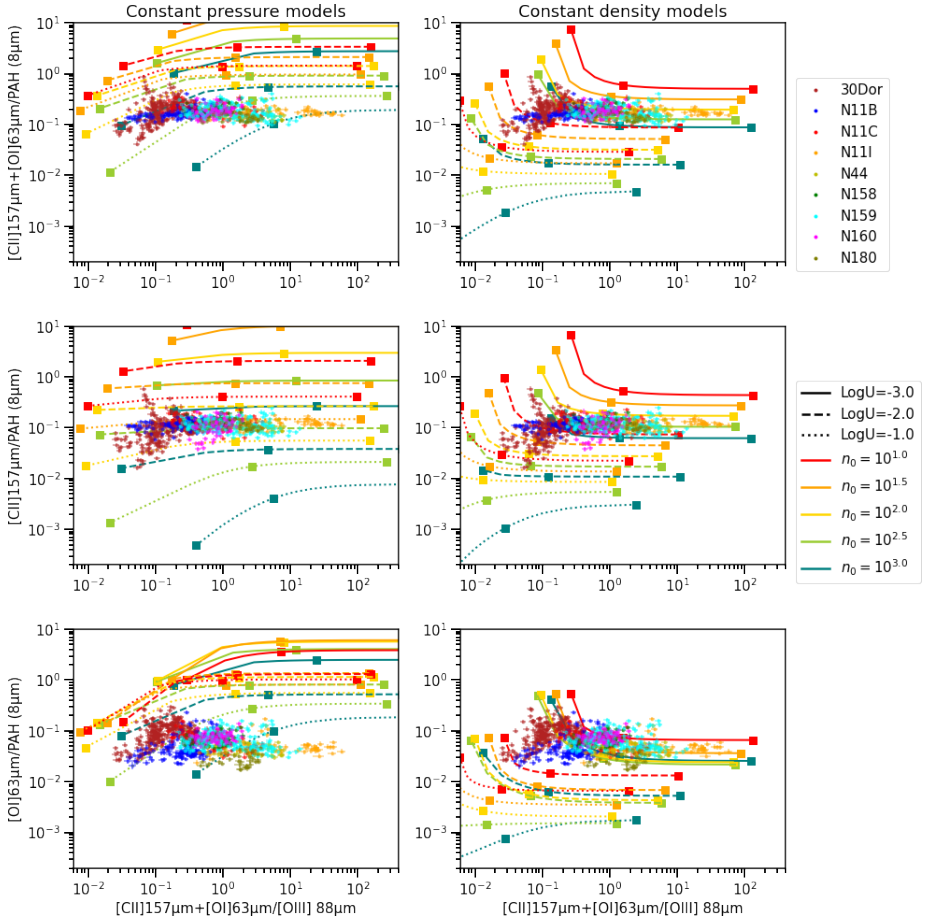

FIGURE 5.13: Similar to Figure 5.8, but replacing the band MIPS 24μm by the PAH emission as described in 5.1.1.

5.5 Discussion and prospects

In Section 5.5.1, we discuss the link between the TIR contamination by the ionized phase and the [C II] deficit. Then, we discuss in more detail the PE heating efficiency in Section 5.5.2. Finally, we inspect the behaviour of N66 in Section 5.5.3, as this region, our only sample from the SMC, can show different behaviour from the LMC regions.

5.5.1 TIR contamination and comparison with IR colors

Our data shows a deficit of the cooling line emission with respect to TIR emission, for increasing TIR (Section 5.2, Figure 5.4, right panels). The three ratios studied, ([C II]+[O I])/TIR (also called $\epsilon_{\rm TIR}$), [C II]/TIR and [O I]/TIR, show somewhat different behaviour: [C II]/TIR ratio has a steeper decrease with respect to increasing TIR than ([C II]+[O I])/TIR, and [O I]/TIR which have a shallower decreasing rate as TIR increases. This difference can be explained by the fact that [O I] dominates the cooling in dense and/or highly-UV-illuminated PDRs while [C II] dominates the cooling in less dense and/or less UV-illuminated PDRs (Kaufman et al., 1999, 2006; Wolfire et al., 1990, 1995). However, this behaviour of the individual PDR tracers does not explain the decrease of $\epsilon_{\rm TIR}$ with increasing TIR. Thus, we investigated the possibility that emission from the ionized phase contaminates the PDR heating tracers we use (Section 5.4).

The two PDR cooling lines, [C II] and [O I], emit only in PDRs ([C II] contamination is ≤30% at our metallicity, see Cormier et al., 2019) and oxygen is ionized in H II regions (Table 5.1). In Section 5.5.1, we showed that TIR is partly emitted by the ionized phase. We used the results in Figure 5.11 to flag pixels where the TIR is contaminated, and removed them (Figure 5.12). The spread of the relation between $\epsilon_{\rm TIR}$ and TIR is controlled by the contamination of TIR by ionized phase emission. The decreasing trend, however, is still present, although weaker.

We now compare our results to the findings of Sutter et al. (2019). They focus on the [C II] deficit problem, by comparing the ratio [C II]/TIR to the IR colors of the galaxies of the KINGFISH sample (Kennicutt et al., 2011), using the ratio of $\nu\, f_\nu(70)/\nu\, f_\nu(160)$. Most of the galaxies in this sample have metallicities higher than those of the Magellanic Clouds. The interest of this comparison is that the dust emission and temperature are often traced by IR colors; a higher ratio of 70μm/160μm corresponds to hotter dust, with enhanced emission at lower wavelengths contributing to the 70μm band. For their 70μm and 160μm bands, they use the PACS photometric observations while we use the MIPS 70μm band since PACS did not map the Magellanic Clouds at 70μm. The data are converted from PACS and MIPS native units to W/m^2/sr, to be compared to maps of spectral lines[1]. We compare the ratio of 70μm/160μm with the two cooling lines, $\epsilon_{\rm TIR}$, and the ratio with [C II] only, to see if we find a similar decrease with the two ratios, and to see in both case the effect of correcting the TIR from H II region contamination.

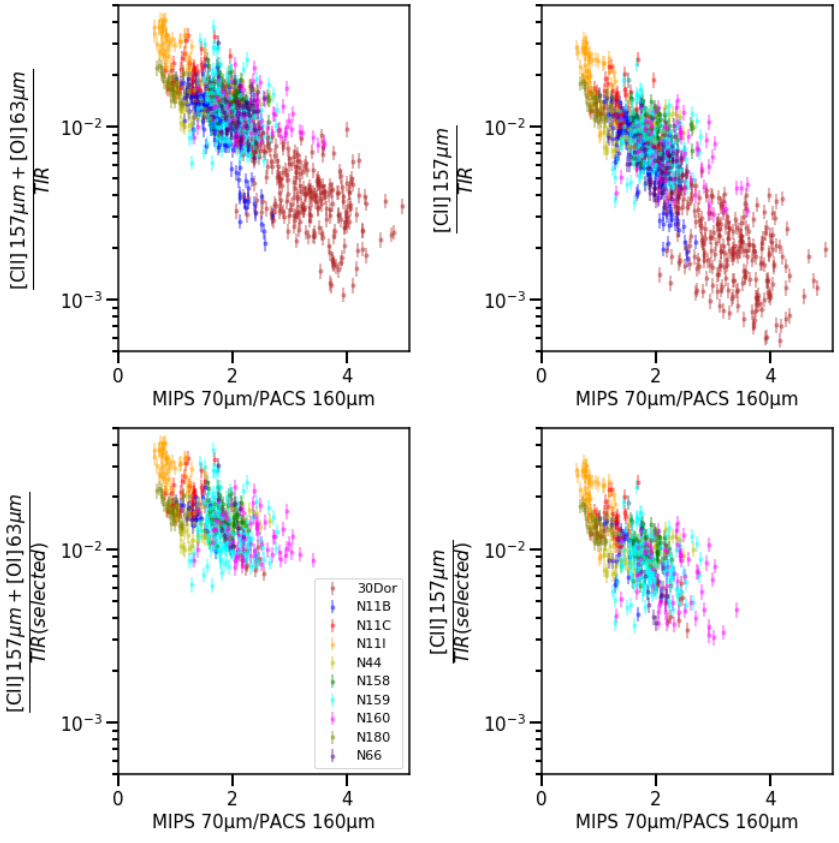

FIGURE 5.14: Evolution of ([C II]+[O I])/TIR for the Magellanic CLoud sources (left panels) and [C II]/TIR (right panels) with IR colors. In upper panels, we display the original data, and in lower panels data without pixels in which TIR is dominated by H II region emission.

[1]While this is not exactly the $\nu\, f_\nu$ units, which are in W/m^2, but as it is a ratio and the maps are all projected onto the same grid it does not cause any issue.

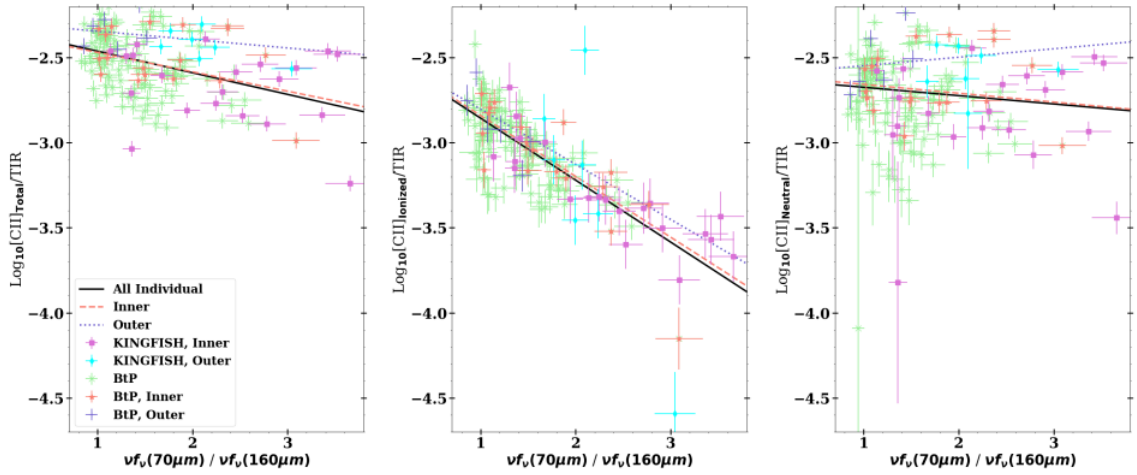

FIGURE 5.15: Evolution of ([C II]+[O I])/TIR with IR colors for the KINGFISH galaxies; left panel: total [C II] emission; middle panel: [C II] emission arising from ionized gas; right panel: [C II] emission arising from neutral gas. Figure from Sutter et al. (2019).

We present in Figure 5.14 the ratios $\epsilon_{\rm TIR}$ and [C II]/TIR. In the upper panels, all of the pixels are used, and in the lower panel, the pixels that are dominated by H II region emission are removed. We see in the lower panels that removing the pixels in which TIR was contaminated by the ionized phase weakens the decreasing trend of $\epsilon_{\rm TIR}$ and [C II]/TIR with colors. The results of Sutter et al. (2019) are shown in Figure 5.15 for comparison. We see that their color values are in the same range as the color values we obtain by removing pixels for which the TIR is dominated by the H II region. The range of [C II]/TIR in our sample is similar to that found for the KINGFISH galaxies in Sutter et al. (2019). By removing the pixels dominated by H II region emission, we have removed most of the 30Dor and N11B regions, the most luminous star forming regions in the LMC. Thus, part of the decrease, and probably part of the dispersion, are driven by the contamination by ionized phase. As the points contaminated by ionized gas phase emission, which were removed from the plots, were corresponding to the higher values of 70μm/160μm, it also strengthens the link between IR color proxy and the amount of hot dust in the H II region.

5.5.2 Photoelectric effect heating efficiency

In Section 5.3, we suggested investigating if the charge of PAHs could play a role in the dispersion of the PE heating efficiency, $\epsilon_{\rm PAH}$. We know that the PE heating efficiency should decrease if PAHs become positively charged (Weingartner & Draine, 2001c; Draine & Li, 2007), and that in dense and/or highly UV-illuminated PDRs (PDR*) the PAHs should be more ionized (Bakes & Tielens, 1994; Draine, 2011; Draine & Li, 2007). In PDR* the cooling is dominated by [O I] emission (Kaufman et al., 1999, 2006). We had anticipated that the ratio [O I]/([C II]+[O I]) would trace f*, the volume fraction of PDR*, but results in Figure 5.5 and Section 5.3 showed that the relation between the ratio [O I]/([C II]+[O I]) and f* is not so simple, and that a careful constraint of all the other parameters of the ISM would be necessary.

To obtain the f* value, one possibility would be to use a two-component model for the PDRs, and to constrain separately the denser and/or higher illuminated PDRs and the more diffuse and/or less illuminated PDRs. It would require a large number of observations to be able to constrain the physical parameters separately. Moreover, there are possibly different components

along the line of sight, which may not have the same conditions. Spectroscopically resolved observations would give access to the different clouds along the line of sight, and thus help in constraining separately their physical conditions. It would also be interesting to have observations with better spatial resolution, to have less mixing of different phases within the telescope beam. Some present and future observational facilities can obtain better spatial and spectral resolution (e.g., ~ 0.5" for ALMA at 950 GHz, equivalent to $\sim 300\mu$m, or 0.1" at 2μm for JWST, or SOFIA/upGREAT with a spectral resolution of 0.022 km s^{-1} for a bandwidth of 630 km s^{-1}), and follow-up observations would be of a great help to spatially disentangle the different types of PDRs.

A spatially-resolved study of the PAH ionization would also be interesting, in order to compare it to different tracers. It would thus be necessary to have spectroscopic observations on the range covered by the PAH features, to be able to inspect the ratios of different bands, which would help to constrain the ionization state of the PAHs.

5.5.3 The special case of N66

N66 is the only SMC region in our sample and we saw in Section 5.2, Figure 5.4 (left panels), that the PE heating efficiency of PAHs,([C II]+[O I])/PAH ($\epsilon_{\rm PAH}$) exhibits a behaviour rather different from the LMC regions: the PAH emission was among the lowest of the sample, and $\epsilon_{\rm PAH}$ was higher than in the LMC regions, with a decrease of $\epsilon_{\rm PAH}$ with increasing PAH intensity, whereas the LMC regions show a relatively flat $\epsilon_{\rm PAH}$. Thus, N66 was excluded at first from the sample for its anomalous behaviour in Sections 5.3 and 5.4, and we investigate it separately here. We compare the two PE heating efficiency proxies, $\epsilon_{\rm PAH}$ and $\epsilon_{\rm TIR}$, to the ratio ([C II]+[O I])/[O III] that we use to disentangle emission of the ionized phase from emission from PDRs.

We see by comparing Figures 5.16 and 5.17 to Figures 5.11 and 5.13 that the models at 1/5 $Z_\odot$ (for the SMC) are similar to models at 1/2 $Z_\odot$ (for the LMC). The models differ by a factor 4, at most, for all of the ratios used, and the models with the highest ionization parameters and densities are affected the most by the different metallicities. We also notice that N66 observations have values similar to LMC regions for $\epsilon_{\rm TIR}$ (Figure 5.16), but almost all of the pixels show a behaviour that corresponds to models with low PDR proportion. Thus, the N66 region shows a high contamination of TIR by the ionized phase. N66 points are a bit offset from the models, but we notice that constant pressure models are in better agreement with observations than constant density models. In a general sense, $\epsilon_{\rm TIR}$ in N66 has values and a behaviour similar to those found for the LMC regions in our sample.

The N66 data cloud for $\epsilon_{\rm PAH}$ lies higher ($\sim$5-6 10^{-1}) than that for all of the LMC regions which have values around a few $\times$ 10^{-1}. Constant pressure models are unable to reproduce the relation between $\epsilon_{\rm PAH}$ and ([C II]+[O I])/[O III] for all of the observations whereas constant density models seem to reproduce the values and behaviour of $\epsilon_{\rm PAH}$ for all of the Magellanic Cloud sources. This is in strong disagreement with models that correspond to $\epsilon_{\rm TIR}$, for which constant density models can not reproduce the data. We discussed potential causes of the differences between N66 and the LMC regions in Section 5.2. Adding more SMC regions would help to understand what drives $\epsilon_{\rm PAH}$ in N66, and observations at different metallicities could also help in investigating a potential effect of metallicity, which affects PAH and lines emission in many different ways (reduced abundances, less shielding of PAH molecules by dust, maybe different chemical formation paths, etc.). To that aim, IC10 (a nearby Local Group galaxy at 800 kpc) would be an interesting target to examine, as its metallicity (1/3 $Z_\odot$) is intermediate between LMC and SMC.

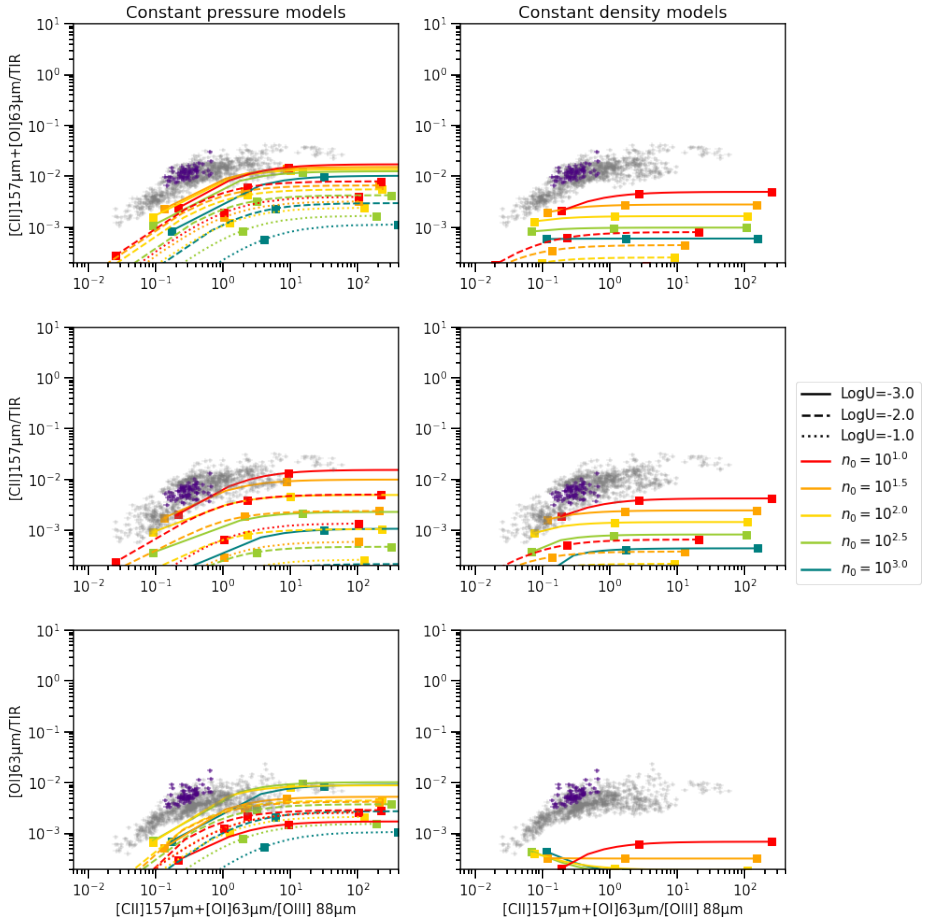

FIGURE 5.16: Evolution of ([C II]+[O I])/TIR (upper panels), [C II]/TIR (middle panels) and [O I]/TIR (lower panels) as a function of ([C II]+[O I])/[O III]. On left panels constant pressure models for a metallicity of 1/5 $Z_\odot$ are overplotted on N66 observations (purple points); on right panels, the models are for constant density and 1/5 $Z_\odot$ metallicity. The purple points are data from N66, and the LMC regions are represented in grey for comparison.

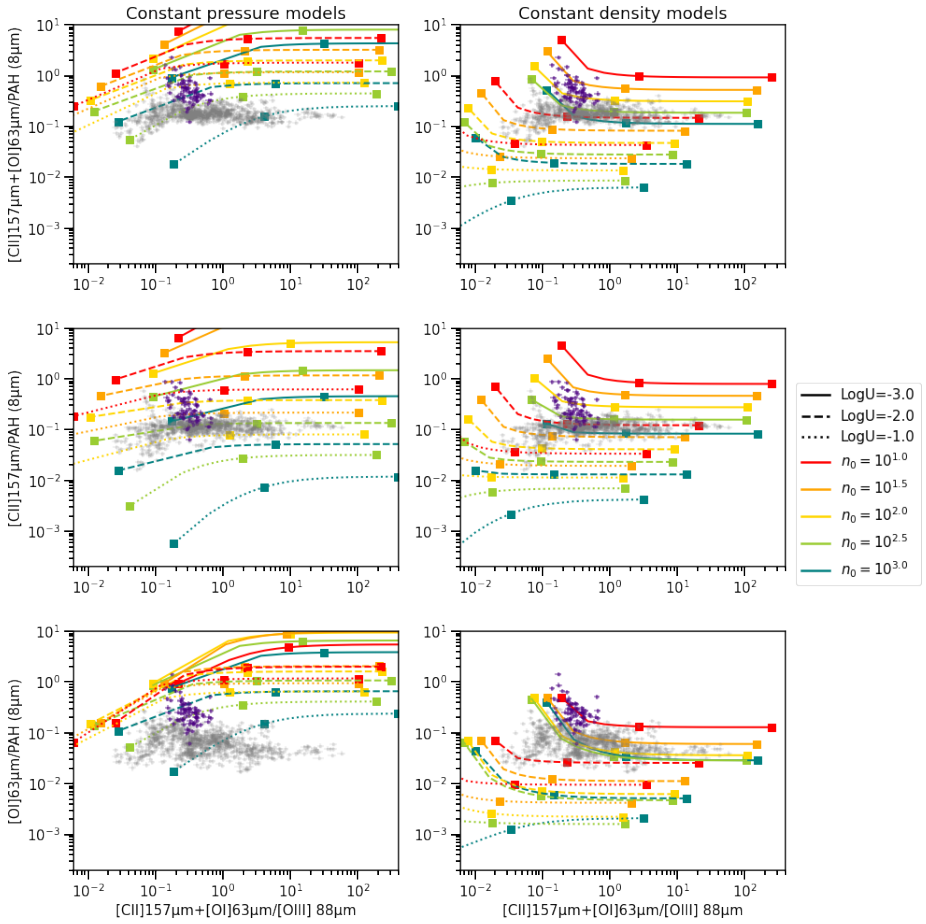

FIGURE 5.17: Similar to Figure 5.16, by replacing TIR emission by PAH emission estimated from the IRAC 8μm band.

5.6 Summary

In this chapter, we investigated two different PE heating efficiency proxies: ([C II]+[O I])/PAH ($\epsilon_{\rm PAH}$), and ([C II]+[O I])/TIR ($\epsilon_{\rm TIR}$) in the resolved regions of the Magellanic Clouds. We learned that $\epsilon_{\rm PAH}$ is a better tracer of PE heating efficiency than $\epsilon_{\rm TIR}$ in the LMC regions of our sample, but the SMC region, N66, does not follow the same trends. Moreover, the TIR emission shows signs of a possible contamination by gas phases other than PDRs, with a large spread and a strong decreasing trend of $\epsilon_{\rm TIR}$ with increasing TIR values. We tried to see if the spread of $\epsilon_{\rm PAH}$ is linked to the ionization state of the PAH molecules by constraining the volume proportion of dense and/or highly UV-illuminated PDRs. However, our data can not constrain this proportion, which is much more complicated to obtain than we expected, and would require complex models and more observational constraints.

We also compared our PE gas heating tracers (PAHs, TIR, 24μm band, 70μm band and 100μm band) to the ratio we use to differentiate PDR from H II regions, namely ([C II]+[O I])/[O III], and to our Cloudy models (Section 5.4). We showed that individual MIR to FIR bands and TIR are contaminated by ionized gas phase emission, and that some pixels are dominated by H II region emission. However, constant pressure models reproduce quite well the observations, and the use of MIPS 70μm band allows us to exclude constant density models. We also found (Figure 5.12) that the spread of $\epsilon_{\rm TIR}$ was linked to the contamination of TIR by ionized phase emission. Removing the data that are dominated by ionized gas phase, tightened and flattened the relation between $\epsilon_{\rm TIR}$ and TIR. We compared our results to the higher metallicity galaxies of the KINGFISH survey in the Sutter et al. (2019) study where IR colors are compared to the [C II]/TIR and [C II]/PAH. They find that correcting [C II] from the ionized phase contamination weakens the trend of the [C II]/TIR and [C II]/PAH ratios with colors. In contrast, for our sample, the contamination of [C II] is expected to be low (Cormier et al., 2019), thus we consider the cooling line [C II] as fully emitted by the PDRs. We found results similar to Sutter et al. (2019), which indicate that the dispersion and the line deficit are linked to the contamination by the ionized gas phase. Moreover, the use of our models to remove the pixels dominated by H II regions showed that the IR colors are indeed a good tracer for the quantity of hot dust from H II regions.

Finally, we discussed the specific case of N66, the only region in our study in the SMC. The TIR PE heating efficiency proxy has similar trends as those of the LMC regions, but the values of the PAH PE heating efficiency proxy are offset compared to the LMC regions. We also notice that for $\epsilon_{\rm PAH}$, the constant pressure models are unable to fit the data in N66, and the constant density models agree better. As we only have one region from the SMC, it is not possible to derive a strong conclusion on N66, which requires more observational constraints and more regions in the SMC.

CONCLUSION AND PERSPECTIVES

Summary of the results

For this work, the objective was to understand the physical conditions and the processes at play in star-forming regions of the Magellanic Clouds. Their proximity to the Milky Way (50 kpc and 61 kpc for the LMC and SMC respectively) and their low metallicity (1/2 $Z_\odot$ and 1/5 $Z_\odot$) allow us to investigate the specific conditions of low-metallicity ISM with excellent spatial resolution in the IR tracers. Low-metallicity ISM is indeed known to harbour conditions and emission different from more metal-rich galaxies due to the low dust content and higher radiation field (Madden et al., 2006; Cormier et al., 2015, 2019).

We conducted our work using the archival data on LMC and SMC, with a specific focus on two samples of star-forming regions, one that has spectroscopic observations of [C II] 157μm, [O I] 63μm and [O III] 88μm from *Herschel*/PACS, and the other that has spectroscopic observations from *Spitzer*/IRS, especially the [S III] 18.7μm, [S III] 33.5μm, [S IV] 10.5μm, [Ne II] 12.8μm and [Ne III] 15.6μm lines. Both samples also have photometric band observations from the *Herschel* and *Spitzer* telescopes.

Modeling In Chapter 3, we described the models we prepared by using a set of tools: the model PopStar (Mollá et al., 2009), that simulates the emission of a full stellar population for different burst ages, and the photoionization and photodissociation code Cloudy (Ferland et al., 2017), that calculates the chemical and physical equilibrium of the ISM and the emission of different tracers based on initial values at the illuminated edge of the clouds. The spectrum computed by the PopStar simulation is used as an input for the Cloudy models. We prepared grids of models with three parameters: the age of the stellar burst, the density, and the ionization parameter. We tested two physical assumptions for the models, considering for one set that the gas has a constant density through the cloud, and for the other set that the ISM has a constant pressure, which is a common assumption for the ISM (e.g., Tielens & Hollenbach, 1985; Hollenbach & Tielens, 1999; Draine, 2011).

Correlation between [O III] 88μm and 24μm In Chapter 4, Section 4.1, we investigated the relation of 24μm, which is often used as an IR tracer of stellar formation, with the [O III] 88μm emission line which is the brightest emission line in low-metallicity dwarf galaxies (Cormier et al., 2015). The [O III] emission line was already tested as a potential tracer of star formation by De Looze et al. (2014), and showed an excellent correlation with SFR calibrated from IR bands and FUV emission. Our results showed that [O III] and 24μm are correlated, with a linear relation in log-log space detailed below:

$$\log(\Sigma_{[\mathrm{OIII}]\,88}) = 0.857(\pm0.013) \times \log(\Sigma_{24}) - 1.57(\pm0.066) \tag{5.10}$$

with $\Sigma_{[\mathrm{OIII}]\,88}$ the surface brightness of [O III] and Σ_{24} the surface brightness of 24μm band, both being in units of W/m^2/sr. We showed in Section 4.2 that this linear relation was also visible with luminosities integrated over the full region maps:

$$\log(L_{[\mathrm{OIII}]\,88}) = 0.910(\pm0.077) \times \log(L_{24}) - 0.447(\pm0.343) \tag{5.11}$$

with $L_{[\mathrm{OIII}]\,88}$ and L_{24} being the luminosities of [O III] and 24μm normalized to solar luminosity. We also showed in Section 4.2 that global values from galaxies from the DGS followed the same relation we find for the LMC and SMC regions. Thus, this relation holds on a wide range of metallicities and size scales for dwarf galaxies. We demonstrated in Section 4.3 the effectiveness of this relation to predict [O III] emission from the 24μm band observation. This relation thus could be used to prepare observations with current or future facilities (e.g., ALMA, SOFIA/FIFI-LS, SOFIA/HIRMES). As this relation is holding on large scales and for the range of conditions probed by DGS, it may even be possible to use it on high-redshift galaxies.

Conditions in H II regions We investigated how the tracers available for the LMC and SMC regions could be used to trace the physical conditions in the ISM. First, we used the capability of Cloudy to save cumulative emission as a function of depth into the cloud to differentiate the emission from the H II region and from the PDR in our models. We separated the emission of the H II region, before the ionization front, and the PDR, beyond the ionization front, for all of the models in our grid. We then mixed our models of H II region and PDR by varying the proportion of each model in the mixture. We thus created a new parameter, "PDR proportion", or c_{PDR}, which is described in detail in Chapter 4, Section 4.4.1. We added examples and some possible physical interpretations for different values of c_{PDR}. By using the ratios of [O III]/24μm, [O III]/70μm and ([C II]+[O I])/[O III], we were able to constrain physical parameters in our star-forming region sample. The lines [C II] and [O I] were chosen to be able to disentangle emission from PDR and from H II region, as they are characteristic tracers of the cooling in PDRs. In our sample, we consider that they are emitted only by PDRs, although a small contamination from ionized phase could be taken into account for some cases ($\leq$30%, see e.g., Cormier et al., 2019). In Section 4.4.2, we showed that the values of [O III]/24μm were not compatible with a burst age older than 4-5 Myrs, demonstrating that allvof the regions in our sample sustained recent stellar formation. We were also able to exclude the most extreme values of ionization parameter and density of our grids, showing that ionization parameters of log(U)=0 or -5 were not compatible with most of the data, and that only models with densities of 10^3 cm^{-3} or lower were able to reproduce the values of [O III]/24μm. We then studied the relation of [O III]/24μm as a function of ([C II]+[O I])/[O III], comparing the spatially resolved data in our sample to the Cloudy models (Section 4.4.3). A first striking result was that the 24μm band emission is arising from both H II region and PDR, with some pixels showing an important PDR contribution. While the 24μm band is often implicitly assumed to trace the dust emission in H II regions, taking into account this possible contamination is important for spatially unresolved studies of the ISM, where it is not possible to disentangle the different phases observed within the beam. By considering together the relation between [O III]/24μm and ([C II]+[O I])/[O III], and the relation between [O III]/70μm and ([C II]+[O I])/[O III], we also showed that constant density models were not able to reproduce the two ratios at the same time. On the other hand, constant pressure models were able to fit [O III]/24μm as a function of ([C II]+[O I])/[O III] and [O III]/70μm as a function of ([C II]+[O I])/[O III] with the same range of physical conditions. We thus used constant pressure models with a burst age of 4 Myrs to constrain the density and ionization parameters for our regions. Using the whole sample, we found that the best fitting model has log(U)=-3, and a density of $10^{2.5}$ cm^{-3}. When comparing data of each individual region to our Cloudy models, we found that the derived parameters were close to that found for the combined sample (see Table 4.2 in Section 4.4.3.2). As the ISM metallicity of the LMC

is close to values that are derived at the peak of cosmic star-formation (redshift ~ 2, see e.g., Madau & Dickinson, 2014), it gives an indication of which conditions and dispersion could be encountered at those redshifts. Moreover, our method is based on two bands that were largely observed for many galaxies, and a few lines that are the brightest ones in the IR range for dwarf galaxies. It could thus be suitable for studies on high-redshift galaxies, where those observations are possible, to probe ISM conditions even without spatial resolution.

Investigation of the phase distribution along the line of sight In Section 4.4.4, we investigated the distribution of the ionized phase and PDRs along the line of sight with the help of the parameter $c_{\rm PDR}$. We compared the ratio ([C II]+[O I])/[O III] with the models, assuming the best-fitting parameters found in Section 4.4.3 for each individual region, and derived maps of the PDR proportion for each region. We saw that the spatial distribution of $c_{\rm PDR}$ is anti-correlated with the distribution of [O III] emission, $c_{\rm PDR}$ peaking where the [O III] emission is low. On the other hand, and more surprisingly perhaps, the distribution of $c_{\rm PDR}$ does not follow well the distribution of the cooling lines of PDRs. Thus, the parameter $c_{\rm PDR}$ is tracing regions where PDRs dominate the mixture of H II region-PDR but for which the PDR cooling line tracers do not necessarily dominate over [O III]. Moreover, we underline that the PDR proportion, $c_{\rm PDR}$, is not a volume filling factor, nor a covering factor of PDRs. It can be linked to those two quantities, but not in a simple, straightforward, way. However, this parameter brings new insight on the matter distribution between H II regions and PDRs along a line of sight, and further studies should be able to precisely define the link between physical parameters (filling and/or covering factors) and the parameter $c_{\rm PDR}$. Here again, as we only use bright IR lines and band tracers, this method should be well suited to study high-redshift galaxies.

Tracers of PE heating efficiency in PDRs In Chapter 5, as the temperature of the ISM is a key parameter in the star-formation process, we decided to investigate the cooling and heating tracers of PDRs. The main coolants of PDRs are the emission lines [C II] and [O I]. As the photoelectric effect is the major gas heating mechanism, and is probably sustained by PAHs and/or VSGs (Weingartner & Draine, 2001c; Tielens, 2005; Draine, 2011), we decided to investigate two proxies for the PE heating efficiency: the ratio ([C II]+[O I])/TIR, which is a classical tracer used in PDR studies (e.g., Croxall et al., 2012), noted as $\epsilon_{\rm TIR}$, and the ratio ([C II]+[O I])/PAH, as the contribution from PAHs may be significant or even dominant (e.g., Weingartner & Draine, 2001c,b; Rubin et al., 2009), noted as $\epsilon_{\rm PAH}$. As we do not have spectroscopic observations over the wavelength range where the brightest PAH bands emit for all our sample, we use a photometric method developed by Seok et al., (in prep.) and described in Section 5.1.1 to estimate the PAH contribution in the IRAC 8μm band. PAH emission in this band accounts for roughly 50% of the total PAH emission in classical PDR conditions (see e.g. models in Draine & Li, 2007). To calculate the TIR emission, we use a calibration based on bands emission from Galametz et al. (2013). We compared the PE heating efficiency proxies for the various heating tracers, and saw that there is a decrease of $\epsilon_{\rm TIR}$ with increasing TIR. On the other hand, $\epsilon_{\rm PAH}$ shows a flat trend with PAH emission for the LMC regions. N66, our only SMC region, shows a strikingly different behaviour, and was further studied apart from the rest of the sample. Due to the flatness of the relation between $\epsilon_{\rm PAH}$ and PAH on almost two orders of magnitude, we consider then that PAH emission is a better tracer of PE heating in PDRs than TIR. We tentatively tried to link the dispersion seen in $\epsilon_{\rm PAH}$ to the ionization of PAHs in Section 5.3. However, the data is insufficient to study PAH ionization as a parameter.

Contamination of heating proxies by H II region emission In Section 5.4, we investigated the possible contamination of the PDR heating proxies by the ionized phase emission, using the ratio ([C II]+[O I])/[O III] to probe PDR and H II region contribution in the emission, and by comparing our data to the Cloudy models presented. The 24μm band, for which we know the emission arises from both H II regions and PDRs (see Chapter 4), is considered as a benchmark to see the effect of contamination of the emission by the ionized phase. We investigated the different potential tracers of heating of the PDR gas, i.e., the 24μm, 70μm and 100μm bands, the TIR, and the PAH emission. We showed that all of the bands show signs of contamination by the emission from the ionized phase, the most contaminated being 24μm, and the less contaminated 100μm. The TIR, which is calculated from the different band emission, also shows signs of some contamination. By restricting the observations to pixels dominated by PDR emission, we showed that this contamination dominates the spread of $\epsilon_{\rm TIR}$, and accounts for a large part of the decreasing trend of $\epsilon_{\rm TIR}$ with TIR. A shallow slope, however, still remains when ignoring the pixels with heavy contamination by the ionized phase, and other causes may need to be investigated. We also looked at the PAH emission as a function of ([C II]+[O I])/[O III], and we saw that the PAH emission does not show strong signs of contamination by the ionized phase, although the spread of $\epsilon_{\rm PAH}$ increases at low values of ([C II]+[O I])/[O III], which is still not well explained.

The peculiar behaviour of N66 N66 is the only SMC region is our sample. Although it shows a behaviour similar to the LMC region for TIR and band tracers, it has a very different behaviour from the LMC regions when coming to PAHs. It is known that as the metallicity decreases, the PAH emission becomes fainter, and is not seen or barely seen at metallicities lower than 1/5 $Z_\odot$ (Engelbracht et al., 2005), which is precisely the metallicity of the SMC. We see in our data that the PE heating efficiency proxy $\epsilon_{\rm PAH}$ showed a strong decrease with increasing PAH emission in N66, and an overall low PAH emission. By investigating this region separately (Section 5.5.3), we confirmed that its behaviour was similar to the LMC regions for TIR and $\epsilon_{\rm TIR}$, the region globally lying on the turnover point, between pixels dominated by H II region emission and pixels dominated by PDR. The best model fits the relation between $\epsilon_{\rm TIR}$ and ([C II]+[O I])/[O III] with a constant pressure hypothesis. However, when we turned to the PAH emission and $\epsilon_{\rm PAH}$, the behaviour of N66 is totally different from LMC regions, with a low PAH value, a globally high $\epsilon_{\rm PAH}$, and models that fit the relation of $\epsilon_{\rm PAH}$ and ([C II]+[O I])/[O III] with a constant density hypothesis. This discrepancy shows that some ingredients may not be well taken into account in $\epsilon_{\rm PAH}$, either from the model or the data point-of-view. A first possibility would be that the method from Seok et al. (in prep.), calibrated on LMC regions, is not accurate to take into account the PAH emission in IRAC 8μm for the SMC. Another possibility would be that the high ISRF of N66, comparable to that found in 30 Doradus, would destroy PAHs more efficiently, and over larger areass than for LMC regions. The lower metallicity of the SMC compared to the LMC would then account for part of this difference, as there is less dust to shield PAH molecules against the high radiation field. However, the absence of other regions from the SMC prevents us to derive a strong conclusion on the behaviour of N66, and especially to understand if it is due to metallicity effects or if is representative in a general sense, of other SMC regions.

Prospective Studies

Spatially resolved ISM conditions We investigated the ISM physical conditions in the individual regions, but without spatial resolution within each region. To this end, the use of grids with finer resolution of parameter space, and a more refined method to find the best model could be applied to each pixel within the regions, in order to obtain a map of the best parameters with spatial resolution. As another way to better understand the spatial evolution of the ISM conditions within one region, we used the *Spitzer*/IRS data. We note that those observations are limited to tracers of the H II region. Our preliminary study relied on the interpolated Cloudy models presented in Chapter 3, Section 3.4. We assumed an age of ∼4 Myrs for all of the regions, and used a 2D grid of density and ionization parameter. We relied on ratios of MIR lines to probe the physical conditions: [S III] 18μm/[S III] 33μm was used to trace the density, and the ionization parameter was probed by either [S IV] 10μm/[S III] 18μm, or [Ne III] 15μm/[Ne II] 12μm. We then computed the 2D probability density function for each pixel separately, and determined the physical conditions that were corresponding to the two ratios selected and produced maps of density and ionization parameter. An example of those results is shown in Figure 5.18.

These maps of density and ionization parameter could be used to constrain the models to use on further investigations, and can be compared to the values obtained with the method developed in Chapter 4. However, the samples observed with *Herschel*/PACS and *Spitzer*/IRS only have two regions in common where the observations exist at the same position (N11B and N66). Thus it was not possible to couple IRS data to the method we developed for all of the regions. Further investigation of the two regions with both *Herschel*/PACS and *Spitzer*/IRS data would help to give a more robust conclusion of possible advantages given by the use of the two methods combined.

Follow-up observations with SOFIA can play an important role in bringing the complementary data to the existing observations. For example, FIFI-LS has two channels covering 51 to 120μm (blue channel) and 115 to 200μm (red channel), which allow us to observe [C II], [O I] 63μm and [O III] 88μm and 52μm, with spectral resolutions of 600 to 2 000, and a spatial resolution of 6″ per pixel for the blue channel and 12″ for the red channel. Obtaining the H II region lines that were available with *Spitzer* is possible with FORCAST on SOFIA, which offers observations between 5 and 40μm, with a spectral resolution of R∼200. In the near future, MIRI onboard JWST covers a wavelength range between 5 and 28μm. Thus, the lines [S IV] 10μm, [S III] 18μm, [Ne II] 12μm and [Ne III] 15μm will be available. As the [S III] 33μm line is not included in the JWST MIRI range, the ratio of the [S III] lines can not be used to trace the density. However, in the range covered by MIRI, there are two [Ar III] lines at 9μm and 21μm that could also trace the density. These lines were marginally detected with *Spitzer*, with low signal-to-noise, but due to better sensitivity, JWST would be able to detect the [Ar III] lines.

Generating spatially resolved maps of the physical parameters of the ISM would provide the possibility to investigate potential trends between them (e.g., test a possible correlation between the ionization parameter and PAH PE heating efficiency, or with ratios of some PAH features, which could help to understand the ionization state of PAHs and compatibility with other physical conditions). The use of tracers from both H II regions and PDRs combined in the models would provide better constraints of the ISM conditions in the regions, and will also help to refine the models. Potential incompatibilities between the models probed by the tracers from H II regions and tracers from PDRs could indicate that a modification of our assumptions is required, e.g., using a specific profile of the density evolution through the cloud. But it can also be an indication of different cloud conditions observed along the line of sight of each pixel, and that

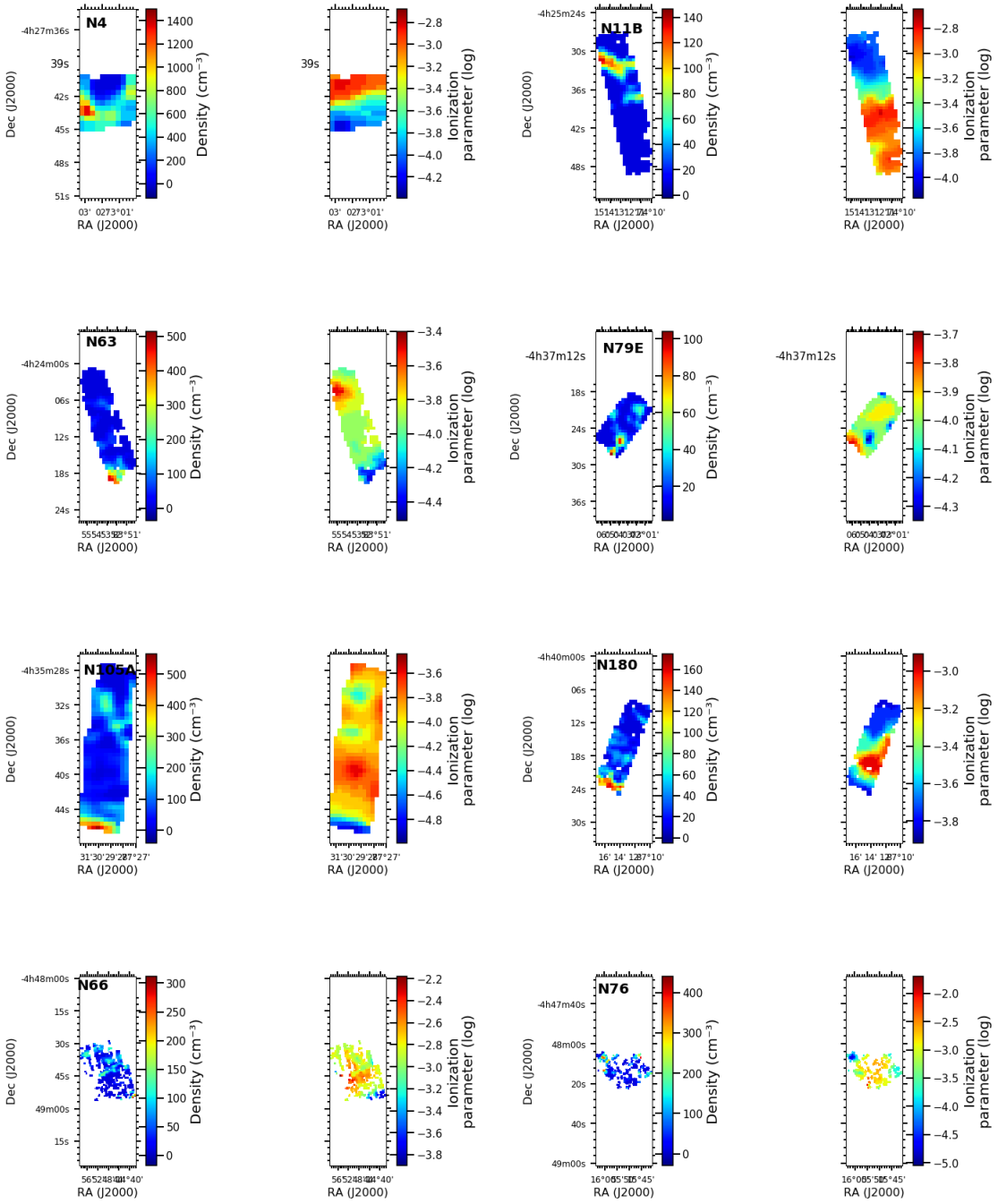

FIGURE 5.18: Maps of the density and ionization parameter fitted for the regions observed with *Spitzer*/IRS. All regions are presented, with the density on the left and ionization parameter on the right. The regions are indicated on the density maps. The maps were obtained by using constant pressure models, and the two ratios [S III] 18μm/[S III] 33μm and [Ne III] 15μm/[Ne II] 12μm.

we have to disentangle multiple components to understand the behaviour of the ISM in these regions.

Investigation of the 3D geometry of the ISM In our analysis, we considered that in each pixel, the H II regions and PDRs along the line of sight have the same initial conditions, i.e.,

were associated with the same cloud and same excitation source. With that assumption, we compared our models and the observations in the individual star-forming regions in our sample (Chapter 4, Section 4.4.3.2), finding that the ISM physical conditions are quite similar between each individual region. However, we determined that toward the star-forming regions, there are more likely multiple clouds along a line of sight, and the phases emitting in one pixels are probably distributed between those clouds. It is thus necessary to disentangle those multiple components to have a better understanding of the structure and conditions of the matter in star-forming regions. One approach consists of separating the different clouds in a line of sight, using velocity-resolved spectroscopic observations. It would then allow us to constrain separately the conditions in different clouds.

The spectrometer upGREAT on SOFIA gives access to the [C II] 157μm, [O I] 63μm and [O I] 145μm lines with high spectral resolution of R$\geq 10^7$, with FWHM between 6$''$ and 14.1$''$. Having access to velocity-resolved observations is also necessary to understand the 3D distribution of ISM material, but it requires other information, such as determining the 3D distribution of the ionizing sources. It is also important to use a self-coherent 3D model that takes into account as much of the physical parameters as possible, and to rely on an accurate and unbiased method to analyze the observations. Many efforts are being made in that direction, such as the use of Bayesian analysis of spectra, or codes that try to disentangle velocity-resolved observation while considering that the pixels are not independent of their neighbouring pixels. Using such new methods, plus new velocity-resolved observations, would help to constrain the geometry. However, even partial information would be valuable, as it would allow the possibility to make systematic blind tests with 3D models.

Extension of the method The method we developed during this work was created and tested on a relatively small set of observations, covering mainly the regions around the brightest peaks of star-forming regions, with little extent into the more diffuse surrounding material. In low-metallicity galaxies, much of the tracers we use arise from H II regions, but additional contamination from other phases can appear if the method is applied to larger integrated regions, or to an entire galaxy. Observations on more extensive regions surrounding the star-forming sites would be important to investigate before transposing the method to unresolved local or high redshift galaxies.

The SOFIA legacy program, LMC+, recently accepted, will target the Molecular Ridge of the LMC, that contains the three bright star-forming complexes, N158, N159 and N160. It also extends the observations of [C II], [O I] 63μm and [O III] 88μm far into the surrounding, more diffuse ISM of the Molecular Ridge. The use of these new observations will allow us to calibrate our new method with inclusion of more diffuse gas, and to characterize the behaviour of our newly-created parameter, c_{PDR}, in the diffuse media. Extending the study of the method developed in this work to larger regions will allow us to determine and adjust the application of our method to unresolved galaxies. Meanwhile, it is also possible to apply our method to the DGS low metallicity targets on global and local scales.

Correction of TIR from ionized phase contamination We saw in Chapter 5 that the TIR emission is arising from both the H II region and the PDRs. As TIR is often used to trace the PE heating in PDR gas, it is thus important to estimate the fraction of TIR coming from each region in order to accurately trace the PDR regions only. We saw that flagging and removing points were the PDR was not dominant already effected the behaviour of ratios using TIR. The next step would be to fit the relation between ([C II]+[O I])/TIR and ([C II]+[O I])/[O III] and derive a prescription to correct TIR from the H II region emission. A comparison with

observations from other galaxies would also be needed, and the DGS targets would help us learn if the prescription for TIR holds on integrated observations and different physical conditions (e.g., metallicity, SFR, etc.). The use of a precise relation to correct TIR would entail creating a spatially resolved map of the TIR fractions arising from the ionized and neutral phases, which can be used to correct for interpretation of the local conditions.

PAH emission in N66 In the end of Chapter 5, we saw that PAH emission in N66 has a peculiar behaviour, quite different from that found in the other regions of our sample. As N66 is the only SMC region, the different metallicities of the LMC and SMC can be suggested as a potential reason for this. PAH features are known to diminish as the metallicity decreases, being barely detectable, for the most part, under a metallicity of 1/5 $Z_{\odot}$, which is the SMC metallicity.

N66 is a very active star-forming region, with a hard and intense radiation field which could be the consequences of the lower dust abundance and the direct cause of a decreased PAH emission compared to other regions in our study. To further investigate this behaviour, it would be interesting to have spectroscopic measurements of the PAH emission in different star-forming regions of the SMC (e.g., N66, N76, N83/84), in order to have better sampling of the conditions in varying star-forming environments at this low metallicity. Additional spatially-resolved observations from other galaxies, with metallicity values different from those of the LMC and SMC, would also help to understand the effect of metallicity on PAH emission, and the PE heating by PAHs. For instance, the Local Group galaxy IC10 would be an obvious target to study the PAH PE heating efficiency, as it has intermediate metallicity ($\sim$1/3 $Z_{\odot}$) between the LMC and SMC and can be partially resolved.

Another test should be carried out on the method we used to derive the PAH emission in the IRAC 8μm band from photometric observations. Indeed, the photometric determination of the PAH intensities that we use in this study was developed on the LMC regions only. Thus further investigation of the capabilities of this method at different metallicities would illustrate the effect on the PAHs in different SMC environments, especially when the conditions hit the limit of detectability of PAH emission. This test also needs to be compared with spectroscopic observations of the PAHs. JWST should bring the possibility to make high spatial resolution spectroscopic observations in the SMC on the range covered by the brightest PAH features, and future follow-up observations using FORCAST on SOFIA would also help to study the PAH PE heating effects in different SMC environments.

APPENDIX A

ROBUSTNESS OF THE RELATION BETWEEN [O III] 88μM AND MIPS 24μM

We investigate the robustness of the relation between [O III] 88μm and MIPS 24μm, studied in Chapter 4 when changing various aspects of the analysis: the pixel size, the method used for the fitting, the correction for point sources and the resolution at which we use the maps.

A.1 Test of the method

Here we investigate the effect of the fitting method on the parameters of the linear relation. We compare three different fitting methods: a simple, non weighted χ^2, to investigate the uncertainties due to the fitting method, a method using a Monte-Carlo simulation to calculate the uncertainties, which can then be considered to be directly linked to the observation uncertainties, and the weighted χ^2 used in Chapter 4, which takes into account uncertainties from the data and the method of fit.

The Monte-Carlo simulation used the observed sample as a base to run 100 simulated samples, with the same number of pixels, each varying inside the limits of 1σ, following a normal distribution. The fit is then calculated with a non-weighted χ^2 on each simulated samples, and the final value for the parameters are the median from all of the resulting fittings, with the median absolute deviation being the uncertainty. The fitted slopes and intercepts for each method, and their uncertainties, are regrouped in Table A.1. We added the value of the R^2 coefficient of the fit, to estimate the difference in fitting accuracy. The three fitted relations are illustrated with the data in Figure A.1.

Method	Slope	Intercept	R^2
Weighted χ^2	0.857±0.013	-1.57±0.068	0.804
Simple χ^2	0.885±0.013	-1.434±0.069	0.811
Monte-Carlo	0.886±0.002	-1.434±0.01	0.899

TABLE A.1: Fitted parameters for the different methods are displayed with their uncertainties. The R^2 parameter is also given, as it is an indication of the goodness-of-fit.

The parameters fitted with different methods are very similar and roughly agreeing within the uncertainties (Table A.1). We also see that the R^2 value is high for all the methods, between 80 and 90%, which correspond to a high probability to have a linear positive correlation. We underline that the different methods give very similar relations when compared to the fitted data (Figure A.1).

The uncertainties derived by the two χ^2 methods are almost identical, and much larger than the uncertainties derived by the Monte-Carlo method. It indicates that the uncertainties derived by the fitting procedure and due to the spread of the data are dominant compared to the effect of observation uncertainties.

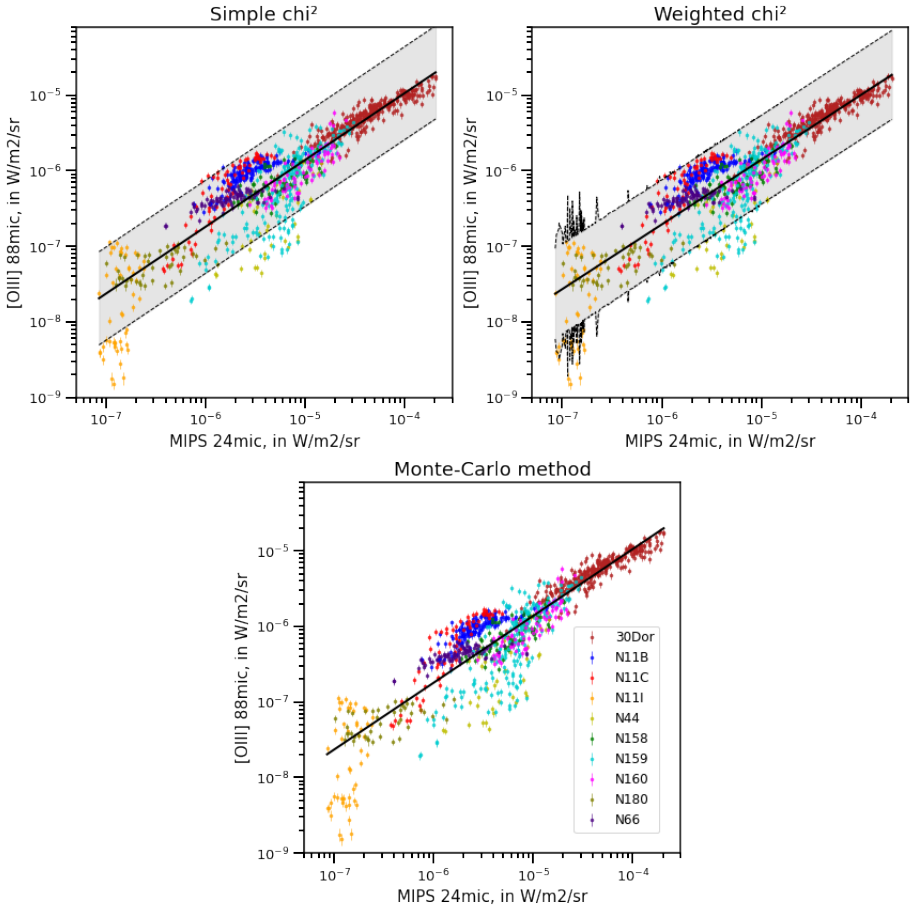

FIGURE A.1: Linear fits between [O III] 88μm and 24μm for the three methods. The 95% confidence intervals are represented with dashed lines and grey fillings for the simple and weighted χ^2 methods. The confidence interval is not determined for the Monte-Carlo method. The upper right panel, corresponding to the weighted χ^2, is identical to the Figure 4.1 in Chapter 4, showing the fit of the correlation.

We can see that the R^2 parameters are very similar for the two χ^2 methods, but it is a bit higher for the Monte-Carlo simulation, indicating that the fit is a bit more representative of the data, but this effect is very small, as the difference between the R^2 values is smaller than 0.1.

We can conclude from this test that the different methods give similar results, both on the fitted value and the accuracy of the fit. The comparison of the non-weighted χ^2 and the Monte-Carlo method shows that the uncertainties on the fitted parameters driven by the fitting method are much larger than the uncertainties driven by data uncertainties. The weighted χ^2, which is the method finally used (see Chapter 4), has the advantage of taking into account both types of uncertainties, although the uncertainties driven by the fitting method are dominating.

A.2 Test on the resolution and sampling of the maps

Here we compare different resolutions and sampling of the map, to investigate the potential effects it can have on the fit. We use a weighted χ^2 method to be consistent with what we use in Chapter 4, and we compare two different resolution with the same sampling, and two different sampling with the same resolution. The resolutions we use are 12", to match the PACS emission lines, and 18" resolution, to match the MIPS 70μm(see Chapter 4, Section 4.4.3). For

both resolutions, we resampled the maps to 12" pixel width, to avoid oversampling of the beam. For the spatial sampling, we compare our final pixel size of 12" to the native sampling of PACS spectroscopy, 3".1. It will also allow us to investigate the effect of oversampling the beam, as we use 12" resolution for the tests on sampling size.

Resolution, pixel size (arcsec, arcsec)	Slope	Intercept	R^2
12, 3.1	0.849±0.004	-1.626±0.019	0.805
12, 12	0.857±0.013	-1.57±0.068	0.804
18, 12	0.87±0.012	-1.493±0.065	0.822

TABLE A.2: The fitted parameters and corresponding uncertainties of the linear relation between [O III] 88μm and MIPS 24μm, for the different resolutions and sampling of the maps. The R^2 parameter is indicated as a goodness-of-fit.

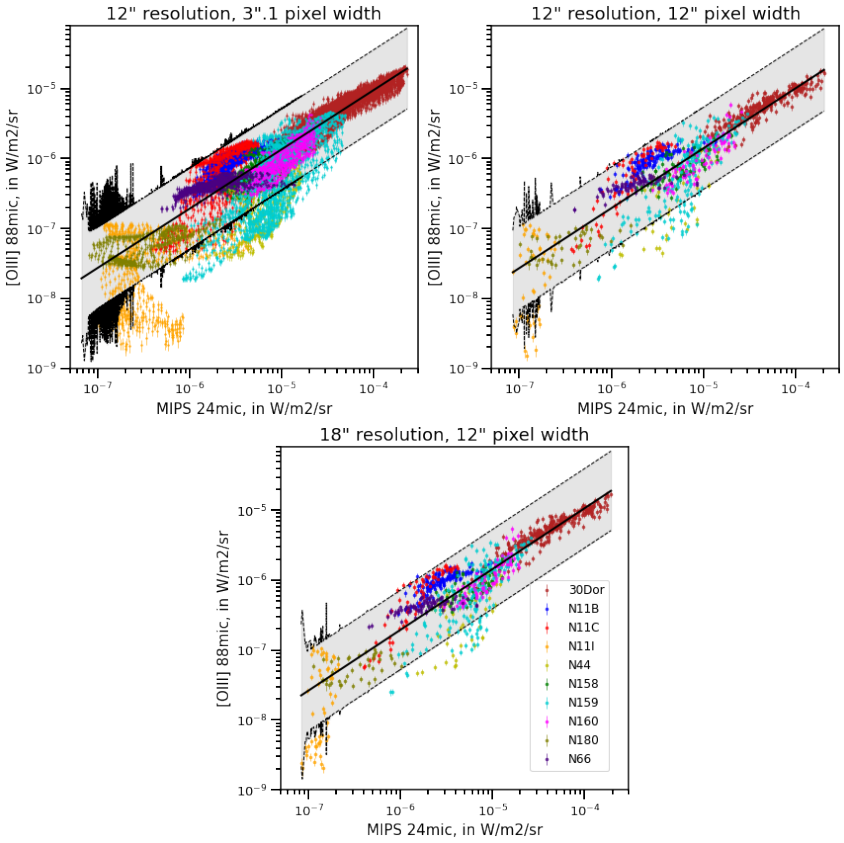

FIGURE A.2: The fitted linear relation and the corresponding data for the different resolution and sampling of the maps. The black solid line is the fit, the dashed black lines and grey filling illustrate the 95% confidence interval. The upper right panel, corresponding to 12" resolution and a pixel size of 12", is identical to the Figure 4.1 in Chapter 4, showing the fit of the correlation.

We can see with Table A.2 The different resolutions and samplings of the maps return very similar results for the fit of the parameters of the relation, which are roughly agreeing within the uncertainties. The R^2 parameter is also very close for each of the data settings.

The derived uncertainties seem to be affected only by the pixel width. For the smallest pixels we see that the uncertainties on the relation parameters are three times smaller than with a pixel

width of 12". This indicates that, for comparable dispersion, the fitting procedure can be more precise where it is carried out on more pixels.

By comparing the fitted parameters from Table A.2 to the data (Figure A.2), we see that the fits do not differ much, but the confidence intervals are affected by both the resolution and the pixel size: at the low resolution and low pixel width (12" resolution and 3".1 pixel width), the confidence intervals are highly irregular, especially at the low brightness end of the relation, but they become more regular when increasing the pixel size (12" resolution and 12" pixel width) and when increasing the beam size (18" resolution and 12" pixel width). It corresponds to a smoothing of the data.

We can conclude from this test that the effect of resolution and pixel size is negligible on the fitted parameters of the relation between [O III] 88μm and MIPS 24μm, even when the beam is largely oversampled, although using a larger number of pixels leads to a better precision on the fitted values.

A.3 Test on method for point sources correction

When we presented the MIPS observations (see Chapter 2, Section 2.2.4), we showed that the maps were contaminated by point sources, for which comparison with point source catalogs mainly indicate as young stars. The suppression of the point source emission is described in detail in Chapter 2. Here, we investigate the effect of this suppression, and the effect of the method used, on the fitting of the relation between [O III] 88μm and MIPS 24μm.

As noted in Chapter 2, there are three ways to estimate the emission from the ISM without the point sources. First, the background is estimated on the maps, but on tiles where it is considered flat. The size of the tiles depends on different parameters, including the size of the map and the spread of the point source emission. Those tiles roughly correspond to the pixel width of 12", except for the 30 Doradus region. The software used also produced a map called "zoom background", which is the estimation of the emission without point sources, with the same resolution as the initial maps. However, those maps are based on the tiled background maps, that are then treated to improve the resolution. For the last evaluation of the ISM emission, we rely on a map of the point source emission only, which is also created by the software. This point source map is subtracted from the initial map, to retrieve the diffuse emission only. This method comes with some caveats, especially in the case of overestimation of the point source emission. It can lead to some artifacts, or some pixels with negative emission, which are artificially set to zero, but a detailed examination of our sample showed that this type of artifact is not present or is negligible in the studied regions.

In order to study the effect of the method used to correct maps from point source emission, we fitted the relation between [O III] 88μm and MIPS 24μm by using four 24μm emission maps: the original MIPS 24μm maps, convolved and resampled, without removing the point sources (later called original data), the two types of diffuse emission maps created by the software, namely the tiled background and zoomed background, and the original data with the point source maps subtracted, which will be referred to as point source subtracted data or simply subtracted data. In region N160, the 24μm data shows a large saturated zone. The saturated pixels were masked, and when trying to apply a point source correction, no point source was found in non-saturated pixels. Thus the N160 24μm masked map is used in all of the four procedures, without attempts to correct from point source emission. Table A.3 summarizes the parameters fitted for the four 24μm maps, and the results are illustrated in Figure A.3.

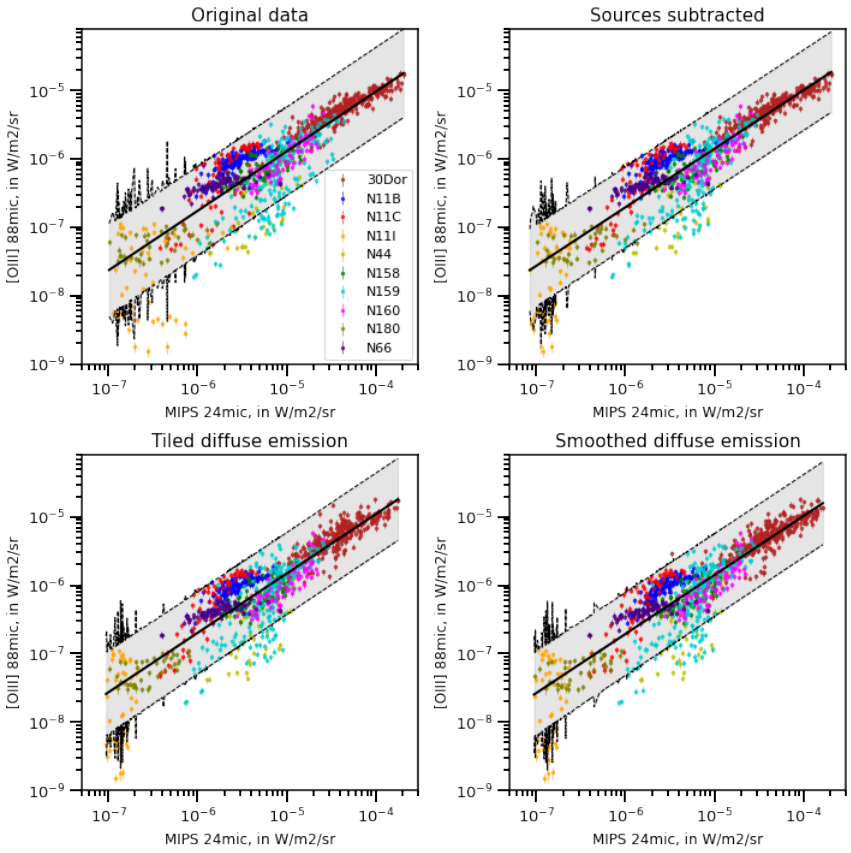

FIGURE A.3: Results of different treatments on the data: the original MIPS 24μm maps, tiled and smoothed background calculated by the software extracting the point sources, and the original maps with extracted point sources emission substracted. The black solid line represents the fitted relation between the [O III] 88μm emission line and the 24μm band and the black dashed lines and the grey filling stands for the 95% confidence intervals.

MIPS data	Slope	Intercept	R^2
Original	0.872±0.015	-1.534±0.077	0.763
Tiled diffuse emission	0.869±0.013	-1.484±0.071	0.797
Zoomed diffuse emission	0.864±0.014	-1.532±0.071	0.793
Point sources subtracted	0.857±0.013	-1.57±0.067	0.804

TABLE A.3: Summary of the fitted parameters for the data with and without point source correction in the MIPS 24μm maps. "Original" is for non-corrected data, "tiled" and "zoomed diffuse emission" are the two calculation of the diffuse emission from the software used to extract the point sources, and "point source subtracted" is for the original MIPS 24μm maps with the extracted emission from point sources subtracted. The slope and intecept of the linear relation are given with their uncertainties, and the R^2 parameter is an indication of the accuracy of the fit.

We notice that the global dispersion is not affected by the method used to correct the 24μm maps from point source emission (Figure A.3), indicating that it linked to the discrepancies between the different regions, as we have already noticed in Section 4.1. However, the internal dispersion for each region is affected by the removal of point sources. The two cases of tiled and zoomed background emission reduce the spread for some regions, like N11I or N159, for the MIPS 24μm data (roughly from 1 dex or a bit more to 0.5 dex); it naturally leaves untouched the spread in [O III] 88μm emission. Some regions, on the contrary, exhibit a spread a bit larger with the tiles and zoomed background than with the original MIPS 24μm data, such as 30 Doradus. This increase of the spread is probably due to the tiling of the diffuse emission used to calculate the point source emission, and thus is identical for the two diffuse emission calculations. The effect is the strongest for the region 30 Doradus, and this is probably due to the fact that this is the only region for which the tiling is done on a scale much larger than the resampling of the maps at 12" pixel width.

The diffuse emission obtained by subtracting the point source emission from the original map also does not influence the global spread, but only the spread of each individual region. In this case, we observe the same reduction of the spread for the regions affected by the other methods of correction for point source emission, but there is no increase of the spread in the other regions.

Removing the point source emission has little effect on the fitted parameters, independently of the method used (Table A.3). The slopes and intercepts are very similar, and completely agreeing within the uncertainties. The R^2 parameter is somewhat affected: the original data give the less accurate fit, the method using two different diffuse emission calculations gives a result a bit more accurate, and the best fitted relation is achieved for the maps with the point source emission subtracted from the original maps.

From this test, we conclude that taking into account the contamination of the 24μm emission by point source emission is important, especially to investigate the behaviour and conditions in the star forming regions of the sample taken individually, but it does not influence much the fitting of the parameters of the relation between [O III] 88μm emission and MIPS 24μm, nor the uncertainties on the fitted parameters. The different methods to take into account the point source emission have different effects to take into account. To avoid increase of the spread in some regions, and the loss of spatial resolution due to the tiling used to calculate the point sources emission, we decided to keep the MIPS 24μm data with point sources subtracted.

APPENDIX B

PHYSICAL CONDITIONS OF INDIVIDUAL STAR-FORMING REGIONS

Contents

Here we show the comparison of [O III]/24μm and [O III]/70μm as a function of ([C II]+[O I])/[O III]. Those ratios are used to understand the physical conditions of the individual regions in Chapter 4, Section 4.4.3.2.

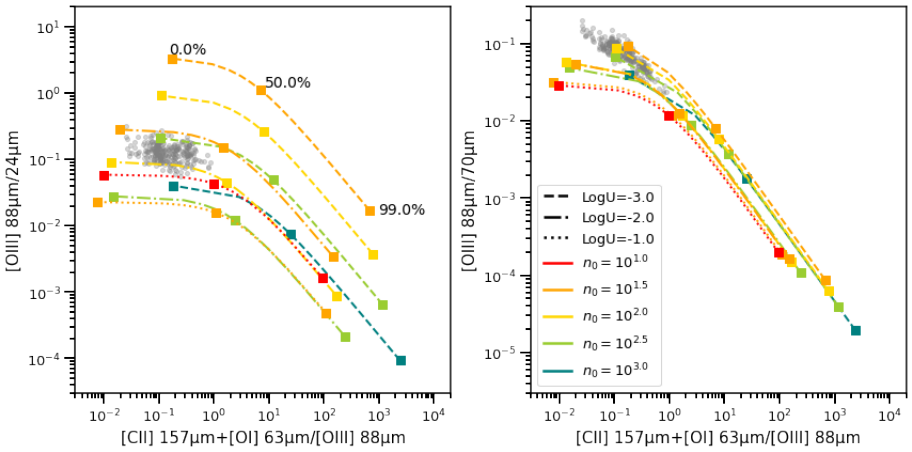

FIGURE B.1: Representation of the data of the region 30 Doradus and models with constant pressure for [O III] 88μm/MIPS 24μm as a function of ([C II]+[O I])/[O III] (left panel), and [O III] 88μm/MIPS 70μm as a function of ([C II]+[O I])/[O III] (right panel). Each model is represented with a color for the initial density and a line style for the ionization parameter, and the lines are following the proportion of PDR emission, with the markers representing the proportions of 0%, 50 % and 99%. The models displayed are calculated for an age of star forming burst of 4 Myrs, and only the data from the 30 Doradus region are represented.

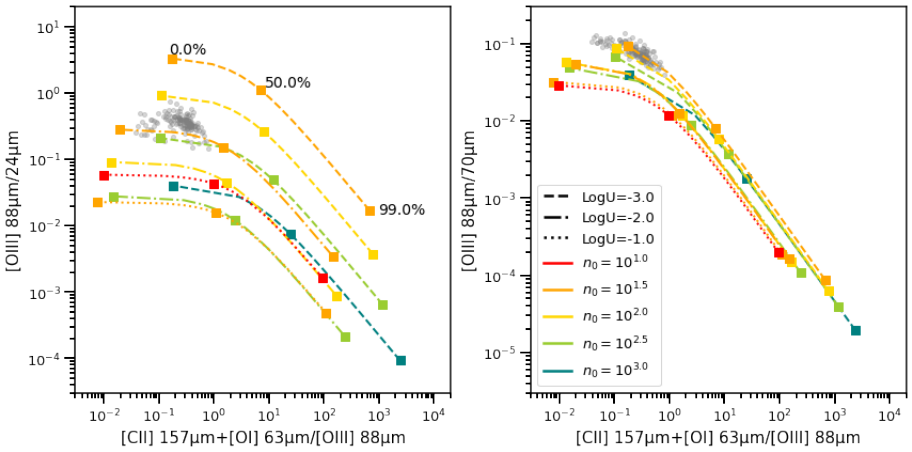

FIGURE B.2: Similar to Figure B.1, for the region N11B.

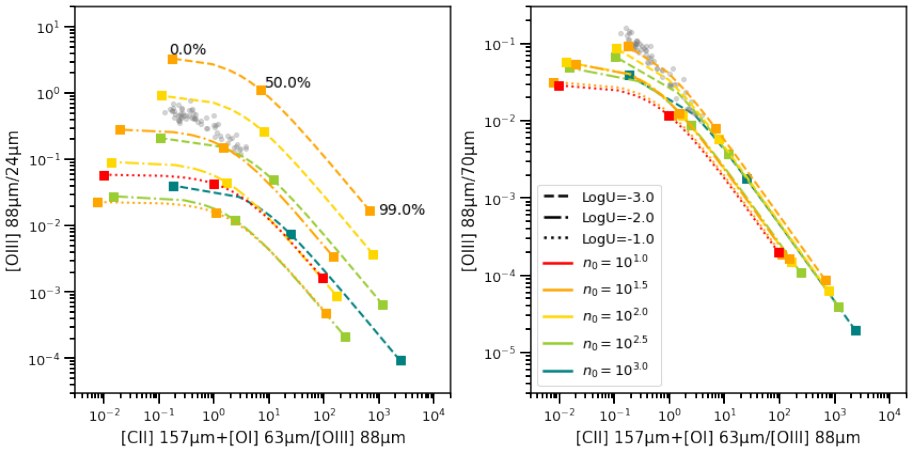

FIGURE B.3: Similar to Figure B.1, for the region N11C.

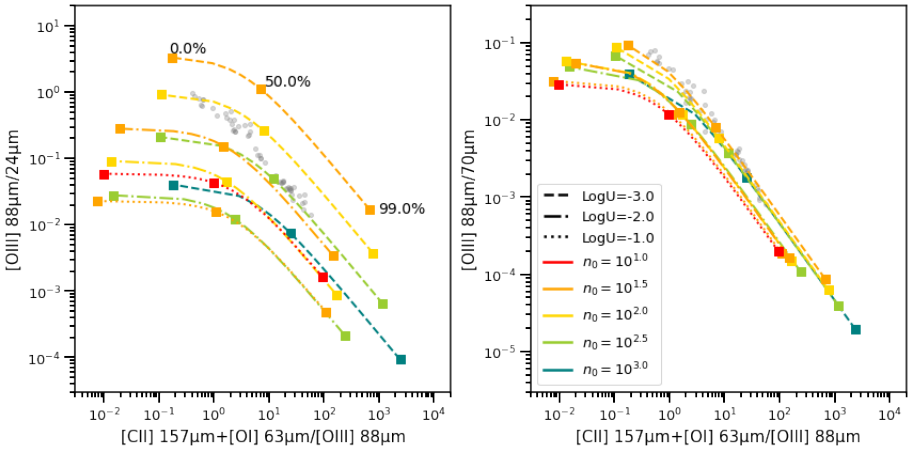

FIGURE B.4: Similar to Figure B.1, for the region N11I.

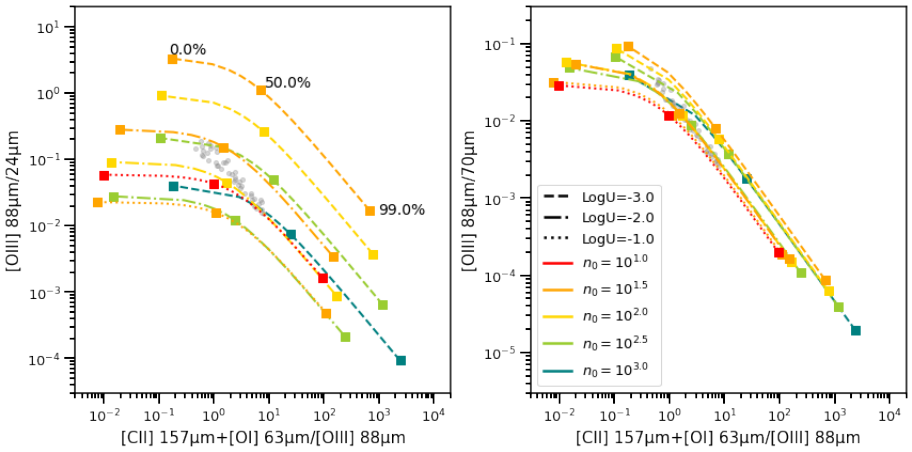

FIGURE B.5: Similar to Figure B.1, for the region N44.

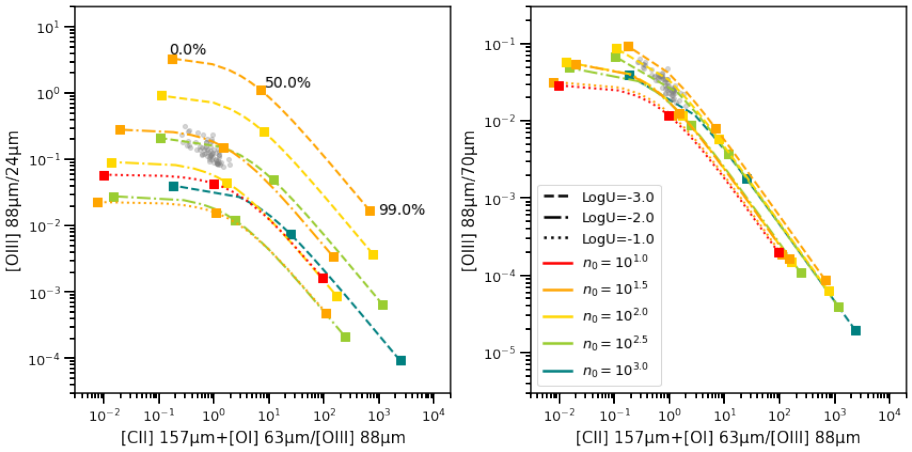

FIGURE B.6: Similar to Figure B.1, for the region N158.

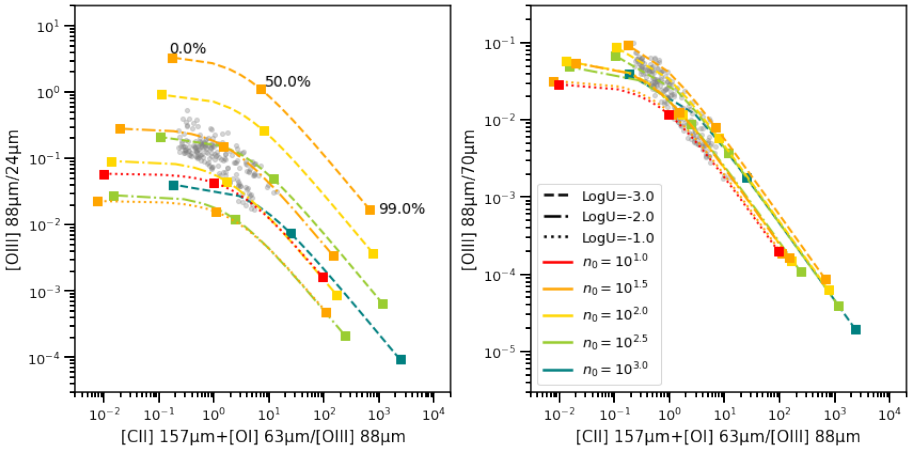

FIGURE B.7: Similar to Figure B.1, for the region N159.

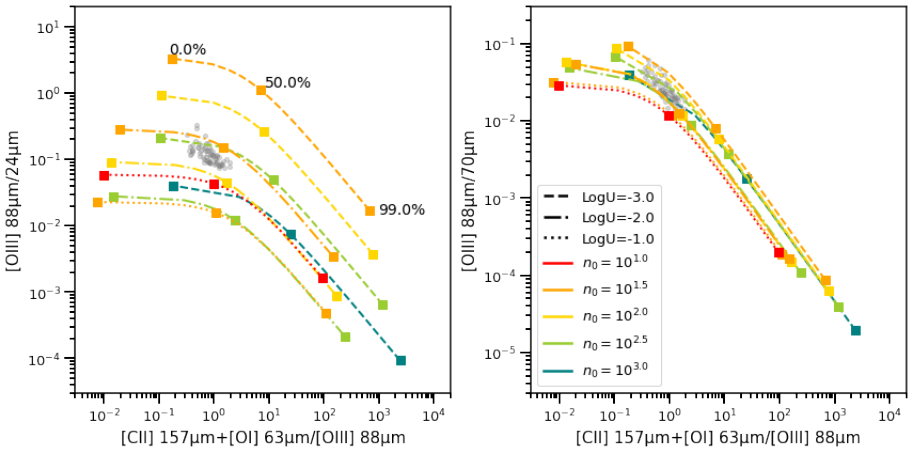

FIGURE B.8: Similar to Figure B.1, for the region N160.

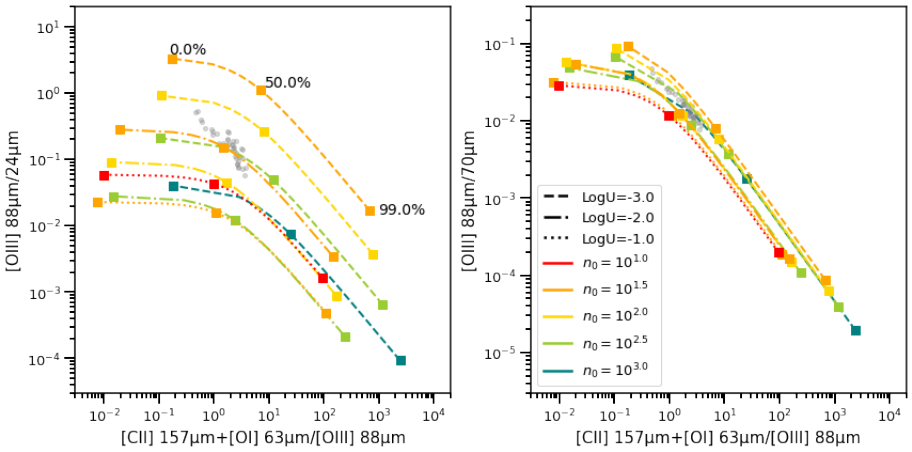

FIGURE B.9: Similar to Figure B.1, for the region N180.

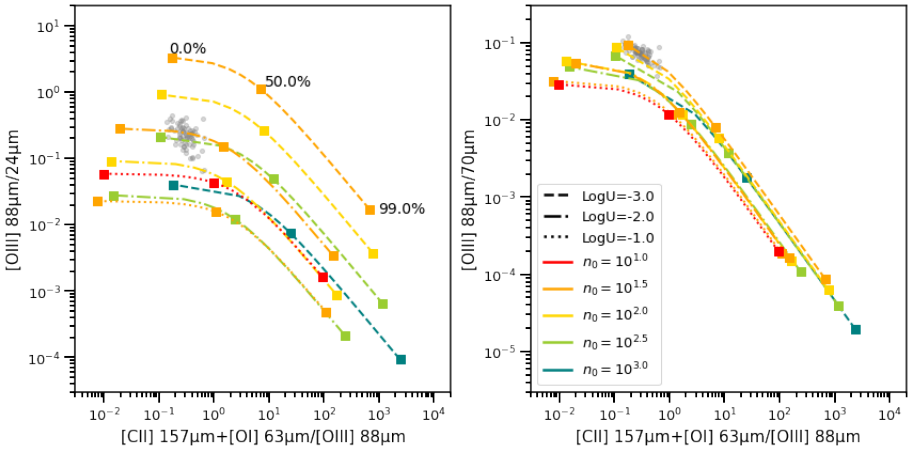

FIGURE B.10: Similar to Figure B.1, for the region N66.

BIBLIOGRAPHY

Abel, N. P., van Hoof, P. A. M., Shaw, G., Ferland , G. J., & Elwert, T. 2008, The Astrophysical Journal, 686, 1125

Accurso, G., Saintonge, A., Bisbas, T. G., & Viti, S. 2017a, Monthly Notices of the Royal Astronomical Society, 464, 3315

Accurso, G., Saintonge, A., Catinella, B., et al. 2017b, Monthly Notices of the Royal Astronomical Society, 470, 4750

Adamo, A., Östlin, G., Zackrisson, E., et al. 2010, Monthly Notices of the Royal Astronomical Society, 407, 870

Adamo, A., Östlin, G., Zackrisson, E., et al. 2011, Monthly Notices of the Royal Astronomical Society, 415, 2388

Ambrocio-Cruz, P., Laval, A., Marcelin, M., Amram, P., & Comeron, F. 1998, Astronomy & Astrophysics, 339, 173

Anderson, C. N., Meier, D. S., Ott, J., et al. 2014, The Astrophysical Journal, 793, 37

Asplund, M., Grevesse, N., Sauval, A. J., & Scott, P. 2009, Annual Review of Astronomy and Astrophysics, 47, 481

Bakes, E. L. O. & Tielens, A. G. G. M. 1994, The Astrophysical Journal, 427, 822

Barbá, R. H., Rubio, M., Roth, M. R., & García, J. 2003, The Astronomical Journal, 125, 1940

Barnes, L. A., Garel, T., & Kacprzak, G. G. 2014, Publications of the Astronomical Society of the Pacific, 126, 969

Bekki, K. & Stanimirović, S. 2009, Monthly Notices of the Royal Astronomical Society, 395, 342

Bendo, G. J., Galliano, F., & Madden, S. C. 2012, Monthly Notices of the Royal Astronomical Society, 423, 197

Bestenlehner, J. M., Crowther, P. A., Caballero-Nieves, S. M., et al. 2020, Monthly Notices of the Royal Astronomical Society, 499, 1918

Bica, E., Claria, J. J., Dottori, H., Santos, J. F. C., J., & Piatti, A. E. 1996, Astrophysical Journal Supplement, 102, 57

Bigiel, F., Leroy, A. K., Walter, F., et al. 2011, The Astrophysical Journal Letters, 730, L13

Bigiel, F., Walter, F., Leroy, A., et al. 2009, in The Evolving ISM in the Milky Way and Nearby Galaxies, ed. K. Sheth, A. Noriega-Crespo, J. G. Ingalls, & R. Paladini, 12

Bolatto, A. D., Jackson, J. M., Israel, F. P., Zhang, X., & Kim, S. 2000, The Astrophysical Journal, 545, 234

Bolatto, A. D., Wolfire, M., & Leroy, A. K. 2013, Annual Review of Astronomy and Astrophysics, 51, 207

Brauher, J. R., Dale, D. A., & Helou, G. 2008, The Astrophysical Journal Supplement Series, 178, 280

Brodie, J. P. & Huchra, J. P. 1991, The Astrophysical Journal, 379, 157

Brüns, C., Kerp, J., Staveley-Smith, L., et al. 2005, Astronomy & Astrophysics, 432, 45

Carlson, L. R., Sewiło, M., Meixner, M., Romita, K. A., & Lawton, B. 2012, Astronomy & Astrophysics, 542, A66

Carniani, S., Ferrara, A., Maiolino, R., et al. 2020, Monthly Notices of the Royal Astronomical Society

Caulet, A., Gruendl, R. A., & Chu, Y. H. 2008, The Astrophysical Journal, 678, 200

Caulet, A. & Williams, R. M. 2012, The Astrophysical Journal, 761, 107

Chabrier, G. 2003, Publications of the Astronomical Society of the Pacific, 115, 763

Chevance, M., Kruijssen, J. M. D., Vazquez-Semadeni, E., et al. 2020a, Space Science Reviews, 216, 50

Chevance, M., Madden, S. C., Fischer, C., et al. 2020b, Monthly Notices of the Royal Astronomical Society, 494, 5279

Chevance, M., Madden, S. C., Lebouteiller, V., et al. 2016, Astronomy & Astrophysics, 590, A36

Cioni, M. R. L. 2009, Astronomy & Astrophysics, 506, 1137

Cioni, M. R. L., Habing, H. J., & Israel, F. P. 2000, Astronomy & Astrophysics, 358, L9

Combes, F., García-Burillo, S., Braine, J., et al. 2013, Astronomy & Astrophysics, 550, A41

Contursi, A., Kaufman, M. J., Helou, G., et al. 2002, The Astronomical Journal, 124, 751

Cormier, D., Abel, N. P., Hony, S., et al. 2019, Astronomy & Astrophysics, 626, A23

Cormier, D., Madden, S. C., Lebouteiller, V., et al. 2015, Astronomy & Astrophysics, 578, A53

Cormier, D., Madden, S. C., Lebouteiller, V., et al. 2014, Astronomy & Astrophysics, 564, A121

Cowie, L. L. & Songaila, A. 1986, Annual Review of Astronomy and Astrophysics, 24, 499

Croxall, K. V., Smith, J. D., Pellegrini, E., et al. 2017, The Astrophysical Journal, 845, 96

Croxall, K. V., Smith, J. D., Wolfire, M. G., et al. 2012, The Astrophysical Journal, 747, 81

Daddi, E., Dannerbauer, H., Liu, D., et al. 2015, Astronomy & Astrophysics, 577, A46

Daddi, E., Elbaz, D., Walter, F., et al. 2010, The Astrophysical Journal Letters, 714, L118

Daddi, E., Renzini, A., Pirzkal, N., et al. 2005, The Astrophysical Journal, 626, 680

Dale, D. A. & Helou, G. 2002, The Astrophysical Journal, 576, 159

de Graauw, T., Helmich, F. P., Phillips, T. G., et al. 2010, Astronomy & Astrophysics, 518, L6

De Looze, I., Cormier, D., Lebouteiller, V., et al. 2014, Astronomy & Astrophysics, 568, A62

de Vaucouleurs, G. 1955, The Astronomical Journal, 60, 126

Dekel, A. & Silk, J. 1986, The Astrophysical Journal, 303, 39

Dickel, J. R., McIntyre, V. J., Gruendl, R. A., & Milne, D. K. 2005, The Astronomical Journal, 129, 790

Doublier, V., Kunth, D., Courbin, F., & Magain, P. 2000, Astronomy & Astrophysics, 353, 887

Draine, B. T. 1978, The Astrophysical Journal Supplement, 36, 595

Draine, B. T. 2011, Physics of the Interstellar and Intergalactic Medium (Princeton University Press)

Draine, B. T. & Li, A. 2000, in American Astronomical Society Meeting Abstracts, Vol. 197, American Astronomical Society Meeting Abstracts, 42.04

Draine, B. T. & Li, A. 2007, The Astrophysical Journal, 657, 810

Dyson, J. E. & Williams, D. A. 1997, The physics of the interstellar medium (Bristol: Institute of Physics Publishing)

Ellingsen, S. P., Whiteoak, J. B., Norris, R. P., Caswell, J. L., & Vaile, R. A. 1994, Monthly Notices of the Royal Astronomical Society, 269, 1019

Engelbracht, C. W., Gordon, K. D., Rieke, G. H., et al. 2005, The Astrophysical Journal, 628, L29

Engelbracht, C. W., Rieke, G. H., Gordon, K. D., et al. 2008, The Astrophysical Journal, 678, 804

Ercolano, B., Barlow, M. J., Storey, P. J., & Liu, X. W. 2003, Monthly Notices of the Royal Astronomical Society, 340, 1136

Erickson, E. F. & Davidson, J. A. 1993, Advances in Space Research, 13, 549

Fariña, C., Bosch, G. L., Morrell, N. I., Barbá, R. H., & Walborn, N. R. 2009, The Astronomical Journal, 138, 510

Fazio, G. G., Hora, J. L., Allen, L. E., et al. 2004, The Astrophysical Journal Supplement Series, 154, 10

Feast, M. W., Abedigamba, O. P., & Whitelock, P. A. 2010, Monthly Notices of the Royal Astronomical Society: Letters, 408, L76

Feldmann, R., Gnedin, N. Y., & Kravtsov, A. V. 2012, The Astrophysical Journal, 747, 124

Ferland, G. J., Chatzikos, M., Guzmán, F., et al. 2017, Revista Mexicana de Astronomía y Astrofísica, 53, 385

Ferland, G. J., Fabian, A. C., Hatch, N. A., et al. 2009, Monthly Notices of the Royal Astronomical Society, 392, 1475

Ferland, G. J. & Mushotzky, R. F. 1984, The Astrophysical Journal, 286, 42

Field, G. B., Goldsmith, D. W., & Habing, H. J. 1969, The Astrophysical Journal Letters, 155, L149

Fischer, C., Beckmann, S., Bryant, A., et al. 2018, Journal of Astronomical Instrumentation, 7, 1840003

Galametz, M., Hony, S., Albrecht, M., et al. 2016, Monthly Notices of the Royal Astronomical Society, 456, 1767

Galametz, M., Kennicutt, R. C., Calzetti, D., et al. 2013, Monthly Notices of the Royal Astronomical Society, 431, 1956

Galametz, M., Madden, S., Galliano, F., et al. 2009, Astronomy & Astrophysics, 508, 645

Galametz, M., Schruba, A., De Breuck, C., et al. 2020, Astronomy & Astrophysics, 643, A63

Galliano, F. 2018, Monthly Notices of the Royal Astronomical Society, 476, 1445

Galliano, F., Galametz, M., & Jones, A. P. 2018a, Annual Review of Astronomy and Astrophysics, 56, 673

Galliano, F., Galametz, M., & Jones, A. P. 2018b, Annual Review of Astronomy and Astrophysics, 56, 673

Galliano, F., Hony, S., Bernard, J. P., et al. 2011, Astronomy & Astrophysics, 536, A88

Galliano, F., Madden, S. C., Jones, A. P., Wilson, C. D., & Bernard, J. P. 2005, Astronomy & Astrophysics, 434, 867

Galliano, F., Madden, S. C., Jones, A. P., et al. 2003, Astronomy & Astrophysics, 407, 159

Galliano, F., Nersesian, A., Bianchi, S., et al. 2021, arXiv e-prints, arXiv:2101.00456

Garnett, D. R., Kennicutt, Robert C., J., Chu, Y.-H., & Skillman, E. D. 1991, The Astrophysical Journal, 373, 458

Garnett, D. R. & Shields, G. A. 1987, The Astrophysical Journal, 317, 82

Giveon, U., Sternberg, A., Lutz, D., Feuchtgruber, H., & Pauldrach, A. W. A. 2002, The Astrophysical Journal, 566, 880

Glover, S. C. O. & Clark, P. C. 2016, Monthly Notices of the Royal Astronomical Society, 456, 3596

Glover, S. C. O., Clark, P. C., Micic, M., & Molina, F. 2015, Monthly Notices of the Royal Astronomical Society, 448, 1607

Glover, S. C. O. & Mac Low, M. M. 2011, Monthly Notices of the Royal Astronomical Society, 412, 337

Gnedin, N. Y. & Draine, B. T. 2014, The Astrophysical Journal, 795, 37

Gordon, K. D., Clayton, G. C., Misselt, K. A., Landolt, A. U., & Wolff, M. J. 2003, The Astrophysical Journal, 594, 279

Gordon, K. D., Meixner, M., Meade, M. R., et al. 2011, The Astronomical Journal, 142, 102

Grand, R. J. J., van de Voort, F., Zjupa, J., et al. 2019, Monthly Notices of the Royal Astronomical Society, 490, 4786

Grebel, E. K. 2001, in Dwarf galaxies and their environment, ed. K. S. de Boer, R.-J. Dettmar, & U. Klein, Vol. 40, 45

Grenier, I. A., Casandjian, J.-M., & Terrier, R. 2005, Science, 307, 1292

Griffin, M., Abergel, A., Ade, P., et al. 2007, Advances in Space Research, 40, 612

Grossi, M., Corbelli, E., Bizzocchi, L., et al. 2016, Astronomy & Astrophysics, 590, A27

Groves, B., Dopita, M. A., Sutherland, R. S., et al. 2008, The Astrophysical Journal Supplement Series, 176, 438

Gruendl, R. A. & Chu, Y.-H. 2009, The Astrophysical Journal Supplement, 184, 172

Habart, E., Verstraete, L., Boulanger, F., et al. 2001, Astronomy & Astrophysics, 373, 702

Hao, C.-N., Kennicutt, R. C., Johnson, B. D., et al. 2011, The Astrophysical Journal, 741, 124

Haser, S. M., Pauldrach, A. W. A., Lennon, D. J., et al. 1998, Astronomy & Astrophysics, 330, 285

Hashimoto, T. 2020, in Uncovering Early Galaxy Evolution in the ALMA and JWST Era, ed. E. da Cunha, J. Hodge, J. Afonso, L. Pentericci, & D. Sobral, Vol. 352, 13–18

Hatano, H., Kadowaki, R., Nakajima, Y., et al. 2006, The Astronomical Journal, 132, 2653

Helou, G., Khan, I. R., Malek, L., & Boehmer, L. 1988, The Astrophysical Journal Supplement, 68, 151

Henize, K. G. 1956, Astrophysical Journal Supplement, 2, 315

Herrera-Camus, R., Sturm, E., Graciá-Carpio, J., et al. 2018, The Astrophysical Journal, 861, 94

Heydari-Malayeri, M., Charmandaris, V., Deharveng, L., et al. 2002, Astronomy & Astrophysics, 381, 941

Heydari-Malayeri, M. & Lecavelier Des Etangs, A. 1994, Astronomy & Astrophysics, 291, 960

Heydari-Malayeri, M., Niemela, V. S., & Testor, G. 1987, Astronomy & Astrophysics, 184, 300

Heydari-Malayeri, M., Royer, P., Rauw, G., & Walborn, N. R. 2000, Astronomy & Astrophysics, 361, 877

Heydari-Malayeri, M. & Selier, R. 2010, Astronomy & Astrophysics, 517, A39

Heydari-Malayeri, M. & Testor, G. 1986, Astronomy & Astrophysics, 162, 180

Heyer, M. & Dame, T. M. 2015, Annual Review of Astronomy and Astrophysics, 53, 583

Hilditch, R. W., Howarth, I. D., & Harries, T. J. 2005, Monthly Notices of the Royal Astronomical Society, 357, 304

Hollenbach, D. J. & Tielens, A. G. G. M. 1999, Reviews of Modern Physics, 71, 173

Houck, J. R., Roellig, T. L., van Cleve, J., et al. 2004, The Astrophysical Journal Supplement Series, 154, 18

Hunt, L. K., García-Burillo, S., Casasola, V., et al. 2015, Astronomy & Astrophysics, 583, A114

Hunter, D. A., Gallagher, John S., I., Rice, W. L., & Gillett, F. C. 1989, The Astrophysical Journal, 336, 152

Hunter, D. A., Zahedy, F., Bowsher, E. C., et al. 2011, The Astronomical Journal, 142, 173

Indebetouw, R., Brogan, C., Chen, C. H. R., et al. 2013, The Astrophysical Journal, 774, 73

Izotov, Y. I., Stasińska, G., Meynet, G., Guseva, N. G., & Thuan, T. X. 2006, Astronomy & Astrophysics, 448, 955

Johnston, R., Vaccari, M., Jarvis, M., et al. 2015, Monthly Notices of the Royal Astronomical Society, 453, 2540

Jones, A. P., Tielens, A. G. G. M., & Hollenbach, D. J. 1996, The Astrophysical Journal, 469, 740

Jones, O. C., Woods, P. M., Kemper, F., et al. 2017, Monthly Notices of the Royal Astronomical Society, 470, 3250

Kamenetzky, J., Privon, G. C., & Narayanan, D. 2018, The Astrophysical Journal, 859, 9

Kaufman, M. J., Wolfire, M. G., & Hollenbach, D. J. 2006, The Astrophysical Journal, 644, 283

Kaufman, M. J., Wolfire, M. G., Hollenbach, D. J., & Luhman, M. L. 1999, The Astrophysical Journal, 527, 795

Kemper, F., Woods, P. M., Antoniou, V., et al. 2010, Publications of the Astronomical Society of the Pacific, 122, 683

Kennicutt, R. C., J. & Hodge, P. W. 1986, The Astrophysical Journal, 306, 130

Kennicutt, Robert C., J. 1998, The Astrophysical Journal, 498, 541

Kennicutt, Robert C., J. & de los Reyes, M. A. C. 2020, arXiv e-prints, arXiv:2012.05363

Kennicutt, R. C., Calzetti, D., Aniano, G., et al. 2011, Publications of the Astronomical Society of the Pacific, 123, 1347

Kennicutt, R. C. & Evans, N. J. 2012, Annual Review of Astronomy and Astrophysics, 50, 531

Kewley, L. J., Dopita, M. A., Sutherland, R. S., Heisler, C. A., & Trevena, J. 2001, The Astrophysical Journal, 556, 121

Kunkel, W. E., Demers, S., Irwin, M. J., & Albert, L. 1997, The Astrophysical Journal, 488, L129

Kunth, D. & Östlin, G. 2000, The Astronomy and Astrophysics Review, 10, 1

Kurt, C. M. & Dufour, R. J. 1998, in Revista Mexicana de Astronomia y Astrofisica Conference Series, Vol. 7, Revista Mexicana de Astronomia y Astrofisica Conference Series, ed. R. J. Dufour & S. Torres-Peimbert, 202

Le Fèvre, O., Bethermin, M., Faisst, A., et al. 2020, in Uncovering Early Galaxy Evolution in the ALMA and JWST Era, ed. E. da Cunha, J. Hodge, J. Afonso, L. Pentericci, & D. Sobral, Vol. 352, 210–215

Le Petit, F., Nehmé, C., Le Bourlot, J., & Roueff, E. 2006, The Astrophysical Journal Supplements, 164, 506

Lebouteiller, V., Bernard-Salas, J., Whelan, D. G., et al. 2011, The Astrophysical Journal, 728, 45

Lebouteiller, V., Cormier, D., Madden, S. C., et al. 2019, Astronomy & Astrophysics, 632, A106

Lebouteiller, V., Cormier, D., Madden, S. C., et al. 2012a, Astronomy & Astrophysics, 548, A91

Lebouteiller, V., Péquignot, D., Cormier, D., et al. 2017, Astronomy & Astrophysics, 602, A45

Lebouteiller, V., Sloan, G. C., Groenewegen, M. A. T., et al. 2012b, Astronomy & Astrophysics, 546, A94

Lee, M. G., Freedman, W., Mateo, M., et al. 1993, Astronomical Journal, 106, 1420

Lee, M. Y., Madden, S. C., Le Petit, F., et al. 2019, Astronomy & Astrophysics, 628, A113

Leger, A. & Puget, J. L. 1984, Astronomy & Astrophysics, 500, 279

Lequeux, J. 2003, The Interstellar Medium (Astronomy and Astrophysics Library)

Lequeux, J., Peimbert, M., Rayo, J. F., Serrano, A., & Torres-Peimbert, S. 1979, Astronomy & Astrophysics, 500, 145

Leroy, A. K., Bigiel, F., de Blok, W. J. G., et al. 2012, The Astronomical Journal, 144, 3

Leroy, A. K., Bolatto, A., Bot, C., et al. 2009, The Astrophysical Journal, 702, 352

Lian, J., Thomas, D., Li, C., et al. 2019, Monthly Notices of the Royal Astronomical Society, 489, 1436

Lucke, P. B. & Hodge, P. W. 1970, The Astronomical Journal, 75, 171

Madau, P. & Dickinson, M. 2014, Annual Review of Astronomy and Astrophysics, 52, 415

Madau, P., Ferguson, H. C., Dickinson, M. E., et al. 1996, Monthly Notices of the Royal Astronomical Society, 283, 1388

Madden, S. C., Cormier, D., Hony, S., et al. 2020, Astronomy & Astrophysics, 643, A141

Madden, S. C., Cormier, D., & Rémy-Ruyer, A. 2016, in From Interstellar Clouds to Star-Forming Galaxies: Universal Processes?, ed. P. Jablonka, P. André, & F. van der Tak, Vol. 315, 191–198

Madden, S. C., Galliano, F., Jones, A. P., & Sauvage, M. 2006, Astronomy & Astrophysics, 446, 877

Madden, S. C., Rémy-Ruyer, A., Galametz, M., et al. 2013, Publications of the Astronomical Society of the Pacific, 125, 600

Malhotra, S., Kaufman, M. J., Hollenbach, D., et al. 2001, The Astrophysical Journal, 561, 766

Marble, A. R., Engelbracht, C. W., van Zee, L., et al. 2010, The Astrophysical Journal, 715, 506

Martín-Hernández, N. L., Peeters, E., & Tielens, A. G. G. M. 2008, Astronomy & Astrophysics, 489, 1189

Marzke, R. O. & da Costa, L. N. 1997, The Astronomical Journal, 113, 185

Massey, P., Waterhouse, E., & DeGioia-Eastwood, K. 2000, The Astronomical Journal, 119, 2214

Mathewson, D. S., Cleary, M. N., & Murray, J. D. 1974, The Astrophysical Journal, 190, 291

Mathis, J. S., Mezger, P. G., & Panagia, N. 1983, Astronomy & Astrophysics, 500, 259

Mathis, J. S., Rumpl, W., & Nordsieck, K. H. 1977, The Astrophysical Journal, 217, 425

McConnachie, A. W. 2012, The Astronomical Journal, 144, 4

McLeod, A. F., Dale, J. E., Evans, C. J., et al. 2019, Monthly Notices of the Royal Astronomical Society, 486, 5263

Meixner, M., Galliano, F., Hony, S., et al. 2010, Astronomy & Astrophysics, 518, L71

Meixner, M., Gordon, K. D., Indebetouw, R., et al. 2006, The Astronomical Journal, 132, 2268

Meixner, M., Panuzzo, P., Roman-Duval, J., et al. 2013, The Astronomical Journal, 146, 62

Meyer, D. M., Jura, M., & Cardelli, J. A. 1998, The Astrophysical Journal, 493, 222

Mollá, M., García-Vargas, M. L., & Bressan, A. 2009, Monthly Notices of the Royal Astronomical Society, 398, 451

Moretti, M. I., Clementini, G., Muraveva, T., et al. 2014, Monthly Notices of the Royal Astronomical Society, 437, 2702

Nazé, Y., Chu, Y.-H., Points, S. D., et al. 2001, The Astronomical Journal, 122, 921

Ochsendorf, B. B., Zinnecker, H., Nayak, O., et al. 2017, Nature Astronomy, 1, 784

Oey, M. S. & Massey, P. 1995, The Astrophysical Journal, 452, 210

Offner, S. S. R., Bisbas, T. G., Bell, T. A., & Viti, S. 2014, Monthly Notices of Royal Astronomical Society, 440, L81

O'Halloran, B., Satyapal, S., & Dudik, R. P. 2006, The Astrophysical Journal, 641, 795

Okada, Y., Güsten, R., Requena-Torres, M. A., et al. 2019, Astronomy & Astrophysics, 621, A62

Olsen, K. A. G., Zaritsky, D., Blum, R. D., Boyer, M. L., & Gordon, K. D. 2011, The Astrophysical Journal, 737, 29

Osterbrock, D. E. & Ferland, G. J. 2006, Astrophysics of gaseous nebulae and active galactic nuclei (University Science Books)

Ott, S. 2010, in Astronomical Society of the Pacific Conference Series, Vol. 434, Astronomical Data Analysis Software and Systems XIX, ed. Y. Mizumoto, K. I. Morita, & M. Ohishi, 139

Pagel, B. E. J. 1997, Nucleosynthesis and Chemical Evolution of Galaxies

Pagel, B. E. J. 2003, in Astronomical Society of the Pacific Conference Series, Vol. 304, CNO in the Universe, ed. C. Charbonnel, D. Schaerer, & G. Meynet, 187

Parker, J. W., Hill, J. K., Bohlin, R. C., et al. 1996, The Astrophysical Journal Letters, 472, L29

Peña, M. & Flores-Durán, S. N. 2019, Revista Mexicana de Astronomía y Astrofísica, 55, 255

Pilbratt, G. L., Riedinger, J. R., Passvogel, T., et al. 2010, Astronomy and Astrophysics, 518, L1

Poglitsch, A., Waelkens, C., Geis, N., et al. 2010, Astronomy and Astrophysics, 518, L2

Polles, F. L., Madden, S. C., Lebouteiller, V., et al. 2019, Astronomy & Astrophysics, 622, A119

Popesso, P., Morselli, L., Concas, A., et al. 2019, Monthly Notices of the Royal Astronomical Society, 490, 5285

Putman, M. E., Gibson, B. K., Staveley-Smith, L., et al. 1998, Nature, 394, 752

Reid, W. A., Payne, J. L., Filipović, M. D., et al. 2006, Monthly Notices of the Royal Astronomical Society, 367, 1379

Rémy-Ruyer, A., Madden, S. C., Galliano, F., et al. 2014, Astronomy & Astrophysics, 563, A31

Rémy-Ruyer, A., Madden, S. C., Galliano, F., et al. 2015, Astronomy & Astrophysics, 582, A121

Requena-Torres, M. A., Israel, F. P., Okada, Y., et al. 2016, Astronomy & Astrophysics, 589, A28

Rieke, G. H., Young, E. T., Engelbracht, C. W., et al. 2004, The Astrophysical Journal Supplement Series, 154, 25

Robitaille, T. P. & Whitney, B. A. 2010, The Astrophysical Journal Letters, 710, L11

Röllig, M., Abel, N. P., Bell, T., et al. 2007, Astronomy & Astrophysics, 467, 187

Roman-Duval, J., Gordon, K. D., Meixner, M., et al. 2014, The Astrophysical Journal, 797, 86

Rosado, M., Laval, A., Le Coarer, E., et al. 1996, Astronomy & Astrophysics, 308, 588

Rubin, D., Hony, S., Madden, S. C., et al. 2009, Astronomy & Astrophysics, 494, 647

Rubio, M., Barbá, R. H., & Kalari, V. M. 2018, Astronomy & Astrophysics, 615, A121

Rubio, M., Contursi, A., Lequeux, J., et al. 2000, Astronomy & Astrophysics, 359, 1139

Ruiz-Lara, T., Gallart, C., Monelli, M., et al. 2020, Astronomy & Astrophysics, 639, L3

Russell, S. C. & Dopita, M. A. 1992, The Astrophysical Journal, 384, 508

Saintonge, A., Catinella, B., Tacconi, L. J., et al. 2017, The Astrophysical Journal Supplement Series, 233, 22

Savage, B. D. & Sembach, K. R. 1996, Annual Review of Astronomy and Astrophysics, 34, 279

Schmidt, M. 1959, The Astrophysical Journal, 129, 243

Schmidt, T., Cioni, M.-R. L., Niederhofer, F., et al. 2020, Astronomy & Astrophysics, 641, A134

Schruba, A., Leroy, A. K., Walter, F., et al. 2012, The Astronomical Journal, 143, 138

Seale, J. P., Looney, L. W., Wong, T., et al. 2012, The Astrophysical Journal, 751, 42

Shin, K., Ly, C., Malkan, M. A., et al. 2020, Monthly Notices of the Royal Astronomical Society, 0, 0

Smith, J. D. T., Armus, L., Dale, D. A., et al. 2007, The Publications of the Astronomical Society of the Pacific, 119, 1133

Stacey, G. J. 2011, IEEE Transactions on Terahertz Science and Technology, 1, 241

Stanimirovic, S., Staveley-Smith, L., Dickey, J. M., Sault, R. J., & Snowden, S. L. 1999, Monthly Notices of the Royal Astronomical Society, 302, 417

Stephens, I. W., Evans, J. M., Xue, R., et al. 2014, The Astrophysical Journal, 784, 147

Sternberg, A., Le Petit, F., Roueff, E., & Le Bourlot, J. 2014, The Astrophysical Journal, 790, 10

Sutter, J., Dale, D. A., Croxall, K. V., et al. 2019, The Astrophysical Journal, 886, 60

Tacconi, L. J., Genzel, R., Neri, R., et al. 2010, Nature, 463, 781

Tacconi, L. J., Genzel, R., & Sternberg, A. 2020, Annual Review of Astronomy and Astrophysics, 58, 157

Thuan, T. X., Hunt, L. K., & Izotov, Y. I. 2008, The Astrophysical Journal, 689, 897

Thuan, T. X. & Martin, G. E. 1981, The Astrophysical Journal, 247, 823

Tielens, A. G. G. M. 2005, The Physics and Chemistry of the Interstellar Medium (Cambridge University Press)

Tielens, A. G. G. M. 2008, Annual Revview of Astronomy & Astrophysics, 46, 289

Tielens, A. G. G. M. & Hollenbach, D. 1985, The Astrophysical Journal, 291, 722

Toribio San Cipriano, L., Domínguez-Guzmán, G., Esteban, C., et al. 2017, Monthly Notices of the Royal Astronomical Society, 467, 3759

Tremonti, C. A., Heckman, T. M., Kauffmann, G., et al. 2004, The Astrophysical Journal, 613, 898

Tsamis, Y. G., Barlow, M. J., Liu, X. W., Danziger, I. J., & Storey, P. J. 2003, Monthly Notice of the Royal Astronomical Society, 338, 687

Valdivia, M. T., Muñoz, M., Rubio, M., & Saldaño, H. 2019, Boletin de la Asociacion Argentina de Astronomia La Plata Argentina, 61, 134

van der Marel, R. P. & Cioni, M.-R. L. 2001, The Astronomical Journal, 122, 1807

Walborn, N. R. & Parker, J. W. 1992, The Astrophysical Journal Letters, 399, L87

Walker, A. R. 2012, Astrophysics and Space Science, 341, 43

Walker, K. M., Song, L., Yang, B. H., et al. 2015, The Astrophysical Journal, 811, 27

Walter, F., Decarli, R., Sargent, M., et al. 2014, The Astrophysical Journal, 782, 79

Watson, W. D. 1972, The Astrophysical Journal, 176, 103

Weingartner, J. C. & Draine, B. T. 2001a, The Astrophysical Journal, 548, 296

Weingartner, J. C. & Draine, B. T. 2001b, The Astrophysical Journal, 563, 842

Weingartner, J. C. & Draine, B. T. 2001c, The Astrophysical Journal Supplement Series, 134, 263

Werner, M. W., Roellig, T. L., Low, F. J., et al. 2004, The Astrophysical Journal Supplement Series, 154, 1

Westerlund, B. E., Azzopardi, M., Breysacher, J., & Rebeirot, E. 1991, in The Magellanic Clouds, ed. R. Haynes & D. Milne, Vol. 148, 116

Whelan, D. G., Lebouteiller, V., Galliano, F., et al. 2013, The Astrophysical Journal, 771, 16

Wilcots, E. M. 1994, The Astronomical Journal, 107, 1338

Wolfire, M. G., Hollenbach, D., & McKee, C. F. 2010, The Astrophysical Journal, 716, 1191

Wolfire, M. G., Hollenbach, D., McKee, C. F., Tielens, A. G. G. M., & Bakes, E. L. O. 1995, The Astrophysical Journal, 443, 152

Wolfire, M. G., Tielens, A. G. G. M., & Hollenbach, D. 1990, The Astrophysical Journal, 358, 116

Wong, T., Hughes, A., Ott, J., et al. 2011, The Astrophysical Journal Supplement, 197, 16

Zahid, H. J., Bresolin, F., Kewley, L. J., Coil, A. L., & Davé, R. 2012, The Astrophysical Journal, 750, 120